

Life Extension for Wind Turbine Structures and Foundations

Tim Rubert

Institute for Energy & Environment
Doctoral Training Center for Wind and Marine Energy Systems
University of Strathclyde, Glasgow

August 30, 2018

Declaration

This thesis is the result of the author's original research. It has been composed by the author and has not been previously submitted for examination which has led to the award of a degree.

The copyright of this thesis belongs to the author under the terms of the United Kingdom Copyright Acts as qualified by University of Strathclyde Regulation 3.50. Due acknowledgement must always be made of the use of any material contained in, or derived from, this thesis.

Signed:

Date:

Contents

List of Figures	vii
List of Tables	xv
Acknowledgements	xxvi
Abstract	xxvii
1 Introduction	2
2 Principal Contributions	10
3 Literature Review	13
3.1 Available Literature	13
3.1.1 Wind Turbine Structural Health Monitoring	13
3.1.2 Economics and Lifetime Extension	16
3.2 Research Proposal	17
3.3 Theoretical Background	19
3.3.1 Optics	19
3.3.2 Civil Engineering Structures	28
3.3.2.1 Support Types	29
3.3.2.2 Euler-Bernoulli Beam Theory	29
3.3.2.3 Reinforced Concrete	34
3.3.2.3.1 Cement Curing	34
3.3.2.3.2 Design of a Reinforced Concrete Beam	36

Contents

3.3.3	Fatigue	42
3.3.3.1	Fatigue General	42
3.3.3.2	Fatigue of Members, Connections, and Joints	50
3.3.3.3	Damage Equivalent Loads	52
3.3.3.4	Crack Initiation and Propagation	53
3.3.4	Economics	55
3.3.5	Wind Turbine Generators	59
3.3.5.1	Factors affecting Individual Turbine Loading	61
3.3.5.2	Wind Turbine Foundations	66
3.3.5.3	Foundation Design	71
3.3.5.3.1	Geotechnical Design	72
3.3.5.3.2	Structural Design	73
3.3.5.4	Life Extension	74
3.3.5.4.1	DNV GL Lifetime Extension Standard	75
3.3.5.4.2	UL Lifetime Extension Standard	79
4	Economic Lifetime Extension Decision-Making	80
4.1	The State-of-the-Art of the UK's Lifetime Extension	81
4.1.1	Introduction	81
4.1.2	The UK's Historical Wind Energy Deployment	81
4.1.3	Survey Methodology	84
4.1.4	Complimentary Survey Results	84
4.1.5	Limitations	86
4.1.6	Section Conclusions	87
4.2	Wind Turbine Performance Degradation	88
4.3	Reproduction of LCOE	90
4.3.1	Input Data	93
4.3.2	Results & Sensitivity Analysis	96
4.3.3	Model Limitations	99
4.4	A Decision Support Tool to Assist with Lifetime Extension of Wind Turbines	101

Contents

4.4.1	Levelised Cost of Energy	102
4.4.1.1	Model Input Parameters	104
4.4.1.1.1	Operational Expenditure	105
4.4.1.1.2	Capital Expenditure	106
4.4.1.1.3	Yield Estimation	107
4.4.1.1.4	Components of Lifetime Extension Analysis . .	108
4.4.1.1.5	Other Tool Parameters	109
4.4.1.2	Lifetime Extension Methodology	110
4.4.2	Lifetime Extension Case Study	112
4.4.3	Results	114
4.4.4	Validation	118
4.4.5	Limitations and Future Work	118
4.4.6	Section Conclusions	120
4.4.7	Section Appendix	121
4.5	The Effect of Upscaling and Performance Degradation on Onshore Wind Turbine Lifetime Extension decision-making	123
4.5.1	Upscaling	123
4.5.1.1	Yield Modelling	124
4.5.1.2	Expenditure Modelling	127
4.5.1.3	Other Assumptions	128
4.5.2	Performance Degradation	128
4.5.3	Results	131
4.5.3.1	Upscaling	131
4.5.3.2	Performance degradation	133
4.5.4	Discussion and Future Work	135
4.5.5	Section Conclusions	138
4.5.6	Section Appendix	139
4.6	Lifetime Extension - The Case of BVG Associates	140
4.6.1	Introduction	140
4.6.2	Methodology	140

Contents

4.6.3	Case Studies	142
4.6.4	Results	142
4.6.4.1	Site A	142
4.6.4.2	Site B	145
4.6.5	Section Conclusions	145
5	Structural Health Monitoring of Wind Turbine Structures	150
5.1	Characterisation of metal-packaged fibre Bragg gratings under fatigue loading	151
5.1.1	Sensor Design	151
5.1.2	Sensor Fabrication	153
5.1.2.1	Methodology	154
5.1.2.2	Results of Brazing Monitoring	154
5.1.3	Thermal Characterisation and Calibration	156
5.1.3.1	Sensor Characterisation and Calibration	156
5.1.3.1.1	Methodology	156
5.1.3.1.2	Results	157
5.1.3.2	Calibration of Sensors Attached to Reinforcement Bar .	162
5.1.4	Fatigue Experiment	165
5.1.4.1	Methodology	166
5.1.4.2	Results	167
5.1.4.2.1	Fatigue Results	167
5.1.4.2.2	Sensor's Characteristics	172
5.1.4.3	Section Conclusions	174
5.2	Sensor Improvement	176
5.2.1	Evaluation of Spot Weld Process	176
5.2.2	Embedded Temperature Test	178
5.2.3	Sensor Improvement Iterations	180
5.3	Installation of Embedded Optical Sensors within a Wind Turbine Foundation at the Windfarm	181
5.3.1	V117 - Foundation and Finite Element Analysis	185

Contents

5.3.1.1	General Information	185
5.3.1.2	Finite Element Model	185
5.3.2	Network Requirements and Sensor Packaging	187
5.3.3	Sensor Preparation	190
5.3.3.1	Sensor Fabrication	190
5.3.3.2	Evaluation of Sensor Brazing	193
5.3.3.3	Thermal Characterisation and Calibration	197
5.3.3.3.1	Methodology	198
5.3.3.3.2	Results	198
5.3.4	Sensor Installation	201
5.3.4.1	Assessment of Sensor Placement and Orientation	201
5.3.4.2	Sensor Installation	205
5.3.4.3	Results	209
5.3.5	Results of Monitoring Campaign	212
5.3.5.1	Sensor Data	212
5.3.5.2	FE Comparison	219
5.3.6	Validation	220
5.3.7	Commercial Evaluation	224
5.3.8	Learning Experience	228
5.3.9	Discussion and Future Work	233
5.3.10	Section Conclusions	234
5.4	New Sensor Design	235
5.4.1	Methodology	235
5.4.1.1	Stage 1	236
5.4.1.2	Stage 2	237
6	Economic Lifetime Extension Based on SHM	239
6.1	SHM Campaign	239
6.1.1	Tower SHM	239
6.1.2	Foundation SHM	246
6.2	Lifetime Extension Methodology	247

Contents

6.3	Lifetime Extension Case Study	248
6.3.1	Strategy	248
6.3.2	Input Data	249
6.4	Results	251
6.5	Discussion and Future Work	256
6.6	Section Conclusions	259
6.7	Section Appendix	260
7	Conclusion	261
7.1	Economic Lifetime Extension	262
7.2	Sensor Development	263
7.3	Supportive Lifetime Extension SHM	264
7.4	Recommendations for Action	267
7.5	Outlook	269
A	Graphs, Figures, and Tables	271
B	LTE Standards	293
B.1	DNV GL	293
B.2	UL	295
C	LTE Survey Questions	301
	Bibliography	301

List of Figures

1.1	European Installed Capacity [4–8]	3
1.2	Turbines reaching End of Lifetime in Europe [4–8]	7
1.3	Turbines Out of Warranty [27]	7
3.1	Fibre Optical Strand	20
3.2	Fibre Bragg Grating [63]	22
3.3	Schematic Reflection Pattern	23
3.4	Beam Support Types	30
3.5	Beam Reaction Force Example	31
3.6	Example of Loads Along Beam	31
3.7	Stress Derivation From Deflection	32
3.8	Beam - Stress and Strain Distribution	33
3.9	Schematic Curing of Concrete	35
3.10	Reinforced Concrete Theory [93]	36
3.11	Idealised Stress Distribution Reinforced Concrete [94]	38
3.12	Vertical Stirrups	40
3.13	Concrete Cover [94]	42
3.14	Crack Control [mm] [94]	43
3.15	Difference in Fatigue Behaviour [94, 96, 97]	44
3.16	Simplistic Fatigue Example	45
3.17	Goodman Diagram [99]	49
3.18	Fatigue strength curves for direct stress ranges. The curves are derived based on a 95% survival probability at a 75% confidence interval. [107].	52

List of Figures

3.19	Wind Turbine Up-Scaling (modified from [122]); 2015: Offshore	60
3.20	Wind Rose Comparison	62
3.21	Rotor: Two-Lumped Parameter Model	63
3.22	Natural Rotor Modes a-c) First Natural Rotor Mode, d) Static Turbine Behaviour e-f) Second Natural Rotor Mode (Umbrella-Mode)	64
3.23	Wind Turbine Loading a) Force Profile; b) Simplified Moment	67
3.24	Foundation Load Center [133]	68
3.25	Dead & Overturning Load	69
3.26	Spread Foundation Types (modified from [106]) a) Plain Slab; b) Stub and Pedestal; c) Tapered Slab; d) Slab and Pedestal with Webs	70
4.1	Annual capacity in the UK that will reach the end of lifetime (20 years) in the future [147].	82
4.2	Annually installed turbines from 1995, paired with the average annually installed turbine size [147].	83
4.3	Distribution of turbine capacity reaching its 20th year of operation [147]. Boundary turbines are categorised in the higher class.	83
4.4	Wind Turbine Performance Degradation [157]	88
4.5	Wind Turbine Performance Degradation (Class ≥ 3 MW)	91
4.6	O&M Cost Breakdown in % [70]	95
4.7	Onshore capacity reaching end of design lifetime in the UK (20 years) [147]	102
4.8	Schematic overview of lifetime extension LCOE methodology	110
4.9	$LCOE_2$ model results	116
4.10	O&M cost breakdown in % [70]	121
4.11	LCOE model results	122
4.12	Distribution of WTGs reaching their end of design lifetime (20 years) [144].	123
4.13	Simulated power curve with respect to the 10-minute mean wind speed, $P_{Sim}(v_a)$ on the left axis and wind speed probability distribution, $P_w(v_a)$ on the right axis.	125

List of Figures

4.14	Modelled turbine parameters and their compound effect on capacity factor and AEP. The mean wind speed (b) is derived from the wind shear power law based on the modelled hub height (a), while the annual energy production (e) and hence capacity factor (d) is the result of the mean wind speed (b), rotor diameter (c) as well as the Weibull distribution and modelled power curve (Figure 4.13). A square displays an average turbine parameter, whereas a dot indicates encountered min/max parameters.	126
4.15	LCOE ₂ +5 years upscaling results. This analysis is CAPEX independent. Subsidy-free (SF)/Renewable Obligation (RO).	132
4.16	Impact of PD on an 18 MW wind farm consisting of 20 x 900 kW WTGs (LCOE applies CAPEX assumption).	134
4.17	Impact of PD on an 18 MW wind farm consisting of 9 x 2 MW WTGs (LCOE applies CAPEX assumption).	139
4.18	Lifetime extension decision methodology [145].	141
4.19	<i>Site A</i> LCOE ₂ of no reconditioning and drive train exchange based on 7 years of additional life.	146
4.20	<i>Site B</i> LCOE ₂ of no reconditioning and drive train exchange based on 7 years of additional life.	146
4.21	<i>Site B</i> with risk LCOE ₂ of no reconditioning and drive train exchange based on 7 years of additional life with risk contingency.	146
4.22	<i>Site A</i> LCOE ₂ of single component replacement (+7 years).	147
4.23	<i>Site B</i> LCOE ₂ of single component replacement (+7 years).	147
4.24	<i>Site B</i> with risk LCOE ₂ of single component replacement (+7 years) with risk contingency.	147
4.25	<i>Site A</i> LCOE ₂ of double component replacement (+7 years).	148
4.26	<i>Site B</i> LCOE ₂ of double component replacement (+7 years).	148
4.27	<i>Site B</i> with risk LCOE ₂ of double component replacement (+7 years) with risk contingency.	148
5.1	Schematic Overview of FBG Temperature Sensors	152

List of Figures

5.2	Schematic Overview of Strain Sensor	153
5.3	Layout of Sensor Manufacture [60]	154
5.4	Shift in FBG centre wavelength during brazing of second capillary end .	155
5.5	Characteristics of the epoxy bonded temperature sensors thermally cycled three times. The characteristics are normalised by subtraction of the y-intercept.	158
5.6	Characteristics of the metal packaged temperature sensors thermally cycled three times. The characteristics are normalised by subtraction of the y-intercept.	159
5.7	Characteristics of the metal packaged strain sensors thermally cycled three times. The characteristics are normalised by subtraction of the y-intercept.	161
5.8	Sensors attached to Reinforcement Bar	163
5.9	Characteristics of the temperature sensors attached to reinforcement bar cycled three times. The characteristics are normalised by subtraction of the y-intercept.	164
5.10	Characteristics of the strain sensors and reinforcement bar cycled three times. The characteristics are normalised by subtraction of the y-intercept.	164
5.11	Instron 8802 Rebar & Sensor Fatigue Test	165
5.12	First Fatigue Test - Rebar & Sensor	169
5.13	Second Rebar and Sensor Fatigue Test	170
5.14	Rebar Fatigue Cycles in Comparison to Available Research	172
5.15	Rebar Fracture Surface	173
5.16	Spot Weld Evaluation	177
5.17	Weld Area FEM	178
5.18	Characteristics of the metal-packaged strain and temperature sensors thermally cycled three times. The characteristics are normalised by subtraction of the y-intercept.	179
5.19	Turbine Site Layout. For the elevation profile, the reader is referred to Figure A.11 of Appendix A.	183

List of Figures

5.20	Wind Rose of Wind Farm.	184
5.21	FE model a) mesh and wind vector; b) boundary conditions; and c) typical normalised strain profiles in circumferential, radial and axial directions.	186
5.22	Schematic optical network diagram	188
5.23	Strain sensor's designed end	189
5.24	Manufactured FBG strain sensor	191
5.25	SSE Sensor Overview	192
5.26	Scatter diagram of manufactured sensor's maximum peak shift vs. the absolute final compression	194
5.27	Example of SSE sensor thermal characterisation	199
5.28	Schematic overview of sensor locations. The A-A line is the foundation centre. Red dots indicate the strain sensor placement within the foundation	204
5.29	Rebar selection	207
5.30	Sensor installation overview - a) surface preparation, b) prepared surface, c) sensor attachment (spot welding), d) attached sensor, e) sensor protection	210
5.31	Inspection of foundation after concrete pour	211
5.32	Signal processing and temperature compensation of a tower location . .	213
5.33	Signal processing and temperature compensation of foundation location	214
5.34	Time series of normalised strain of circumferential foundation and parallel tower sensor. Each sensor is normalised separately.	215
5.35	Time series of normalised strain of circumferential foundation and 90 deg rotated tower sensor. Each sensor is normalised separately.	215
5.36	Normalised correlation of shear link strain with parallel tower sensor.	215
5.37	Normalised correlation of shear link strain with 90 deg rotated tower sensor.	215
5.38	Time series of normalised strain of shear foundation and parallel tower sensor. Each sensor is normalised separately.	217

List of Figures

5.39	Time series of normalised strain of shear foundation and 90 deg rotated tower sensor. Each sensor is normalised separately.	217
5.40	Normalised correlation of shear link strain with parallel tower sensor.	217
5.41	Normalised correlation of shear link strain with 90 deg rotated tower sensor.	217
5.42	Time series of sensor measurements. The red line indicates the dead load condition.	218
5.43	Normalised change in strain in shear link and circumferential rebars, extracted from the FE model. Positive overturning moments follow the wind vector given in Figure 5.21	220
5.44	Mesh and sensor locations before and after loading (deformed mesh scaled by 10^3).	220
5.45	Power spectral density of strain and temperature sensors with rotational sampling and harmonics. Temperature sensor: raw data; FBG strain gauge: temperature compensated.	221
5.46	Power spectral density of strain and temperature sensors with natural frequencies. Temperature sensor: raw data; FBG strain gauge: temperature compensated.	222
5.47	Power spectral density of foundation and bottom tower FBG strain gauges. Temperature sensor: raw data; strain gauge: temperature compensated.	223
5.48	Long term validation based on yaw retwist events for tower sensor 1. The x-axis represents separate time events with the exact date of retwist illustrated in the legend. Each retwist event is roughly a 10-minute period. The legend also states the magnitude of the observed signal at the given time.	224

List of Figures

5.49	Long term validation based on yaw retwist events for tower sensor 2. The x-axis represents separate time events with the exact date of retwist illustrated in the legend. Each retwist event is roughly a 10-minute period. The legend also states the magnitude of the observed signal at the given time.	225
5.50	Long term validation based on yaw retwist events for circumferential foundation strain. The x-axis represents separate time events with the exact date of retwist illustrated in the legend. Each retwist event is roughly a 10-minute period. The legend also states the magnitude of the observed signal at the given time.	225
5.51	Detailed commercial Evaluation	227
5.52	Commercial evaluation results	227
5.53	New Sensor Iteration Testing	236
5.54	New Sensor Iteration Testing Results	238
6.1	Schematic of tower sensor positions with respect to prevailing wind di- rection	241
6.2	Strain data of base tower measurement (T1)	241
6.3	Strain data of 90° rotated base tower measurement (T2)	242
6.4	Identification of prevailing wind direction, β based on $\gamma(t)$ binning. . . .	243
6.5	Strain data of derived prevailing wind direction	244
6.6	Impact of binning width on lifetime prediction	245
6.7	Impact of sampling frequency on lifetime prediction based on a 0.2 MPa binning width	246
6.8	Lifetime extension decision methodology [145]	248
6.9	LCOE ₂ of lifetime extension period with annual energy production (no retrofitting and drive train exchange)	252
6.10	LCOE ₂ of lifetime extension period with annual energy production (sin- gle retrofit)	253
6.11	LCOE ₂ of lifetime extension period with annual energy production (dou- ble retrofit)	253

List of Figures

6.12 Monte Carlo analysis of LCOE ₂ of no component replacement	255
6.13 Monte Carlo analysis of LCOE ₂ of drive train exchange	256
7.1 Overview of Thesis Research Approach	262
A.7 Non Pre-Stressed Sensor - Characteristics	272
A.8 Pre-Stressed Sensor - Characteristics	273
A.9 Overview of fatigue test results	274
A.13 Lifetime Extension - Inspection List (DNV GL) [23]	275
A.14 SSE sensor characteristics - Channel 1	276
A.15 SSE sensor characteristics - Channel 2	277
A.16 SSE sensor characteristics - Channel 3	278
A.17 SSE sensor characteristics - Channel 4	279
A.18 Foundation ring cage	280
A.1 PhD First Year Project Plan	281
A.2 Mind Map - Life Extension Parameters	282
A.3 Sensor Temperature Characterisation	283
A.4 Second Brazing - Change in Spectrum	284
A.5 Hysteresis of Non-Prestressed Sensor and Machine Data	285
A.6 Hysteresis of Prestressed Sensor and Machine Data	286
A.10 Methodology - Wind Turbine Performance Degradation	287
A.11 Site Layout	288
A.12 Foundation Layout	289
A.19 SSE sensor site installation	290
C.1 Semi-structured survey questions (1/4)	302
C.2 Semi-structured survey questions (2/4)	303
C.3 Semi-structured survey questions (3/4)	304
C.4 Semi-structured survey questions (4/4)	305

List of Tables

3.1	Properties of Optical fibres (modified from [59])	21
3.2	Advantages and Disadvantages of FBGs (modified from [32])	27
3.3	Estimates of S_{1000} . (USS - Ultimate Shear Strength)	47
3.4	Crack growth parameters	54
3.5	DECC's Onshore >5 MW Wind Energy Deployment Cost Assumptions [117]	59
3.6	ULS & ALS Loadfactors [128]	66
3.7	ULS Example Design Load Case [139]	73
3.8	IEC Wind Turbine Classes [140]	74
3.9	Reasons for Continued Operation [141]	75
4.1	Performance Based Maintenance Overview of Analysed Wind Farms \geq 3 MW	92
4.2	LCOE - Wind Turbine Parameters	94
4.3	LCOE - Sensitivity Analysis (1/2)	97
4.4	LCOE - Sensitivity Analysis (2/2)	98
4.5	Comparison of fixed and variable O&M expenditure for a 900 kW wind turbine over 20 years. The turbine is the modelled type of the case study presented in Section 4.4.2. Inflation data from References [178–180]. Currency conversion factor from historical 5 year average (2014-2018). .	105
4.6	Difference in UK OPEX Assumptions [117, 181].	106
4.7	Components of lifetime extension analysis in the UK. Derived from [144] and expert knowledge (Table 4.11 of the Appendix)	108

List of Tables

4.8	LCOE - Wind turbine parameters	113
4.9	Lifetime extension cost estimations for a wind farm consisting of six 900 kW WTGs	114
4.10	$LCOE_2$ annual contingency results. N/A: investment is not applicable (cost above set TH)	117
4.11	Overview of consulted UK experts	122
4.12	Sensitivity of lifetime extension model	122
4.13	Upscaling input parameters of selected 18 MW wind farm configurations. Cost estimates origin from literature [145].	124
4.14	Lifetime extension tool parameters [145]. Optimistic and pessimistic parameters are further presented for the supplement database [219]. . .	128
4.15	Comparison of available PD identification approaches	129
4.16	Comparison of the impact of PD on LCOE and $LCOE_2$ of a 0.9 MW versus a 2 MW WTG in %.	135
4.17	Comparison of the impact of PD on annual contingency of a 0.9 MW versus a 2 MW WTG in %.	136
4.18	Wind farm operational parameters. Operational, $CAPEX_{LTE}$, and component replacement expenditure is further subjected to a $\pm 10\%$ variation.	143
4.19	Site A annual contingency of 7 additional years under RO based on mean AEP of 1.78 GWh.	149
4.20	Site B annual contingency of 7 additional years under RO based on mean AEP of 0.95 GWh. N/A: costs are higher than the set threshold.	149
4.21	Site B with risk annual contingency of 7 additional years under RO based on mean AEP of 0.95 GWh with risk contingency. N/A: costs are higher than the set threshold.	149
5.1	Second Brazing Process - Wavelength Shift	156
5.2	Correlation Machine and Sensor Data	170
5.3	Testing Series	173
5.4	Initial Reflective Wavelength & STC	174
5.5	Summarised sensor fatigue tests	182

List of Tables

5.6	FEM Parameters and Possible Ranges	186
5.7	Sensor identification overview	193
5.8	Overview of all strain sensors' thermal characteristics	200
5.9	Overview of all temperature sensors' thermal characteristics	200
5.10	Dead Load Condition	219
5.11	Natural Frequencies of Wind Turbines [Hz]	221
5.12	Categorised learning experience	231
6.1	Process of Data Manipulation. PW: prevailing wind, HC: height correction, SC: section correction. Frequency of 380 times the first tower mode.	247
6.2	Wind turbine parameters	249
6.3	Lifetime extension cost estimations for a wind farm [145]	250
6.4	Annual Contingency [£] for 15 year LTE under different scenarios. N/A: costs exceed revenue	254
6.5	Project expenditure percentiles [£] based on Monte Carlo simulation	255
6.6	Tower & foundation inspection guideline. D is damage, C is cracks, Co is corrosion, Sp is safety sign plates, Ps is prestress, Cf is connection/fitting, and F is function. [23]	260
A.1	Stress distribution on tower elements (input data from [272]). The cross sectional moment of inertia and derived sectional stress are calculated with Equation 3.25 and 3.24.	291
A.2	Stress distribution on tower elements (input data from [267, 268]). The cross sectional moment of inertia and derived sectional stress are calculated with Equation 3.25 and 3.24.	292

List of Abbreviations

PV Photovoltaic

SSE Scottish and Southern Energy

SPR Scottish Power Renewables

UK United Kingdom

FiT Feed-in Tariff

EU European Union

WTG Wind Turbine Generator

EEG German Renewable Energy Act

GW Gigawatt

ROI Return On Investment

RO Renewable Obligation

LCOE Levelised Cost of Energy

IRR Internal Rate of Return

MW Megawatt

DNV GL Det Norske Veritas and Germanischer Lloyd

FBG Fibre Bragg Grating

List of Abbreviations

RUL Remaining Useful Lifetime

GFRP Glass Fibre Reinforced Plastic

CFRP Carbon Fibre Reinforced Plastic

SHM Structural Health Monitoring

EAW European Wind Energy Academy

NREL National Renewable Energy Laboratory

LCA Life Cycle Assessment

SCADA Supervisory Control and Data Acquisition

FEA Finite Element Analysis

MPa Mega Pascal

UV Ultraviolet

LED Light Emitting Diode

EMI Electromagnetic Interference

RFI Radio Frequency Interference

ULS Ultimate Limit State

SLS Serviceable Limit State

BMD Bending Moment Diagram

DLC Design Load Case

IEC International Electrotechnic Commission

UTS Ultimate Tensile Strength

DEL Damage Equivalent Load

NPV Net Present Value

List of Abbreviations

CAPEX Capital Expenditure

OPEX Operational Expenditure

AEP Net Annual Energy Production

CF Net Capacity Factor

DECC Department of Energy and Climate Change (now BEIS)

WACC Weighted Average Cost of Capital

HAWT Horizontal Axis Wind Turbines

LEI Lifetime Extension Inspection

CMS Condition Monitoring System

OEM Original Equipment Manufacturer

LTE Lifetime Extension

RPN Risk Priority Number

NDI Non-Destructive Inspection

PBMC Performance Based Maintenance Contract

IAV Inter-Annual Variability

REWS Rotor Equivalent Wind Speed

LTEA Lifetime Extension Analysis

TH Threshold

LEE Leading Edge Erosion

PD Performance Degradation

LCOE2 Levelised Cost of Energy of Lifetime Extension Period

SF Subsidy-free

List of Abbreviations

OREC Offshore Renewable Energy Catapult

MWh Megawatt Hour

EIA Environmental Impact Assessment

ID Inner Diameter

OD Outer Diameter

nm Nanometre

B500B Type of Reinforcement Steel

STC Strain Transfer Coefficient

kN Kilonewton

FFT Fast Fourier Transform

kHz Kilohertz

CAD Computer Aided Design

PSD Power Spectral Density

Nomenclature

c Speed of light in vacuum

v Phase velocity in a medium

n Material's refractive index

ν Frequency

θ_I Incidence angle

θ_R Refraction angle

E Young's Modulus

α Coefficient of thermal expansion

C Strain and temperature coefficient

N Number of cycles

λ Reflective wavelength

Λ Grating period or grating length

T Temperature

ϵ Strain

σ Stress

M Moment

Nomenclature

F Force

V Shear force

R Radius

I Cross sectional moment of inertia

EI Bending stiffness

A Area

d Diameter

λ_{fck} Concrete design class strength

λ_{fcd} Design stress for concrete

γ Safety factor

D Damage

B Stress related material constant

m Stress related material constant

Z Goodman exponent

K Material toughness

d Discount rate

i Interest rate

P Power

v Wind speed

C_p Power coefficient

β Pitch angle

C_T Thrust coefficient

Nomenclature

h Hub height

e Eccentricity

LC Load center

$^{\circ}C$ Degree celsius

$m\epsilon$ Millistrain

Acknowledgements

I would like to acknowledge both my supervisors Pawel Niewczas and David McMillan for their continuous support and contribution to this thesis, Grzegorz Fusiek for introducing me to the world of fibre optic sensing, my dear colleagues Giorgio Zorzi and Chandra Pun for the friendship and mutual support over the years, and Drew Smith for being the most awesome administrator at Strathclyde and a good friend.

Thanks to all individuals working at the Centre for Doctoral Training in Wind and Marine Energy, especially to my 2014 cohort consisting of James Stear, Owain Roberts, Ben McGilton, Rohaida Binti Hussain, Paul Hammond, Edward Hart, Oswaldo Barrera Martin, Giorgio Zorzi and Chandra Pun - each and every single one of you made the first training year a special memory for me. Thanks to my dear colleagues Alexander Giles and Cagatay Cebeci for all the good banter. I wish youse all the best in the future.

I also thank my industrial partners SSE and SPR as well as BVGAassociates for supporting this work for which I am very grateful. In addition, I would like to thank RES, Everoze, Innogy SE, Natural Power, and Siemens for contributing to the lifetime extension study in the UK.

Finally, thanks to my family, especially to my mother and father as well as Elisabeth who have supported me to finalise this chapter of my life.

Abstract

This thesis explores economic and technical lifetime extension considerations of wind turbine generators. The research unveils that onshore support structures will likely have sufficient fatigue reserves left, beyond the initial design life, to support an extended operation. However, suitability is strongly dependent on the difference between the design and encountered load profile, asset maintenance activities, operational knowledge, and the policy environment.

A lifetime extension decision model is developed and input parameters are scrutinised revealing the feasibility to replace the entire drive train of a wind turbine and yet, be profitable when exposed to a non-subsidised environment. The designed decision model is further applied based on operational data of two wind farms in the UK to derive an asset specific lifetime extension strategy.

In addition, a methodology and field trial is presented to monitor operational foundation stresses based on optical sensor networks aimed at reducing conservative design assumptions, enabling the reuse of foundations for greater rated turbines as well as to support the lifetime extension decision-making.

Furthermore, this thesis provides guidance on how to evaluate and obtain the strategic lifetime extension decision-making at an early stage (year 10-14) by means of a fatigue analysis of tower strain measurements. Fatigue tower findings in conjunction with operational data of an asset are subsequently assessed to define the turbine's/wind farm's unique economic lifetime extension boundaries.

Chapter 1

Introduction

The renewable energy industry is driven by governmental policies and incentives, as in the past devices fuelled by wind and solar energy as well as biomass have not been economically competitive with fossil energy resources such as oil, gas, and coal. Policy making is “the process by which governments translate their political vision into programmes and actions to deliver ‘outcomes’ - desired changes in the real world” [1]. The difficulty here is that energy regulation is complex, as the environment is under constant transition and additionally there are competing aims; e.g., (i) cost of energy, (ii) security of energy supply, (iii) clean energy, (iv) economic growth, etc. Furthermore, the government as well as the country’s economy itself undergo changes too, since a legislative period is limited to usually four to five years and the economic situation can change considerably as well as rapidly. The latter triggered for example due to slowing growth in emerging markets and its subsequent effects within today’s globalisation or shocks within commodities as experienced in 2015. Due to the nature of the wind resource; i.e., unsteady and difficult to predict much in advance, it is of high importance to review and scrutinise policies to maintain control within various objectives as briefly described before. As such, reviews can be used to either discard, maintain, scale up or scale down current policies. In general, reviews are positive mechanisms in order to control deliverables, especially if a program’s expenses surpass estimations as occurred in Germany and Italy with photovoltaic (PV) applications. Unfortunately, due to political and economic fluctuations, policy reviews may be impacted by governmen-

Chapter 1. Introduction

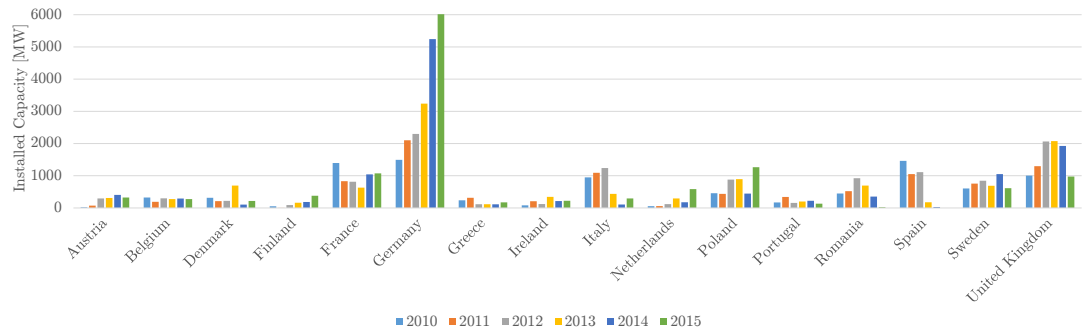


Figure 1.1: European Installed Capacity [4-8]

tal short-termism. Therefore, the political dependency is quite severe as when under jurisdiction by lawmakers, it is challenging to provide security and long term stability of energy policies. As power plants are defined by high investment costs, political uncertainty can have negative influences concerning the likelihood of investors to invest in renewable energy sources due to increased perceived risk.

The following introduction is based on findings in 2015, in order to justify the research objectives; however, at the end of the introduction an update is provided, highlighting the most severe changes, aimed at revealing how the environment has changed in 2018.

Stimulated by high subsidies at the beginning of the 21st century in order to reach the European 2020 targets, the recent boom within the European wind energy market has governments led to actively discuss and challenge their policies as most countries are well on track to reach their set targets, although the UK, France, Ireland, and the Netherlands appear to struggle [2,3]. The philosophy here is to not over-subsidise, hence to utilise governmental budgets most economically and to encourage the industry to innovate so that wind energy continuous to become more competitive. Figure 1.1 illustrates the total installed wind energy capacity of the European countries with the greatest wind energy investment between 2010 and 2015. A clear contrast emerges; on one hand, installed capacity increased notably (Germany and France) and on the other hand, it decreased significantly (Spain, Italy, and the United Kingdom). When look-

ing into governmental policies of these countries with significant changes, it is further verified that there exist a strong correlation between a country's wind energy policy or policy review and the changes in terms of installed wind energy.

With regards to France, the introduction of a new marked based subsidy scheme is expected in 2016, however it is unclear whether this policy change will account for on-shore wind too, since a new feed-in tariff (FIT) was introduced in March, 2014 which is valid for the next 10 years [9]. This happened because the old FIT was not compliant with European Union (EU) regulations; nevertheless, the current FIT is expected to be revised later on. In Germany wind turbine generators (WTG) receive compensation payments according to the revised German Renewable Energy Act (EEG) of 2014. The scheme consists of two compensation payments, the initial compensation of currently €8.9 ct/kWh for the first five years, which then is prolonged depending on the individual turbine performance. Initial compensation payment is based upon an operational period of 12 years. The superior the wind conditions and thereby the generated energy, the lower the time frame of compensations. For example, a turbine characterised by a capacity of 130% (80%) with regards to a reference capacity will receive 5 (20) years of initial compensation payments. After this variable period the base payment of €4.95 ct/kWh is paid throughout the rest of the entire life cycle (20 years) [10]. Overall, in Germany there have been constant subsidies for the past fifteen years and are expected to remain constant in the future as pointed out in [11]. At the same time, a new on-shore installation cap was introduced with an annual limit of 2.5 GW of newly installed capacity per year excluding re-powering investments [12]¹. This change is significant in comparison with previous installed capacity as illustrated in Figure 1.1. Concerning offshore energy, new installations have been capped to a total of 6,5 GW in 2020 and 15 GW in 2030 [13], thus there will be a limited amount of sites authorised. Also, with the changes of the renewable energies act (EEG) in 2016, latest in 2017 a tendering and auction process will be implemented where investors compete like in the United Kingdom (UK) with contract for difference (CfD) auctions [14]. Therefore, Germany and France are identifiable for continuity and secured investment resulting in growth in

¹The re-powering bonus of the previous EEG was removed

installed capacity, although Germany has introduced factors to limit installed power in order to maintain affordability and France has yet to decide on how to move forward. A different picture present Spain, Italy, and the UK. In 2012, Spain declared an end to its entire subsidies that led to halt the entire wind industry as shown in Figure 1 with zero installations in 2015 [15]. Caused by this severe outcome, Spain reintroduced a new subsidy in June, 2014 that caps earnings of all renewable energy plants with an aimed return on investment (ROI) of 7.5% [16]. This rate is based on the average interest rate of a ten years sovereign bond, plus an additional 3%, which is revised every three years. These measures are retroactively accountable (June 2013) to achieve the following three objectives: stability, allow a reasonable ROI, as well as certainty. This example demonstrates well that at present wind energy cannot compete without subsidies, hence the industry came to a standstill. Italy experienced a rapid development of wind and solar until 2012; however, active incentive mechanisms became too costly, resulting in a reduction of their FIT as well as an overall cap on total subsidy expenditure [17]. Despite high wind energy deployment rates, the UK is facing significant changes with regards to its onshore wind energy policy. In more detail, the current FIT for installations below 5 [MW] was intended to be reviewed in 2015 and is constantly decreasing since 2012 [18]. Further the government decided to terminate the renewable obligation (RO) scheme one year earlier (first of April, 2016) for onshore wind deployment, with an unlikely transition into the second allocation round of the CfD mechanism, introduced in 2014, as expressed by Amber Rudd, UK's former energy secretary [19]. With the successful introduction of the first CfD auction in 2015, results revealed that under competitive tendering the average strike price for onshore (\approx £80 per MWh) and for offshore (\approx £117 per MWh) was much lower than anticipated [20]. However, it is yet to discover whether these projects can be delivered on budget. Conclusively, wind energy investors, operators, and ultimately wind turbine manufacturers are under increased pressure as such transformation from an over-subsidised environment to a more competitive allocation will have significant impacts on economic wind energy parameters such LCOE, internal rate of return (IRR), and ROI. This will then reflect upon the decision whether to invest in wind farms or otherwise capitalise

in alternative options.

These changes are well observed within the industry too; i.e., Gamesa declared this transition as the credit crunch within the wind industry and highlighted the requirement for wind turbine life extension as of 2014: “new alternatives such as reliability-centred maintenance and reconditioning programs play an ever increasingly important role. However, these improvements are just the first glimpse of a much more ambitious and promising opportunity: turbine life extension” [21]. In addition Gamesa has been the first manufacturer making use of the recently introduced life extension certificate provided by Det Norske Veritas and Germanischer Lloyd (DNV GL) to extend the operation of wind turbines up to a total of 30 years, issued on the 16th of December 2014 [22, 23]. Figure 1.2 displays the installed wind energy capacity for onshore (green) and offshore (blue) installations until 2015 as well as the total cumulative installed capacity. Beyond 2015 the installed capacity is mirrored in order to graphically represent annual capacity that is reaching its 20th year of operation, where the operator is required to decide how to move forward; i.e., to decommission, repower, or recondition (life extension). As one can see there will be a significant capacity reaching its end of lifetime from 2018 onwards for onshore and 2035 for offshore turbines. Consequently, market interest as well as offered services are growing in this area.

Enercon started to offer their extended wind turbine service package within the first quarter of 2016, encompassing scheduled maintenance and remote monitoring for turbines beyond 20 years with a guaranteed technical availability of 97% [24]. Additionally Enercon’s newest 4MW turbine platform has a designed life of 30 years, initiating a potential new standard in wind energy deployment [25]. Further SSE plc and Scottish Power/Iberdrola share a keen interest in wind turbine life extension which are industrial partners for this work.

As Gamesa points out “all manufacturers have increased rotor sizes and improved the efficiency of their turbines to harvest the maximum amount of energy from any given wind” it is of high importance to evaluate costs versus benefits [21]. As Mark Hancock, former chief blade designer at Vestas stated “any improvement for a wind turbine might decrease the cost of energy by a few percent; however, the actual implementation within

Chapter 1. Introduction

the company in terms of new knowledge, new materials or processes have significant costs attached, thus from a cost-benefit point of view the actual gain can be severely impacted” [26].

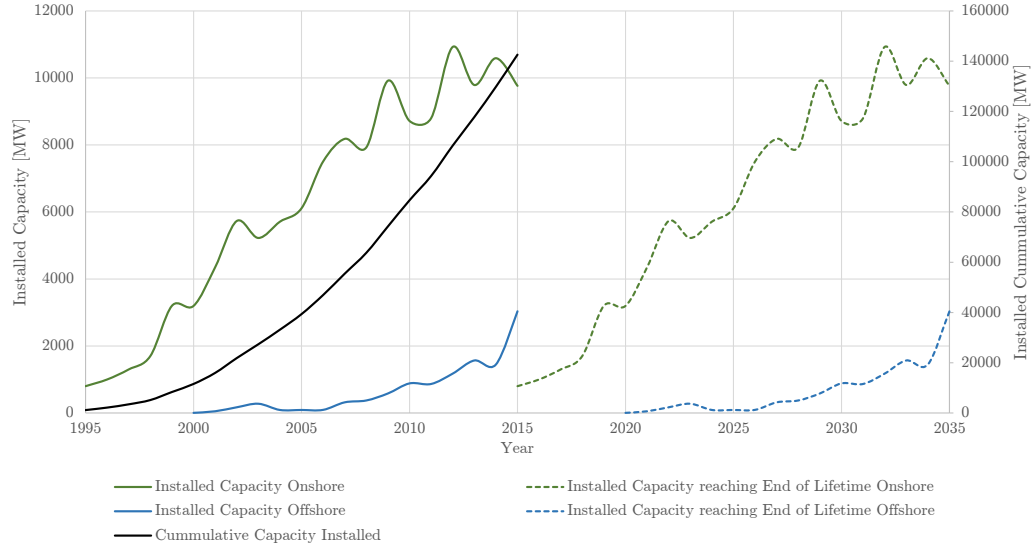


Figure 1.2: Turbines reaching End of Lifetime in Europe [4–8]

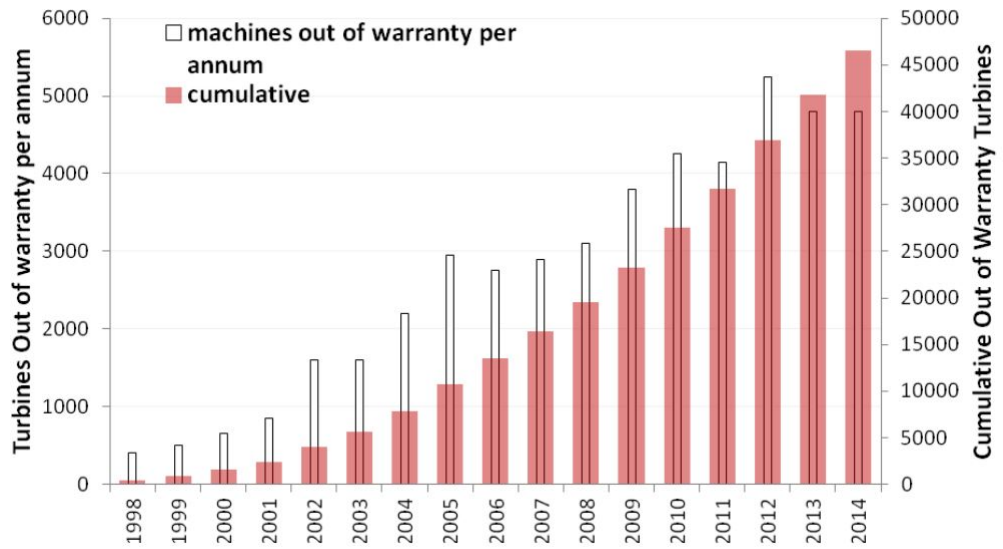


Figure 1.3: Turbines Out of Warranty [27]

Additionally, recent work by McMillan et al. [27] concludes that after the global wind energy deployment boom, a significant share of wind turbines are out of warranty as illustrated in Figure 1.3. That implies O&M strategies and processes as well as condition monitoring will play an increased importance for wind turbine operators worldwide, where the health status of the system is desired to be evaluated. Here, foundation condition monitoring with optical based sensor networks could play an important role to give informed data on structural health to determine an individual turbine's operational loading and the potential for life extension in order to maximize generator efficiency beyond a lifetime of 20 or 25 years.

2018 Update

- In France, the FIT for onshore wind was terminated and the successor auction-based policy introduced through a contract for difference mechanism in 2017 with a target remuneration of €72-74/MWh [28].
- The OEMs are further under pressure, due to an overcapacity in Europe, thus more and more focus is placed internationally. Siemens merged with Gamesa becoming the biggest turbine manufacturer followed by Vestas in 2017, Enercon bought Lagerwey aimed at redesigning their asset portfolio more cost efficiently, Nordex merged with Acciona, while there remains a growing Chinese competition to watch out for [29].
- Offshore prices are further reducing with auctioned strike prices as low as £57.50 in the UK and €0 subsidy bids in Germany (contrary to the UK, in Germany the offshore grid connection is covered by the transmission operators). This sets new records, market interest, and LCOE cost reduction pressure in the offshore industry, especially with the potential of an additional 6 GW of offshore capacity in the UK to be delivered by 2030.
- Spain recovered from the doldrums with observed record bids as low as €43/MWh with an agreed onshore development of nearly 3 GW [30].

- Since the closure of the RO in the UK, there has been no change in the onshore legislation, thus onshore developments are expected to reduce drastically; however, first onshore £0 subsidy projects are under development, with construction starting in 2018 for the 8.2 MW Witherwick II extension project [31].

Summing up, operators and investors of wind farms are under increased pressure due to reductions in governmental support. Further, there are significant numbers of turbines that reach their end of designed lifetime that require decision-making, where life extension could become a beneficial consideration. Recognising the need as well as potential market for lifetime extension, this PhD thesis will look into wind turbine life extension using a hybrid approach. On one hand, wind turbine lifetime extension economics are modelled that can subsequently be used to justify investment decisions in novel sensors aiding lifetime extension. On the other hand, the application of advanced sensing and diagnostics based on optical sensors to monitor the operation of wind turbine foundations is evaluated with the aim to facilitate LTE or alternatively, the reuse of foundations in repowering projects with greater rated turbines.

In more detail, a tool is developed to assess lifetime extension economics based on different scenarios and operational conditions. Concerning the technical application, this work entails embedding optical sensors within wind turbine foundations and towers to assess fatigue damage, operational loading, and ultimately the component's remaining useful lifetime (RUL) as this can be heavily influenced by local site conditions such as shear, turbulence intensity, mean wind speed, atmospheric stability as well as a turbine's specific design parameters such as its control strategy, natural frequencies, etc. It is aimed to derive information about the ability to reuse the foundation for greater rated turbines than originally designed to save costs when repowering; however, findings are not limited to reuse purposes. Further merit may be to apply sensor data for design optimisation and verification of Finite Element Models (FEM) as well as LTE.

Chapter 2

Principal Contributions

The following items are this thesis's principal contributions to advance the knowledge in the area of structural health monitoring and lifetime extension decision-making:

- Pathway to form an operational lifetime extension strategy at an early stage through tower measurements.
- Development of an economic tool to derive the lifetime extension business case and sensitivity analysis under varying input parameters and component replacements along the drive train.
- A sensor network implementation methodology to evaluate the health status of reinforced concrete foundations and, with refinement, use data for foundation reuse purposes and or to reiterate conservative design assumptions in future work.
- Gather high frequency (100 Hz) tower strain measurements of a 3.5 MW, individual pitch regulated, onshore wind turbine generator and evaluate fatigue sensitivity parameters as well as carry out a fatigue analysis.
- Provide learning experience of embedding optical sensor networks in reinforced concrete structures with complex reinforcement cages.
- Review the lifetime extension environment in the UK, common practises, and their challenges.

Chapter 2. Principal Contributions

- Fatigue testing and subsequent improvement of bespoke optical foundation strain sensor characteristics.

The following articles originate from this thesis.

Journal Papers

1. T. Rubert, D. McMillan, P. Niewczas, "A Decision Support Tool to Assist with Lifetime Extension of Wind Turbines", Renewable Energy, DOI:10.1016/j.renene.2017.12.064.
2. T. Rubert, M. Perry, G. Fusiek, J. McAlorum, P. Niewczas, Field Demonstration of Real-time Wind Turbine Foundation Strain Monitoring, Sensors 18(1):97, DOI:10.3390/s18010097.
3. L. Ziegler, E. Gonzalez, T. Rubert, U. Smolka, J-J. Melero, "Lifetime extension of onshore wind turbines: A review covering Germany, Spain, Denmark, and the UK", Renewable and Sustainable Energy Reviews, 82(1), 1261-1271.
4. T. Rubert, G. Zorzi, G. Fusiek, P. Niewczas, D. McMillan, J. McAlorum, M. Perry, Wind turbine lifetime extension decision-making based on structural health monitoring *in review for journal publication/accepted at APWSHM-2018 conference*.

Conference Contributions

1. T. Rubert, P. Niewczas, D. McMillan, "Life Extension of Wind Turbine Structures and Foundations", International Conference on Offshore Renewable Energy, Glasgow, 2016.
2. T. Rubert, D. McMillan, P. Niewczas, "The Effect of Upscaling and Performance Degradation on onshore Wind Turbine Lifetime Extension decision making", WindEurope 2017, DOI:10.1088/1742-6596/926/1/012013.
3. T. Rubert, L. Ziegler, E. Gonzalez, D. McMillan, U. Smolka, and J. J. Melero, The UKs state-of-the-art of lifetime extension of onshore wind turbines, in RenewableUK – Onshore Asset Management, 2017.

Chapter 2. Principal Contributions

4. G. Fusiek, T. Rubert, P. Niewczas, J. McAlorum, M. Perry, "Preliminary characterization of metal-packaged fiber Bragg gratings under fatigue loading", 2017 IEEE International Instrumentation and Measurement Technology Conference (I2MTC), DOI: 10.1109/I2MTC.2017.7969945, May 2017.

Internal Reports

1. T. Rubert, G. Fusiek, P. Niewczas, J. McAlorum, M. Perry, "Field Demonstration of Real-time Wind Turbine Foundation Strain Monitoring", AM06 TIC Report for SPR and SSE.
2. T. Rubert, G. Fusiek, P. Niewczas, J. McAlorum, M. Perry, "Characterisation of metal-packaged fibre Bragg gratings under fatigue loading for structural health monitoring in civil engineering applications", AM06 TIC Report for SPR and SSE.
3. T. Rubert, G. Fusiek, J. McAlorum, P. Niewczas, M. Perry, "Installation of embedded optical sensors within a wind turbine foundation at the windfarm", AM06 TIC Report for SPR and SSE.

Chapter 3

Literature Review

This chapter initially presents an overview of available literature in Section 3.1 looking at economic modelling and optical sensor based structural health monitoring, followed by a brief research proposal based on the findings of the literature review in Section 3.2. Lastly, in Section 3.3 the fundamental theory is presented to enhance the reader's understanding of the content as multiple areas are covered in this thesis.

3.1 Available Literature

3.1.1 Wind Turbine Structural Health Monitoring

Available research of fundamental principles as well as applications and improvements of optical sensing devices are abundantly available. Review papers dealing with the fundamental theory and potential applications are given by Rao [32], Kersey [33], and Hill and Meltz [34] highlighting the application within the telecommunications sector, structural monitoring, or packaged as accelerometers in mechanical engineering applications. Early work on optical fibres embedded in concrete structures is given by Proshaka in 1992 [35] with small reinforced concrete beams and Maaskant in 1994 [36], the latter reporting on a Bragg grating sensor network being embedded in a bridge in Canada. Habel and Krebber [37] provide an overview of different fibre-optical sensor technologies in engineering applications and present a new design for monitoring the alkaline state of reinforced concrete structures to assess internal corrosion processes.

Chapter 3. Literature Review

Salo and Korhonen [38] attached sensors externally to a concrete beam to determine its deflection, whereas Higuera et al. [39] presented optical fibre sensors in general structural health monitoring applications, giving examples of best practice in different industries such as renewable energy, transportation, civil engineering, and the oil and gas industry. Regarding the renewable energy sector, Higuera highlights the importance to apply FBG based sensors to monitor wind turbines due to varying localised stochastic loading and the consequent fatigue damage of the structure. Further Higuera reviews application and research cases such as: FBG based strain sensors in blades [40], foundation piles [41], gearboxes [42, 43], accelerometers [44], and for temperature and generator current measurement [45]. The latter where the optical sensor research team at Strathclyde University investigates various applications [46, 47]. The paper on FBGs in blades, by Schroeder et al. [40], describes how an FBG array is retrofitted to a blade of an Enercon E-112 blade. In this work the grating is embedded in a glass fibre reinforced plastic (GFRP) patch in order to monitor fatigue damage, site conditions, as well as to scrutinise state of the art blade design. Furthermore, FBGs embedded in GFRP are tested under fatigue of up to $1.3 * 10^8$ cycles with a strain of up to $2 \text{ m}\epsilon$ aimed at simulating a turbine lifetime of 20 years assuming a continuous rotor operation at 12 revolutions per minute (rpm). Arsenault et al. attach a FBG based sensor network to a small scale rotor [48] and extract natural frequencies. In commercial practise according to Jacob Deleuran Grunnet, Senior Control Engineer at Vestas each new manufactured turbine comes with an optical based blade strain sensor to alleviate loads as of means of individual pitch control. This sensor is based upon two fibres (one as a temperature reference) that transmitted power drops by applied force¹ making it a simple and cost effective methodology to monitor loads [50]. Kister et al. [41] embed FBG arrays in concrete piles of building's foundations via a clip on system fabricated out of carbon fibre reinforced plastic (CFRP) encompassing steel tendons. Results reveal how initial monitored tensile stress caused by thermal expansion during curing gradually transforms into compressive stresses as the temperature cools down and the building is subsequently constructed, hence the sensor responds to the added weight. Based upon

¹a more complex sensor has been designed in [49]

Chapter 3. Literature Review

this work, Higuera suggests to apply optical sensors in onshore wind turbine foundations, however there is no evidence that this has been performed by other researchers at present. Concerning offshore foundations, Wernicke et al. [51] attach four sensor arrays to an offshore meteorological mast (met. mast) and demonstrated the ability to extract the mast's natural frequency. Jiang et al. [52] further evaluated the best weld type for the tower-flange connection and points out that the temperature history of the welding process is governing the residual stress.

Related condition monitoring work on onshore wind turbine foundations is available by Currie et al. [53,54] evaluating vertical can displacement by monitoring the displacement between the tower and foundation. Based upon this work Bai et al. [55] evaluate crack development by embedding sensors separately in concrete blocks to monitor displacement and crack development at the bottom of the inserted can flange that area is prone to crack. In addition, empty steel tubes to be filled with water are further vertically inserted to allow horizontal ultrasonic testing to identify the exact crack location. General information on onshore foundations and its design codes is given in [56], highlighting field experience of critical structural crack behaviour, their origin and methodologies to prevent such instances from occurring.

Concerning the sensor design and application available research for this thesis offer Li et al. [57–59] evaluating strain transfer rates of fibre Bragg gratings (FBG) in different host materials. Concerning the metal-packaged sensors investigated in this report, early work by Niewczas and Fusiek [60] showed how metal coated fibre, with an inscribed FBG can be hermetically sealed within a kovar capillary based on a localised induction heating process. Furthermore, based on these research results, sensors were designed for different applications such as condition monitoring of cracked wind turbine foundations [61], monitoring of prestressing tendons [62], and monitoring of prestressing tendons in nuclear concrete vessels [63]. Also, research by McKeeman et al. presents a methodology to thermally calibrate metal-packaged FBG sensors in terms of temperature and strain response [64], as well as a method to detect fabrication defects during the induction heating process [65].

Although FBG fatigue resistance has been evaluated with an endurance limit of $N = 10^6$ cycles for pure silica embedded in composites by Ang et al. [66] as well as for aerospace application by Davis et al. [67]. At present, no study has yet considered to evaluate metal-packed FBG fatigue behaviour (for example, as experienced by a wind turbine foundation), which fatigue lifetime requirement is much greater than in the automotive or aerospace industries with 10^8 up to 10^9 cycles, where large scale turbines are placed at the lower end as the angular velocity reduces with rotor diameter [68]. Although much research focused on the application and implementation of such metal-packaged sensors, at present no analysis has been carried out to evaluate the sensor's characteristics under fatigue loading. Many engineering applications such as those in the renewable energy sector (wind, wave, and tidal devices), aeronautics, automotive industry, and civil engineering experience fatigue loading, and hence the sensors used to monitor such structures must be resilient to repeated loading regimes, demonstrating sufficient accuracy over time.

Consequently, in this work a metal-packaged optical structural health monitoring (SHM) system is designed and implemented in an onshore reinforced concrete wind turbine foundation.

3.1.2 Economics and Lifetime Extension

Concerning available research on economical modelling, Milborrow [69] presents a fundamental overview on modelling economic parameters, recommended practice, and limitations with focus on wind turbines. Isabell Blanco, the former Policy Director of the European Wind Energy Academy (EAWA) reviews available research on wind turbine capital as well as operation and maintenance (O&M) costs, extracting a set of modelling parameters for wind energy deployment which findings are subsequently scrutinized by a sensitivity analysis [70]. Most of the suggested parameters are derived from EAWA's experts and accumulated research, hence being a reliable source for this thesis' analysis. Country specific economic wind energy parameters are further given

by the National Renewable Energy Laboratory (NREL) [71,72]; however, NREL's identified costs differ significantly to European findings, hence information should be used with caution. Junginger [73] presents experience curves for turnkey wind parks, deriving cost reduction curves for wind turbines in the 600-700 kW range, present changes in capital turbine costs due to size; however, the authors do not account for changes in operation and maintenance. Neither bigger turbines above 2 MW are evaluated in depth, although investment costs are given for a three years period, in which investment costs develop laterally within a band of €50.000. Luengo and Kolios [74] state positive effects on ROI and LCOE if wind turbine life is extended, although fail to back this up with data or sources, addressing wind turbine failure modes and its importance for offshore turbines. Perek and Hoz [75] perform a life cycle assessment (LCA) of a Gamesa wind turbine designed for 20 years and further perform a sensitivity analysis under life extension scenarios (+5 years/+10 years).

Finally, in terms of wind turbine life extension, DNV GL [23,76] presents a guided overview of the possibilities to gain life extension certification similarly to the Danish MegaVind group [77] aimed at supporting the decision-making process within the Danish industry. In addition, Ziegler et al. [78] present a basic decision-making model between repowering and lifetime extension, whereas Loraux and Bruehwiler [79] attached strain gauges onto an onshore Vestas V90 wind turbine steel tower and extract the remaining fatigue life. In 2016, a global survey on the development of LCOE with 166 participants was executed [80]. Results in the optimistic scenario predict an onshore lifetime extension of 25% based on an expected lifetime of 20.7 years (offshore: +25% based on 20.3 years of life expectancy). In the pessimistic scenario 0% of lifetime extension is assumed in both cases. Overall, literature does not provide an economic analysis of lifetime extension of wind turbines. Thus, there is sufficient merit to scrutinise the economic decision-making process.

3.2 Research Proposal

Based on the outcomes of the literature review in Section 3.1, the overall research plan for the first 19 months of this project is illustrated in Figure A.1 of the Appendix.

Chapter 3. Literature Review

Initially, the aim is to thoroughly review, process and extract available research that is in connection with this PhD topic; i.e., a general overview of performed related work. Further relevant, and fundamental theoretical concepts are presented concerning optical sensors, civil engineering, economics, and wind turbine technology.

Meanwhile, a tool is developed to economically model life extension of wind turbine generators, which will assess lifetime extension costs under variable economic, and environmental parameters. This economic modelling will be initially set-up in a simple reference frame, then along the course of this project more and more layers of additional complexity are introduced. Eventually, the model is aimed to evaluate if certain SHM costs are viable to be spend in order to justify the lifetime extension support.

Moreover, experimental settings for embedded sensors in reinforced concrete beams under fatigue loading are evaluated and prepared. This involves fatigue testing of sensors attached to metal samples, and subsequently sensor are aimed to be embedded in concrete. This is important, since any non-linear sensor behaviour or degradation under fatigue loading can highly influence field trial measurement readings. Further critical sensor areas are identified, possibly allowing to improve sensor design. Once, the metal-packaged strain sensor is fully evaluated the subsequent aim is to embed the transducer in a reinforced concrete beam. Data will then be processed and analysed with regards to their fatigue behaviour.

At the same time, in May 2016 the FBG wind turbine foundation deployment was prepared, enclosing the production of sixteen FGB sensors and set-up of all equipment. This had to be finalised by the end of June, as on the 1st of August 2016 the aimed turbine foundation was constructed at SSE's approved wind farm with a total of 32 turbines based near Fort Augustus, Scotland [81]. The wind farm consists of 30 Vestas V117-3.45 MW and two Vestas V112-3.45 MW turbines with a total capacity of 108 MW. Once the foundation was built the turbine was installed and commissioned in late 2016.

As soon as sufficient operational turbine data is available the project's aim is to evaluate measurements by taking previous experimental sensor strain characteristics into consideration. Further, the turbine's SCADA data as well as tower strain values from

attached FBGs can be accessed to correlate measured stress/strain in the foundation with wind/tower reactions. The measurement campaign is supported by a finite element analysis (FEA) of the turbine's foundation for validation purposes and the structure's unique fatigue loading and remaining useful life is evaluated. Also, findings are aimed to be analysed for non-linear structural responses and the development of cracks. Based on findings it is further aimed to provide information on the ability to reuse the equipped onshore foundation.

In addition, a test rig to dynamically cycle reinforced concrete beams is designed, machined, and commissioned jointly with a fellow PhD student; however, this is not part of this PhD thesis due to delays in the overall process and was passed on to a fellow PhD student.

Before presenting this thesis's research, the following Section covers the theoretical background aimed at facilitating an understanding of the different topics covered in this thesis.

3.3 Theoretical Background

This section is not an integral part of this thesis's research; however, presented fundamental knowledge covers several different fields such as optics (Section 3.3.1), civil engineering (Section 3.3.2), fatigue analysis (Section 3.3.3), economics (Section 3.3.4), and turbine technology (Section 3.3.5) to help the reader's understanding of the different topics.

3.3.1 Optics

An optical fibre is a flexible, transparent strand made of pure glass (fused silica) with a cladding diameter of 125 microns and a core diameter of 50 microns for multi-mode fibres (9 microns for single-mode), the latter that serves as a wave-guide to transmit light [66,82]. Advances in applying such fibres as optical sensors, were discovered about 40 years ago, when Hill et al. subjected a germania-doped optical fibre to argon-ion laser radiation, observing an increasing reflectivity that advanced until almost all light was reflected in 1978 [34]. Further research concluded that exposure of silica to selected

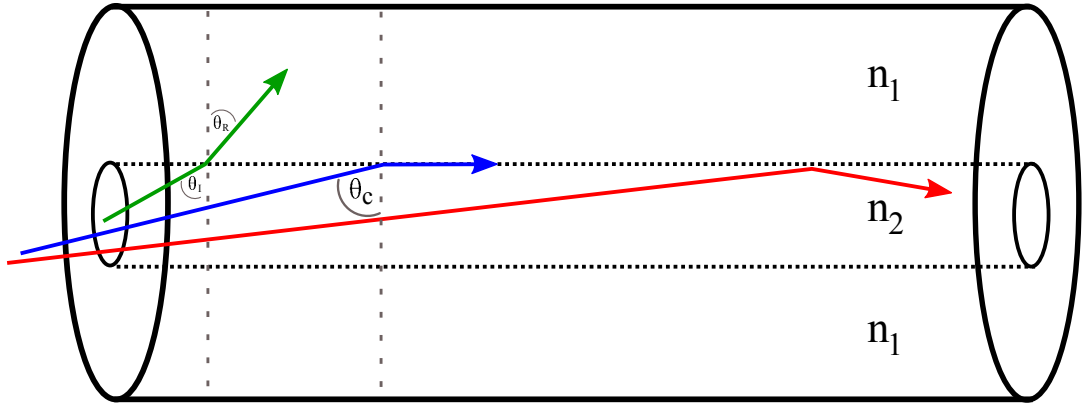


Figure 3.1: Fibre Optical Strand

radiation sources changes the material's refractive index n , a dimensionless number,

$$n = \frac{c}{v} \quad (3.1)$$

where c is the speed of light in vacuum, and v the phase velocity in a medium. Essentially n describes how light travels through a medium; i.e., how much light is bent and refracted when entering a material [83], which is describes by Snell's law,

$$n_1 \sin \theta_1 = n_2 \sin \theta_2 \quad (3.2)$$

where θ is the angle of incident and n_i the refractive index of the entrance as well as exit medium. Snell's law is further illustrated in Figure 3.1, where the difference between reflection and refraction is schematically contrasted. In more detail a light source travelling from one material (low n_1) into another (high n_2) is refracted (green) according to Equation 3.2 with the incident angle θ_I and refraction angle θ_R . An example for refraction is, how light propagates in between salt and freshwater. Reflection occurs until a critical angle θ_c is reached (blue) and if θ_I is greater than θ_c a light source experiences total internal reflection (red), hence light travels through the medium. This allows to transmit information with the speed of light over long distances, as performed with fibre optical cable in the communication sector. Table 3.1 presents an overview of mechanical properties of optical fibres that are manufactured from high-silica glasses.

Table 3.1: Properties of Optical fibres (modified from [59])

Material Properties	Symbol	Value	Unit
Young's Modulus of silica fibre	E_{sf}	$73 * 10^9$	Pa
Young's Modulus of silica coating	E_{sc}	$2.55 * 10^6$	Pa
Poisson's ratio of silica coating	ν	$0.17 \sim 0.48$	-
Shear modulus of silica coating	G	$8.5 * 10^5$	Pa
Strength of silica fibre	σ	$350 \sim 460 * 10^6$	Pa
Breaking strain of silica fibre	ϵ	$\sim 10\%$	-
Density	ρ	2200	Kgm^{-3}
Coefficient of thermal expansion	α_f	$0.54 * 10^{-6}$	K^{-1}
Fatigue endurance limit of silica - cycles [66]	N	10^6	-
Fatigue endurance limit of silica - strain [66]	ϵ_f	$3.5 * 10^{-3}$	ϵ

Since the material is glass it is characterised by amorphous material properties unlike crystalline materials such as metals. Therefore, due to glass's amorphous nature, optical fibres do not exhibit well-defined transition periods; instead, properties vary over a large temperature range. Another result of amorphous material properties are unavoidable internal and surface flaws, which intensity can vary with manufacturing processes and thus impact individual performance when exposed to stress. As a consequence, Table 3.1 presents average characteristic parameters.

In general optical fibres have a Young's Modulus, E_{sf} , of 73 GPa, with a maximum strength, σ , of between 350 and 480 MPa corresponding to a maximum strain, ϵ , of 10%; however, this 10% accounts for silica without flaws, thus the average guaranteed strength is 350 MPa with a corresponding strain of around $5 m\epsilon$ [84]. Concerning fatigue behaviour, Ang et al. [66] state a fatigue endurance limit of 10^6 cycles paired with a cyclic strain ϵ_f of $3.5 m\epsilon$. Inevitably, optical fibres are brittle in nature, thus a coating is applied to protect a strand from breaking. Usually, a $62.5 \mu m$ acrylate or metal layer is applied as a base protection and depending on the individual application further coatings can be added.

The actual sensor element applied in this thesis; i.e., the fibre Bragg grating is a periodic change of the refractive index within the fibre core of a length of between 3 to 14 mm [85]. Nowadays, this is achieved by a two beam interferometer (two mirrors and

two lenses create an interference pattern which is directed normal to the fibre axis) or a phased mask method (silica mask creates interference) applying an ultraviolet (UV) light source at around 244 nm; however, there are more techniques and variations as pointed out by Rao [32]. An example of a reflective index modulation is illustrated

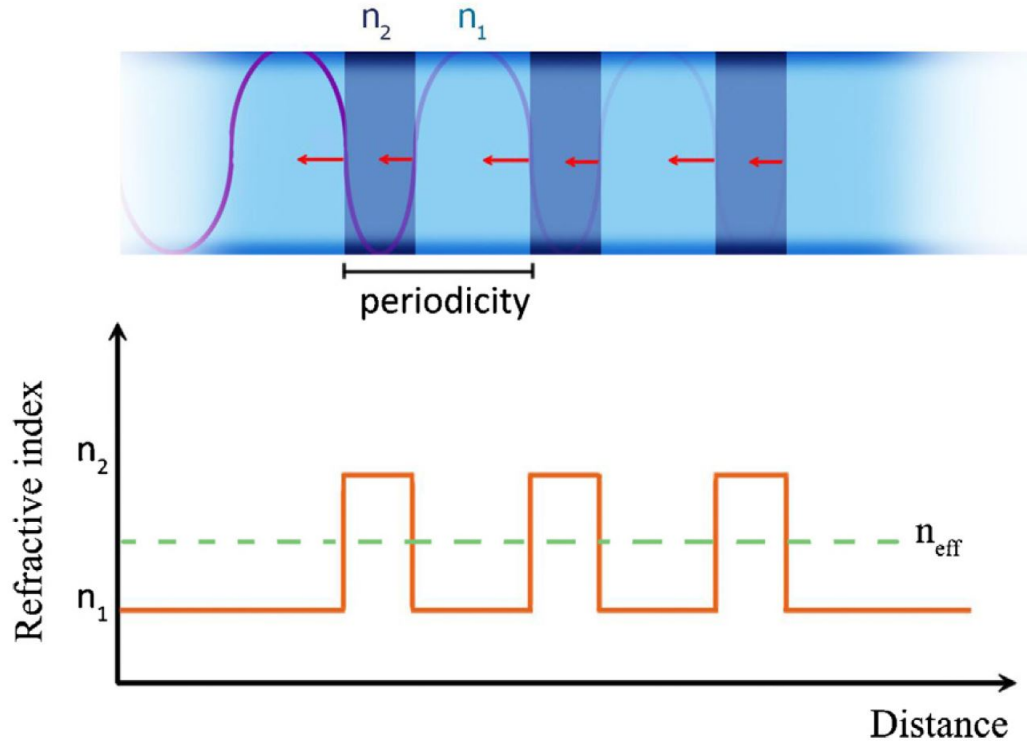


Figure 3.2: Fibre Bragg Grating [63]

in Figure 3.2, where n_2 is defined by a high refractive index and n_1 by a low. Both indices form the effective refractive index n_{eff} which is given by the average of n_2 and n_1 . Now, depending on the parameters of the Bragg modulation, if broadband light travels through optical fibre, for example produced by a light emitting diode (LED), a narrowband of light is reflected, λ_B ,

$$\lambda_B = 2n_{eff}\Lambda \quad (3.3)$$

where Λ is the grating period or grating length; i.e., the width of n_2 and n_1 , also referred to as periodicity. “The bandwidth of the reflected signal depends on several parameters,

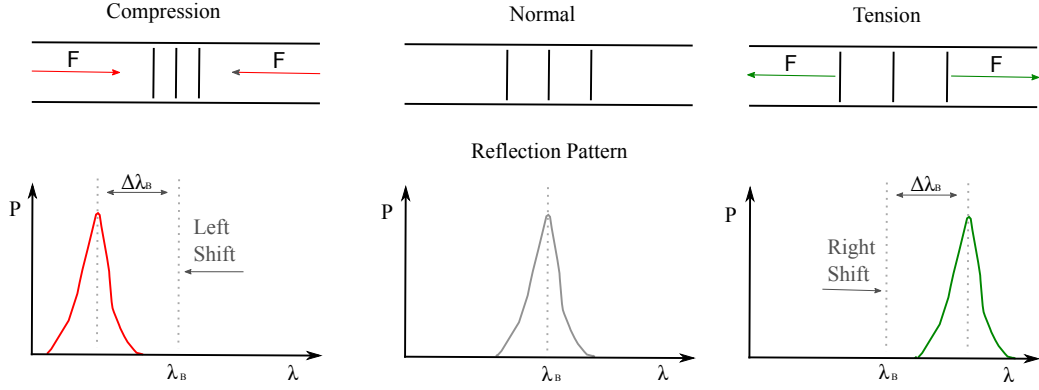


Figure 3.3: Schematic Reflection Pattern

particularly the grating length, but typically is ~ 0.05 to 0.3 nm " [33]. Consequently any change of Λ or n_{eff} will cause either a positive or negative shift in the reflected spectrum that can be monitored with an interrogation device. Due to this, Bragg gratings are able to capture strain changes (compression and tension) as well as temperature changes in terms of a change in reflected wave length $\Delta\lambda_B$,

$$\Delta\lambda_B = [C_\epsilon\Delta\epsilon + C_T\Delta T]\lambda_B \quad (3.4)$$

where C_ϵ and C_T are the strain and temperature coefficient and $\Delta\epsilon$ and ΔT the change in strain and temperature. Such a change is schematically illustrated in Figure 3.3. Assuming the applied strain is homogeneous and isotropic, then the change in reflected wavelength can be simplified from the Ricatti Differential Equation [33, 34] to,

$$\begin{aligned} \Delta\lambda_{BS} &= (1 - p_e)\lambda_B \cdot \epsilon \\ &\cong 0.78\lambda_B \cdot \epsilon \end{aligned} \quad (3.5)$$

where ϵ is the applied strain and p_e is the effective photoelastic coefficient characterised by:

$$p_e = (n^2/2)[P_{12} - \mu(P_{11} + P_{12})] \quad (3.6)$$

where $P_{i,j}$ are the Pockel's coefficients of the FBG sensor and μ is Poisson's ratio. Numerically p_e is around 0.22, hence the change in λ_{BS} per millistrain can be approx-

imated. For example under axial strain, if the interrogation wavelength λ_{BS} equals to 1300 nm, then the sensor's sensitivity is 1 nm per millistrain (820 nm: $0.64 \text{ nm } (m\epsilon)^{-1}$). Possible measurement resolution is much lower though, with devices measuring strain changes as accurate as one $\mu\epsilon$ [86].

Equally an FBG's sensitivity to temperature can be approximated; however, $\Delta\lambda_{BT}$ is a combination of the change of index of the refraction of the silica with temperature and its thermal expansion coefficient α . Due to this, the wavelength shift with regards to temperature can be expressed as

$$\begin{aligned}\Delta\lambda_{BT} &= [(d\alpha/dT)/\alpha + (dn/dT)/n] \cdot \lambda_B \Delta T \\ &\cong 6.7 \cdot 10^{-6} \text{ }^\circ\text{C}^{-1} \cdot \lambda_B\end{aligned}\tag{3.7}$$

that parameters are empirically evaluated through experiments [87]. Adding the previously applied interrogation wavelength (1300 nm), results in a sensitivity of around 0.009 nm per $^\circ\text{C}$. Also $\Delta\lambda_{BT}$ can be expressed as

$$\Delta\lambda_{BT} = \lambda_B(\alpha + \xi)\Delta T\tag{3.8}$$

where α in the coefficient of thermal expansion of the optical fibre ($=0.54 \cdot 10^{-6} \text{ }^\circ\text{C}^{-1}$ - from Table 3.1) and ξ the thermo-optical coefficient ($=6.1 \cdot 10^{-6} \text{ }^\circ\text{C}^{-1}$) [32, 41]. Consequently, in order to achieve high sensitivity, high optical source wavelength are necessary as well as interrogators to provide such resolutions. Concerning multiplexing it is therefore important to take changes in wavelength response into account, as multiple FBGs have different λ_B .

When attaching a FBG sensor to a structure aimed at monitoring strain caused by operational loading it is important to isolate temperature induced strain. This can easily be achieved by taking a reference FBG that solely measures temperature; i.e., each sensor is composed of a strain measurement FBG attached on both sides to the structure as well as a temperature reference FBG fixed only on one side in close proximity. Therefore by experimentally evaluating C_T and C_ϵ of the embedded strain sensor

Chapter 3. Literature Review

as well as C_T of the temperature reference, generates the following two formulas,

$$\frac{\Delta\lambda_1}{\lambda_1} = C_{\epsilon 1}\Delta\epsilon + C_{T1}\Delta_T \quad (3.9a)$$

$$\frac{\Delta\lambda_2}{\lambda_2} = C_{T2}\Delta_T. \quad (3.9b)$$

where Equation 3.9a is defined by the strain impact due to loading as well as the temperature induced strain and Equation 3.9b by the temperature compensation sensor fixed only to one end, hence no external load induced strain is measured. Under the assumption that the temperature induced change is equal in both sensors; i.e., both sensors are placed in close proximity, Equation 3.9a and 3.9b can be expressed according to Δ_T and hence equate as:

$$-\frac{1}{C_{T1}}C_{\epsilon 1}\Delta\epsilon = \frac{1}{C_{T2}}\frac{\Delta\lambda_2}{\lambda_2} - \frac{1}{C_{T1}}\frac{\Delta\lambda_1}{\lambda_1}. \quad (3.10)$$

Therefore the induced strain in the strain and temperature transducer can be calculated with the following equation:

$$\Delta\epsilon = \frac{1}{C_{\epsilon 1}} \left[\frac{\Delta\lambda_1}{\lambda_1} - \frac{C_{T1}}{C_{T2}} \frac{\Delta\lambda_2}{\lambda_2} \right]. \quad (3.11)$$

Concerning the stress distribution it is further important to account for the compound sensor-structure stress transfer coefficient (α_s); i.e., whether the entire strain in the monitored structure or a fraction is transferred to the FBG. Monette et al. [88] concluded that the strain distribution of a fibre depends on the modulus of elasticity of fibre and matrix, hence stress transfer efficiency increases as the value E_f/E_m increases. As an example, under the assumption that the concrete behaves elastically and the strain experienced by the concrete is perfectly transferred to the rebars a simple way to evaluate strain transfer coefficients is to expose a sensor to a specified stress that has been estimated manually or through a simulation and then measure the actual change in wavelength reflection, thus:

$$\alpha_s = \frac{\epsilon_{FBG}}{\epsilon_{rebar}} \quad (3.12)$$

Chapter 3. Literature Review

Consequently, once α_s is known, in order to evaluate locally measured stress based on the FBG strain measurement, following formula is required

$$\sigma = \left[\frac{\epsilon_{FBG}}{\alpha_s} \right] E_{RC} \quad (3.13)$$

where E_{RC} is the elasticity of the reinforced concrete that can be estimated using the volume fractions of the steel rebar and concrete.

In case sensor measurement results are not accessible there are empirical formulas, to estimate the strain transfer rate based on the fibre's Young's modulus, the shear modulus of interlayer and host material, as well as their radii as stated by Li et al. [59] for a single interlayer and multiple interlayers [57], respectively. If the application allows, it is further possible to subject the sensor/structure to heat and evaluate the change in response to calibrate the sensor in-situ [64].

Contrary to other conventional measurement sensors such as strain gauges or Fabry-Perot devices, FBG sensors have numerous advantages as itemized in Table 3.2. One main advantage is that fibre Bragg gratings can be multiplexed; i.e., several sensors can be attached within one optical fibre, as each individual grating is defined by a specific spectral reflection as exemplified in Equation 3.4. This allows to monitor certain points as well as areas in form of quasi-distributed sensor network. On the downside, in case the fibre breaks several sensors can be impacted at once. Alternatively, distributed sensing (Brillouin and Raman scattering) allows to measure strains and stresses over a specified length; however, such applications are impacted by a reduced interrogation frequency and more expensive interrogators than for multiplexed FBG measurements [90].

Second, with one measurement raw material (the Bragg grating), multiple physical properties can be assessed, such as temperature, strain, pressure, current, acceleration and pH level based on different packaging; allowing different sensors to be multiplexed and interrogated synchronously. As FBGs apply light as the data transfer medium, it is possible to transmit data with high speed over long distances up to several km. Immunity to EMI, RFI, and electrical isolation (lightning strikes) are one of the main

Table 3.2: Advantages and Disadvantages of FBGs (modified from [32])

Advantages	
	<ul style="list-style-type: none"> • Multiplexing (up to 100 FBGs [51]) • Multi-functionality (temperature, strain, pressure, etc.) • Long transmission distance - several km [39] • Immune to electromagnetic interference (EMI)/radio frequency interference (RFI) • Electric isolation • Potential for high resolution and accuracy • Fatigue resistance [40, 66] • Small size and weight, capable of integration in tight spaces [37] • Linear response to mechanical stress and temperature [89] • Direct correlation between wavelength and strain [37] • Recalibration of sensor, even after signal-processing unit has been exchanged, not necessary [37] • Response to temperature is smaller than to strain, thus suitable for civil engineering applications [35]
Disadvantages	
	<ul style="list-style-type: none"> • Bleaching of sensor above 500 °C • The cost is still greater than conventional strain gauges, particularly due to the expensive interrogation optoelectronics (these costs have been steadily decreasing due to the technological progress) • Degradation under water ingress due to e.g. micro cracks or inappropriate sealing. • Requires wired interrogation (not wireless) • Installation requires specialist knowledge

advantages of FBGs over strain gauges and hence deliver a higher signal integrity and reliability, especially within coupled electric-mechanic applications. This especially applies to the energy sector. Under certain load conditions, experimental results have further demonstrated fatigue resistance embedded within GFRP up to $1.3 * 10^8$ cycles that is enough for most industrial applications. Concerning industrial applications, such sensors are further defined by small size and low weight, thus attachment or embedding within tight or sensitive areas is possible. Linear responsiveness under elastic deformation is suitable to capture linear elastic material behaviour, as naturally components are designed to operate in this region. Regarding civil engineering applications it is further noteworthy that in terms of magnitude of response, temperature induced spectral shifts are much smaller than strain induced, allowing it to decouple strain and temperature measurement.

On the downside, gratings start to bleach if exposed to environments above $500\text{ }^{\circ}\text{C}$, which will be discussed later on, as parts this work will entail to braze capillaries around copper-coated optical fibre. Lastly, another barrier are component, installation, operation and maintenance costs as depending on the scale of application these can be significant and consequently might not deliver required cost-benefit characteristics to reason economical or technical gain. Overall, these advantages present FBG application superior in some applications to electro-mechanical measurement technologies for example strain gauges (interference by EMF, exposure to lightning strikes, no multiplexing) as well as competing optical technologies such as Fabry-Perot sensors (no multiplexing) acting as narrow band-pass filters, or SOFO long-gauge displacement sensors applying low coherence interferometry, where the length difference between two optical fibres is measured (greater size, multiple fibres, no multiplexing).

3.3.2 Civil Engineering Structures

This section will provide an overview of concrete structures based on Euler-Bernoulli beam theory and further gives an overview on the design considerations of a simple steel reinforced concrete structure. This is because many applications can be simplified to a beam to understand the loading.

3.3.2.1 Support Types

There are several different support types of beams such as fixed, roller, pinned, spring etc. with different displacement constraints and forces as illustrated in Figure 3.4 that are encountered in engineering applications. It is important to understand that based on the constraints, forces along the beam such as a point or distributed load will cause a reaction force and moments (depicted in red) to take into account in the design. Furthermore, any external load will cause moments and shear forces along the beam, that internally are exhibited by strain and thus stresses.

3.3.2.2 Euler-Bernoulli Beam Theory

Euler-Bernoulli beam theory applies linear theory of elasticity in order to calculate load-carrying and deflection information of beam structures. The following assumptions are made in order to derive fundamental equations:

- plane sections perpendicular to the neutral axis before deformation stay plane and perpendicular after deformation
- deformations are small
- the beam is linear elastic isotropic and Poisson's ratio effects are ignored.

When looking at a beam supported at point A and B with a load point F as exemplified in Figure 3.5, the reactionary support forces can be obtained by the equilibrium equations, in which the sum of all forces and moments equate to 0 in order to be at a stable equilibrium. The colour scheme in Figure 3.5 is applied in the following equations to ease capturing the mathematical derivation. With three unknown reaction forces, it is possible to define three equilibrium equations to determine reaction forces:

$$\sum F_x = 0 \rightarrow F_{Ax} = 0 \quad (3.14)$$

$$pt.A : \sum M = 0 \rightarrow -Fd + F_{By}L = 0 \rightarrow F_{By} = Fd/L \quad (3.15)$$

$$\sum F_y = 0 \rightarrow F_{Ay} + F_{By} - F = 0 \rightarrow F_{Ay} = F - F_{By} \rightarrow F(1 - d/l). \quad (3.16)$$

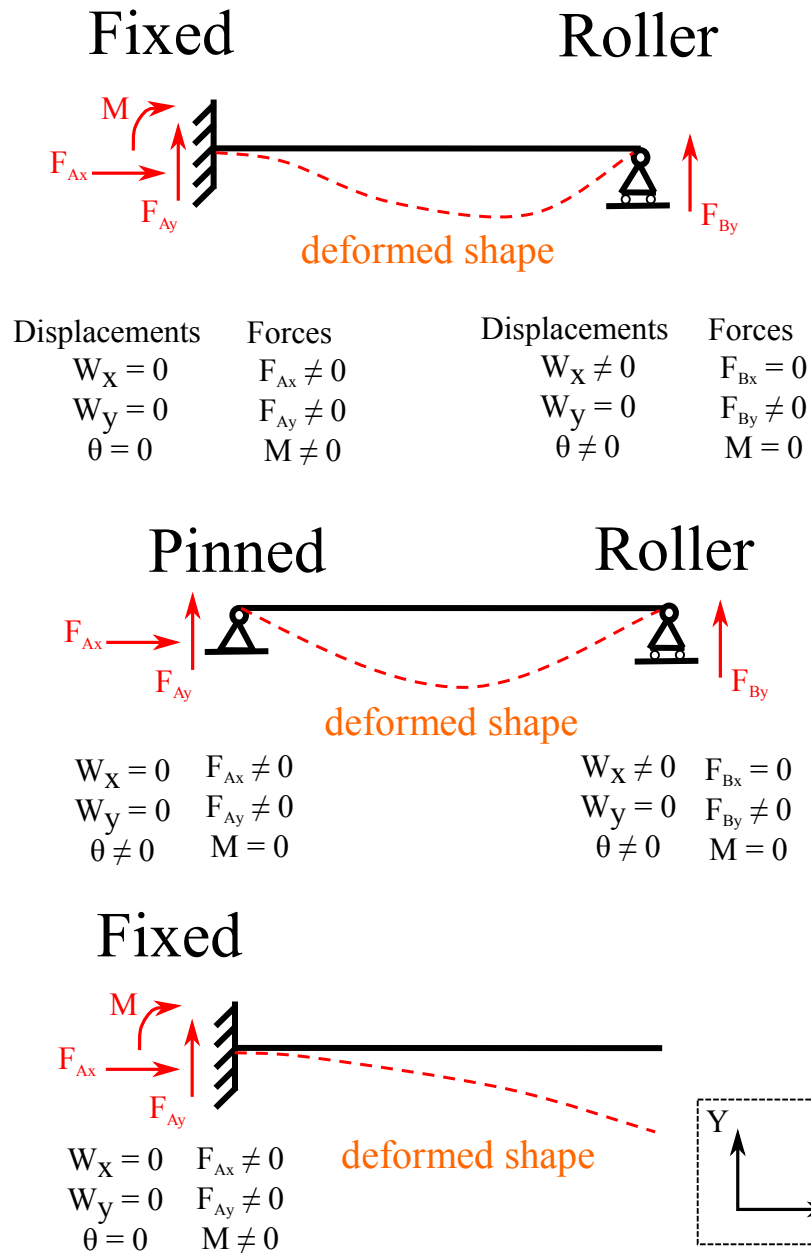


Figure 3.4: Beam Support Types

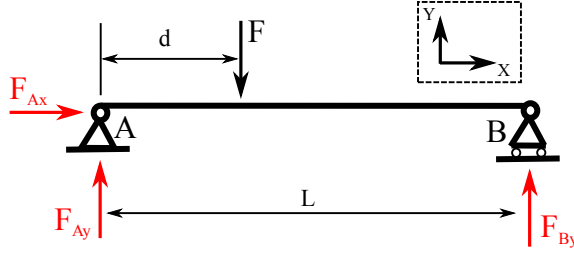


Figure 3.5: Beam Reaction Force Example

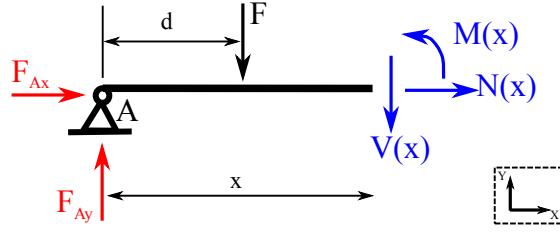


Figure 3.6: Example of Loads Along Beam

In addition to the derived reactionary loads, along the beam there will be normal forces $N(x)$, shear forces $V(x)$, and Moments $M(x)$ as exemplified in Figure 3.6 that require evaluation.

Equally for each cross section, the equilibrium equations are derived to determine moments and forces:

$$\sum F_x = 0 \rightarrow F_{Ax} + N(x) = 0 \rightarrow N(x) = -F_{Ax} = 0 \quad (3.17)$$

$$\sum F_y = 0 \rightarrow F_{Ay} - F - V(x) = 0 \rightarrow V(x) = F - F_{Ay} = Fd/l \quad (3.18)$$

$$pt.A : \sum M(x) = 0 \rightarrow -Fd + V(x)x = 0 \rightarrow M(x) = Fd + V(x)x = Fd(1 + x/l) \quad (3.19)$$

These loads will thus cause a beam to deflect as illustrated in Figure 3.7. The beam curvature κ is therefore defined by the inverse of the radius R :

$$\kappa = \frac{1}{r} = \frac{\Delta\theta}{\Delta S} \rightarrow \Delta S = \Delta\theta R \quad (3.20)$$

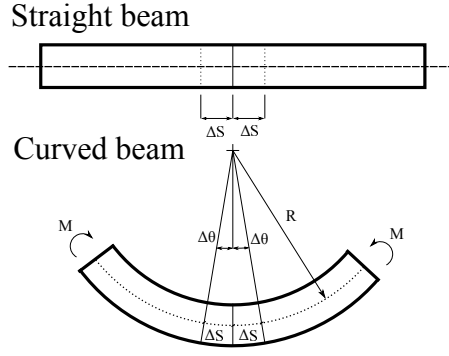


Figure 3.7: Stress Derivation From Deflection

that can also be translated into the fraction of the deflection angle $\Delta\theta$ over the section width ΔS .

The strain, caused by the elongation of the neutral axis reaching ΔS_z is now a linear function based on the distance z by substituting ΔS with Equation 3.20:

$$\epsilon = \frac{\Delta S_z - \Delta S}{\Delta S} = \frac{(R + z)\Delta\theta - R\Delta\theta}{\Delta S} = \kappa z \quad (3.21)$$

as illustrated in Figure 3.8.

Based on the strain distribution, the stress is thus:

$$\sigma = E\epsilon = E\kappa z. \quad (3.22)$$

The moment can then be derived by integrating over the cross-sectional area A :

$$M(x) = \int_A \sigma z dA = \kappa(x) \int_A E z^2 dA = \kappa(x) E \int_A z^2 dA = \kappa(x) EI. \quad (3.23)$$

where I is the cross sectional moment of inertia and EI is known as the bending stiffness.

Rearranging Equation 3.22 after κ and substituting this in Equation 3.23 results in:

$$\sigma = \frac{M(x)z}{I}. \quad (3.24)$$

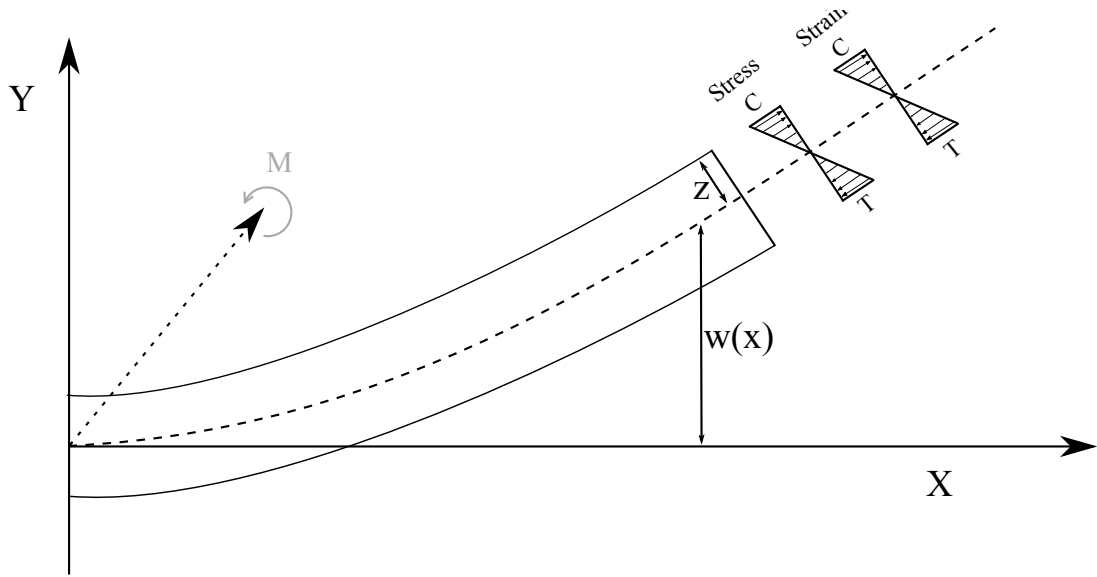


Figure 3.8: Beam - Stress and Strain Distribution

Thus, knowing the cross sectional moment of inertia I that can be calculated based on the cross sectional geometry (a guidance document is accessible by Dupen [91]) as well as the sectional bending moment, the stresses in the material can be derived.

In the case of a wind turbine tower, I_{tower} is:

$$I_{tower} = \frac{\pi}{64}(d_{OD}^4 - d_{ID}^4) \quad (3.25)$$

where d_{OD} is the outer and d_{ID} the inner diameter, respectively. The bending moment can be calculated based on the turbine thrust multiplied by the respective distance along the considered tower segment, although care needs to be taken to take the tower's varying diameter and thickness into consideration. Thus, the moment of inertia is essentially a function with respect to the tower height $I(x)$.

Alternatively, the beam rotation can be defined by the first derivative of the deflection with respect to x ; i.e., the slope of the deflection:

$$\theta(x) = \frac{dw(x)}{dx} \quad (3.26)$$

Chapter 3. Literature Review

where the beam curvature is:

$$\kappa(x) = \frac{d\theta(x)}{dx} = \frac{d^2w(x)}{dx^2}. \quad (3.27)$$

Based on Equation 3.23, $M(x)$ is thus:

$$M(x) = \kappa(x)EI = EI \frac{d^2w(x)}{dx^2} \quad (3.28)$$

and the shear force $V(x)$:

$$V(x) = EI \frac{d^3w(x)}{dx^3}. \quad (3.29)$$

Alternatively, the beam deflection can be derived from $M(x)$:

$$w(x) = \int \int_0^X \frac{M(x)}{EI} dx. \quad (3.30)$$

Alternatively, if the boundary conditions and the load is known, w can be calculated and thus strains and stresses derived based on prederived formulas [92]. Also, there are certain rules to derive e.g. the shear and bending moment diagram while a wind turbine tower example is illustrated in Equation 3.24 and 3.25.

3.3.2.3 Reinforced Concrete

3.3.2.3.1 Cement Curing

Concrete is a combination of cement, water, aggregates, as well as chemicals that when it cures, cement and water react to form chemical bonds between suspended aggregates. This reaction is known as Hydration and is responsible for concrete's strength and rigidity [89]. Figure 3.9 schematically displays the process of concrete curing in terms of the development of compressive strength on the left axis illustrated in black, as well the the temperature development on the right axis in red. Initially the temperature increases significantly caused by a rapid hydration reaction rate, contrary to the development of compressive strength that develops slowly over time in the form of a hyperbolic $\cosh^{-1}x$ function.

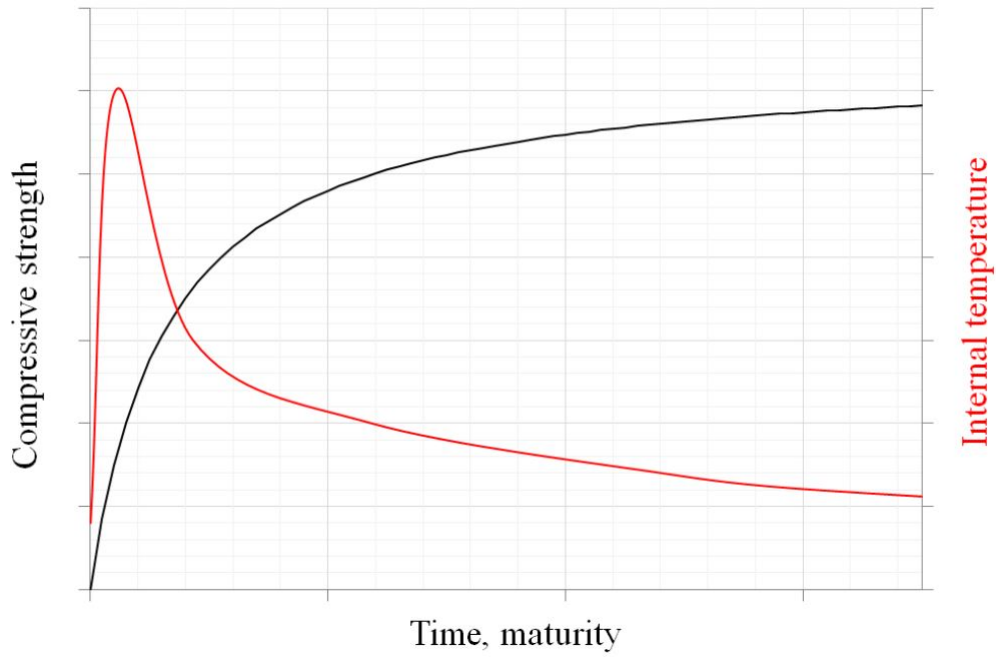


Figure 3.9: Schematic Curing of Concrete

The maturity time can be mathematically expressed,

$$t_e = \sum_{t=0}^{t'} \alpha(T, t) \Delta t \quad (3.31)$$

where t_e is the equivalent age at the reference curing temperature, $\alpha(T, t)$ the age conversion factor and Δt the time interval. Concerning the age conversion factor there are two methods to compute this variable; 1) Nursen-Saul, a linear and hence more practical approach and 2) Arrhenious, which is a non-linear variable. The Nursen-Saul age conversion factor is calculated by:

$$\alpha_{ns} = \frac{T_c - T_0}{T_R - T_0} \quad (3.32)$$

where T_c is the average conversion factor for Δt , and T_0 as well as T_R the datum and reference temperature, typically 0° and 20° Celsius respectively. Arrhenious's method

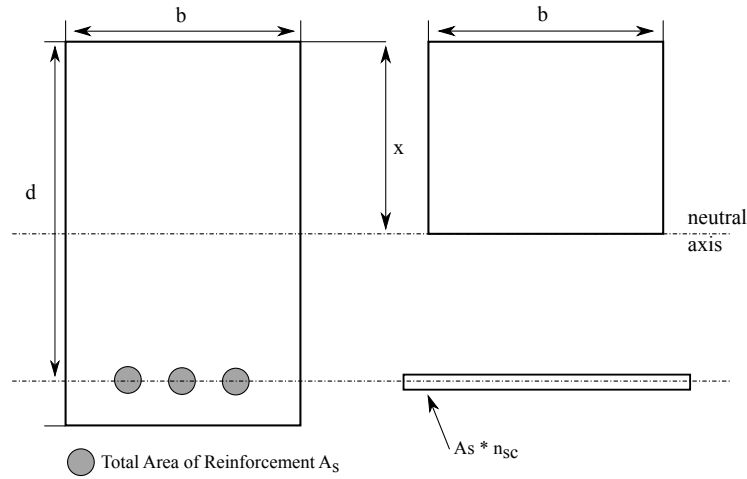


Figure 3.10: Reinforced Concrete Theory [93]

can also be applied,

$$\alpha_{ar} = e^{\frac{-E}{R} \left[\frac{1}{273+T_c} - \frac{1}{273+T_R} \right]} \quad (3.33)$$

where E is the activation energy and R the universal gas constant, $8.314 \text{ [J/(mol.K)]}$. Contrary to Nursen-Saul, Arrhenious takes into account that concrete cures slower below the reference temperature and quicker above.

3.3.2.3.2 Design of a Reinforced Concrete Beam

The structural design process is highly dependent on the purpose and environmental conditions to be exhibit by the structure. This mainly includes the design lifetime, the type of loading, climate effects, as well as aesthetic considerations. “Concrete is assumed to only contribute to the strength resisting bending in the compressive region above the neutral axis i.e all tensile forces are resisted by the steel reinforcement” [93]. As a consequence, in this section, a simple structure; i.e., a reinforced concrete beam is used to exemplify design consideration. These include analysis for sectional moments, shear, and fatigue.

Design for Moments

In order to evaluate tensile stresses in the reinforcement as well as in the concrete

Chapter 3. Literature Review

based on a design moment at section M, it is necessary to compute moments about the neutral axis x. Since all load and geometry parameters are usually known, the neutral axis requires evaluation as illustrated in Figure 3.10. Multiplying the area of the reinforcement bars by the modular ratio ($n_{sc} = E_S/E_C$) results in an equivalent concrete area as demonstrated on the right hand side of Figure 3.10.

Therefore the effective moments of areas are:

$$bx\frac{x}{2} = n_{sc}A_s(d-x). \quad (3.34)$$

Rearranging this results in a quadratic equation,

$$\frac{bx^2}{2} + n_{sc}A_sx - n_{sc}A_sd = 0 \quad (3.35)$$

where the only relevant solution is the positive value, which gives the position of the neutral axis x:

$$x = \frac{n_{sc}A_s}{b} \left(\sqrt{1 + \frac{2bd}{n_{sc}A_s}} - 1 \right). \quad (3.36)$$

The second moment of area I_c of the equivalent concrete section is thus,

$$I_c = \frac{bx^3}{3} + n_{sc}A_s(d-x)^2 \quad (3.37)$$

where the maximum stress at the extreme concrete fibre end is,

$$\sigma_c = \frac{Mx}{I_c}. \quad (3.38)$$

Under the assumption that the beam section remains plane during bending, it can be shown that the strain distribution is linear as illustrated in Figure 3.11 for an ultimate limit state (ULS) analysis. According to [94], the height of the compression zone is set to $\lambda(f_{ck})x$:

$$\lambda(f_{ck}) = \begin{cases} 0.8 & \text{if } f_{ck} \leq 50 \text{ MPa} \\ 0.8 - \frac{f_{ck}-50}{400} & \text{if } 50 \text{ MPa} \leq f_{ck} \leq 90 \text{ MPa} \end{cases} \quad (3.39)$$

where $\lambda_{f_{ck}}$ is the concrete design class strength. Further, the compression stress in the

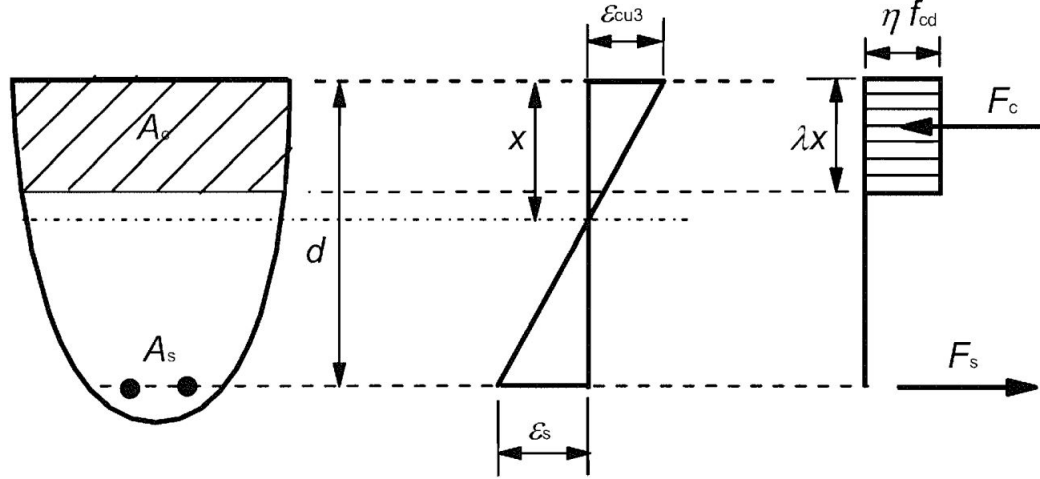


Figure 3.11: Idealised Stress Distribution Reinforced Concrete [94]

concrete is set to $\eta(f_{ck})f_{cd}$:

$$\eta(f_{ck}) = \begin{cases} 1 & \text{if } f_{ck} \leq 50 \text{ MPa} \\ 1 - \frac{f_{ck}-50}{200} & \text{if } 50 \text{ MPa} \leq f_{ck} \leq 90 \text{ MPa} \end{cases} \quad (3.40)$$

where f_{cd} is the design stress for concrete. The design stress depends on the different strength classes of concrete (Table 3.1 of the Eurocode 2 [94]); e.g. the maximum strain in the outermost compression fibre, ϵ_{cu} equals to 3.5‰ if $f_{ck} \leq 50$ MPa.

As visualised in Figure 3.11, simple equilibrium equations are as following:

$$F_s = F_c \iff A_s \sigma_s = f_{cd} \lambda x b \quad (3.41)$$

$$M = \begin{cases} F_s(d - 0.5\lambda x) \\ F_c(d - 0.5\lambda x). \end{cases}$$

Based on the rule of uniform triangles, the following strain ratio is defined:

$$\frac{\sigma_s/E_s}{(d-x)} = \frac{\sigma_c/E_c}{x} \iff \frac{\epsilon_s}{(d-x)} = \frac{\epsilon_{cu}}{x}. \quad (3.42)$$

Chapter 3. Literature Review

which when rearranged becomes:

$$\sigma_s = \sigma_c \frac{E_s}{E_c} \frac{(d-x)}{x} = \sigma_c n_{sc} \left(\frac{d-x}{x} \right). \quad (3.43)$$

Substituting σ_c with Equation 3.38 results in the stress at the section in the reinforcement bars:

$$\sigma_s = \frac{M}{I_c} n_{sc} (d-x). \quad (3.44)$$

Therefore by calculating σ_s , with given beam geometries, Young's modulus of steel and concrete as well as the section moment M that can be calculated with a bending moment diagram (BDM), it can be evaluated whether a structure is within designed load limits. If the considered design is not within limits, through iterations the right properties may be calculated.

Alternatively, with the defined maximum strain in the concrete, ϵ_{cu} the strain in the steel, ϵ_s may be calculated with Equation 3.42 that can be transformed into σ_s via Equation 3.22. With Equation 3.41 it is thus possible to calculate the amount of required reinforcement area of the section.

Generally, the safety factor for concrete, γ_c is 1.5, whereas for the steel reinforcement, $\gamma_s = 1.15$. The higher concrete safety factor is due to a higher uncertainty in material properties that is dependent on i) the batch composition, ii) the casting temperature, iii) the curing type and duration, and iV) the casting vibration and adopted procedure.

Design for Shear

According to Eurocode 2, the design value for the shear resistance $V_{Rd,c}$ without shear reinforcement, but with bending reinforcement is given by:

$$V_{Rd,c} = C_{Rd,c} k (100 p_1 f_{ck})^{1/3} b_w d \quad (3.45)$$

where

$$C_{Rd,c} = 0.18 / \gamma_c$$

$$k = 1 + \sqrt{200/d} \leq 2.0 (d \text{ in [mm]})$$

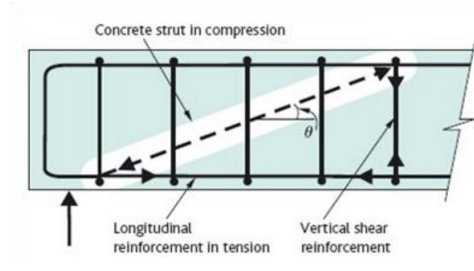


Figure 3.12: Vertical Stirrups

$$p_1 = \frac{A_{sl}}{b_w d} \leq 0.02$$

A_{sl} is the area of the tensile reinforcement

b_w is the smallest width of the cross-section of the tensile area [mm].

$V_{Rd,c}$ must be greater than V_{min} :

$$V_{Rd,c} > k^{2/3} f_{ck}^{1/2} = V_{min}. \quad (3.46)$$

Overall, the greatest shear force in the considered section must be smaller than either V_{min} or $V_{Rd,c}$. The beam's sectional shear values may either come from a BMD or FE analysis.

If $V_{Rd,c}$ is insufficient, stirrups are required to increase the shear capacity as illustrated in Figure 3.12. If sections have vertical stirrups, the shear resistance, V_{Rd} is the smaller value of:

$$V_{Rd} = \frac{A_{sw}}{S} z f_{ywd} \cot \theta \quad (3.47)$$

$$V_{Rd,max} = \frac{\alpha_{cw} b z v_1 f_{cd}}{\cot \theta + \tan \theta} \quad (3.48)$$

where

$$1 \leq \cot \theta \leq 2.5, \text{ this depends on the applied shear force. } \theta_{max} = 21.8$$

S is the spacing of the stirrups

Chapter 3. Literature Review

A_{sw} is the reinforcement area of the stirrups

$\alpha_{cw} = 1$, for structures without pretension

f_{ywd} is the design yield strength of the shear reinforcement

$$V_1 - 0.6(1 - \frac{f_{ck}}{250})$$

$$z = 0.9d \text{ (approximated)}$$

Design for Fatigue Loading

Reinforced concrete structures that are exposed to a cyclic loading are further designed for fatigue. This is a two-fold approach for the steel reinforcement and concrete.

For concrete, sufficient fatigue capacity exists if the following condition is met:

$$\frac{\sigma_{c,max}}{f_{cd,fat}} \leq 0.5 + 0.45 \frac{\sigma_{c,min}}{f_{cd,fat}} \leq 0.9, \text{ for } f_{ck} \leq 50\text{MPa} \quad (3.49)$$

$$\frac{\sigma_{c,max}}{f_{cd,fat}} \leq 0.5 + 0.45 \frac{\sigma_{c,min}}{f_{cd,fat}} \leq 0.8, \text{ for } f_{ck} \geq 50\text{MPa} \quad (3.50)$$

where

$\sigma_{c,max}$ is the highest compression stress in the section under the frequent load combination (compression measured positive)

$\sigma_{c,min}$ is the minimum compressive stress at the same fibre where $\sigma_{c,max}$ occurs.

If $\sigma_{c,min}$ is a tensile stress, then $\sigma_{c,min}$ should be taken as 0.

$$f_{cd,fat} = f_{cd}(1 - \frac{f_{ck}}{250}).$$

σ_c can be calculated with Equation 3.38.

With regards to the steel reinforcement fatigue capacity, the following section (3.3.3) will present the idea of fatigue in more detail. In a nutshell, depending on the expected lifetime cycles and stress range, reinforcement fatigue capacity can be derived.

Concrete Cover

The required concrete cover depends on several factors such as the design lifetime, the quality of concrete, the reinforcement type, the exposure to chlorides, the variation of

Environmental Requirement for $c_{min,dur}$ (mm)							
Structural Class	Exposure Class according to Table 4.1						
	X0	XC1	XC2 / XC3	XC4	XD1 / XS1	XD2 / XS2	XD3 / XS3
S1	10	10	10	15	20	25	30
S2	10	10	15	20	25	30	35
S3	10	10	20	25	30	35	40
S4	10	15	25	30	35	40	45
S5	15	20	30	35	40	45	50
S6	20	25	35	40	45	50	55

Figure 3.13: Concrete Cover [94]

wet and dry state, the chemical environment, the orientation of the surface, and on the construction temperature. According to Eurocode 2, the cover may vary between 10-55 mm. This is the minimum concrete thickness between the outside reinforcement elements and the structure's edges. Guidance with respect to the structural class (design lifetime, concrete strength class - Table 4.3N of EC2) and concrete exposure class (Table 4.1 of EC2; corrosion due to environmental conditions) is illustrated in Figure 3.13.

Crack Control

"Cracking is normal in reinforced concrete structures subject to bending, shear, torsion or tension resulting from either direct loading or restraint or imposed deformations" [94]. Although cracking is expected to some degree, there is a crack width limit, w_{max} [mm] that is governed under the SLS limit state. The acceptable crack width is dependent on the concrete exposure class and type of reinforcement as illustrated in Figure 3.14.

3.3.3 Fatigue

3.3.3.1 Fatigue General

According to the definition by [95] "fatigue failure 'damage' is added to a material cycle by cycle, irrespective of constant amplitude loading or varying amplitude loading. Therefore quantification of 'damage' is important for life evaluation. The fatigue failure process of a material is composed of two stages, i.e., crack initiation and crack propaga-

Exposure Class	Reinforced members and prestressed members with unbonded tendons	Prestressed members with bonded tendons
	Quasi-permanent load combination	Frequent load combination
X0, XC1	0,4 ¹	0,2
XC2, XC3, XC4	0,3	0,2 ²
<div>AC2</div> XD1, XD2, XD3, XS1, XS2, XS3 <div>AC2</div>		Decompression
Note 1: For X0, XC1 exposure classes, crack width has no influence on durability and <div>AC1</div> this limit is set to give generally acceptable appearance. In the absence <div>AC1</div> of appearance conditions this limit may be relaxed.		
Note 2: For these exposure classes, in addition, decompression should be checked under the quasi-permanent combination of loads.		

Figure 3.14: Crack Control [mm] [94]

tion processes”. In 1945 M.A. Miner popularised the famous Miner’s rule that has been first published in 1924 by A. Palmgren, thus often also referred to as Palmgren-Miner rule, which is widely applied such as e.g. in the Eurocode 2 for structural buildings [94]. The Palmgren-Miner rule quantifies the linear damage concept where the cumulative damage, D is obtained from N sources:

$$D_{tot} = \sum_{i=1}^N \frac{D_i}{D} \quad (3.51)$$

where D_i/D is the fractional damage received from the i th source. As the component damage is dependent on the applied stress, unique S-N² curves can be determined through experimental material testing that state the amount of cycles until failure for a given stress range, σ as illustrated in Figure 3.15 for different materials³. This allows to quantify a component’s fatigue damage characteristics.

²stress (S) against the number of cycles to failure (N)

³Different materials have different S-N characteristics. The illustrated Eurocode 2 example is a design assumption for concrete reinforcement

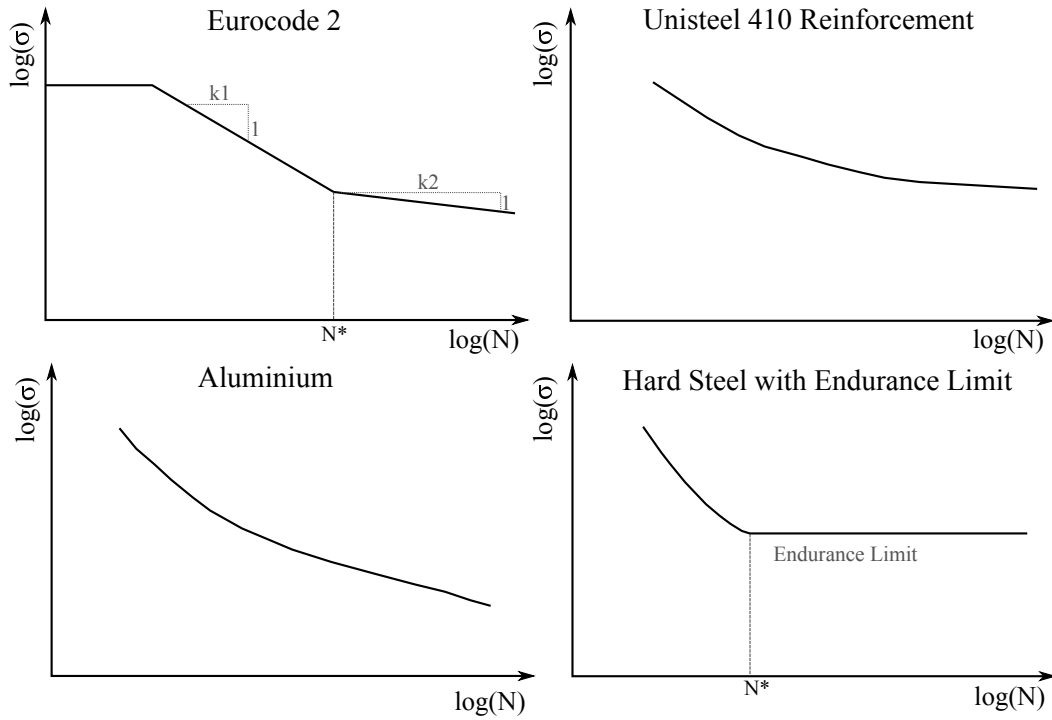


Figure 3.15: Difference in Fatigue Behaviour [94, 96, 97]

Based on the experimentally derived S-N curve, it is possible to evaluate the fractional fatigue damage n_i/N_i for the observed stress ranges σ_i , so that the Palmgren-Miner rule predicts fatigue failure when

$$D = \sum_{i=1}^N \frac{n_i}{N_i} = 1. \quad (3.52)$$

Figure 3.16 presents a simplistic scenario defined by a component loading with 2 load sources. The first load source is depicted in red and defined by n_1 , the number of cycles subjected to a stress of σ_1 with the fraction of $a_1/(a_1 + a_2)$ representing the fatigue damage D_1 . The second load source is depicted in green and defined by n_2 , the number of cycles subjected to a stress of σ_2 with the fraction of $b_1/(b_1 + b_2)$ representing the fatigue damage at the experienced stress D_2 . Therefore the total fatigue damage of the

example, $D_{Example}$ is given by:

$$D_{Example} = \sum_{i=1}^N \frac{n_i}{N_i} = \frac{a_1}{a_1 + a_2} + \frac{b_1}{b_1 + b_2}. \quad (3.53)$$

As long as a component's fatigue damage is below 1, the condition is non-critical; however, if the damage is approaching 1, inspections and potential component replacement are required.

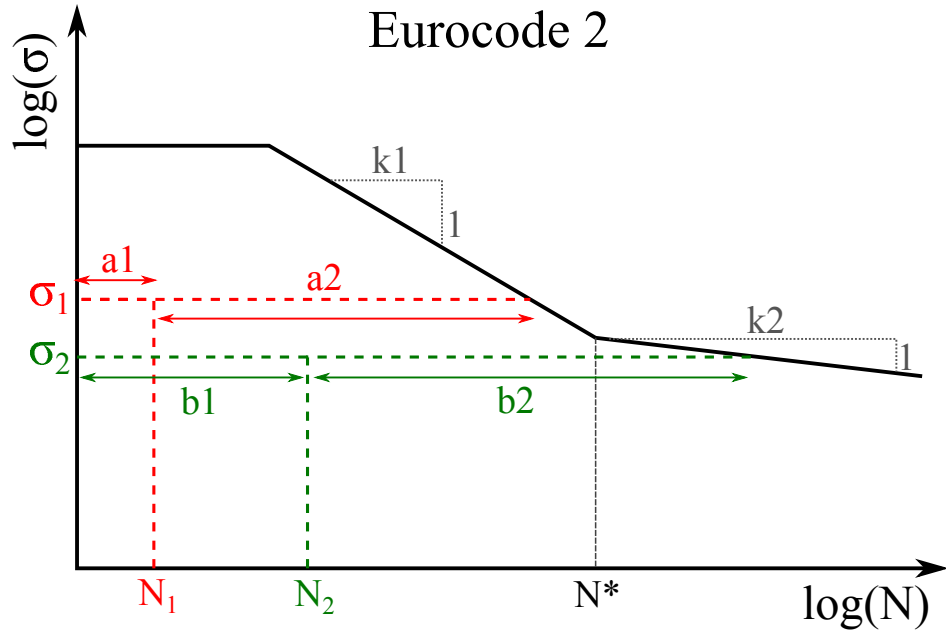


Figure 3.16: Simplistic Fatigue Example

As illustrated in Figure 3.15, different materials have different S-N characteristics. The Eurocode 2 calculation guideline for straight and bent bars starts at the yield point of the reinforcement and is characterised by:

- $N^* = 10^6$
- $k_1 = 5$
- $k_2 = 9$
- $\gamma_{S,fat} = 1.15$

Chapter 3. Literature Review

- $\Delta\sigma_{RSK}$ at $N^* = 162.5$ [MPa] (straight bars)

where the obtained resisting stress range at N^* cycles, $\Delta\sigma_{RSK}$, should be divided by the safety factor $\gamma_{S,fat}$. Since, the S-N curve is approximated to a linear relationship in a log-log graph its underlying characteristics are exponential in nature, thus a power law can be defined:

$$N_1 = N_2 \left(\frac{S_1}{S_2} \right)^{1/b} \quad (3.54)$$

where b is the slope of the line, often referred to as the Basquin slope that is calculated by:

$$b = \frac{-(\log S_1 - \log S_2)}{\log N_2 - \log N_1}. \quad (3.55)$$

In order to obtain the number of cycles to failure at a given stress amplitude or vice versa, the Basquin-Equation is applied:

$$\Delta\sigma = BN_i^b \quad (3.56)$$

where, the constant B is a stress related material constant, and N_i the maximum amount of cycles at stress range $\Delta\sigma$. Thus, if the stress exponent is known, as well as any point in the approximation, B can be derived. The S-N curve is material dependent, experimentally derived, and characterised in the material factor m ($m = 4$ for steel and $m = 10$ for composites) where the slope of the S-N curve is $-1/m$. Therefore by taking the inverse of Equation 3.56 and substituting b with $-1/m$

$$\begin{aligned} \frac{\Delta\sigma}{B} &= N_i^b \\ \frac{B}{\Delta\sigma} &= \frac{1}{N_i^{-1/m}} \end{aligned}$$

allows to derive the following Equation:

$$\left(\frac{B}{\Delta\sigma} \right)^m = N_i \quad (3.57)$$

which is often encountered in literature. Substituting Equation 3.57 in Equation 3.52,

thus results in the fatigue Damage:

$$D = B^{-m} \sum_i^N n_i \Delta \sigma_i^m. \quad (3.58)$$

A wind turbine is expected to operate in different conditions. Therefore, a total wind turbine lifetime fatigue design damage assessment is calculated based on weighted series:

$$D_{tot} = B^{-m} \sum_j^{N_{series}} \left(f_j \sum_i^{N_{ranges}} n_i \Delta \sigma_i^m \right)_j. \quad (3.59)$$

where f_j is the weighting coefficient for the total time period the turbine is expected to operate in the conditions simulated by the time series of different design load cases (DLC). For example, this can be the fatigue power production case (DLC 1.2 – other cases are accessible in the IEC 61400 standard), where f_j is dependent on the Weibull probability that is dependent on the mean wind speed; i.e., each wind speed would require a time simulation.

Overall, sufficiently developed S-N curves are derived from numerous testing series. Gained data is subjected to statistical analysis and the actual derived curve is normally given based on median points, thus a presented S-N curve usually presents a failure probability of 50% [98]. Therefore, it is likely to encounter S-N curves with additional probability bands. In addition, most S-N curves tend to commence at 10^3 cycles paired with a fatigue strength, S_{1000} , that according to literature can be determined to be a fraction of the ultimate tensile strength [99, 100] and is dependent on the loading type and material as illustrated in Table 3.3.

Table 3.3: Estimates of S_{1000} . (USS - Ultimate Shear Strength)

Type of Material	Type of Loading	S_{1000}
All	Bending	0.9 x UTS
All	Axial	0.75 x UTS
Steel	Torsion	0.9 x USS = 0.72 x UTS
Nonferrous	Torsion	0.9 x USS = 0.63 x UTS
Cast Iron	Torsion	0.9 x USS = 1.17 x UTS

Chapter 3. Literature Review

As demonstrated in Figure 3.15, some material types are approximated by an endurance limit, usually at $5 * 10^6$ cycles where the material is assumed to sustain a given stress range indefinitely (bottom right) or where the stress exponent is reduced significantly as in the case of the Eurocode (top left). According to Dieter and Bacon [101], materials that are “strain ageing”⁴ such as steel and titanium, experience a stress enhancement so at low stresses it is not sufficient to cause failure. On the other hand, non strain ageing material types (majority of non-ferrous alloys); e.g., aluminium or derivatives of copper (Figure 3.15 bottom left) do not have such an advantageous response at low stresses.

Besides cycled loading, a structure may be exposed to a static load profile due to e.g. gravity or pre-stress. The latter might be a wind turbine tower flange/foundation bolt that when tightened, will be subjected to a significant mean stress σ_m , originating from the bolt tensioning; besides being exposed to operational loading σ_a . In essence, in order to determine the cycles to failure, the S-N curve will draw an unrealistic picture as the method is incapable of taking the mean stress into consideration since the y-axis of the S-N curve is defined by the stress amplitude, irrespectively of any mean stress. In order to overcome this limitation the Goodman diagram is applied that is based upon the S-N curve; however, in the analysis σ_m is introduced within the fatigue calculation. A generic Goodman diagram is illustrated in Figure 3.17. As a first step the yield point Y , in tension and compression for σ_m as well as for σ_a is placed and connected, thus forming a triangle. Basically if any σ_m - σ_a combination lies above this line a given design will yield. From the S-N curve a designed cycles until failure reference value can be selected that will express the design stress amplitude for a determined number of cycles σ_d that usually includes a safety factor. σ_d is plotted on the stress amplitude axis as well as the UTS on the mean stress axis and connected by a straight line. Any design point that is thus within the grey shaded safe area will be safe from fatigue or yield failure. The component’s geometry can be iterated in order to find the most suitable σ_m - σ_a combination.

⁴The strength of the material changes with the experienced cycles, thus the yield point increases.

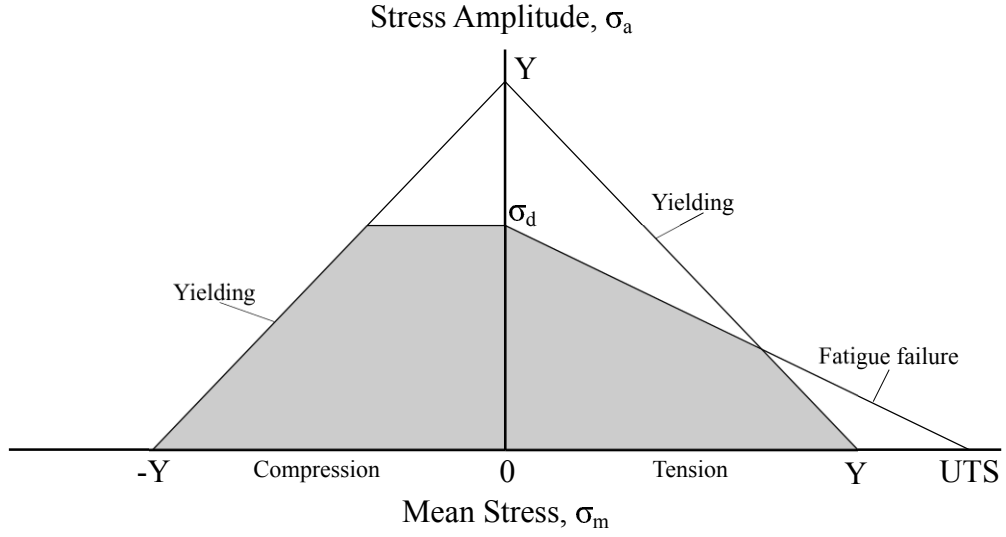


Figure 3.17: Goodman Diagram [99]

The application of S-N curves and Goodman diagrams is recommended to be applied with caution since the experimental basis is stochastic in nature and thus can exhibit variations in fatigue response. As a consequence safety factors are introduced to ensure the safety of a component's design. The Eurocode's safety factor for straight reinforcement is 1.15, whereas for bend bars a reduction factor based on the mandrel and bar diameter is applied.

Apart from the Goodman methodology there are other approximations (Gerber, Morrow, Soderberg) that have been contrasted to actual failure points [102] where the Goodman and Soderberg (σ_d to Y) line was identified as the most suitable approach to effectively separate observed failures.

The corrected equivalent stress range $\Delta\sigma_0$ is thus obtained by adjusting the stress ranges after the rainflow counting⁵,

$$\Delta\sigma_0 = \frac{\Delta\sigma_{\bar{\sigma}}}{\left(1 - \left[\frac{\bar{\sigma}}{\sigma_{UTS}}\right]^Z\right)} \quad (3.60)$$

where $\Delta\sigma_{\bar{\sigma}}$ is the stress range at a non-zero mean stress $\bar{\sigma}$ (usually the monitored

⁵This methodology is presented at a later stage.

stress), σ_{UTS} the ultimate tensile stress of the material, and $Z = 1$ the Goodman exponent [103]. For the Gerber relation, $Z = 2$ and σ_{UTS} is exchanged with the yield stress. “Mean stress correction models are applicable in the tensile range only, therefore $\Delta\sigma_{\bar{\sigma}} = \Delta\sigma_0$ is used in compression” [104]. This is because in tension cracks appear and grow over time, whereas in compression this failure mechanism does not occur. Hence more conservatism is applied in tension than compression. For the case of wind turbine tower measurements, the Goodman correction procedure is not applicable due to a lack of mean tension (though having the rotor on one side will likely cause tension, which is to some degree counter balanced by the gravitational loading).

In many applications, it is of interest to measure and thus evaluate a component’s loading or cumulated fatigue damage, the latter if sufficient measurements are available. Apart of measurement and installation uncertainties, a measured loading profile requires to be translated into a form where a signal can be decomposed into different σ_a bands. Once determined how many cycles a component experiences at n^{th} σ_a the cumulative actual damage can be determined as illustrated in Figure 3.16. The conventional signal decomposition methodology is Rainflow Counting first proposed by Matsuishi and Endo in 1968 that is widely applied in industry [105, 106]. In order to efficiently decompose any given signal, bin ranges are normally defined that can potentially skew the analysis thus its sensitivity and selection of bin width requires careful consideration. The rainflow counting algorithm process is illustrated by Marsh et al. [104] based on a three or four point criterion and the subsequent residue analysis.

3.3.3.2 Fatigue of Members, Connections, and Joints

According to EC3 – EN 1993–1–9:2005, members, connections, and joints require fatigue adjustment that include “the effects of geometrical and structural imperfections from material production and execution (e.g. the effects of tolerances and residual stresses from welding)” [107]. With regards to welded joints, fatigue life is defined in the weld class, $\Delta\sigma_C$ that basically defines the endurance limit at 2 million cycles; this is also known as the FAT class. A wind turbine steel tower is commonly manufactured

from hot rolled steel plates that are welded longitudinally and circumferentially into 20-30 m tubular tower sections [108]. However, “one of the most important reasons of structural failure observed in wind turbine towers is fatigue failure of welds” [109]. Since welding impacts fatigue endurance, the S–N curve requires adjustment. According to EC3, the S–N curve is defined by $\Delta\sigma_C$, the endurance limit at 2 million cycles, and $\Delta\sigma_D$, the constant amplitude fatigue limit at 5 million cycles with an S–N slope of -1/3. Basically, if the stress spectrum is above and below $\Delta\sigma_D$, the fatigue strength is based upon the extended fatigue strength curve, where the slope reduces to -1/5 between $5 * 10^6$ and $1 * 10^8$ cycles, the latter at which point the cut-off limit, $\Delta\sigma_L$ is reached. Corresponding S–N curves for different weld classes ($\Delta\sigma_C$) are illustrated in Figure 3.18.

If $\Delta\sigma_C$ is known, $\Delta\sigma_D$ can be calculated by:

$$\begin{aligned}\Delta\sigma_D &= \frac{2^{1/3}}{5} \Delta\sigma_C \\ &= 0.737\Delta\sigma_C\end{aligned}\tag{3.61}$$

and $\Delta\sigma_L$ by:

$$\begin{aligned}\Delta\sigma_L &= \frac{5^{1/5}}{100} \Delta\sigma_D \\ &= 0.549\Delta\sigma_D.\end{aligned}\tag{3.62}$$

Overall, the wind turbine tower has different welded and bolted connections; i.e. tower sections that are circumferentially welded are defined as “transverse splices in plates, flats, rolled sections or plate girders” with a FAT class of $\Delta\sigma_C = 80$ [MPa], whereas the tower-flange intersection, which can either be designed as i) a “tube socket joint with 80% full penetration butt welds” ($\Delta\sigma_C = 71$ [MPa]) or ii) a “tube socket joint with fillet welds” ($\Delta\sigma_C = 40$ [MPa]) or iii) a “full-sectional butt weld of rolled sections without cope hole” with a FAT class of $\Delta\sigma_C = 90$ [MPa] all of which can have a T or L flange connection. In literature, $\Delta\sigma_C$ varies between 40-80 MPa; however, this is likely be defined by the tower-flange weld assumption [108, 110, 111]. Therefore, if $\Delta\sigma_C = 80$

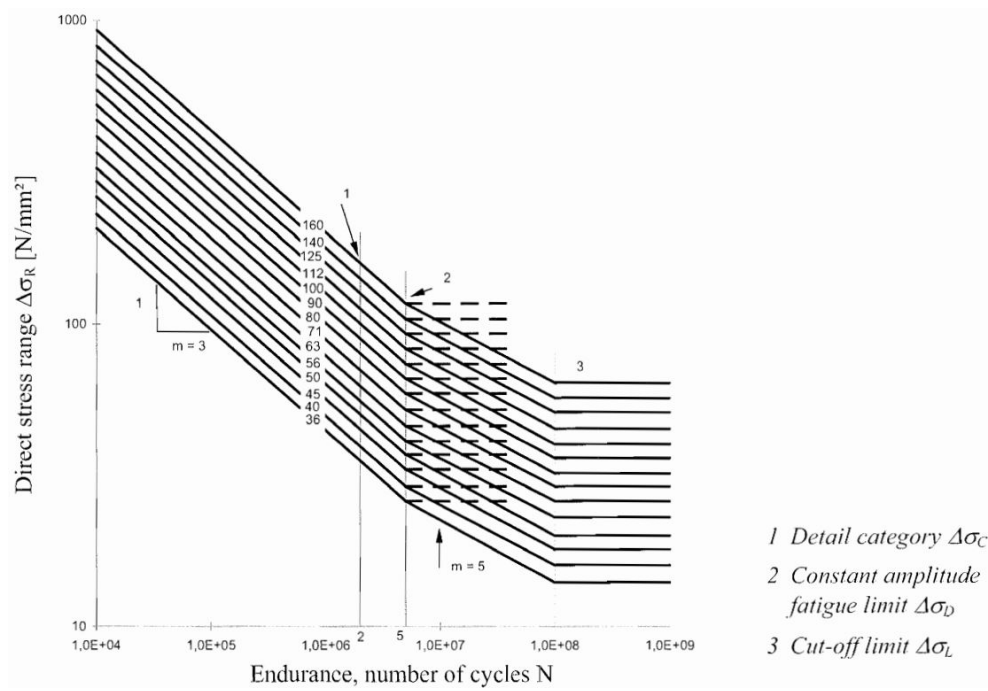


Figure 3.18: Fatigue strength curves for direct stress ranges. The curves are derived based on a 95% survival probability at a 75% confidence interval. [107].

[MPa], $\Delta\sigma_D$ is 59 [MPa] according to Equation 3.61, and $\Delta\sigma_L$ is 32 [MPa] according to Equation 3.62. With the established S-N curve, Miner's damage calculation can be applied to assess the cumulated fatigue damage as exemplified in Equation 3.51.

With regards to fatigue welds and FEM simulations, it is important to familiarize oneself with the phenomena of singularities and its effect when simulating corners. For welded sections it is recommended to take the average stress along the welded line as a reference stress/strain for design purposes as suggested by Snnerlind [112].

3.3.3.3 Damage Equivalent Loads

In engineering, often short-term simulations are executed and the load profile translated into a damage equivalent load (DEL) to gain a simplistic and informative comparison. The concept is based on Equation 3.59; however, a selected n_{eq} locks the number of

cycles (for wind turbines usually $10^6 - 10^7$) and S-N curve slope:

$$D_{tot} = B^{-m} n_{eq} \Delta \sigma_{eq}^m.$$

Therefore, the damage equivalent load $\Delta \sigma_{eq}$ is calculated by:

$$\Delta \sigma_{eq} = \left(\frac{D_{tot} B^m}{n_{eq}} \right)^{1/m} = \left(\frac{\sum_j^{N_{series}} f_j \sum_i^{N_{ranges}} n_i \Delta \sigma_i^m}{n_{eq}} \right)^{1/m}. \quad (3.63)$$

3.3.3.4 Crack Initiation and Propagation

“After the tower experiences a through-thickness crack, the remaining fatigue life attributable to crack propagation can still be substantial. In fact, the crack will continue to propagate gradually after each cycle until it reaches the critical size where brittle fracture occurs after certain cycles of loading” [113]. In design codes, due to conservatism, the remaining lifetime of structures is defined irrespectively of the cracked state fatigue life; however, in reality a structure would remain stable up to the critical crack length.

The crack propagation is defined by the Paris law:

$$\frac{da}{dN} = C(\Delta K_{eff})^m \quad (3.64)$$

where C is the crack growth rate coefficient; ΔK_{eff} the effective stress intensity factor range, which depends on the effective stress range S_{reff} , the crack length a as well as other geometric factors.

According to Do et al. [113], the critical crack length of failure of a tower weld is:

$$a_f = \frac{1}{\pi} \left(\frac{K_r * K_{IC}}{S_{t,max}} \right)^2 \quad (3.65)$$

where K_r is the stress intensity factor (0.707), K_{IC} the material toughness (100 MPa \sqrt{m}), and $S_{t,max}$, the maximum tensile stress at the tower base.

In order to evaluate the number of cycles after first crack appearance until brittle

failure:

$$N_{if} = \frac{a_f^{1-m/2} - a_i^{1-m/2}}{C(S_{reff}\sqrt{\pi})^m(1 - m/2)} \quad (3.66)$$

where a_i is the initial crack length, which can be set as the detectable crack size or the visible through-thickness crack. The latter that can be assumed to be twice the thickness of the tower wall. S_{reff} can be substituted with $\Delta\sigma_{eq}$ and the period in years until brittle failure calculated by $N_{if}/N_{eq} * Y_d$, where Y_d is the design life of D_{tot} .

The analysis is highly dependent on C , thus careful evaluation is necessary to identify the correct crack growth rate. Depending on the applied equation the growth rate can be given in m/cycles or mm/cycles.

In the following exercise, the illustrated crack propagation methodology is applied to evaluate the potential crack growth development of the considered turbine in Section 6. The respective parameters are illustrated in Table 3.4. The damage equivalent load in the prevailing wind direction was identified as 48.5 MPa based on Equation 3.63.

Table 3.4: Crack growth parameters

Parameter	Value	Comment
Wall thickness [m]	0.04	From foundation FEM
S_{reff}	48.5	$N_{eq} = 10^6$, $m = 3$, 25 years
K_r	0.707	From [113]
K_{IC} [MPa \sqrt{m}]	100	From [113]
a_i [m]	0.08	Double the wall thickness
m	3	For steel
$S_{t,max}$ [MPa]	131	Half the maximum $\Delta\sigma$ of rainflow count (+5%)
C (high) [m/cycle]	$1.65 * 10^{11}$	From [114]
C (low) [m/cycle]	$1.24 * 10^{11}$	From [113]

The crack growth rate is dependent on several parameters, such as the geometry of the component, the material composition as well as environmental parameters. In literature, C varies as contrasted in Table 3.4 resulting in either 1.2 or 1.6 years to failure after initial crack detection. At this stage the crack has reached a final critical length of 0.1 m. In theory, this should allow for sufficient time to identify a growing crack given half year inspection intervals. However, in practise the loading is stochastic, thus if a critical event occurs the time to catastrophic failure may be shortened significantly.

3.3.4 Economics

Within the world of economics there are different parameters to simplify complex calculations and models to easily understandable parameters, such as levelised cost of energy, internal rate of return, and return on investment (ROI). Essentially, all parameters provide financial information; however, the usage and degree of detail within the analysis differs. The most basic and hence least realistic method is the simple ROI,

$$ROI_{simple} = \frac{\text{Gain from Investment} - \text{Cost of Investment}}{\text{Cost of Investment}} \quad (3.67)$$

where the gain from investment mirrors all monetary income flows, and the cost of investment is the cumulated value of all associated investment costs. Consequently by dividing with all costs, the ROI will provide a financial parameter on how much money is generated per unit investment (€,£,\$, etc). Equally the ROI can be expressed as a percentage; i.e., based on the investment sum, how much profit is generated. Although simple and easily understandable, the ROI lacks a very important bit of information; the value of money over time. This is called discounting and fundamentally defines that an amount of money at present has a higher value than the equivalent value in the future. Because, hypothetically the present value could be invested, hence the gained interest rate increases the total value in the future. This can be marginally within short time periods; however, modelling 20 years of cash flows or more which is industrial standard for wind turbine investments makes a difference due to compound interest.

The net present value NPV is today's value of future money flows,

$$NPV = \sum_{t=1}^T \frac{Income_t - Costs_t}{(1+i)^t} - C_i \quad (3.68)$$

where T is the total amount of years, t any specific year, i the interest rate, and C_i the capital investment cost. Now the IRR, is the interest rate where the total discounted

Chapter 3. Literature Review

investment/NPV is zero, hence all information is captured in one relative figure related to all cash flows (positive and negative), whereas the NPV is an arbitrary amount, which is not based to any reference. In other words the NPV will for example give £20.000, however this could be any percentage of total investment costs, whereas the IRR will give a profit percentage much more like the ROI with more realistic assumptions; i.e., discounting. The IRR can be iteratively calculated with the following Equation by varying i so that the $IRR(i)$ becomes 0:

$$IRR(i) = \sum_{t=1}^T \frac{Income - Costs}{(1 + i)^t} - C_i = 0. \quad (3.69)$$

Ultimately if a company has a minimum required return, hence referred to as internal rate of return i_{Min} (also referred to as hurdle rate) and the project proposal's estimated interest rate $i_{Project}$ is greater than i_{Min} , an investment is advised and vice versa.

LCOE is a parameter to be able to compare different competing energy technologies such as gas, coal, nuclear, solar, and so on and so forth. According to the National Renewable Energy Laboratory (NREL) [71] LCOE is defined by the following formula,

$$LCOE_{Simple} = \frac{\text{Present Value of Total Costs (\$)}}{\text{Lifetime energy production (MWh)}} \quad (3.70)$$

where irrespective of any revenue income streams, the discounted and hence present value of total costs is divided by the lifetime energy production. Therefore, the result of Equation 3.70 generates the cost per generated energy unit, here MWh. In fact LCOE is a much more complex calculation as taxes, depreciation, and costs (variable & fixed) have to be combined together,

$$LCOE_{True} = \frac{(CapEx \cdot FCR) + OpEx}{AEP_{net}} \quad (3.71)$$

where

Chapter 3. Literature Review

$$\begin{aligned}
FCR &= \frac{i(1+i)^T}{(1+i)^T - 1} \cdot \frac{1 - (\tau \cdot PV_{dep})}{(1 - \tau)} \\
CapEx &= \text{Capital expenditures } [\$/\text{MWh}] \\
AEP_{net} &= \text{Net annual energy production } [\text{MWh}/\text{MW}/\text{yr}] \\
&= MW_{net} \cdot 8760 \cdot CF \\
OpEx &= \text{Operational expenditures } [\$/\text{MW}/\text{yr}] \\
&= LLC + OPER + MAIN \\
\tau &= \text{Effective tax rate } [\%] \\
PV_{dep} &= \text{Present value of depreciation } [\%] \\
CF &= \text{Net capacity factor } [\%] \\
LLC &= \text{Land lease costs } [\$/\text{MW}/\text{yr}] \\
OPER &= \text{Pretax levelized operation costs } [\$/\text{MW}/\text{yr}] \\
MAIN &= \text{Pretax levelized maintenance costs } [\$/\text{MW}/\text{yr}].
\end{aligned}$$

Basically the first fraction of the fixed charge rate (FCR) is multiplied with the $CapEx$ which will generate a constant annuity payment per year based on the present value ($CapEx$). The second fraction of FCR accounts for the fact that if different technologies are compared depreciation and taxes can be inhomogeneous and have to be accounted for. For example a wind turbine with high investment costs and zero fuel costs, will have a much longer time to account for depreciation than a gas turbine, with operational fuel expenditure [115]. Given that this thesis analyses the changes of LCOE for wind energy deployment, this part will not be accounted for. However, in terms of ROI and IRR, depreciation and taxes are considered, as income cash flows are considered, hence such changes do matter. Operational costs ($OpEx$) include all running costs; however, as taxes are not accounted for, the present value of all expenses are applied in agreement with Equation 3.70. Lifetime energy production and AEP_{net} basically express the same, the difference is the former is the lifetime energy production whereas the latter is the yearly energy production. Therefore, depending what denominator format is applied (Equation 3.70 versus 3.71), the numerator has to be in agreement and vice versa. Operational expenditure accounts for all additional costs to run the power plant, such as land lease costs (LLC), operational costs ($OPER$) and maintenance costs ($MAIN$) that based on available sources can account between 11 to

30% of total lifetime costs [70, 116].

A different metric for LCOE is applied by the Department of Energy and Climate Change (DECC) than the one demonstrated by NREL as presented in Equation 3.71. Essentially in order to compute LCOE, the net present value (NPV) of total costs needs to be calculated, where the actual investment cost is considered as an overnight cost, contrary to NREL's application of constant annuity payments. Further, with regards to the discount factor NREL applies a weighted average cost of capital (WACC), which is real; i.e., cleaned for inflation and after tax corrected that is within the order of 6.5% [71]. DECC applies a hurdle rate, which is basically the required return by an investor very similar to the IRR i_{Min} metric, which is set at 10% although in form of a sensitivity analysis 7.5% is applied as well [117–119]. An overview of cost estimations for onshore wind park deployments above 5 MW elaborated by DECC in July 2013 are given in Table 3.5. It is important to notice that additionally to O&M costs insurance, connection, and use of system charges are taken into consideration as part of OpEx.

$$NPV_{TotalCosts} = \sum_{n=1}^T \frac{\text{total capex and opex costs}_n}{(1+i)^n} \quad (3.72a)$$

$$NPV_{ElectricityGeneration} = \sum_{n=1}^T \frac{\text{net electricity generation}_n}{(1+i)^n} \quad (3.72b)$$

As generated electricity flow is a monetary metric, it has to be discounted as well, which might be counter-intuitive because a specified amount of delivered electricity at present supplies the same energy as the equivalent delivery in the future. The point is that from this electricity supply, a revenue stream is created and money is exchanged, hence discounting is necessary (Equation 3.72b). If a turbine's physical parameters are known, the energy yield can be estimated by application of a Weibull distribution that can be modified according to local recorded wind rose statistics (mean wind speed, turbulence intensity, and standard deviation) with the shape and scale factor as well as the mean recorded wind speed. Finally in order to calculate DECC's LCOE, the

Table 3.5: DECC's Onshore >5 MW Wind Energy Deployment Cost Assumptions [117]

Cost Item	Scenario	2016	2017	2020
Pre-development [£/kW]	High	240.00	240.00	240.00
	Medium	100.00	100.00	100.00
	Low	30.00	30.00	30.00
Construction costs [£/kW]	High	1,800.00	1,800.00	1,700.00
	Medium	1,500.00	1,500.00	1,400.00
	Low	1,100.00	1,100.00	1,100.00
Fixed O&M [£/MW/y]	Medium	37,100.00	37,100.00	37,200.00
Variable O&M [£/MWh]	Medium	5.00	5.00	5.00
Insurance [£/MW/y]	Medium	3,000.00	3,010.00	3,010.00
Connection & Use of System Charges [£/MW/y]	Medium	4,510.00	4,510.00	4,510.00

$NPV_{TotalCosts}$ is divided by $NPV_{ElectricityGeneration}$ as exemplified in Equation 3.73.

$$LCOE = \frac{NPV_{TotalCosts}}{NPV_{ElectricityGeneration}} \quad (3.73)$$

DECC's estimated LCOE values are within the order of £90-100 per MWh, whereas the American Department of Energy (DOI) as well as NREL conclude \$70/MWh [72, 117, 118]. Therefore, depending on the applied metric and input assumptions, LCOE can vary significantly. Nevertheless, for this thesis DECC's metric is applied, because this work mainly covers the European sector, and second a more realistic picture is achieved by discounting costs and energy yield over the years as identified by Aldersey-Williams and Rubert [120].

3.3.5 Wind Turbine Generators

Wind Turbines generate electricity from a stochastic wind input that causes high fluctuations in loading over the estimated lifetime of 10^8 cycles and beyond [121]. Accordingly, fatigue resistance is one of the major design aspects besides the ability to withstand extreme loads, such as the 50 year gust as defined in the IEC 61400 standard issued by the International Electrotechnical Commission [106]. Over the past decade, the wind industry's trend has been to up-scale horizontal axis wind turbines (HAWT) as the available power in the wind scales quadratically with the rotor radius as illustrated in

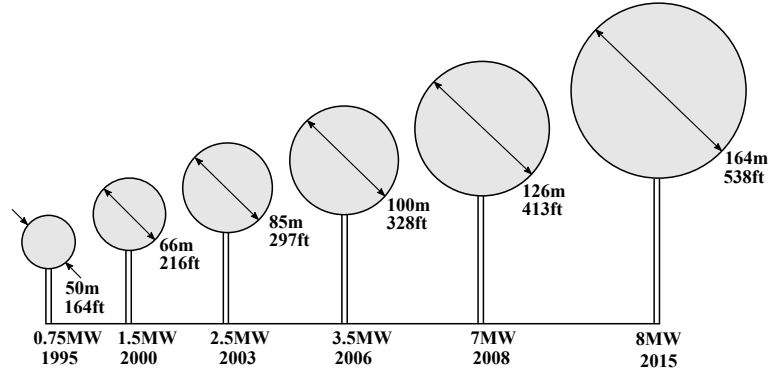


Figure 3.19: Wind Turbine Up-Scaling (modified from [122]);
2015: Offshore

Equation 3.74,

$$P_{wind} = \frac{1}{2} \rho \pi r^2 v^3 C_p(\lambda, \beta) \quad (3.74)$$

where P_{wind} is the power generated, ρ is the density of the air, v is the wind speed, and C_p is the power coefficient, which is a function of the tip-speed ratio λ and pitch angle β .

Therefore, as further demonstrated by Figure 3.19, turbine manufacturers have started to produce machines with capacities well above 7 MW, such as the onshore gearless Enercon E-126 (7.58 MW) or the MHI Vestas V164-8.0 (8 MW) designed for the offshore market, the former with 126 m rotor diameter and the latter with 164 m, respectively. Upscaling in general offered quick and successful product development; however, today's rotor diameters' advancements are accompanied by critical factors. First, research identified that turbine components do not scale linearly; e.g., blade mass scales between $R^{2.3}$ to $R^{2.7}$ [123], thus gravity forces increase notably. Second, rather than a point wind speed, the rotor experiences spatial and temporal wind speed variations over the entire swept area (πr^2), hence each blade cuts through a changing wind profile often referred to as rotational sampling [124]. As a result, stochastic as well as deterministic loadings such as tower shadow, gravity and wind shear significantly increase too, since the swept area scales quadratically. Most of these loadings will propagate in form of vibration through the drive-train and subsequently absorbed by the tower and foundation, although to some degree the blades provide aerodynamic damping (only fore-aft).

Likewise, operational loading is further caused by a turbine’s control; i.e., nacelle yawing, start-up and emergency shut-down procedures that also subject a turbine to load events [125].

3.3.5.1 Factors affecting Individual Turbine Loading

Figure A.2 of the appendix presents an overview of parameters that can affect individual turbine loading. From this graph, one can see that there are a significant amount of items to be considered to be able to confidently state whether a turbine is fit for lifetime extension. Besides wind turbine control that can significantly affect wind turbine loading, individual site conditions are the main characteristics that are impossible to influence due to their natural occurrence. Factors affecting a turbine are numerous such as the local Weibull distribution with its scale and shape parameter, turbulence intensity, mean wind speed, wind rose (frequency-direction distribution), atmospheric stability, terrain, shear and veer profile, frequency of extreme events, as well as potential wake impacts due to surrounding wind turbines or other obstacles. As a confidential source from SPR pointed out: “we see now 50 year gusts on a monthly scale” and illustrated in [126], hence even if such information of the past is available, the system is in a dynamic state where loads are difficult to predict for a structure’s design life. To give an example, Figure 3.20 displays two wind roses of different locations. The left graph’s location is characterised by a bidirectional wind inflow, whereas the right location is more evenly spread. Applying this information to foundation and tower fatigue loading, it is very obvious that the left turbine’s foundation will experience much higher fatigue loads at a particular section of the foundation than for example the right turbine.

Additionally, throughout one rotor revolution, each blade will be exposed to varying deterministic and stochastic loads, the former such as wind shear, wind veer, tower shadow, as well as gravity, and the latter defined by wind turbulence. Therefore, there will be sinusoidal load inputs that affect turbine loading, especially if their frequency lies within the natural frequency of the wind turbine’s components. In order to extract a turbine’s natural frequencies of its components such as the rotor, drive train, and

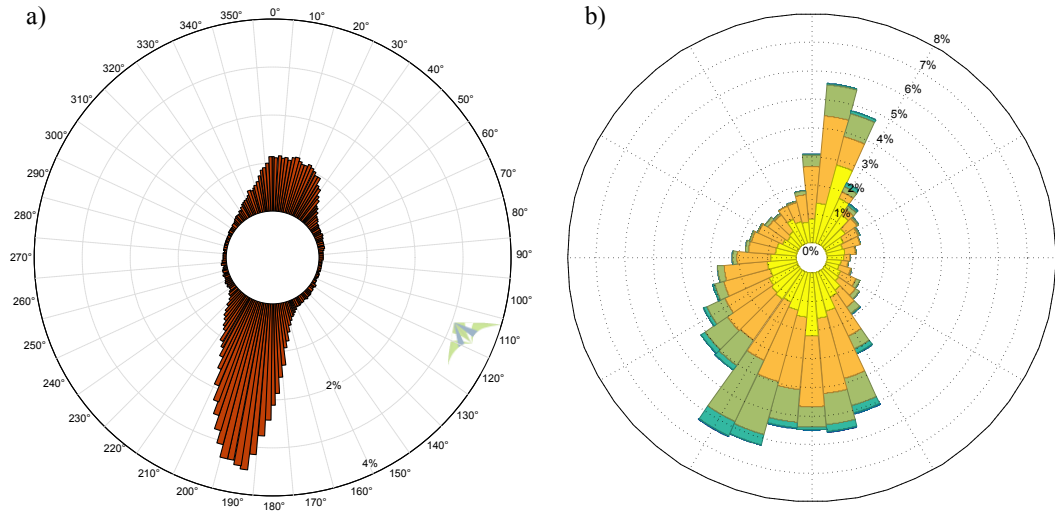


Figure 3.20: Wind Rose Comparison

tower, there are formulas and models to approximate these. For example the natural rotor frequencies can be approximated by application of a simple two-lumped parameter model as illustrated in Figure 3.21. With either Newtonian or Lagrangian mechanics the equations of motion for this system can be stated,

$$Hub : 3I_H\ddot{\theta}_H = k(-3\theta_H + \theta_1 + \theta_2 + \theta_3) \quad (3.75a)$$

$$Blade1 : I_B\ddot{\theta}_1 = k(-\theta_1 + \theta_H) \quad (3.75b)$$

$$Blade2 : I_B\ddot{\theta}_2 = k(-\theta_2 + \theta_H) \quad (3.75c)$$

$$Blade3 : I_B\ddot{\theta}_3 = k(-\theta_3 + \theta_H) \quad (3.75d)$$

where I_H is the hub inertia, θ_H is the hub angle, $\ddot{\theta}_H$ the hub acceleration, I_{1-3} each blade inertia which is assumed to be equal, θ_{1-3} each blade angle, $\ddot{\theta}_{1-3}$ the acceleration of each blade and k the stiffness of the blade. In this simple model aerodynamic blade

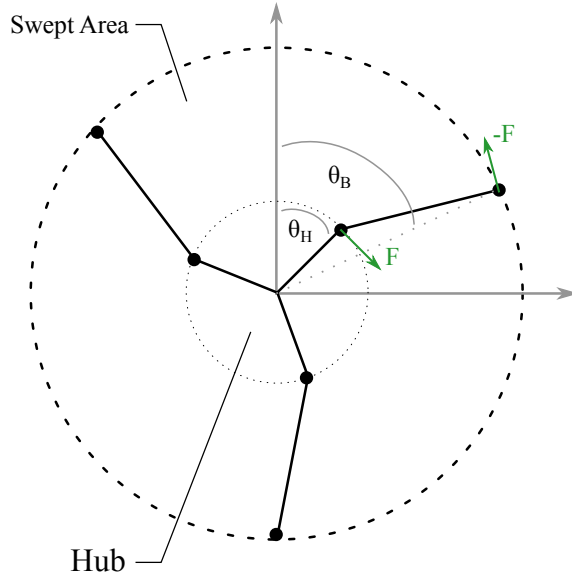


Figure 3.21: Rotor: Two-Lumped Parameter Model

damping is not accounted for. Rewriting Equation 3.75a - 3.75d into matrix form,

$$\begin{bmatrix} 3I_H & 0 & 0 & 0 \\ 0 & I_B & 0 & 0 \\ 0 & 0 & I_B & 0 \\ 0 & 0 & 0 & I_B \end{bmatrix} \begin{bmatrix} \ddot{\theta}_H \\ \ddot{\theta}_1 \\ \ddot{\theta}_2 \\ \ddot{\theta}_3 \end{bmatrix} = \begin{bmatrix} -3k & k & k & k \\ k & -k & 0 & 0 \\ k & 0 & -k & 0 \\ k & 0 & 0 & -k \end{bmatrix} \begin{bmatrix} \theta_H \\ \theta_1 \\ \theta_2 \\ \theta_3 \end{bmatrix} \quad (3.76)$$

results in Equation 3.76. Performing an Eigenvector, Eigenvalue decomposition of Equation 3.76, it is possible to extract natural rotor frequencies as well as the type of behaviour (mode) as exemplified in Figure 3.22. Essentially, in the first natural rotor mode, any combination of the three blades move in antiphase with each other at a frequency of $\omega^2 = k/I_B$ as illustrated in Figure 3.22 a-c). Figure 3.22 e-f) displays the second rotor mode where the three blades move in phase but in antiphase with the hub out-of-plane e) as well as in-plane f) with a frequency of $\omega^2 = k/I_B + k/I_H$.

In fact the second rotor mode is also known as the umbrella mode and translates into the first tower mode (side-side and fore-aft), due to the motion of the hub. Further the turbine's parked position, where the tower moves fore-aft in phase with the hub and blades, also propagates into the tower (Figure 3.22 d). In this case, since the mass of the

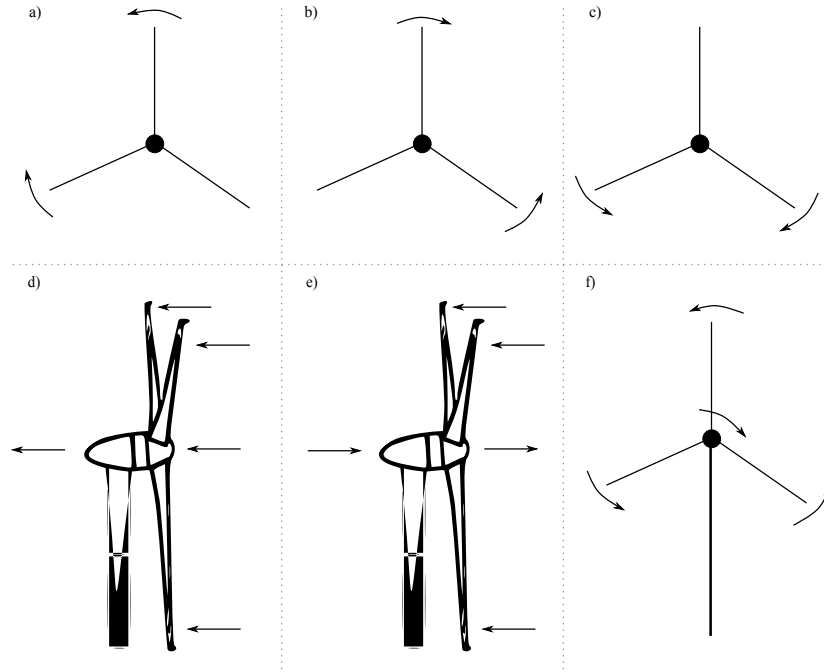


Figure 3.22: Natural Rotor Modes a-c) First Natural Rotor Mode, d) Static Turbine Behaviour e-f) Second Natural Rotor Mode (Umbrella-Mode)

tower is much greater than the hub and rotor combined, the frequency of oscillation is at around the natural tower frequency, however the blades deliver aerodynamic damping. The rotor umbrella mode in Figure 3.22 e) propagates into the tower resulting in fore-aft movement at the rotor frequency. Given that the blades deliver aerodynamic damping, analysis in the frequency domain would result in a broad peak. The rotor mode in Figure 3.22 f) propagates into the tower resulting in side to side movement at around the natural tower frequency with little aerodynamic damping (spike in frequency domain). Concerning the second tower mode, basically the hub remains stationary, whereas the center of the tower moves either fore-aft or side to side.

According to Tempel and Molenaar [127] the first structural tower frequency can be approximated by a flagpole with a top mass M ,

$$f_1^2 = \frac{3.04}{4\pi^2} \frac{EI}{(M + 0.227\mu L)L^3} \quad (3.77)$$

where f_1 is the first natural frequency, M the top mass, μ the tower mass per meter, L the tower height, and EI the tower bending stiffness. When designing an operational turbine strategy, it is of crucial importance to not coincide the blade passing frequency with the first as well as second natural tower frequency⁶ and multiples thereof as this could excite resonant behaviour. According to Bonnett [128] for a turbine with a diameter as well as hub height of 60 m, the first tower frequency is at around 0.5 Hz; however, as illustrated in Equation 3.77 for bigger turbines the frequency decreases as M and L increase. Since turbine components do not scale linearly as demonstrated in Section 3.3.5, increasing the rated power through the swept area (πr^2), results in significant frequency reductions. Bonnett further suggests to keep the system's natural frequency (rotational speed) at least 10% away from its structural excitation frequencies.

Programs such as DNV GL Bladed are also able to compute natural frequencies, based on input data such as tower/blade - geometry, mass and stiffness data, drive train topology, etc. When it comes to the design of the actual foundation, there is usually a wealth of loading data provided by such programs through simulations for parked and operational loading under turbulent wind fields, which is run in large numbers combined with statistical analysis. For safety considerations, there are also loadfactors applied to simulated design loads, which vary slightly as illustrated in Table 3.6. Here, the ultimate limit state (ULS) is where peak load is reached and the structure must not collapse, whereas the accidental limit state (ALS) is applied for accidental load cases where; parallelly two unlikely conditions take place. In addition, there is the serviceable limit state (SLS) that reflects loading under normal usage.

“It is important to note that despite this high level of modelling effort, wind loads are variable, and there is always a probability that design loads will be exceeded” [128]. Vice versa, designed loads may be greater than actual loads. Under such circumstances, life extension can become a crucial operating strategy in order to maximise efficiency and increase the ROI.

⁶contrary to the first turbine mode, the second has no aerodynamic damping since the hub is stationary

Table 3.6: ULS & ALS Loadfactors [128]

Design code	ULS loadfactor	ALS loadfactor
IEC 61400-01	1.35	1.1
EC2	1.5	1
BS 8110	1.4	1.05
BAEL 91	1.5	1

3.3.5.2 Wind Turbine Foundations

Essentially onshore wind turbine foundations are regulated by the following design codes; Eurocode 2 - design of concrete structures [94], Eurocode 3 - design of steel structures [129] as well as published standards such as the previously mentioned IEC 61400 or DNV GL guidelines.

“The type and the size of the foundations used for the wind power turbines are governed by the geotechnical conditions of the site, the maximum power of the turbine and the type of the tower” [56]. Therefore, depending on soil conditions there are two different types of foundations; i.e., spread foundations and piled foundations [130], the prior is designed to spread the load within an area where the soil bearing and soil backfill is sufficient to resist tilting under load and the latter is to reinforce stability, given insufficient soil conditions to support the turbine’s tilt movement⁷ [131].

The spread foundation, as defined by its name, consists of a big bottom reinforced concrete plate in the form of a cylinder, square, or octagonal prism. In essence, the greater the area of the bottom plate the less ground pressure is transmitted per m^2 soil. In addition, the width of the bottom plate has to be sufficiently wide in order to prevent the turbine from over-turning as illustrated in Figure 3.23 that depicts a simplistic turbine load model. There exists the dead load of the wind turbine components as well as foundation and backfill that is governed by gravity forces. Further, the incoming wind profile with its naturally given shear profile will under simplistic consideration result in an overturning moment at the root of the tower. The overturning moment M_{res} can be calculated by,

$$M_{res} = F_T * h \quad (3.78)$$

⁷e.g. the Enercon E-101/3MW nearly weights 1 kilotonne without its foundation

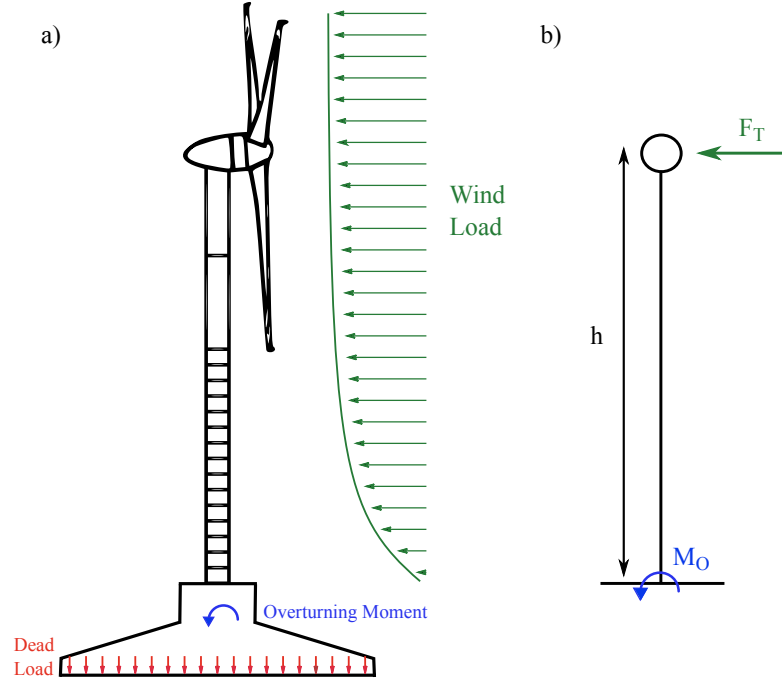


Figure 3.23: Wind Turbine Loading a) Force Profile; b) Simplified Moment

where F_T is the thrust force, and h is the hub height. In order to obtain M_{res} , the thrust force can be obtained by:

$$F_T = C_T \frac{1}{2} \rho v^2 \pi r^2 \quad (3.79)$$

where C_T is the thrust coefficient that can be calculated with aero-elastic codes, ρ the density of air $1.225 [kg/m^3]$, v the apparent wind speed, and r the radius of the rotor [106]. The highest thrust force for a pitch regulated variable speed turbine is at around rated power (thrust increases with wind speed until rated where the turbines pitch and shed the load). For a 3 MW rated turbine, forces of 384 kN and more can thus be expected [132]. This is as if 38.4 tonnes are pushed against the hub, hence the M_{res} will be around a hundredfold (example hub height of 100 m); i.e., 38.4 MNm. For any load pattern, the foundation soil interface will experience a load center (LC) that is characterised by an eccentricity e as exemplified for a wind turbine in Figure 3.24 a). The eccentricity in [m] from the foundation centre can be calculated by:

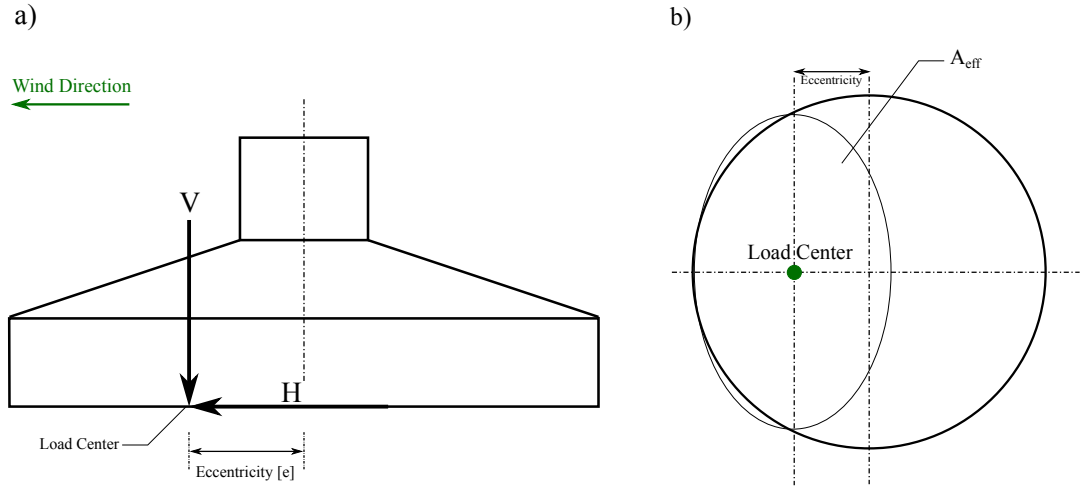


Figure 3.24: Foundation Load Center [133]

$$e = M_{res}/V. \quad (3.80)$$

where M_{res} is the overturning moment and V are gravitational forces.

As a consequence of this eccentricity, the resultant load area A_{eff} will only be a part of the bottom surface and can be expressed in form of an eclipse for a cylindrical foundation type (Figure 3.24 b) and expressed in the following equation:

$$A_{eff} = 2[R^2 \arccos(\frac{e}{R}) - e\sqrt{R^2 - e^2}]. \quad (3.81)$$

where R is the foundation's radius.

The elliptic major axes are further:

$$b_e = 2(R - e)$$

$$l_e = 2R\sqrt{1 - (\frac{b_e}{2R})^2}$$

where b_e is the height, and l_e the width of the eclipse. Subsequently the load area can

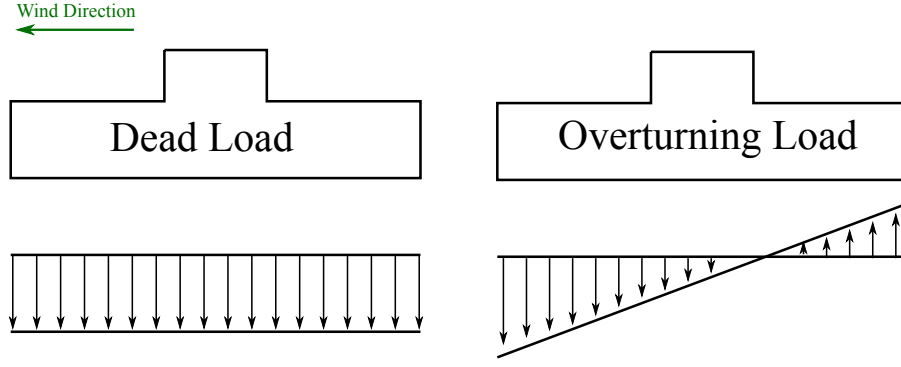


Figure 3.25: Dead & Overturning Load

also be reduced to a rectangle for ease of design calculations [133]:

$$L_{eff} = \sqrt{A_{eff} \frac{l_e}{b_e}} \quad (3.82)$$

$$B_{eff} = \frac{L_{eff}}{l_e} b_e \quad (3.83)$$

where B_{eff} is the height, and L_{eff} the width of the rectangle.

Besides the overturning moment, a wind turbine is also impacted by yaw errors, the yawing activity as well as wind veer. According to [134], if torsion, hence a twisting moment, M_z is acting on the wind turbine foundation, this moment can be replaced by an equivalent horizontal force, F_{res} :

$$F_{res} = \frac{2M_z}{L_{eff}} = \sqrt{\left(\frac{2M_z}{L_{eff}}\right)^2 + H^2} \quad (3.84)$$

where H is the horizontal force acting on the foundation. If there are no horizontal forces acting on the foundation $H = 0$.

Figure 3.25 gives a schematic overview of the turbine's loading. There acts the dead load, hence gravity force that causes compressive stress profile as well as an overturning load profile, which is hybrid; i.e., compressive and tensile stresses. The interconnection of the tower and foundation is a crucial transmission point where in the past inserted rings, embedded in the top of the concrete slab allowed tower installation; however, meanwhile turbines underwent up-scaling the transition design piece's structural in-

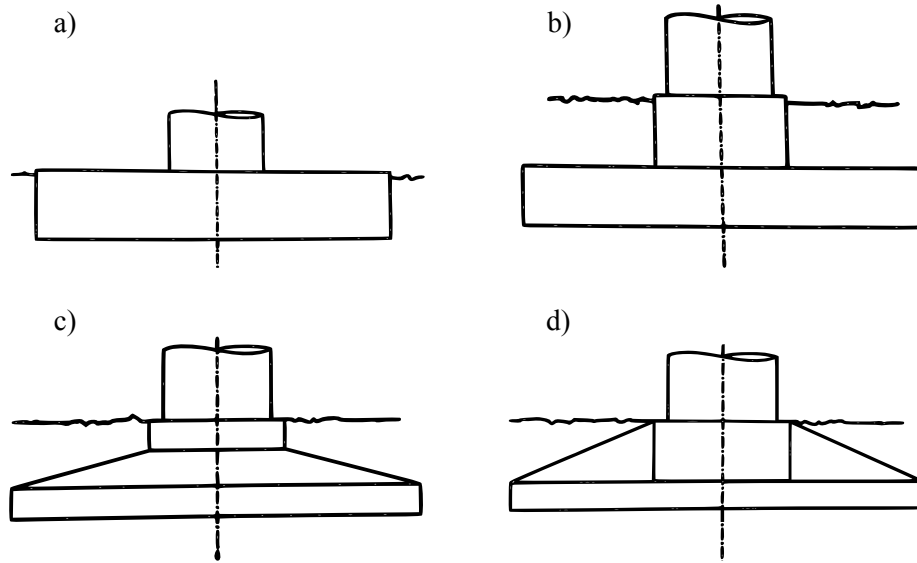


Figure 3.26: Spread Foundation Types (modified from [106]) a) Plain Slab; b) Stub and Pedestal; c) Tapered Slab; d) Slab and Pedestal with Webs

tegrity was not sufficient any more as forces do not scale linearly [53–55]. Therefore, nowadays the interconnection is enabled by means of a steel adapter as illustrated in Figure A.18.

Also, the soil settlement is of paramount importance and more specifically the differential settlement along the bed plate, since the soil beneath a turbine can either expand, contract or shift. Spread foundations, which are wide in diameter but less deep are usually applied in shallow soils and can further vary in their shape depending on soil condition and turbine selection as exemplified in Figure 3.26. According to Burton et al. [106] the tapered layout enables to apply less material while it is more difficult to carry out, whereas the pedestal is applied where the bedrock is at a greater depth than the depth of the slab. The slab and pedestal with web layout is illustrated in Figure 3.26 d) which is a design to reduce costs; however, overall there is less structural integrity than in layout a–c). At present, the tapered layout in Figure 3.26 c) presents a typical spread foundation for a conventional multi-megawatt wind turbine.

Under the circumstance that the soil and bedrock beneath a proposed wind turbine location is insufficient for a spread foundation, it is possible to overcome this obstacle by adding multiple reinforced concrete piles that are directly connected to the spread

foundation with overlapping reinforcement bars. These piles can be significant in depth (10-18 m) as well as in quantity; i.e., more than 20 piles are possible depending on local requirements. An example for required piled layouts is in areas where permafrost exists, as water expands and thaws, thus these forces can lift an entire or partial area of a turbine [135]. Inevitable the application of such piles increases total capital expenditure with additional costs of multiple tens of thousands [133].

3.3.5.3 Foundation Design

In this section, a simplistic overview of the design considerations of a spread wind turbine foundation is presented. The overall design process is illustrated in the following itemized list based on findings from [94,131,133,136]. Basically, the design consideration is twofold. On the one hand there are the geotechnical design considerations of the soil composition and on the other hand there are the structural design considerations of the interaction of the turbine with the foundation. The latter is usually based on a FE model or hand calculation to derive moments, shear forces, and loads at various increments from the centre of the model to the edge, top and bottom faces of the concrete section in X and Y directions (radially and circumferentially) and then reinforce as required in line with design standards [137].

- Geotechnical design
 - Soil bearing capacity
 - Soil settlement
- Structural design
 - Stability analysis (eccentricity)
 - Concrete cover
 - Steel can/bolt cage calculation
 - Ultimate Limit States
 - * Design for bending moment
 - * Design for shear force

Chapter 3. Literature Review

- * Design for fatigue
 - Concrete
 - Reinforcement
- Serviceable Limit States
 - * Crack Control

3.3.5.3.1 Geotechnical Design

In order to withstand the forces transmitted from the foundation to the soil, a soil's bearing capacity requires evaluation under the ULS load case. Equation 3.85 illustrates the general formula for a plate's bearing capacity, where the shear strength parameters (cohesion c and angle of internal friction ϕ) are gathered from a geotechnical analysis [130]:

$$q_b = cN_c s_c d_c i_c g_c b_c + qN_q s_q d_q i_q g_q b_q + 0.5\gamma' B_{eff} N_\gamma s_\gamma d_\gamma i_\gamma g_\gamma b_\gamma \quad (3.85)$$

where

q_b is the bearing capacity

c is the cohesion

q is the surrounding load at the foundation level

γ' is the effective bulk density of the soil

B_{eff} is the effective width of the footing

N_c, N_q, N_γ are bearing capacity factors that depend on ϕ

s_c, s_q, s_γ are correction factors for the shape of the footing

d_c, d_q, d_γ are correction factors for the foundation depth

i_c, i_q, i_γ are correction factors for inclined loading

g_c, g_q, g_γ are correction factors for inclined adjacent ground surface

b_c, b_q, b_γ are correction factors for inclined base area of the footing.

Due to the simplistic evaluation, the bearing soil capacity factors are not further presented, but can be accessed in [138]. Overall, the soil bearing capacity must be adequate to withstand the foundation's forces and moments.

Besides the bearing capacity, another important factor to check is the settlement; i.e., the differential settlement in between the foundation edges. If piles are required this will naturally affect the analysis.

Lastly, if a twisting moment M_z or horizontal load H is acting on the foundation, sufficient sliding resistance is required. This is fulfilled if the following two conditions are met:

$$\frac{A_{eff}c + V \tan \theta}{H} > 1 \quad (3.86)$$

$$\frac{H}{V} < 0.4. \quad (3.87)$$

3.3.5.3.2 Structural Design

For the load calculations (ULS, SLS, fatigue) the turbine manufacturer usually provides the following design information and load denotations including partial safety factors; the overturning moment M_{res} , the gravitational force of the turbine F_z , the twisting moment M_z , and the resulting force from the twisting moment F_{res} . An example is illustrated in Table 3.7 for a Vestas V117 3.5 MW rated wind turbine. As a first step,

Table 3.7: ULS Example Design Load Case [139]

Load Type	Unit	ULS
M_{res}	[MNm]	50.3
M_z	[MNm]	5.9
F_{res}	[kN]	661
F_z	[kN]	3497

it is necessary to evaluate the structure's stability, by evaluation of the eccentricity (Equation 3.80) to prevent loss of soil contact and uplift. This is met if:

$$e = \frac{M}{V} = \frac{M_{res} + F_{res}(h + t)}{F_z + G_{tot}} < B/6 \quad (3.88)$$

Chapter 3. Literature Review

where h is the foundation height, t the height of the steel ring's plinth, G_{tot} the foundation's and backfill's gravitational force and B is the diameter of the foundation [133].

A wind turbine foundation is exposed to a combination of loads; i.e., the soil acts as a distributed pressure on the foundation's bottom, while the soil backfill acts as a distributed load on the top. In addition, there are the forces from the operational wind turbine as discussed in Section 3.3.5.2.

This results in a complex combination of bending moments and shear forces along the foundation's cross-section. Typically a FE model is applied to identify sectional moments and forces in order to design the foundation's geometry as well as required reinforcement for the tensile loading. As exemplified in Section 3.3.2.3.2 for a simple cantilever, the analysis includes scrutiny for bending moment and shear (under the ULS while for the crack control under the SLS), radially and circumferentially as well as under fatigue loading. In addition, the application of a steel ring or bolt cage requires evaluation for the foundation's center/turbine anchorage.

3.3.5.4 Life Extension

A wind turbine and its components are designed and certified under specified static and dynamic loading conditions originating from a turbulent wind field that is specified in the IEC 61400-1 standard in order to represent most site characteristics as illustrated in Table 3.8.

There are three different wind turbine design classes (I, II, III) that are characterised by

Table 3.8: IEC Wind Turbine Classes [140]

Wind Turbine Class		I	II	III	S
Vref	(m/s)	50	42.5	37.5	Values
Vavr (0.2*Vref)	(m/s)	10	8.5	7.5	specified
A	Iref (-)		0.16		by
B	Iref (-)		0.14		the
C	Iref (-)		0.12		designer

a different reference wind speed, V_{ref} (extreme 50 years reoccurring 10 minute average)

paired with a turbulence intensity (standard deviation divided by mean wind speed) A, B, or C. Also, there is a third option S, where a turbine is designed according to specific site conditions. Consequently, in each category for example IA or IIIC there exists a range with two possible extremes (min/max), hence potential to allow for life extension, if actual site conditions are less severe than the design maximum. Besides, lower operational wind speeds and turbulence intensities, Table 3.9 presents alternative reasons that may result in potential to extend an asset's operation.

Table 3.9: Reasons for Continued Operation [141]

Consideration	Explanation
Site Classification	Structure was designed for wind class III, but operated in wind class II
Turbulence	Turbulence are less then considered in the design assumptions
Level of downtime	Due to curtailment or faults
Yield analysis	Due to curtailment or faults, wind speeds, etc.
Design reserves	Design reserves are determined by extreme loads
Repairs and replacements	Reset/change of cumulated fatigue damage

Therefore, the overall aim of wind turbine life extension is to extend the originally intended operational design life by taking into account the local site conditions that have been collected for close to two decades at a specific site by SCADA or a nearby met. mast.

3.3.5.4.1 DNV GL Lifetime Extension Standard

DNV GL offers their life extension certification based on three different methods, i) the simplified, ii) detailed, and iii) probabilistic approach in which each method consists of an analytical and practical part to ensure proof of strength and stability [23]. Main outcome of both parts are the specification of possible life extension, specification of required inspection scope and intervals, and the specification of restrictions and limiting conditions. The latter could for example result in the requirement to exchange a component or to install a condition monitoring system to ensure reliability.

In order to go through DNV GL's certification process, the considered wind turbine or wind farm has to pass the lifetime extension inspection (LEI) where life extension suitability of all load transferring and safety relevant components is evaluated. Other

Chapter 3. Literature Review

evaluation criteria is itemised below:

- visual inspection of all load-transferring and safety-relevant components
- review of maintenance reports and inspection reports for specific turbine
- consideration of SCADA data
- consideration of wind turbine type related field experience
- simple tests

In addition, to item one (visual inspection) Table A.13 of the Appendix depicts an overview of the inspection scope in conjunction with evaluation criteria per component.

With regards to life extension certification, there exist three approaches that are presented in Appendix B.1⁸. Unless environmental conditions are more benign than design criteria, DNV GL’s life extension certification solely evaluates fatigue loading and damage rather than extreme loads in all three methods.

In the simplified lifetime extension approach, analytical load calculations shall be performed with a generic wind turbine model and controller in combination with a state-of-the-art aero-elastic simulation code; for example, DNV GL’s Bladed software package. Concerning required environmental conditions, data must be available representing the current state of the art, including the influence of wakes from neighbouring turbines. Depending on the outcomes of both parts’ evaluation criteria, loads shall then be calculated for an extended lifetime with local site conditions. “A verification of all components taking into account the extension of lifetime shall be conducted based on a comparison of loads. Based on the results of these verifications, conditions on operation/maintenance/inspection of the turbine may be defined, for example if a component shall be monitored by a conditions monitoring system (CMS)” [23].

⁸LEI can also be used to receive a life extension certificate. This seems to be only valid for single turbines [76].

Contrary to the simplified approach, the detailed approach for lifetime extension requires a wind turbine type specific analytical part. Also, this approach requires a more detailed investigation of environmental conditions (wind, waves, soil, influence of wind farm configuration, temperature, humidity, ice aggregation, salt content etc.). Concerning the required maintenance and inspection reports of the presented practical part, as a minimum the commissioning as well as maintenance reports, and reports from inspection, failure reports/reports on extraordinary maintenance activities, documentation of component exchange, as well as field experience shall be taken into consideration.

Finally, the probabilistic approach “allows for the use of stochastic methods in the assessment of structural integrity” [23]. In order to do so each component is evaluated under a structural reliability analysis (SRA) to model component reliability. This method requires to set target reliability levels, and the identification of failure modes connected to a limit state function (also known as g-function) based on engineering theory. With this reliability and failure probabilities are determined with for example a first order reliability method (FORM). If specific turbine component information are not available, the use of generic models is recommended. The outcome of this method is the potential life extension per component, where some items require specific action such as replacement or the installation of CMS; however in terms of possible inspection and maintenance procedures, risk-based methods may be developed based on statistical results.

Limitations

The published standard by DNV GL offers a good overview to evaluate the scope and focus of life extension certification; however, there are some factors that remain unclear and thus are subjected to a discussion.

Overall DNV GL offers three different methods that vary greatly in the analytical part, whereas the practical part seems to be roughly the same procedure. Nonetheless, it is not discussed or disclosed who actually decides on the required approach; i.e., is the

operator/investor able to select the most suitable approach?

Across the industry, resources are ideally allocated in the most economical manner, but based on the presented differences, it becomes clear that the simplified approach will consume much less resources (time, costs) than the detailed and probabilistic method. With this in mind, the risk is high that operators and investors will most likely select the simplified approach and thus gain certification by committing least resources.

Also, in the case of the detailed and probabilistic approach, the wind farm operator/investor has to obtain relevant component data from the original equipment manufacturer (OEM) that can be tiresome to obtain or in the worst case scenario, the OEM can refuse to disclose required data. As presented in the introduction, DNV GL and Gamesa have cooperated together to certify life extension at the end of 2014. Nevertheless, in the light of the complete halt of the Spanish wind industry with zero installations in 2015 (Figure 1.1), Gamesa is under significant pressure to remodel and shift their services to existing turbines, rather than new installations. It is questionable though, how other manufacturers such as Vestas, Siemens, Enercon, etc. will react, since this can be seen as a risk that could potentially cannibalise sales of new installations with greater profit margins. On the other hand, there is evidence that Enercon is looking into life extension as well with their offered service contract for turbines above 20 years of operational life, in which case a life extension certificate can increase acceptability based on a standardised process [24, 141]. This acceptability through certification can greatly help negotiations between the operator and insurance companies or building authorities to ease life extension processes.

Certification costs will also determine industry's interest as gathering, processing, and documenting all relevant required information can be a tedious process, hence the cost-benefit from extended lifetime is reduced by an unknown percentage. Operators will also consider life extension based on their own due diligence in the past, so if most relevant reports are readily available, well structured and written in an understandable way for a third party, data gathering will be much easier than if data is lost or archived in a non-structured fashion.

With regards to the practical part, despite providing inspection criteria for wind tur-

bine foundations in order to identify damaged, cracked, and corroded areas, evaluation is not specified beyond visual inspection (are sections of the foundation going to be excavated? how are the soil conditions evaluated beneath the foundation? what about internal damage, corrosion or cracks?). Since the foundation is difficult to access, damage might be invisible at accessible sections. Therefore, novel foundation conditioning monitoring methods can greatly help to improve the health assessment.

In 2017, a Dutch lifetime extension standard was published that is essentially a copy of DNV GL's recommended approach [142].

3.3.5.4.2 UL Lifetime Extension Standard

The UL 4143 "Wind Turbine Generator - Life Time Extension" standard suggest to implement six steps to extend an asset's lifetime. The main difference to the approach by DNV GL is that the UL standard allows to cluster turbines. The evaluation steps are further presented in Appendix B.2.

The UL standard is in some sections more detailed than DNV GL's standard, especially in the operational assessment and risk assessment. The latter that is a less complex approach to the one suggested by DNV GL. Both standards are similar in terms of the split to divide the analysis in a practical and analysis part. However, similarly to DNV GL's approach, the UL's methodology requires significant resources to facilitate lifetime extension. Resources, that may not be available in cost-sensitive projects.

According to a UL webinar [143], the P50 values are derived for the economic model and don't contain any uncertainty in the analysis, whereas the P90 value is observed as a very conservative approach with high safety requirements.

Although limitations are presented in form of a discussion concerning life extension certification, in the following Chapter it is assumed that a turbine can be considered safely and reliably to life extension.

Chapter 4

Economic Lifetime Extension Decision-Making

In this Chapter several work packages are covered. Initially, a review of the state-of-the-art of lifetime extension in the UK is presented in Section 4.1 that was part of a European research cooperation with the overall results published by Ziegler et al. [144]. Subsequently, work is presented with regards to quantification of performance degradation of wind farms that was carried out in cooperation with Iain Staffell from Imperial College, London in Section 4.2. Section 4.3 is dedicated to the reproduction, discussion, and sensitivity analysis of LCOE published by DECC for a sanity check of the model, while Section 4.4 presents a derived model to support the economic lifetime extension decision making. Based on the developed model the effect of upscaling and performance degradation of wind turbines is analysed in Section 4.5. Finally, Section 4.6 presents a lifetime extension consultation for one of BVGAssociates's clients for two wind farms that reach their end of design lifetime in 2020 in the UK where the derived LTE extension methodology is applied to real operational data.

4.1 The State-of-the-Art of the UK's Lifetime Extension

4.1.1 Introduction

The lifetime extension analysis of wind turbines depends on country-specific circumstances such as i) the available subsidy scheme, ii) site and turbine conditions, iii) repowering characteristics, as well as iv) legal requirements [78, 144, 145]. Therefore, the framework of analysis is a key driver governing the degree of due diligence and resource commitment of the assessment. Where Ziegler et al. [144] aim to provide a comprehensive overview on the state-of-the-art of lifetime extension in Europe, this work presents additional information gathered during the interviews aimed at presenting a more detailed picture of the situation in the UK. This is facilitated by a thorough market analysis and the consultation of experts in the UK. The latter through 6 guideline-based interviews originating from [144]. The semi-structured interview questions are illustrated in Figure C.1-C.4 of Appendix C. The remaining text is structured as follows. Section 4.1.2 presents an analysis of the UK's historical wind energy development, whereas in Section 4.1.3 the UK's survey methodology is discussed followed by the presentation of complimentary survey results in Section 4.1.4. Section 4.1.5 presents this work's limitations and eventually in Section 4.1.6 findings are concluded.

4.1.2 The UK's Historical Wind Energy Deployment

The UK's wind energy market has increased significantly with the beginning of the 21st century, reaching a total installed capacity of 13.6 GW as illustrated in Figure 4.1. This capacity in MW is distributed among 63% of onshore and 37% of offshore wind turbine generators (WTGs). However, offshore installations are expected to become the dominant share in the future due to the overall reduction of onshore subsidies [146]. Historically, until 2007 the growth in capacity was mainly driven by upscaling in conjunction with increasing installation numbers as illustrated in Figure 4.2. From 2007 onwards the average installed turbine size has maintained a relatively stable power rating reaching a plateau of 2.28 MW for onshore and 3.58 MW for offshore turbines, respectively. Onshore, legal requirements are likely to be the result of this scaling plateau, whereas

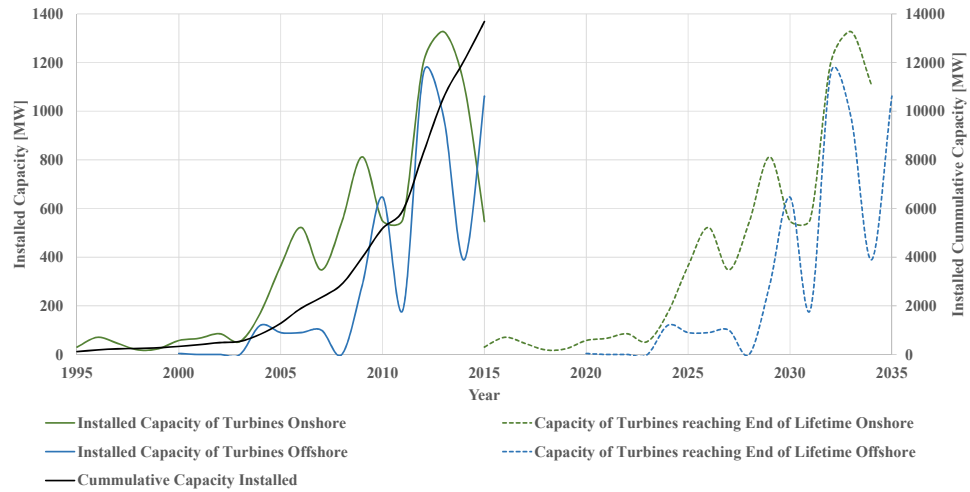


Figure 4.1: Annual capacity in the UK that will reach the end of lifetime (20 years) in the future [147].

offshore the two main turbine suppliers (Siemens and Vestas) have been very successful with their turbines rated at around 3 and 3.6 MW [147]. Nevertheless, it is expected that new offshore turbine models will soon increase the mean installation rating with the installation of 5 MW offshore turbines in 2015, 7-8 MW models in 2016 [148], and presumably > 10 MW models in the near future. Consequently, in between 2007 and 2015 the growth was mainly driven by installation figures rather than upscaling.

Contrary to recent installations, it is important to analyse the share of turbines that will reach its end of designed lifetime with the detailed numbers illustrated on the right-hand side of Figure 4.1. At present there is a small but yet substantial onshore capacity with an average rating below 1 MW (Figure 4.3) reaching their end of design lifetime. These turbines are predominantly located in Wales, Northern Ireland, and England with an average fleet age of 10.5, 8, and 6.6 years respectively [149]. For assets that reach their end of design lifetime, the owner or operator must decide whether to decommission, repower, or life extend either a wind farm or individual turbine. The capacity of end-of-life turbines is relatively small until 2024 (20-70 MW/year), which subsequently is growing exponentially reaching 400 MW in 2025. Assuming a capacity factor, CF of 0.28 as well as an electricity spot price of £40/MWh, this results in an annual revenue stream of £39,2 million/year.

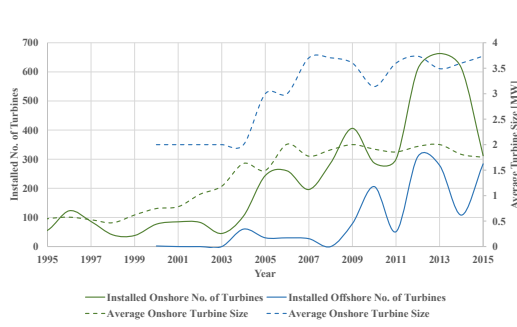


Figure 4.2: Annually installed turbines from 1995, paired with the average annually installed turbine size [147].

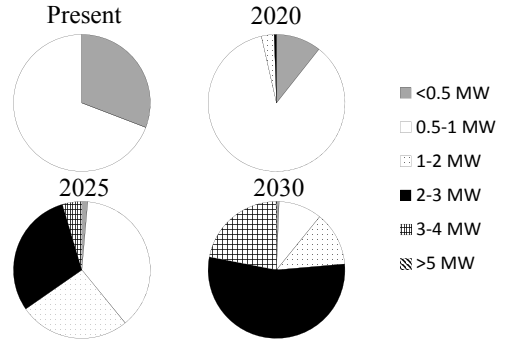


Figure 4.3: Distribution of turbine capacity reaching its 20th year of operation [147]. Boundary turbines are categorised in the higher class.

In addition, the first offshore turbines (Blyth wind farm) will reach their 20th year of operation in UK waters in 2020 (2nd: North Hoyle and Scroby Sands wind farm in 2024) [147].

At this stage the size distribution of turbines in their 20th year will also have changed significantly as depicted in Figure 4.3; i.e., in 2025, 1.4% of the turbines will be below 0.5 MW, 37.7% in between 0.5 and 1 MW, 26.2% in between 1 and 2 MW, 30% in between 2 and 3 MW and finally 4.6% in between 3-4 MW. After 2025 the share of 2-3 MW turbines reaching their end of operational lifetime will increase continually, whereas the share of turbines below 0.5 MW will drop substantially.

At present, 15 onshore wind farms are beyond 20 years of operation in the UK [150]. While the renewable obligation (RO) is in its final termination stage, for the successor subsidy scheme contract for difference (CfD) continuous onshore subsidies are unclear [151]. With the removal of onshore subsidies for new as well as repowering investments, the likelihood of lifetime extension is becoming more and more thought-provoking as identified by Everoze [149].

Especially, due to extended subsidies beyond 20 years of operation; i.e., the installed capacity that entered the RO prior to June 2008 is eligible for subsidies beyond 20 years of operation until the closure of the old RO scheme in 2027 [152,153]. For this capacity, economic profitability will subsequently be defined by the spot-market electricity price from the beginning of 2027. With regards to the capacity that entered the RO scheme

after June 2008, there is a fixed compensation period of 20 years, thus capacity reaching its 20th design life will directly be exposed to the market electricity price, although in 2027 there will be a move to a fixed price certificate [154]. With the termination of the grace period in 2019, the RO will be closed in 2039.

Further, the northern parts of the UK have one of the highest wind resource in Europe resulting in lower cost of energy [145, 146, 149, 155] and thus in comparison to other countries, there exist increased profit potential beyond the design life.

4.1.3 Survey Methodology

The overall survey design and execution is published by Ziegler et al. [144]. With regards to the detailed UK survey execution, in total 12 individuals were pre-determined to be suitable to participate based on their degree of industrial exposure on lifetime extension in the UK. 6 out of the 12 identified experts agreed to participate in a guideline-based interview that was conducted in person as well as over the phone.

4.1.4 Complimentary Survey Results

The collected data was transcribed and contrasted to identify differences and similarities of participant's responses. As presented by [144], survey participants of all targeted countries agreed to life extend in order to maximise the ROI. In addition, participants in the UK highlighted the existing and hard-won local stakeholder relationships and an asset's available infrastructure. Participants further stressed that for many wind farms there are local constraints (tip height, access, noise), thus options such as repowering are not perceived as advantageous especially under the light of the terminated RO.

In practise, participants agreed on a two-split lifetime assessment approach based on i) data evaluation as well as ii) inspections. For the former, in-house designed assessment approaches were encountered in the UK as there is no governmental lifetime extension regulation in place, contrary to for example Germany and Denmark [144].

With regards to the applied toolbox to identify the health status of an asset, participants mentioned the following activities. A review of: i) maintenance reports (maintenance history, operation, reliability and failure data), ii) structural survey reports (if

available), iii) operational reports (turbine availability as well as lifetime output), and iv) the wind history (permanent met. mast and hub anemometer). In addition, the asset manager was consulted besides reliability based analysis with supervisory control and data acquisition (SCADA) systems. Also, data from condition monitoring systems (CMS) is taken into consideration if available (predominantly drive train accelerometers). Mentioned data processing techniques are benchmarking of individual turbines (turbulence intensity, mean wind speed¹, yawing and pitching activity.) and trend evaluation. Operators are further looking into measurement campaigns to evaluate loading of the tower, blades, and drive train, although at present, this has not been executed. All participants highlighted the requirement for inspections, with most participants being aware of the component inspection list of DNV GL's guideline [23]. Recertification was not seen essential to the analysis. Details concerning intended/executed inspections are annual drive train inspections, non-destructive inspection (NDI) of all welded and bolted connections (e.g. measurement of bolt torque), checking for corrosion as well as the overall health evaluation of the blades (6/12-month inspection intervals). Annual maintenance strategies are continued as business as usual. With regards to the electrical equipment, respondents mentioned to check oil samplings of transformers.

The considered extension age is a combination of the historic wind conditions as well as the technical asset status. In terms of the optimal evaluation timing, in theory year 12-15 was mentioned as options narrow down quickly; however, in practise this is rather dealt with in year 18-20. With regards to obtaining turbine data from OEMs, results showed a pessimistic expectation/experiences, thus for potential future in-depth load analyses, generic data is likely applied.

Concerning difficulties and concerns, interviewees pointed at the requirement for more dedicated services and the general lack of experience. For example, it requires skilful and experienced technicians with a critical eye to thoroughly inspect turbines and identify critical components. Ideally critical components are repaired, replaced or monitored by CMSs. With regards to the availability of spare parts to retrofit turbine components, participants responded incoherently with some seeing the sourcing as a challenge while

¹A higher uncertainty was expressed for the turbulence intensity than the mean wind speed due to terrain impacts

others do not expect any difficulties. Uncertainty in the UK’s policies and regulation further feed into the tendency to limit the considered lifetime extension period in order to ensure economic feasibility. Also, there is a lack of clarity, if a few turbines within a wind farm require decommissioning (likely the ones with the more severe historical loading) as selected turbine removal may require amendment of the asset’s land lease and grid connection agreement as well as planning consent and thus may consume significant resources. In fact, the younger the wind farm the tougher are its contracts in place; i.e., there are examples of indefinite and limited contract lengths concerning an asset’s land lease, grid connection as well as planning consent. This further prohibits a standardised lifetime extension approach. With regards to the wind history, participants stressed that data from permanent met. masts or nacelle anemometers may become unreliable and require adjustment. Further changes to an asset’s environment can influence the local wind regime as occurred in a case where a forest was planted within the vicinity of a wind farm. Lastly, participants stressed that procurement of original design standards can be challenging to obtain. If original design standards were not accessible, IEC design standards were applied as an alternative. It was also mentioned that lifetime extension does not generate “balance sheet growth” and thus is not necessarily appreciated by investors.

Overall, interviewees are confident about their in-house lifetime extension practices, albeit the previously mentioned difficulties and concerns. It is important to maintain a holistic view on lifetime extension in order to determine economic as well as technical feasibility. From a strategic point of view, there may be different extension approaches emerging in the future such as i) short-term < 5 years (lowest operational expenditure oriented or continuation in the form of business as usual) and ii) long-term > 5 years (investment based – retrofits).

4.1.5 Limitations

This work relies on experiences from a total of 8 onshore wind farms that have been subjected to a lifetime extension assessment by industry. Consequently, this research gives an insight at a few case studies within the UK that give an impression about

current lifetime extension practises as well as associated difficulties and concerns. The findings are further limited to the UK market and may change in the future due to more improved LTE approaches, thus results are not likely to be applicable in other countries. Lastly, the UK is leading the offshore installation capacity in Europe; however, offshore assets experience a different loading profile than onshore, thus results are not generically applicable.

4.1.6 Section Conclusions

This work presents complimentary market data and survey results that depict challenges and concerns in the UK's lifetime extension environment. Findings may guide operators, third party service providers as well as governmental institutions to tailor projects to streamline and support the lifetime extension assessment framework within the UK. Due to the current changes within the country's subsidy scheme, lifetime extension is expected to become an ever-increasing field of interest for researchers, owners and investors, third party service providers as well as certification bodies. At the same time gathered survey results reveal that lifetime extension is not a straightforward process, thus requirements and evaluation processes are uniquely dependent on an asset's environment.

Based on the interview findings, the UK government is actively encouraged to draft a lifetime extension guideline as this was observed as a key operational risk in long-term decision-making. From a technical point of view this may include to develop the potential for more qualified inspection personnel. One possible strategy may be to provide governmental certification for independent institutions to train and certify wind turbine technicians for end of lifetime inspections. This will ensure a thorough and more robust inspection process with a critical eye for detail. This could reduce the need for costly aero-elastic simulations as aimed for in the Danish legislation [156].

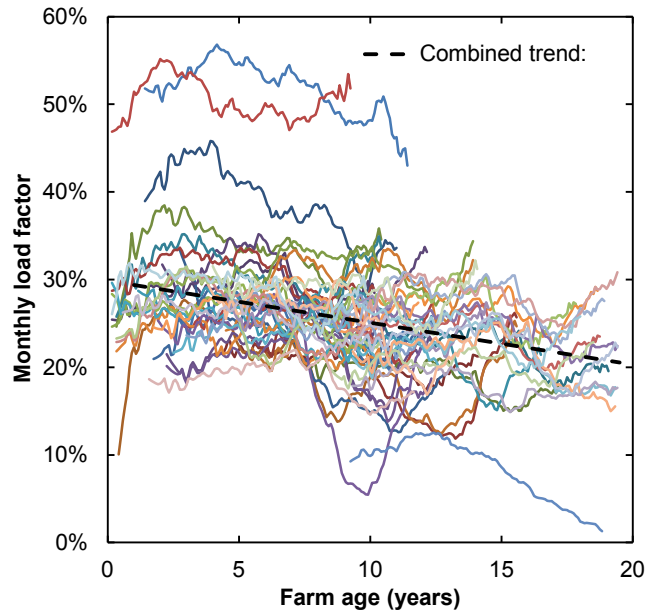


Figure 4.4: Wind Turbine Performance Degradation [157]

4.2 Wind Turbine Performance Degradation

“Ageing is a fact of life. Its effects are inevitable for all kinds of machinery, reducing the efficiency, output and availability of steam and gas turbines, solar PV modules, batteries and automobiles alike” [157]. Ageing is also believed to contribute to the wind turbine drive train as well as the aerodynamic efficiency of blades affecting the overall availability and power output. Consequently this reduces a turbine’s load factor Y_L that is the ratio of the actual output of a turbine for a given period and the theoretical output as if the turbine operates at full capacity. For a reasonably windy site, load factors within the range of 30% are encountered in the UK for the onshore fleet [158], although in the UK DECC calculates with an average load factor of 28% [117]. Depending of the performance degradation rate, there is a threshold where it is worthwhile to prematurely replace the turbines with new models or parts; i.e., the economical life is shorter than the technical designed life expectancy. Research by Staffell and Green [157] suggests that wind turbines are significantly exposed to performance degradation as exemplified in Figure 4.4 with an average load decline of 1.6 % per annum. After looking closely

into this dataset it is evident that most of the generator types are from a commercial perspective small in size at around 700 kW with around three wind farms that consist of 1500 kW machines. However, since available power scales quadratically with the radius of the blade, bigger turbines deliver much more energy, hence O&M becomes a more critical factor in order to maximise energy yield. Based on this, the hypothesis is that operators of a relatively small turbine will focus less effort on O&M than machines greater in size. With this background information and hypothesis Iain Staffell from Imperial college was contacted and a collaboration was set-up in order to review wind turbine performance based on different turbine classes in terms of rated power. The approach to gain such data is identical to Staffell's and schematically depicted in Figure A.10 within the Appendix. The only differences to the original work are 1) the moving average is calculated less complex (25 month moving average was selected with results in agreement with the previous filtering), 2) the ROC database was updated by roughly two years, and 3) all wind farms were updated with a rating above 1.5 MW. Performance degradation results for the class equal or above of 3 MW are illustrated in Figure 4.5.

Although data is only available for a maximum of 8 years onshore and 8.5 years offshore, performance indicators illustrate a fairly stable output over time that is significantly different from previous findings as illustrated in Figure 4.4. Findings reveal how onshore as well as offshore load factors increase for the first initial four years, although the effect for offshore wind farms is much more prominent than onshore. This is likely due to the effect of the change of reliability over time, since according to [159, 160] failures in wind turbines are more likely to happen at the beginning as well as the end. Due to the shape of this failure distribution, it is often referred to as the reliability bathtub curve. Also, improvements as well as learning in O&M processes can have significant initial impacts in order to increase a turbine's energy yield. The latter is much more significant for offshore, since deployed offshore turbines are much younger and fewer in quantity than onshore turbines, hence less knowledge is available by operators. This is also in agreement with information given by Graeme Wilson, an asset performance engineer at SSE stating that their offshore O&M processes experience a steep learning

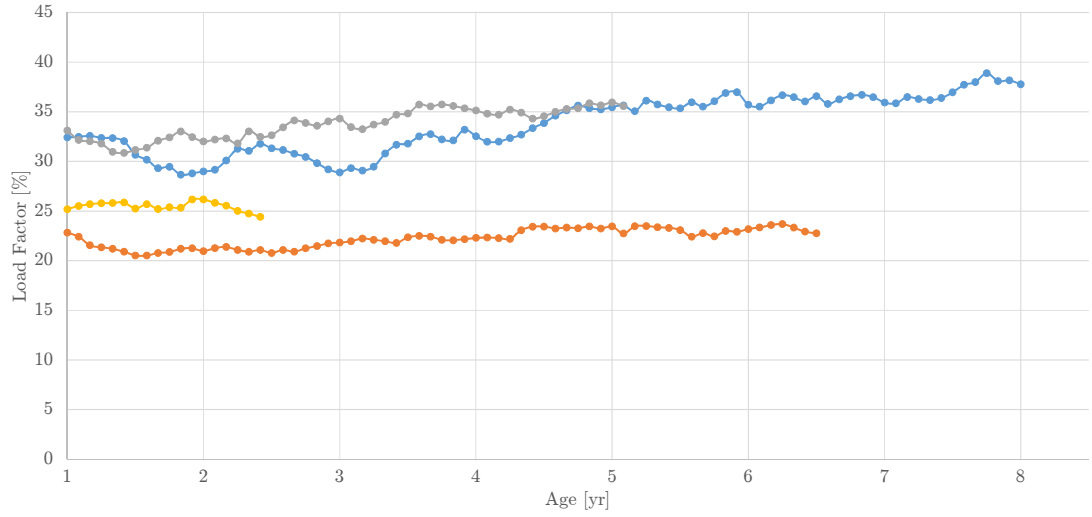
curve resulting in improved and more efficient processes and thus an increased availability and load factor [161] over the initial operational years.

Upon evaluation of results, it became evident that most wind farms are operated under a performance based maintenance contract (PBMC) in which the owner of the wind farm is able to penalise the operator when a specified agreed availability is not met where weather impacts are taken into account. Table 4.1 presents an overview of what wind farms have or have had a PBMC signed. Overall, 70% of all offshore wind farms presented in Figure 4.5b are under such an PBMC, whereas for onshore turbines (Figure 4.5a) this is difficult to say as relevant data was not available. However, judging from the size and type of ownership of the analysed onshore wind farms with no PBMC information access (community ownership), it appears highly likely that PBMC are agreed.

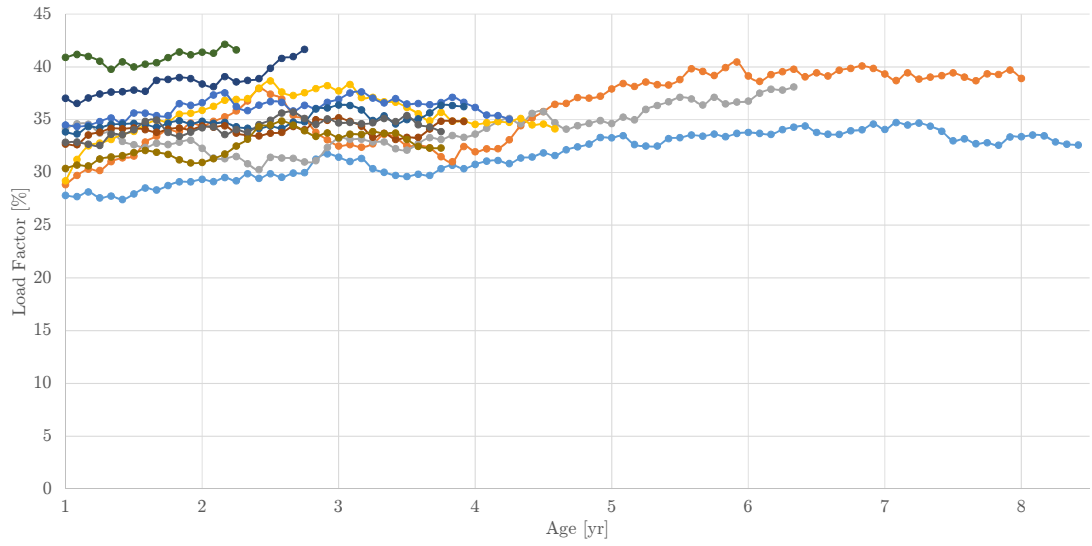
In fact, wind turbine performance degradation has two distinct origins when the actual wind resource is not taken into account or normalised for, on the one hand there is wear and tear of components where the degradation process is characterised by a low rate of change and on the other hand there is downtime and hence reduced availability caused by parts that break down characterised by a high rate of change (failure/sensor activation). Also, if data is based upon ROCs (Staffell and Green), derated periods constrained by the operator naturally results in a reduced availability and thus negatively impacts a wind farms' load factor resulting in an introduced potential for error.

4.3 Reproduction of LCOE

As an initial step to economically model wind turbine life extension it is important to reproduce available LCOE parameters by combining multiple sets of data that is discussed in this section. For this analysis cost parameters are derived for a 3 MW class turbine, since such rated power is slightly greater in size than the current average installed onshore turbine [162]. Also, the selected rated power is roughly in agreement



(a) Onshore Wind Turbine Performance Degradation (3 MW)



(b) Offshore Wind Turbine Performance Degradation (3-3.6 MW)

Figure 4.5: Wind Turbine Performance Degradation (Class ≥ 3 MW)

Table 4.1: Performance Based Maintenance Overview of Analysed Wind Farms ≥ 3 MW

Wind Farm	Owner	Turbine	Maintenance	Performance Based Maintenance Information
Onshore				
Wardlaw Wood - A	Community WindFamrs	Vestas V90 3 MW	N/A	N/A
McCain Foods Whittlesey	McCain Foods	Vestas V90 3 MW	Vestas	Yes, 95% Availability - 2nd 5 year contract
Aikengall Windfarm	Community WindFamrs	Vestas V90 3 MW	N/A	N/A
Fullbrook Wind Farm	Devon Wind Power Ltd.	Vestas V90 3 MW	N/A	N/A
Offshore Wind Farms				
Burbo Offshore Windfarm - A	Dong Energy	Siemens SWT-3.6-107	In-House	Stopped PBMC in 2014
Robin Rigg Offshore Wind Farm (West)	EON	Vestas V90 3 MW	In-House	
Gunfleet Sands II	Dong Energy	Siemens SWT-3.6-107	In-House	
Gunfleet Sands I	Dong Energy	Siemens SWT-3.6-107	In-House	Stopped PBMC in 2014
Robin Rigg Offshore Wind Farm (East)	EON	Vestas V90 3 MW	In-House	
Ormonde Wind Farm	Vattenfall	Senvion/Repower 5MW	In-House	
Rhyl Flats Wind farm	RWE	Siemens SWT-3.6-107	Siemens	Yes, first 5 yr contract and 15 year extension signed in 2015 Yes, 95% Availability - 5/15 Year Contract
Walney Offshore Wind Phase I	DONG/SSE	Siemens SWT-3.6-107	Siemens	
Sheringham Shoal	Statoil/Statkraft	Siemens SWT-3.6-107	Siemens	
Walney Offshore Wind Phase II	DONG/SSE	Siemens SWT-3.6-107	Siemens	Yes, 5 year contract until 2020 Yes, 95% Availability - 5/15 Year Contract
Kentish Flats Ltd - A,C	Vattenfall	Vestas V90 3 MW	Vestas	
Barrow Offshore Windfarm - A	Dong Energy	Vestas V90 3 MW	Vestas	
Thanet Offshore Wind Farm	Vattenfall	Vestas V90 3 MW	Vestas	Yes 95% Turbine level, 97% Park Level unit 2 nd contract ends 2017 Yes 95% Turbine level, 97% Park Level unit 2011/2012 then own O&M

with the turbine that is equipped with foundation sensors within the field implementation (Vestas – V117-3.45 MW). As illustrated in Section 4.3.3 any LCOE model is based upon various assumptions, hence individual parameters can vary significantly. In addition, published available data is often difficult to reproduce as important information is missing. Therefore, LCOE is reproduced from DECC for onshore wind farms based on 3 MW class turbines in an installation above 5 MW as it offers the most abundant data available (investment costs and O&M costs).

4.3.1 Input Data

Investment costs for wind turbines can vary significantly, based on the size of turbine, size of contract, location, region, material prices, current demand and supply, level of subsidies etc. [70]. For this tool investment costs are taken from DECC with expenditure assumed at £1,400,000 per installed MW including turbine ex works, civil works, and grid connection [118]. Also, DECC's pre-development costs are taken into account at £100,000 per installed MW, thus in total capital expenditure is modelled at £1,500,000 per installed MW. Based on the cost distribution by Blanco [70] the CAPEX cost distribution is as following: turbine ex works - £3,408,000, grid connection £576,000, civil works £432,000, and other capital costs (site monitoring, permissions, planning costs, transportation, etc.) £384,000.

The annual turbine yield is obtained by defining the probability of turbulence according to wind speed v that is assumed to be normally distributed,

$$p_t(v) = \frac{1}{\sqrt{2\pi\sigma^2}} e^{-\frac{(v-v_a)^2}{2\sigma^2}} \quad (4.1)$$

where v_a is the 10 minute mean wind speed and σ the standard deviation defined by the product of turbulence intensity I and v_a . Since the Weibull distribution $p_w(v_a)$ is based on 10 minute mean data the power curve as a function of mean wind speed is,

$$P_a(v_a) = \int_0^\infty P(v) p_t(v, v_a) dv \quad (4.2)$$

Table 4.2: LCOE - Wind Turbine Parameters

Parameter	Value
Rotor Radius	50 [m]
Mean Wind Speed	6.6 [m/s]
Cut-In Wind Speed	3 [m/s]
Cut-Out Wind Speed	23 [m/s]
Turbulence Intensity	0.1
Cp-Max	0.48
Drive Train Efficiency	0.85
Weibull Shape Factor	2
Weibull Scale Factor	Gamma Function

where $P(v)$ is the turbine specific power curve and $p_t(v, v_a)$ the normal distribution of turbulence intensity. With this the point wind speed of turbulence intensity is transformed into the 10 minute mean value.

$$P_{year} = \int_0^{\infty} P_w(v_a) P_a(v_a) 8760 dv_a \quad (4.3)$$

Finally by integrating from zero to infinity the product of Weibull distribution, the power curve as a function of mean wind speed and the amount of hours per year, the annual yield P_{year} can be approximated as illustrated in Equation 4.3.

Wind turbine characteristics were modelled according to parameters summarized in Table 4.2, which yearly yield values are in agreement with models from [163]. For this specific case, in order to reproduce DECC's LCOE data, parameters are adjusted in order to achieve a capacity factor of 0.28 that is defined as the central case by DECC [117]. Based on given data in Table 4.2 the annual energy yield is estimated to account to 7.17 GWh.

Another important factor is the cost for operation and maintenance (O&M) that can once again depend on multiple factors as briefly summarised before and thus published data varies significantly. Usually O&M accounts for multiple factors as illustrated in Figure 4.10; however, published data from sources such as DECC, EWEA, Windpower-Monthly, NREL, and IEA deviate significantly making it difficult to determine reliable parameters. Since, this Section deals with the reproduction of LCOE, DECC's input

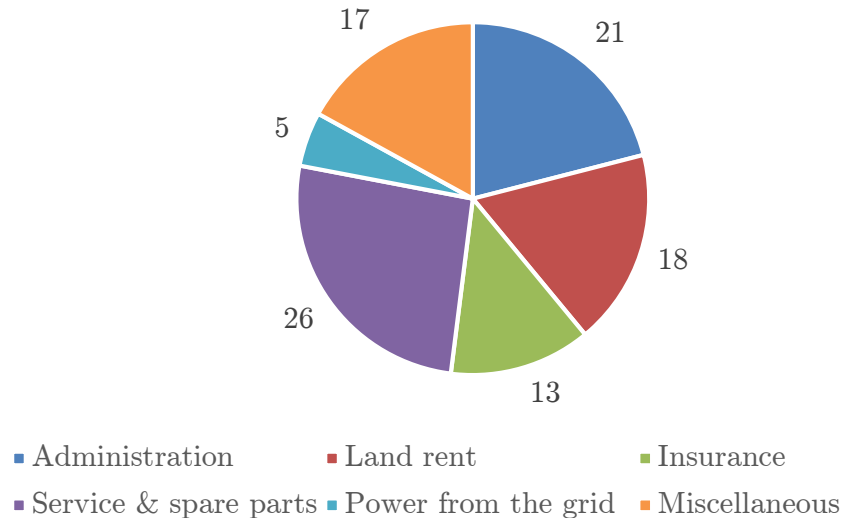


Figure 4.6: O&M Cost Breakdown in % [70]

parameters are selected. Detailed cost assumptions by DECC are illustrated in Table 3.5 based on different years of installation (2016, 2017, 2020), where costs are broken down into fixed and variable costs as well as insurance and connection/use of system charges.

As illustrated in Section 4.2 wind turbines experience performance degradation due to wear and tear of the electrical equipment such as generator or gearbox as well as the aerodynamic performance with e.g. leading edge erosion or damage formation in the adhesive layer of 1) joining skin and main spar flanges and 2) joining the up- and downward skins as both latter failure types account to 33% of total blade failures [164]. Hence as suggested by Staffell and Green [157] performance degradation shall be modelled linearly; i.e., with a constant reduction of 1.6% per year. However, DECC's metric does not account for performance degradation at all, hence at this stage this data is not included [119].

Concerning decommissioning expenses, there are different models and suggestions as well; e.g., in DECC's assumptions [119] the scrap value at the end of the lifetime is assumed to equalise decommissioning costs, whereas sources such as [165,166] require securities within the region of £90,000 for a 2.5 MW turbine in order to ensure that the operator is able to decommission the turbine eventually. For onshore wind turbines,

the UK has no jurisdiction whether securities have to be in place in order to guarantee the proper execution of decommissioning, whereas in Germany securities are required. The latter is governed by each federal state's law, for example in Hessen securities are required since 2004 based upon a rule of thumb,

$$Security[€] = HubHeight[m] * 1000[€] \quad (4.4)$$

where the required security is based upon the turbine hub height, as the required crane to decommission the turbine is the most expensive piece of equipment that cost factor increases with height [167]. This is crucial as the owner might become bankrupt during the course of a turbine's lifetime that could impact decommissioning requirements. Especially in offshore environments this is crucial due to limited turbine access restricted by weather conditions and significantly increased costs of equipment and service charges as a lifting vessel can easily cost more than £180,000 a day [168]. Since the aim is to reproduce DECC's LCOE, decommissioning costs are assumed to equalise with the turbine's scarp value; however, when the model is subjected to sensitivity of input parameters, decommissioning costs are also modelled at £90,000 at the end of a turbine's lifetime.

Also inflation for manual labour concerning operational expenditures are accounted for based on a yearly inflation of 3% that in this model affects only labour costs. Consequently, inflation affects administration charges (21% of O&M), and based upon the assumption that a third of service and spare parts is composed of manual labour, thus 8.6% of O&M (Figure 4.10). The discount rate is taken from DECC's parameters with a rate of 10% and as an alternative scenario 7.5%.

4.3.2 Results & Sensitivity Analysis

Based on all presented and discussed parameters in Section 4.3.1, LCOE values for this model's 3 MW wind turbine are £99.60 per MWh (discount rate: 7.5% - £86.18) that is in agreement with the central case of DECC's LCOE for onshore wind applications [117, 118].

In order to evaluate the robustness of this model a sensitivity analyses to certain input parameters is conducted. Results of this analysis are presented in Table 4.3 where certain input parameters are adjusted while Table 4.4 presents selected cases' results. Table 4.3's cases are quite straight forward, where defined parameters in Section 4.3.1 are reduced by 10%. Concerning the selected cases presented in Table 4.4, the first two

Table 4.3: LCOE - Sensitivity Analysis (1/2)

Case [-10%]	LCOE [£]	Δ Baseline	Blanco 2009 [70]
Investment Costs	92.22	-7.41%	-7.6%
O&M	97.01	-2.60%	-2.4%
Capacity factor	109.88	10.32%	8.5%
Interest Rate ¹	94.11	-5.51%	-2.1%
Lifetime ²	98.41	-1.19%	-4.0%
Weibull Shape Factor	97.95	-1.66%	N/A
Mean Wind Speed	127.63	28.14%	N/A

¹Blanco based on 7.5%, ² +10%

cases take the inter-annual variability (IAV) of mean wind speed into consideration. In other words any location's site characteristics can change; i.e., the annual mean wind speed can deviate over several decades that can be modelled as a normal distribution according to findings based on several locations such as multiple sites in the UK as well as in Minnesota, Unites States, and Norway [169–171]. Observations from the UK present an overall standard deviation of 7% of mean wind speed based on records up to 50 years [169]. Based on the mean wind speed and standard distribution a Monte Carlo simulation is modelled for the mean annual yield over the wind turbine's lifetime of 25 years based on 5000 iterations in order to satisfy the 98% confidence interval [172]. Out of these 5000 simulations the minimum and maximum 25 year mean wind speed is defined as the IAV optimistic and IAV pessimistic parameter.

As expressed previously, performance degradation is not considered by DECC; however as Staffell and Green present evidence based degradation results, there are two cases where the annual turbine yield is exposed to an annual linear reduction in efficiency of 1.6% [157]. Additionally, data is presented for an annual linear reduction in efficiency of 0.8%.

Lastly, decommissioning costs are evaluated as previously discussed with assumed costs

of £90,000 at the end of a turbine’s lifetime. Since securities are normally required to be given at installation, the present value is calculated based on a UK Government 30 year bond yield at 2.36% (25 years - interpolated at 2.145%). Therefore, at construction £50,223 are required as a security deposit (25 years yield: £89,583).

Table 4.4: LCOE - Sensitivity Analysis (2/2)

Case	LCOE [£]	Δ Baseline
IAV Optimistic	88.97	-10.62%
IAV Pessimistic	109.88	10.32%
1.6% Performance Degradation	112.17	12.62%
0.8% Performance Degradation	106.07	6.5%
0.2% Performance Degradation	101.19	1.6%
Decommissioning (30 yrs yield)	100.37	0.77%
Decommissioning (25 yrs yield)	100.41	0.81%

The first two sensitivity cases (investment costs, O&M) are in agreement with findings from Blanco, whereas the sensitivity case of interest rate, capacity factor and life extension deviate. These changes could be introduced due to the differences in the model as Blanco models 20 years of lifetime, with a specified debt/equity ratio and a different interest rate for debt and equity. Also, the model’s methodology is not disclosed, hence it is difficult to evaluate if there are fundamental differences in calculating LCOE as illustrated in Section 3.3.4.

Overall the analysis reveals that the greatest sensitivity to LCOE is annual fluctuation in mean wind speed that based on a reduction of 10% can increase LCOE by 28.14%. At the same time it is important to notice the unlikelihood of such a change over 25 years as expressed in the IAV optimistic/IAV pessimistic sensitivities of Table 4.4. This is also in agreement with the reduction in capacity factor that can be caused by a reduction in mean wind speed or availability due to downtime caused by faults. These findings are in agreement with Blanco “the wind resource - which matters the most” [70]. Further, turbine’s investment costs can impact LCOE significantly as seen with a reduction in LCOE of 7.41% which is anticipated as initial investment costs are the biggest cost factor [71]. It is interesting to observe that a 10% reduction in lifetime O&M costs contribute to a small proportion of LCOE, which findings are also

in agreement with Blanco. It is important to note here that parameters are not decoupled; i.e., changes in O&M expenditure impact downtime and availability that also changes LCOE parameters, hence reducing O&M costs could potentially reduce LCOE, although increased downtime might equalise or even increase LCOE eventually.

Concerning the effect of wind turbine performance degradation due to wear and tear, results based on findings by Staffell and Green increase LCOE by 12.62%, although as further findings by Staffell and Rubert reveal (Section 4.2), turbines in the multi-megawatt range have not shown equal degradation results, hence the effect is less prominent or not present at all. Here, further research is required to be conducted taking greater periods of data into account in order to analyse this effect in-depth. Nevertheless, different intensities (1.6, 0.8, 0.2%) of annual linear performance degradation and its effect on LCOE are presented to allow an idea on the impact over a turbine's lifetime.

Lastly, decommissioning costs do impact LCOE, although depending on regulatory frameworks securities are required to be deposited or not. Since the UK does not have any requirements there will be no direct impacts on the LCOE; however, as many countries have a different approach (Germany and Denmark) its sensitivity is illustrated with an impact of around £0.80 per MWh. With focus on life extension and decommissioning costs, from an operator's point of view there is a strong argument to delay such costs as interest will accumulate and the payment is shifted to a later date, once a turbine reaches its end of life cycle. This is especially valid for offshore wind farms.

4.3.3 Model Limitations

Naturally, this model is based upon numerous assumptions, thus parameters can vary significantly; however, the aim is to find a simple enough tool to model the medium case although different alternatives and approaches are discussed in this section. Overall the greatest parameters for uncertainty are itemised below.

- Investment costs/capital expenditure

- Operation and maintenance costs
- Site and turbine parameters
- Discount rate
- Methodology

Following the analysis, investment costs are a significant parameter in determining LCOE. Nevertheless, published data displays great ranges as in the case of Blanco [70] ranging in between €869-1,680 per kW, in the case of DECC [117] ranging in between £1,200-2,000 per kW, as well as in the case of the UK Government [173] £1,361 per kW, which is slightly lower than the medium case of DECC. Besides publishing expenses per installed kW, there exists uncertainty how costs are defined, although for the applied UK Government data, an itemised breakdown is given as mentioned before.

To allow an impression, how CAPEX assumptions are subjected to specific cases, can be illustrated by means of local soil conditions and depth of groundwater. If the given soil conditions are not sufficient, expensive reinforced concrete piles (Section 3.3.5.2) are required to stabilise soil or if the depth of groundwater does not meet requirements, expensive reinforcement and water barriers are required during foundation installation. In both cases, additional expenses can easily exceed £100,000 based on personal wind farm construction experience. A second example are grid connection cost that depend on the connection type; i.e., transmission or distribution access. This dictates the required distance to travel as well as costs for the actual interconnection deviate significantly based upon a specified location. Additionally costs vary with economies of scale, hence an entire wind farm's grid connection charges are different than for a single turbine.

Equally, O&M costs (also known as OPEX) can vary based upon multiple parameters as described before. Additionally it is also problematic to fully evaluate expenditures, since there is no accepted standard of what is included in O&M costs and what is excluded. This is quite challenging, since for example the cost distribution by DECC is defined fundamentally different to the presented cost structure in Table 4.10 as costs are broken down in variable costs (probably service and spare parts), fixed costs (likely

administration, land rent), insurance costs, as well as connection and use of system charges that might be covered by the power from the grid item, which is unlikely though. Therefore, different applied methods and cost categorisation approaches can result in deviations of LCOE.

Further, turbine parameters can slightly deviate such as cut-in and cut-out wind speed, aerodynamic efficiency (C_p -max), as well as the shape and scale parameter of the locally recorded Weibull distribution. All parameters affect the approximated annual turbine yield and thus LCOE.

Another limitation is the applied discount rate (10%) that deviates from other studies, where in some cases interest rates are split into debt and equity and a weighted average cost of capital (WACC) is taken into account. Also, the nominal value of 10% is found to be different in other studies, although DECC also displays LCOE results for an alternative discount rate of 7.5%. In fact, DECC has pointed out that it was impossible to update their assumption of the discount rate in the call for evidence; however it is expected that this will be adjusted in the future [117].

Lastly, as presented in Section 3.3.4 the entire method of LCOE may deviate; e.g., NREL applies a significantly different methodology and hence same parameters result in different LCOE estimations that cannot be compared due to such fundamental modelling differences [120].

Having understood the metric of LCOE, the following Section will assess the lifetime extension economics and present a methodology to support the economic lifetime extension decision-making.

4.4 A Decision Support Tool to Assist with Lifetime Extension of Wind Turbines

Although, there are already significant numbers of wind turbines reaching their end of lifetime [144, 147] as exemplified in Figure 4.7 for the UK, at present there exists no research analysing the economics of lifetime extension and decision-making at the

end of lifetime. Consequently, the applied economic LCOE metric is presented and input variables discussed in Section 4.4.1 alongside a proposed application methodology to assist economic lifetime extension decision-making. This is followed by a lifetime extension case study presented in Section 4.4.2 based on a wind farm with a capacity of 5.4 MW, consisting of six 900 kW rated wind turbine generators (WTGs). Section 4.4.3 presents the case study's results while in Section 4.4.4 this research's validation is presented. In Section 4.4.5 limitations and future work are discussed and finally in Section 4.4.6, findings are concluded.

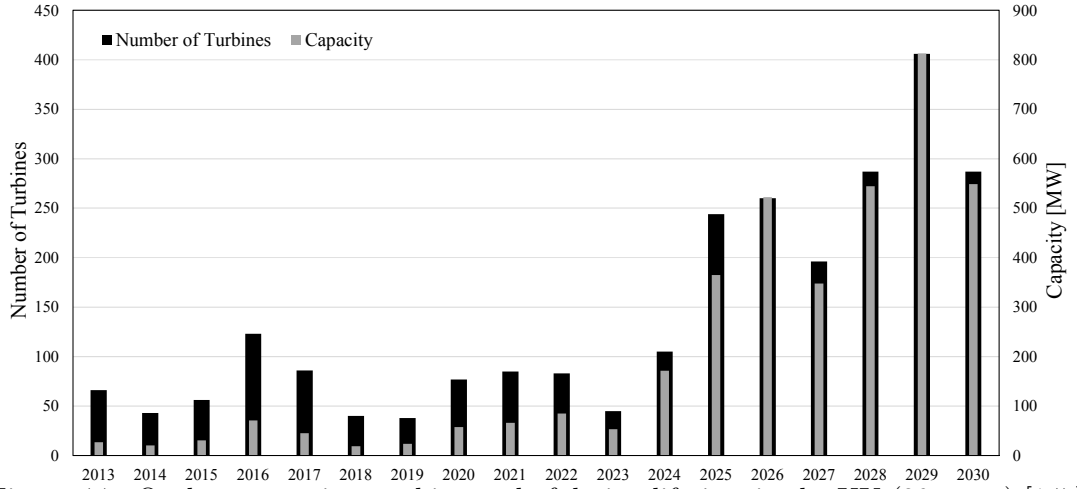


Figure 4.7: Onshore capacity reaching end of design lifetime in the UK (20 years) [147]

4.4.1 Levelised Cost of Energy

This work's adapted approach is the following. The net present value (NPV) of lifetime costs accrued of capital- and operational expenditure (CAPEX and OPEX) is estimated for each year, n and summed over the design lifetime as illustrated in Equation 4.5:

$$NPV_{TotalCost} = \sum_{n=0}^T \frac{CAPEX_n + OPEX_n}{(1+i)^n} \quad (4.5)$$

where T is the design lifetime and i the discount factor. Generated electricity flow is a monetary metric, thus future energy delivery requires discounting as well. This might be counter-intuitive, because a specified amount of energy delivered in the future is through discounting worth less quantity at present; however, based on the electricity supply a

revenue stream is created and money exchanged. Hence, discounting is necessary as illustrated in Equation 4.6:

$$NPV_{Yield} = \sum_{n=1}^T \frac{AEP_n}{(1+i)^n} \quad (4.6)$$

where AEP_n is the annual energy production of year n .

LCOE is the cost to generate a defined amount of energy; i.e., [\pounds /MWh], hence the NPV of lifetime generation costs defined in Equation 4.5 is divided by the NPV of the lifetime generated energy defined in Equation 4.6, thus:

$$LCOE = \frac{NPV_{TotalCost}}{NPV_{Yield}}. \quad (4.7)$$

Therefore, to determine LCOE for a project, its lifetime expenditure as well as estimated yield requires evaluation. Within the wind energy industry, different organisations apply different LCOE models; i.e., model varieties originate from different design assumptions such as the CAPEX that can be dealt with as an overnight cost as suggested by the Department of Energy and Climate (DECC) [119], or alternatively as a constant annuity payment as suggested by the National Renewable Energy Laboratory (NREL) [71]. Further model differences can originate from the discount factor, selection of which requires caution and due diligence. In essence, the discount factor represents a project's risk and thus requires case specific evaluation that is dependent on several factors. For wind energy investments, this includes the investor and investment size, historical data, contracts in place, type of power purchase agreement, the subsidy scheme as well as assumptions in yield estimation and operations and maintenance (O&M) expenditure. Methodologies concerning the applied discount rate may deviate as well; i.e., NREL [71] takes a project's debt-equity ratio and corporate tax rate into consideration by application of the weighted average cost of capital (WACC). On the contrary, less complex models define a hurdle rate² aimed at forming a specified project's return as applied by DECC that is set at 10%, although in form of a sensitivity

²Internal required rate of return on investments.

analysis a rate of 7.5% is modelled as well [117–119].

Apart from a WTG’s input, the output requires analysis as well in order to predict an asset’s annual electricity production. If a turbine’s physical parameters are known its energy yield can be estimated by application of a Weibull distribution defined by the shape and scale factor as well as the mean recorded wind speed [106]. The Weibull distribution can thus be modified according to locally recorded environmental conditions. Once the yield for a given period is estimated or known based on a turbine’s output, the capacity factor can be calculated. The latter that is defined as the ratio of the actual output of a turbine for a given period and the theoretical output at full capacity.

4.4.1.1 Model Input Parameters

In this Section the detailed LCOE methodology is presented, highlighting how parameters are obtained in order to allow reproduction of the findings presented in Section 4.4.3. As illustrated in Equation 4.7, a LCOE estimation requires two sets of input, a turbine’s expected yield and the estimated expenditure over the asset’s design lifetime. Within the wind energy sector, LCOE cost parameters are accessible from several sources such as DECC [117, 119, 174, 175], WindEurope [70], Milborrow [69, 176], NREL [71], and the International Renewable Energy Agency (IEA) [116], while Miller et al. [177] present a comparison for the US market; however, in agreement with the latter input parameters deviate significantly (a comparison of OPEX is illustrated in Table 4.5). This presents challenges to select appropriate model parameters.

Further complexity arises from the time domain, as a wind farm that reaches its end of design life at present experiences current OPEX, while the asset’s initial CAPEX was paid for in the past. This modelling challenge is addressed in the proposed lifetime extension methodology in Section 4.4.1.2.

Table 4.5: Comparison of fixed and variable O&M expenditure for a 900 kW wind turbine over 20 years. The turbine is the modelled type of the case study presented in Section 4.4.2. Inflation data from References [178–180]. Currency conversion factor from historical 5 year average (2014–2018).

Source	Year	Type	Expenditure	2018 Price	2018 in [£]
DECC (2017) [117]	2013	Fixed	£802,980	£824,982	£824,982
		Variable	£198,200	£203,631	£203,631
		Total	£1,001,180	£1,028,612	£1,028,612
ARUP (2015) [181]	2016	Fixed	£501,012	£532,024	£532,024
		Variable	£206,128	£218,887	£218,887
		Total	£707,140	£750,910	£750,910
NREL [182]	2015	Fixed	\$570,960	\$605,586	£411,963
		Variable	\$303,642	\$322,056	£219,085
		Total	\$874,602	\$927,642	£631,049
Blanco [70]	2009	Total	€475,680	€504,048	£413,154
		Variable	€311,616	€325,296	£266,636
IEA [183]	2013				
Milborrow UK [176] [69]	2009	Total	€713,520	€756,072	£619,731
	2012	Total	\$828,000	\$906,557	£616,706

4.4.1.1.1 Operational Expenditure

Operational expenditure covers all occurring activities that are necessary to ensure a safe, reliable, and continuous operation. Costs include administration, land lease, insurance, service and spare parts, power from the grid, as well as miscellaneous items that can vary significantly with an example cost breakdown structure illustrated in Figure 4.10 of the Appendix. To allow an impression on the variance in cost estimations, Table 4.5 presents the cumulated fixed and variable O&M expenditure of different published estimates for a 900 kW wind turbine over 20 years. Overall, a substantial expenditure range is observable which reveals the degree of uncertainty within LCOE calculations. In addition, in Germany there is evidence that the O&M costs are 10% higher in year 11–20 in comparison to year 1–10 [184]. For a UK deployment, the two most recent LCOE cost parameters are published by DECC in 2013 with a 2017 estimate [117] as well as ARUP in 2016 with a 2015 estimate [181]. As contrasted in Table 4.6, significant differences are observable. Both institutions are respected in the field

Table 4.6: Difference in UK OPEX Assumptions [117, 181].

Cost Item	DECC 2017	ARUP 2015
Fixed O&M [£/MW/y]	37,100.00	23,284.00
Variable O&M [£/MWh]	5.00	5.20
Insurance [£/MW/y]	3,010.00	1,441.00
Connection & system charges [£/MW/y]	4,510.00	3,109.00

and used for governmental estimations; however, taking the global OPEX expenditure comparison into consideration (Table 4.5), DECC’s fixed cost assumptions appear much higher in comparison. In this work, the annual OPEX, $OPEX_n$ is modelled as:

$$OPEX_n = R(C_F + C_I + C_U) + AEP_n C_V \quad (4.8)$$

where R is the asset’s rated power, C_F is the fixed O&M expenditure, C_I the insurance cost, C_U the connection and use of system charges, and C_V the variable O&M expenditure.

4.4.1.1.2 Capital Expenditure

Wind turbine investment cost can vary substantially, based on the turbine type, size of contract, location, region, commodity prices, demand and supply, as well as the level of subsidies as discussed in [70]. Furthermore, Wiser and Bolinger [185] identified investments with a greater project size than 5 MW experience a significant reduction in CAPEX. This agrees with DECC’s cost assumption threshold. In the central 2017 scenario, DECC’s CAPEX is assumed at £1,500,000 per installed MW, including turbine ex. works³, civil works, and grid connection. Also, DECC’s pre-development costs are taken into account at £100,000 per installed MW. CAPEX and development costs are in agreement with ARUP’s 2015 estimate [181]. At present, an onshore WTG’s construction is thus likely to cost £1,600,000 per installed MW, resulting in the following CAPEX cost distribution: turbine ex. works £1,136,000, civil works £144,000, grid connection £192,000, and other capital costs £128,000 (site monitoring, permissions, planning costs, transportation, etc.) based on the cost breakdown structure published by Blanco [70]. In this work, the asset’s overnight CAPEX is therefore modelled:

³Incoterm - direct from the factory or place of manufacture, thus not including transport expenses.

$$CAPEX = C_E + C_C + C_G + C_O \quad (4.9)$$

where C_E is the ex. works expenditure, C_C the civil expenditure, C_G the grid connection expenditure, and C_O other capital costs.

4.4.1.1.3 Yield Estimation

In order to establish the annual energy production AEP of a wind farm, a turbine's power curve requires modelling. As reviewed by Carrillo et al. [186] as well as Lydia et al. [187], there exist different power curve modelling techniques with varying accuracy and complexity. In this work the static power curve is modelled according to the approximated cubic power curve, $P_S(v)$:

$$P_S(v) = \frac{1}{2} \rho \pi R^2 C_{p,max} v^3 \quad (4.10)$$

where ρ is the air density (1.225 kg/m^3), R the rotor radius, $C_{p,max}$ the maximum effective power coefficient, and v the instantaneous wind speed. The selected approximation technique offers a reasonable estimate [186] as well as ease of implementation that is suitable for this work.

While a site's inflow conditions are dynamic, the static power curve is further adjusted to account for a 10-minute mean wind speed, v_a . As a result, the simulated power curve with respect to mean wind speed, $P_{Sim}(v_a)$ is:

$$P_{Sim}(v_a) = \int_0^\infty P_S(v) P(v, v_a) dv \quad (4.11)$$

where $P(v, v_a)$ is the mean wind speed probability distribution, assumed as Gaussian in nature, hence characterised by the turbulence intensity parameter, TI and v_a [188]. The annual energy production of a wind farm can therefore be estimated by:

$$AEP = Z(1 - \eta_W) h \eta_A \int_0^\infty P_W(v_a) P_{Sim}(v_a) dv_a \quad (4.12)$$

where Z is the number of turbines, η_W the factor for wake induced losses (5-15 %

- [157, 189–191]), h the number of hours in a year (8760), η_A the machine availability (95% in agreement with [192]), and $P_w(v_a)$ the Weibull distribution as a function of v_a . Although the long-term wind resource at a site may change over time [193, 194], in this work the annual resource is assumed constant. Further, as determined by Wagner et al. [195], ideally the rotor equivalent wind speed (REWS) shall be calculated that depends on the shear profile of the wind, the modelled hub height, as well as the number of measurement heights. The application of the REWS is further discussed in the case study.

As identified in [177], NREL applies a capacity factor of 38%, whereas other estimates are within the range of 18-53%. For a WTG deployment in the UK, on average a capacity factor of 28% is recommended by DECC [118, 119]; however, as stated by Sindon [196] and Cannon et al. [193] this parameter is underestimated. The latter based on a study of average, annual capacity factors over the past 33 years in the UK.

4.4.1.1.4 Components of Lifetime Extension Analysis

Table 4.7 presents an overview of the range of activities that are typically considered as state-of-the-art of the end of lifetime analysis in the UK. Results are derived from feedback gathered in [144] as well as the additional consultation of experts in the UK. In order to qualify as an expert, at least 5 years of experience is required within the

Table 4.7: Components of lifetime extension analysis in the UK. Derived from [144] and expert knowledge (Table 4.11 of the Appendix)

Item	Activity
Visual inspection	Visual inspection of: 1) blades (potentially internal for greater rated turbines), tower, flanges, and drive train 2) non-destructive testing of bolted connections, and 3) drive train vibrational analysis (if considered necessary)
Operational analysis	Review of: 1) operational SCADA data, 2) repair and maintenance log, and 3) conditioning monitoring data (if available)
Loads analysis	Review of wind inflow conditions (with met. mast if available) and compare to initial design assumptions (likely) Apply an aero-elastic code e.g. Bladed to redo load analysis of components based on reviewed wind inflow conditions (unlikely at present)
Administration	Consulting and overheads to facilitate LTE

industry (the mean consulted industry experience is 18 years) with a track record of

LTE exposure as illustrated in Table 4.11 of the Appendix.

In essence, the lifetime extension analysis (LTEA) can be broken down into: i) visual inspection, ii) operational analysis, iii) loads analysis as well as iv) administration. Project specific activities depend on several environmental parameters such as availability of data, global and local standards, legal requirements as well as an entity's considered best practise [23, 77, 144, 197]. While in the UK no legal requirement exist for the lifetime extension phase contrary to e.g. Denmark [156] and Germany [198], the presented activities may deviate from project to project. This is reflected in the UK's commonly performed load analysis, that presents substantial cost savings compared to e.g. the use of aero-elastic simulations as required in Germany. On the other hand, there is the example of Denmark where the analysis is legally sufficient based on visual inspections. The lifetime extension capital expenditure, $CAPEX_{LTE}$ is thus modelled as:

$$CAPEX_{LTE} = Z(c_v + c_l) + c_o + c_a + c_{r,r} \quad (4.13)$$

where c_v is the visual inspection cost per WTG, c_l the loads analysis expenditure per WTG, c_o the operational analysis expenditure, c_a the administration expenditure, and $c_{r,r}$ the cost for necessary repairs and retrofits.

4.4.1.1.5 Other Tool Parameters

Overall, the LCOE methodology is designed in agreement with DECC's LCOE assumptions, thus inflation in labour expenditure and performance degradation are not considered, whereas decommissioning costs are assumed to be equalised with the turbine's scrap value. The discount rate in the central scenario is conservatively selected at 10%. With regards to the validation of the tool, a sensitivity analysis was executed in [146] albeit based on a model with less complexity than presented in this work. In order to overcome the significant variance in published LCOE parameters, this work's LCOE estimations are subjected to three scenarios; i.e., a pessimistic, central, and optimistic case.

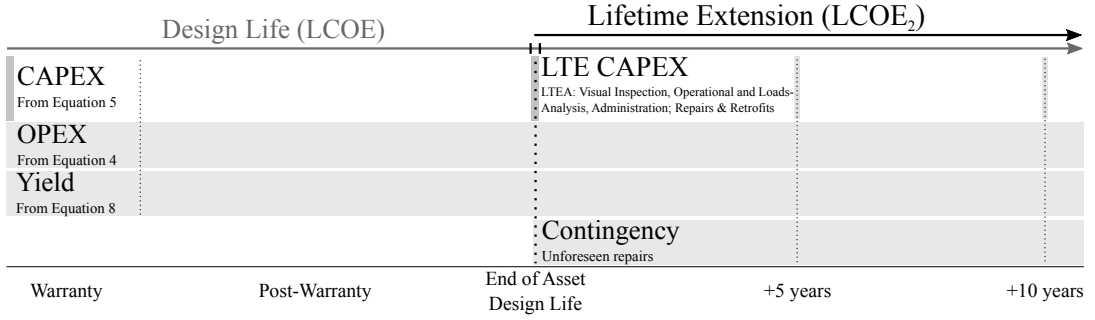


Figure 4.8: Schematic overview of lifetime extension LCOE methodology

4.4.1.2 Lifetime Extension Methodology

For the economic lifetime extension assessment, we propose a three-pronged approach aimed at i) evaluation of the development of total lifetime LCOE (design life and life-time extension), depicted in this thesis as LCOE, ii) evaluation of solely the LCOE of the extension period (+5-15 years), depicted in this thesis as $LCOE_2$, and iii) to develop a contingency investment decision model for alternative re-investment scenarios deviating from this work's modelling or one-off unexpected repairs and retrofits.

The applied LCOE methodology is schematically illustrated in Figure 4.8. Throughout the entire model, OPEX and yield parameters are modelled as static cash-flows. The CAPEX is dealt with as an overnight cost for the initial investment in year 0 (Section 2.1.1) as well as for the investment required at the end of design lifetime referred to as $CAPEX_{LTE}$ (see activities presented in Table 4.7). In addition, the cost of repairs and retrofitting components is budgeted as well if deemed unsafe for continuous operation due to; e.g., wear and tear. Modelling lifetime extension investments as an overnight cost enables treating the extended period as a separate investment since at the end of an asset's lifetime its investment schedule is terminated and the asset is fully written off. In addition, at the lifetime extension stage, the LCOE model breaks down due to severe discounting. Therefore, we propose to economically model the lifetime extension separately as depicted in Figure 4.8 with the presented $LCOE_2$ estimation model. Note that the $LCOE_2$ analysis is thus independent of the initial CAPEX in year 0.

If a life extended wind farm is under operation and a severe failure occurs in a WTG or

within a cluster of turbines, ideally a rapid management process is required to minimise downtime. Failure modes, their frequency and cost implications are published by a limited amount of sources; however, published data tends to be either generic (no impact breakdown; e.g., in minor, major or replacement) [199] or coarse; i.e., specified on the drive train level, hence lacking a component breakdown [200]. In addition, there exist limited operational experience at the end of design lifetime and beyond [144]. Since, access to failure data beyond the design lifetime as well as component replacement data as an outcome of the LTEA is confidentially treated, this presents challenges in sensible modelling.

From the point of view of an operator, operating beyond a WTG's design life can therefore result in sudden unexpected cost implications that may or may not require substantial remedial action in subsequent years. If a failure occurs, this generally entails a technical assessment to identify what remedial action is required, paired with a cost estimation for a given failure mode. This can occur because a turbine experienced a failure, or as an outcome of an inspection resulting from the LTEA. Assuming an identified failure can be repaired at a given cost, economic feasibility is not guaranteed and requires further analysis.

Given the necessary operational flexibility and challenge to sensibly model failure rates, we propose the application of a contingency based analysis; i.e., a metric on i) how much money is viable to spend on the LTEA (repairs and retrofits) and ii) how much money is viable to spend on top of general O&M expenditure before a certain specified cost threshold is reached in subsequent years. The threshold target may be to maintain the expenditure 10% below a certain guaranteed subsidy per MWh or below the average one-day ahead spot market price in a non-subsidised environment, respectively. Therefore, with the proposed contingency thresholding, an operator can apply the proposed end-of-life decision-making support tool to rapidly evaluate a certain situation and determine case specific economic feasibility for a given operational scenario (required expenditure vs. contingency budget). If the cost is below the contingency budget, execution of remedial action is supported and the asset is advised to continue to operate. If, however, the cost is greater than the contingency budget, the remedial action is

advised against and instead, decommissioning of the asset is recommended.

4.4.2 Lifetime Extension Case Study

Based on findings presented by Ziegler et al. [144], a wind farm rated at 5.4 MW consisting of six 900 kW rated turbines is modelled with a design lifetime of 20 years. This turbine type was selected as its configuration is typical of wind farms approaching their end of design life in the near future. Based on findings by [70,146], throughout all input parameters, the mean wind speed has the greatest impact on LCOE. Therefore, careful evaluation is required. Sinden [196] extracted historical capacity factors for UK onshore turbines (average 30%), while Cannon et al. [193] extracted more recent historical capacity factors for UK onshore and offshore turbines (average 32.5 %). The latter concluding a likely increase due to the inclusion of windier offshore regions. As a result, for this work's onshore case study, Sinden's modelled WTG power curve (Nordex N80) [196] was replicated, resulting in a mean wind speed of 7.1 m/s scoring a capacity factor of 30% at a hub height of 82.5 m. While the Nordex N80 sits at a higher hub height than the 900 kW modelled WTG, the wind shear log-law was applied (roughness length, $z_0 = 0.03$ - open farmland, few trees and hedges), resulting in a reduction of the average wind speed by 0.25 m/s based on the modelled hub height of 61.5 m [106]. The turbine was further subjected to identify the REWS; however, in agreement with Wagner et al. [195], the impact was observed to be low in magnitude (reduction of 0.015 m/s) and is thus not taken into consideration. Consequently, 6.85 m/s was applied as the average mean wind speed. This wind speed is also in agreement with the UK's wind atlas [155].

The WTGs' and environmental parameters are further summarised in Table 6.2. The turbine's maximum effective power coefficient is selected at 0.44 in order to address the design state of the industry in between 1997 and 2000. Table 6.3 illustrates the case study's overall input assumption for the central scenario, paired with their estimated range. Each input parameter's highest and lowest estimate⁴ serve as an input for the optimistic and pessimistic scenario respectively. Where possible, parameter ranges

⁴Wake losses and availability are applied vice-versa

Table 4.8: LCOE - Wind turbine parameters

Parameter	Value
Rotor radius	25.3 [m]
Hub height	61.5 [m]
Cut-in wind speed	3 [m/s]
Cut-out wind speed	25 [m/s]
Turbulence intensity	0.1
$C_{p,max}$	0.44
Mean wind speed	6.85 [m/s]
Weibull shape factor	2
Scale factor (Gamma function)	7.72

were extracted from available research and paired with expert knowledge (Table 4.11 of the Appendix) to ensure model input parameters appear realistic for a UK based deployment and lifetime extension.

Regarding the LTEA, the specified turbine's lifetime is assumed to be extended by either 5, 10, or 15 years under the assumption that O&M costs remain static as modelled over the initial 20 years of operation. In addition, as stated in the DNV GL's lifetime extension guideline, if components are likely to fail in the near future, structural health monitoring (SHM) or component replacement is necessary, thus the following retrofits are modelled:

- One-off: blades, gearbox, or generator
- Two of: blades, gearbox, or generator
- Replacement of blades, gearbox, and generator.

Cost estimations of retrofits are based on findings presented in [70,123,201,202] and estimated as a percentage of WTG's ex. works CAPEX. In the case where multiple sources were available, average percentage figures are applied. Time and rate assumptions were made to the installation expenditure consisting of i) crane mobilisation/demobilisation (Mob/DMob), ii) crane operation, and iii) service personal expenditure that estimates were verified by an expert in the field (Table 4.11 of the Appendix). For example, in the central scenario the installation cost of a generator replacement is conservatively priced at £10,050 (100t crane Mob/Dmob - £7,500, crane operation - £810, and service

Table 4.9: Lifetime extension cost estimations for a wind farm consisting of six 900 kW WTGs

Parameter	Central	Range	Unit	Source
CAPEX				
Pre-development	100	30-240	£/kW	[118, 181]
Construction costs	1,500	1,100-1,800	£/kW	[118, 181]
O&M				
Fixed	30,192	22,644-37,740	£/MW/y	[118, 181] $\pm 25\%$
Variable	5.1	3.83-6.38	£/MWh	[118, 181] $\pm 25\%$
Insurance	2,226	1,669-2,782	£/MW/y	[118, 181] $\pm 25\%$
Connection/system charges	3,810	2,857-4,762	£/MW/y	[118, 181] $\pm 25\%$
Other parameters				
Discount rate	10	7.5-12.5	%	[118] & Expert Knowledge
Wake losses	10	5-15	%	[157]
Availability	95	93-97	%	[157, 203]
Resulting capacity factor	25.47	23.55-27.45	%	[193, 196, 204]
CAPEX LTE				
Visual inspection	2,150	1,613-2,688	£/WTG	[144] Expert Knowledge $\pm 25\%$
Loads Analysis	3,500	2,625-4,375	£/WTG	Expert Knowledge $\pm 25\%$
Operations Analysis	10,000	7,500-12,500	£/Wind Farm	Expert Knowledge $\pm 25\%$
Spare parts				
3 blades (21% of ex. works)	214,704	151,635-273,745	£/WTG	[70, 123, 201, 202] $\pm 25\%$
Gearbox (13% of ex. works)	132,503	93,580-168,941	£/WTG	[70, 202] $\pm 25\%$
Generator (8.2% of ex. works)	84,041	59,380-107,153	£/WTG	[70, 202] $\pm 25\%$
Installation expenditure				
Crane (100 t) Mob/Dmob	7,500	5,625-9,375	£/Wind Farm	Expert Knowledge $\pm 25\%$
Crane operation	810	608-1,013	£/day	Expert Knowledge $\pm 25\%$
Service personal	58	43.1-71.9	£/h	Expert Knowledge $\pm 25\%$

personal - £1,740).

With regards to the LTEA expenditure, multiple expert cost estimations were gathered, averaged and reverted back to participants for agreement as advised by Yin [205] (except of visual inspection data, secondary data was not available). Overall, little discrepancies in responses were observed. Therefore, inspection costs are assumed at £2,150/WTG with the load analysis budgeted at £3,500/WTG respectively. For the modelled wind farm the operational analysis is estimated at £10,000 and the overall administration expenditure for consultants is included in the mentioned budgets (owner administration is not included in the analysis). The analysis extension period is valid for 5 years until reassessment is required [144]; i.e., for the 15-year lifetime extension estimate, 3 reassessment budgets are modelled (year 20, 25, and 30). For the subsequent LTEAs in year 25 and 30, the cost for the loads and operational analysis is reduced by 50% based on the learning curve of the initial assessment in year 20 (only critical components require loads analysis and operations analysis procedures are established).

4.4.3 Results

Results of the LCOE model baseline scenario as well as the $LCOE_2$ estimates for the case study presented in Section 3 are shown in Figure 4.9. Complimentary, Figure 4.11

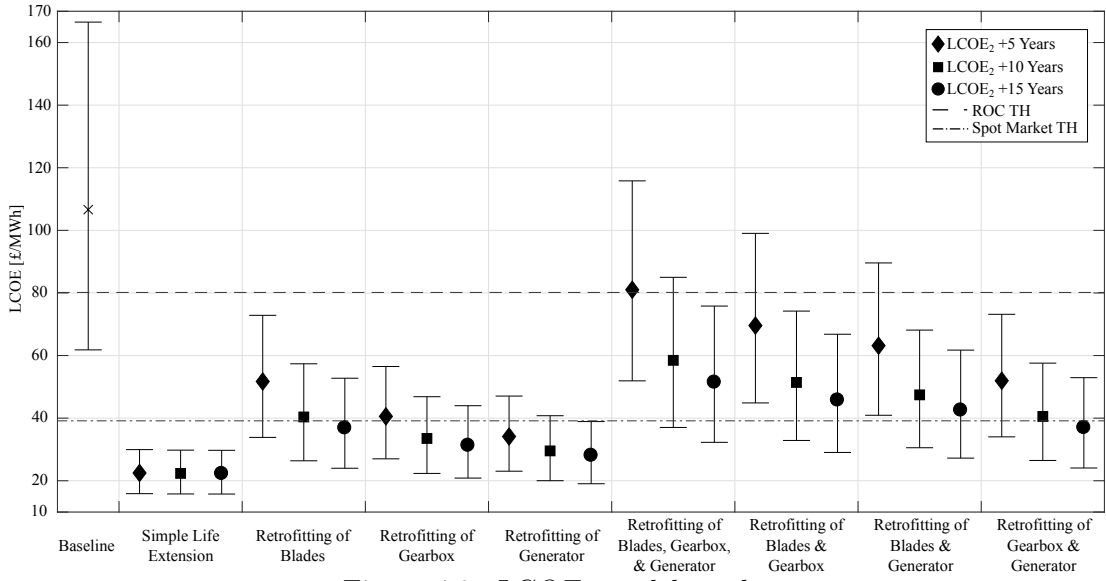
of the Appendix presents the life extended LCOE results, while Table 4.10 illustrates the annual available contingency. Overall, findings are presented for the different model combinations of i) lifetime extension (5-15 years), ii) input assumptions (pessimistic, central, optimistic), and iii) re-investment type.

Figure 4.9 as well as Figure 4.11 are further equipped with defined thresholds (TH) aimed at budgeting the LCOE 10% below the average day-ahead spot-market electricity price of the past 5 years (£39.14 [206]) for life extension scenarios in a subsidy-free environment. A further TH is set under the Renewable Obligation (RO) environment. The latter is aimed at budgeting the LCOE 10% below the RO revenue stream defined by the 2017-2018 buy-out price and day ahead spot-market electricity price (£41.02+39.14 [206, 207]).

First and foremost, in the baseline scenario (no lifetime extension), findings result in LCOE estimates of 106.6 £/MWh for the modelled wind farm in the central scenario with an optimistic estimate of 61.81 £/MWh and 166.53 £/MWh for the pessimistic case respectively. While in the central scenario the LCOE estimate appears higher in relation to other publications [208–211], the optimistic estimate is well in agreement. The higher central estimate is likely caused by multiple modelling differences, namely i) the exclusion of wake losses and availability, ii) the deployment of greater scale turbines as the power scales quadratically with the rotor radius [106], iii) the application of a lower discount factor, iv) different central CAPEX and OPEX assumptions, v) higher wind speeds due to increased hub heights, vi) a higher design lifetime (25 years) and vii) increased power coefficient efficiencies (an old design is essentially modelled).

In the simple life extension case (no repairs, nor retrofits), this work's proposed $LCOE_2$ methodology, estimates a cost range of 15.87-29.95 £/MWh for a lifetime extension of 5 years with the central case at 22.48 £/MWh (+10 years: 15.78-29.77 £/MWh, 22.34 £/MWh; +15 years: 15.75-29.72 £/MWh, 22.30 £/MWh). These results are paired with significant annual contingency to meet the defined aim to remain 10% below the average day ahead spot-market price as well as ROC revenue respectively, albeit with less contingency (Table 4.10: shaded area).

For the LCOE estimates presented in Figure 4.11, results reveal that in the central

Figure 4.9: $LCOE_2$ model results

scenario, LCOE can be reduced by 4.9% paired with a lifetime extension of 5 years. For an aimed extension strategy of 10 years, the LCOE reduces by 7.7%, whereas in the 15-year extension scenario LCOE reductions within the order of 9.3% are achievable. Overall, economic success is endangered under the RO as well as in a subsidy-free environment, though the derived LCOE metric breaks down as discussed in Section 3, thus its application is not advised.

For a single component re-investment, the central $LCOE_2$ estimates are well below the RO target; however, in the defined subsidy-free case, cost estimations are in close proximity to the defined target (except of retrofit of blades +5 & +10 years and gearbox +5 years). Further, where cost estimations are in close proximity to the set threshold; e.g., a gearbox replacement paired with a lifetime extension strategy of 10 years; caution is required. Here due diligence and risk management activities are necessary, due to a relatively low remaining annual contingency (£67k).

For any two-component re-investments, all central scenarios are below the RO target where the least cost intensive re-investment scenario (gearbox and generator) paired with a life extension greater than 15 years is below the defined subsidy-free target. Once again, caution is required as a 15-year extension commitment scores an annual contingency of £26k. Apart from the comparatively low contingency budget, a 15-year

Table 4.10: $LCOE_2$ annual contingency results. N/A: investment is not applicable (cost above set TH)

Scenario	Lifetime Extension [years]	Contingency to maintain $LCOE_2$ 10% below average day-ahead spot market electricity price [£]			Contingency to maintain $LCOE_2$ 10% below RO revenue stream [£]		
		Pessimistic	Central	Optimistic	Pessimistic	Central	Optimistic
Simple Life Extension (no repairs/retrofits)	5	101,312	198,730	299,039	553,593	687,915	826,271
	10	103,254	200,296	300,219	555,535	689,481	827,451
	15	103,832	200,781	300,595	556,114	689,966	827,828
Retrofit of Blades	5	N/A	N/A	68,005	80,625	339,316	595,237
	10	N/A	N/A	164,041	251,362	474,419	691,273
	15	N/A	27,043	194,701	302,222	516,228	721,934
Retrofit of Gearbox	5	N/A	N/A	156,034	260,902	472,176	683,266
	10	N/A	67,200	215,928	367,300	556,385	743,160
	15	N/A	93,259	235,049	398,995	582,444	762,282
Retrofit of Generator	5	N/A	59,696	206,791	365,023	548,881	734,023
	10	N/A	114,522	245,845	434,263	603,706	773,077
	15	2,607	131,488	258,314	454,888	620,673	785,546
Retrofit of Blades, Gearbox, & Generator	5	N/A	N/A	N/A	N/A	N/A	363,065
	10	N/A	N/A	27,192	N/A	258,780	554,424
	15	N/A	N/A	88,286	47,988	342,024	615,518
Retrofit of Blades & Gearbox	5	N/A	N/A	N/A	N/A	126,197	453,622
	10	N/A	N/A	80,569	65,698	342,939	607,801
	15	N/A	N/A	129,793	147,250	410,012	657,025
Retrofit of Blades & Generator	5	N/A	N/A	N/A	N/A	202,901	504,379
	10	N/A	N/A	110,486	132,660	390,260	637,719
	15	N/A	N/A	153,057	203,143	448,240	680,289
Retrofit of Gearbox & Generator	5	N/A	N/A	65,777	77,012	336,403	593,009
	10	N/A	N/A	162,727	249,038	472,622	689,960
	15	N/A	25,592	193,680	300,283	514,776	720,913

lifetime extension strategy is further accompanied by a significant external risk factor (policy changes/spot-market fluctuations).

In the unlikely case of retrofitting a wind farm's blades, generator, and gearbox, economic success under the defined thresholding cannot be met in a subsidy-free environment, thus decommissioning is advised in the central scenario. In contrast, economic success can be met under the defined RO target, if subjected to a lifetime extension strategy above 10 years.

Apart from a single/combination of gearbox, generator or blade replacement, a WTG can have many different faults or failures with deviating cost implications. For such cases, the presented simple life extension contingency data (Table 4.10: shaded area) can be compared to an actual cost/failure scenario to support the economic decision-making.

4.4.4 Validation

According to Mitchell [212] validation is the process of testing whether a model represents a viable and useful alternative means to real experimentation. Further, as argued by Pidd [213], validation is impossible if seen as a comprehensive demonstration that a model is fully correct. With respect to the presented LTE model and case study application, confidentiality and limited experience challenge the degree of ability to validate. In addition, this is the first published attempt aimed at assisting LTE decision-making. Hence comparisons to alternative models are beyond the bounds of possible. Lastly, the proposed method is not designed to generate a definite answer to the overall decision-making process, it is designed as an economic decision-making support tool. Given such challenges, a pragmatic validation approach is selected. This includes i) a model sensitivity analysis (Table 4.12 of the Appendix), ii) a case study sensitivity analysis (central, optimistic, and pessimistic scenario), and iii) the collection of feedback from industrial experts in the field. For further validation or comparison purposes, all assumptions and input parameters are disclosed for model replication.

4.4.5 Limitations and Future Work

The application of LCOE is always accompanied by a great number of assumptions and generalisations that can be significantly different from project to project. Investment costs are a substantial parameter in determining LCOE; nevertheless, published data covers a great variety; e.g., Blanco [70] estimates the CAPEX range between €869-1,680 per kW, whereas this work's CAPEX ranges between £1,130-2,040 per kW. Although the derived $LCOE_2$ does not directly depend on a project's initial CAPEX, there is an indirect impact since the cost of spare parts are ex. works dependent.

Equally, OPEX expenditure can vary based upon multiple parameters with significant modelling deviation as illustrated in Table 4.5. Additionally, it is also problematic to fully evaluate OPEX expenditures, since there is no accepted standard of what is included in O&M costs and what is excluded. This is quite challenging, since for example the cost distribution by DECC is defined fundamentally differently to the cost structure

presented in Figure 4.10. Therefore, different applied methods and cost categorisation approaches can result in deviations of LCOE.

With respect to the yield modelling, overall the methodology considers that a 20-year old turbine design is less efficient in power conversion than today's WTGs on the market ($C_{p,max}$: 0.44 vs. 0.49); however, adjustments and developments in i) rotor design or 2) turbine topology (e.g. fixed or variable speed and pitch or stall regulated turbines or drive train topology, i.e. synchronous generators with a gearbox vs. direct drive generator) affect the aerodynamic and drive train efficiency [163]. This will thus impact the extractable power coefficient, C_p that is also dependent on the tip speed ratio, λ and pitch angle, β [106,186]. Therefore, a different drive train topology or rotor design will in return impact an asset's capital expenditure and AEP.

Furthermore, turbine parameters can slightly deviate such as the cut-in and cut-out wind speed as well as the mean, shape and scale parameter of the locally recorded Weibull distribution. All parameters affect the approximated annual turbine yield derived in Equation 4.15 and thus LCOE; however, the mean wind speed will have the most significant impact on the overall calculation as highlighted in Section 3 and Table 4.12 (e.g. Scotland has a higher mean wind speed than England; The UK is windier than southern Europe [155,214,215]). Given that input parameters can vary significantly, enclosed to this work is a published database allowing users to adjust any combination of the mean wind speed, $C_{p,max}$, turbulence intensity, and Weibull shape factor for the central, optimistic, and pessimistic scenario [216].

The consideration of expert judgement is essential in order to allow a representative state-of-the-art analysis; however, with respect to LTE in the UK, the industry's characteristics are young and confidentiality making it challenging to collect a representative amount of expert opinions. In order to account for personal bias at least two experts were aimed to take into consideration.

As presented in Section 1 the entire methodology of LCOE may deviate; e.g., NREL applies a different methodology, thus similar parameters result in different LCOE estimations that cannot be compared due to fundamental modelling differences. With the applied capacity factor of 38% by NREL, significantly windier sites and or greater

rated turbines are considered in the central scenario compared to the UK (since 2006 the UK's average installed onshore turbine is 2 MW [147]).

With regards to the presented results of the case study, it is overall unlikely yet possible that all WTG require the same component replacement. Therefore, different scenarios are modelled paired with their contingencies, thus researchers, wind turbine operators and investors are able to identify economic boundaries for a given project. In addition, if no re-investment type appears similar to the presented combinations (e.g. the expenses for a generator rewinding, the purchase of a condition monitoring system or a SCADA upgrade), it remains possible to compare the required investment sum to the annual available contingency (Table 4.10: shaded area).

Lastly, the analysis reveals a proportionality between the extension period and estimated contingency. This is vital, since the available annual contingency can be seen as the likelihood that a set target can be met, thus indicating the risk of an end of lifetime investment; however, a greater extension period also results in a higher uncertainty as identified in [144], thus in essence the increasing contingency is out-balanced by a greater long-term risk perception. In the UK, this is greatly accompanied with the change to a static RO allocation scheduled in 2027 [154] and the non-existent lifetime extension regulation contrary to; e.g., Denmark and Germany.

Future work entails to add further complexity, by taking parameters such as performance degradation, up-scaling, inflation, WACC, and end-of-life failure rates into consideration. In addition, the time of re-investment in this work is assumed at the end of lifetime; however, this is certainly not the optimised investment time and thus requires further scrutiny. Lastly, repowering and refurbishment decision-making synergies of other industries might be explored.

4.4.6 Section Conclusions

Despite the limitations that have been highlighted, this work provides the reader with a flavour of the complexity and economic boundaries of lifetime extension and offers guidance for operators, investors, and academics dealing with the subject of LTEA. The study gives an idea what investment and cost estimates are achievable for differ-

ent practical scenarios. Based on the outcomes of this research, the application of the derived $LCOE_2$ metric is proposed where the life extended period is modelled as a separate investment in conjunction with the presented contingency methodology.

Overall, the results reveal that significant cost reductions are achievable with an estimated $LCOE_2$ of 15.87-29.95 £/MWh that is shown to be well below the set target within the RO environment and when exposed to a non-subsidised market. Based on this work's identified LCOE, the more competitive allocation of onshore subsidies, and the termination of the RO in 2017 (grace period until 2019; runs until 2037), we are confident that lifetime extension will play an ever-increasing role in the UK's onshore wind energy market.

4.4.7 Section Appendix

As a supplement to this work, a database is published allowing users to adjust any combination of the mean wind speed, $C_{p,max}$, turbulence intensity, and Weibull shape factor for this work's central, optimistic, and pessimistic scenario [216].

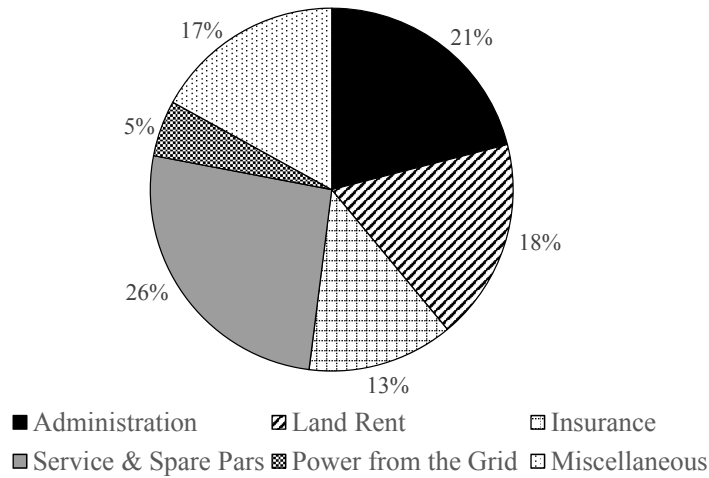


Figure 4.10: O&M cost breakdown in % [70]

Table 4.11: Overview of consulted UK experts

Generalised job title	Degree	Years of experience in wind energy	Knowledge area	UK LTE exposure
Head of Department	MSc	15	Technical & commercial	Supervised 5 wind farms on LTE
Director	MEng	11	Technical & commercial	Load monitoring campaigns, commercial evaluation
Director	MEng	14	Commercial	Load monitoring campaigns, commercial evaluation
Director	MSc	23	Commercial	Secondhand wind turbines, spare parts
Director	MEng	16	Technical	Supervised 2 wind farms on LTE
Head of Department	PhD	35	Technical & commercial	General commercial project cost
Manager	PhD	10	Commercial	General commercial project cost
Director	MSc	23	Commercial	Commercial project cost

Table 4.12: Sensitivity of lifetime extension model

Case [-10%]	Gearbox retrofit [+10 years]		No retrofit [+10 years]	
	$LCOE_2$ [£]	Δ Baseline [%]	$LCOE_2$ [£]	Δ Baseline [%]
Mean wind speed	40.89	22.03	26.83	20.05
OPEX	31.36	-6.42	20.19	-9.62
$C_{p,max}$	35.40	5.66	23.50	5.16
CAPEX (spares)	32.42	-3.24	N/A	N/A
Weibull shape factor	33.14	-1.08	22.12	-0.98
CAPEX LTE	33.42	-0.25	22.26	-0.38

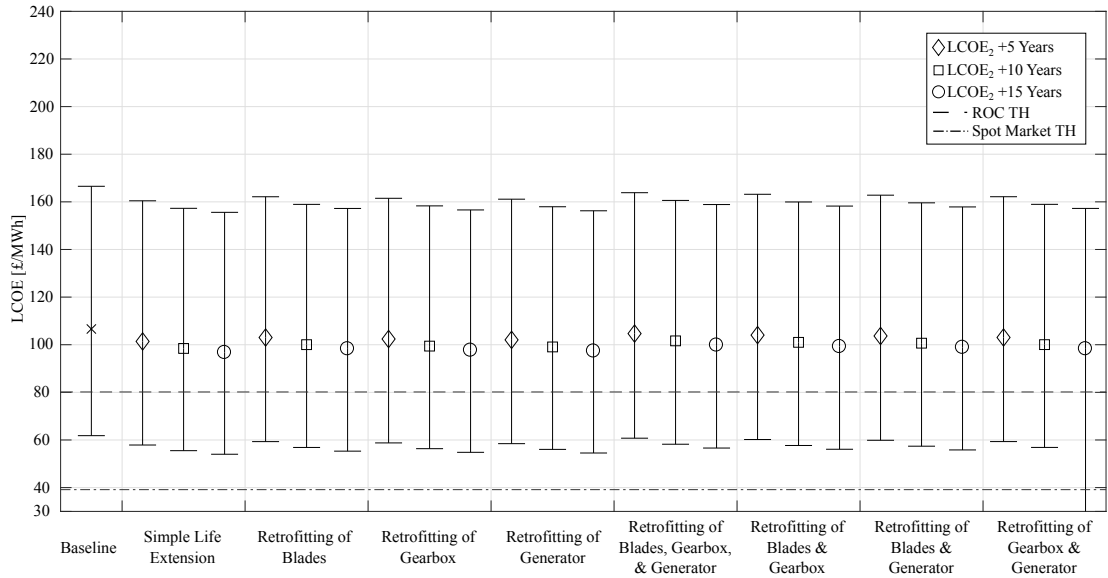


Figure 4.11: LCOE model results

4.5 The Effect of Upscaling and Performance Degradation on Onshore Wind Turbine Lifetime Extension decision-making

Having developed a lifetime extension decision-making tool, this Section will analyse the impact of upscaling and performance degradation on the lifetime extension decision-making.

4.5.1 Upscaling

Naturally, as increasingly greater rated turbines have been commercially developed and installed, there is an inevitable fact of greater rated turbine classes reaching their end of design lifetime as illustrated in Figure 4.12.

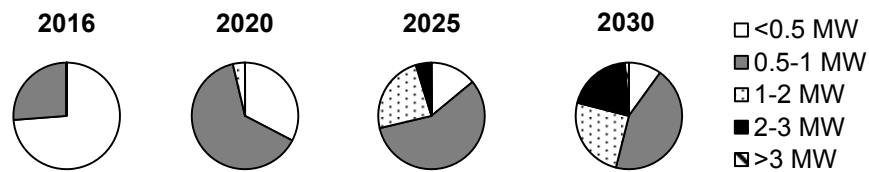


Figure 4.12: Distribution of WTGs reaching their end of design lifetime (20 years) [144].

In order to compare the impact of upscaling of turbines on LTE economics, an 18 MW rated wind farm consisting of different generic turbine classes is modelled. The corresponding blade radii and hub heights are taken from commercially available turbines. If a significant variance in rotor size and hub height was observed at an equal rated power, the mean encountered turbine is modelled, indicated by an [M] besides individual upscaled and downscaled models, indicated by an [S]. Adjusted parameters for some turbine models are summarised in Table 4.13.

4.5.1.1 Yield Modelling

Based on findings from [145], the site's mean wind speed is characterised by 6.85 m/s at a reference hub height of 82.5 m. Due to the natural shear profile of the wind inflow [106], each modelled turbine's mean wind speed at hub height, $U(z)$ varies. Therefore, $U(z)$ is extracted through the wind shear log-law:

$$U(z) = U(z_r) \frac{\ln \frac{z}{z_0}}{\ln \frac{z_r}{z_0}} \quad (4.14)$$

where z_r is the reference hub height, $U(z_r)$ the average wind speed at reference hub height, z the modelled turbine hub height (Table 4.13 and Figure 4.14a), and z_0 the surface roughness length (assumed as 0.03 m for open farmland, few trees and buildings) [201]. The application of the wind shear log-law assumes neutral atmospheric stability and is designed up to heights of 100 m, with evidence of inaccuracies above [217] and proposed methods to overcome this limitation [218]. The latter method requires empirical knowledge of a site, presenting challenges to adequately address in this work, thus for simplicity the shear log-law is applied above 100 m. The annual energy production AEP , of a wind farm is estimated by:

$$AEP = Z(1 - \eta_W)h\eta_A \int_0^\infty P_W(v_a)P_{Sim}(v_a)dv_a \quad (4.15)$$

where Z is the number of turbines, η_W the factor for wake induced losses, h the number of hours in a year (8760), η_A the machine availability (95% in agreement with [192]),

Table 4.13: Upscaling input parameters of selected 18 MW wind farm configurations. Cost estimates origin from literature [145].

Parameter	500 kW [S]	900 kW [M]	2 MW [M]	3 MW [M]
Turbines	36	20	9	6
Hub Height [m]	46.5	61.5	95.5	121.7
Blade Radius [m]	19.5	25.25	44.6	54.32
$C_{p,max}$	0.44	0.44	0.44	0.48
Wake Losses [%]	10	5.55	2.5	1.66
Wind Speed at Hub Height [m/s]	6.6	6.85	7.25	7.45
Turbulence Intensity	0.1	0.1	0.1	0.1
Weibull Shape Factor	2	2	2	2
Weibull Scale Factor [m/s]	7.44	7.73	8.18	8.41
Resulting Capacity Factor	0.25	0.27	0.37	0.39
Visual Inspection [£/Turbine]	2,150	2,150	2,688	2,688
Loads Analysis [£/Turbine]	3,500	3,500	3,500	3,500
Operational Analysis [£/Wind Farm]	59,400	33,000	15,000	10,000

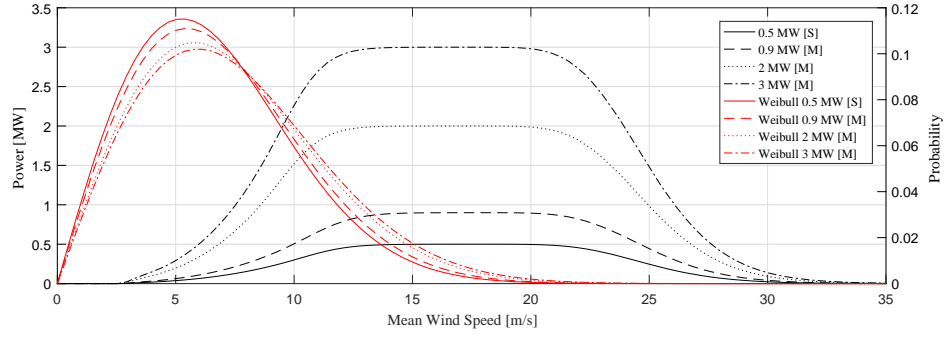


Figure 4.13: Simulated power curve with respect to the 10-minute mean wind speed, $P_{Sim}(v_a)$ on the left axis and wind speed probability distribution, $P_w(v_a)$ on the right axis.

$P_w(v_a)$ the Weibull distribution as a function of the 10-minute mean wind speed, v_a , and $P_{Sim}(v_a)$ the simulated power curve as a function of v_a [145]. The detailed yield modelling methodology of $P_{Sim}(v_a)$ can be accessed in the literature [145] and is further detailed in Section 4.4.1.1.3.

Wake losses depend on multiple factors, such as terrain topology, wind distribution, atmospheric stability, turbine thrust coefficient, C_t , spacing and the array layout [106, 189–191, 217]; however, in this work the wind farm with the most turbines (36 x 500 kW) is assumed to experience a medium wake loss of 10%. Each of the modelled wind farm wake losses are scaled linearly with the number of turbines deployed in the respective wind farm.

Further, all modelled turbine topologies have the same cut-in/out wind speed while the drive train and rotor efficiency is modelled depending on the encountered efficiencies of turbines deployed in between 1997 and 2000. Figure 4.13 illustrates the simulated power curve with respect to the 10-minute mean wind speed (underlying standard distribution) as well as the wind speed probability distribution on the right y-axis for the selected turbine generator classes presented in Table 4.13.

Under the presented modelling parameters, the 0.5 [S], 0.9 [M], 2 [M], and 3 MW [M] turbines achieve a capacity factor of 0.25, 0.27, 0.37, and 0.39 respectively. In addition, Figure 4.14 illustrates the modelled input parameters of all considered turbine types; i.e., hub height (a), mean wind speed (b), and rotor diameter (c) as well as output parameters, i.e., capacity factor (d) and AEP (e) respectively. The turbine model's

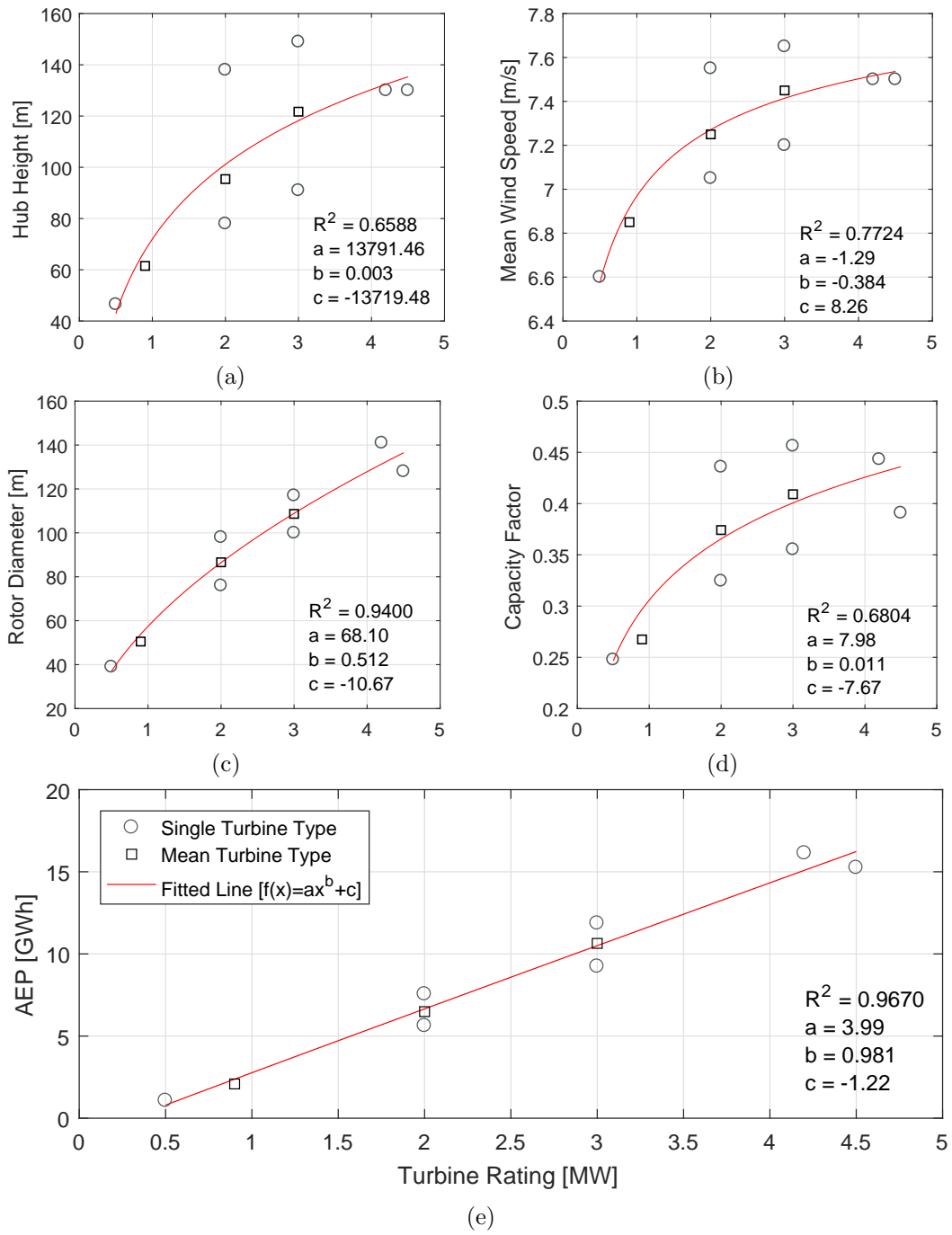


Figure 4.14: Modelled turbine parameters and their compound effect on capacity factor and AEP. The mean wind speed (b) is derived from the wind shear power law based on the modelled hub height (a), while the annual energy production (e) and hence capacity factor (d) is the result of the mean wind speed (b), rotor diameter (c) as well as the Weibull distribution and modelled power curve (Figure 4.13). A square displays an average turbine parameter, whereas a dot indicates encountered min/max parameters.

annual energy production (AEP) was further compared to [163], giving confidence in the model.

4.5.1.2 Expenditure Modelling

It is important to highlight that for the life extended period's $LCOE_2$ estimate, the cost per MWh is dependent on the AEP, OPEX, and lastly by the LTEA's capital expenditure ($CAPEX_{LTE}$) [145]. Since the initial CAPEX is not considered in the published lifetime extension $LCOE_2$ framework as illustrated in Figure 4.8, the derived generation cost is thus independent of an asset's initial investment cost.

With respect to the $CAPEX_{LTE}$, the cost for visual inspection for a multi-MW turbine is assumed 25% more expensive, since the total inspection area is larger. The expenditure for the loads and operational analysis is assumed to scale linearly with the number of turbines; however, economies of scale and clustering individual turbines into cells certainly reduce costs. Since available cost figures of clustering activities are not available and highly site dependent, for ease of analysis, linearity is assumed. The cost for administration of consultants is included in the other LTEA's budgets, while the owner's administration expenditure is not included in the analysis. $CAPEX_{LTE}$ is thus modelled as:

$$CAPEX_{LTE} = Z(c_v + c_l) + c_o + c_a + c_{r,r} \quad (4.16)$$

where c_v is the visual inspection cost per WTG, c_l the loads analysis expenditure per WTG, c_o the operational analysis expenditure, c_a the administration expenditure, and $c_{r,r}$ the cost for necessary repairs and retrofits.

The annual OPEX, $OPEX_n$ is modelled as:

$$OPEX_n = R(C_F + C_I + C_U) + AEP_n C_V \quad (4.17)$$

where R is the asset's rated power, C_F is the fixed operations and maintenance (O&M) expenditure, C_I the insurance cost, C_U the connection and use of system charges, and C_V the variable O&M expenditure. Cost parameters are illustrated in Table 6.3 that are based on a deployment within the UK [145].

Table 4.14: Lifetime extension tool parameters [145]. Optimistic and pessimistic parameters are further presented for the supplement database [219].

Parameter	Central	Range	Unit
CAPEX			
Pre-development	100	30-240	£/kW
Construction costs	1,500	1,100-1,800	£/kW
O&M			
Fixed	30,192	22,644-37,740	£/MW/y
Variable	5.1	3.83-6.38	£/MWh
Insurance	2,226	1,669-2,782	£/MW/y
Connection/system charges	3,810	2,857-4,762	£/MW/y
Other parameters			
Discount rate	10	7.5-12.5	%
CAPEXLTE			
Visual inspection	Table 4.13	±25%	£/WTG
Loads analysis	3,500	2,625-4,375	£/WTG
Operations analysis	Table 4.13	±25%	£/Wind Farm

4.5.1.3 Other Assumptions

In this work inflation in labour expenditure is not considered, whereas decommissioning costs are assumed to be equalised to the turbine’s scrap value. The discount rate is selected at 10%.

4.5.2 Performance Degradation

“Ageing is a fact of life. Its effects are inevitable for all kinds of machinery, reducing the efficiency, output and availability of steam and gas turbines, solar PV modules, batteries and automobiles alike” [157]. Essentially, if ageing effects are observable on a wind turbine, this will naturally impact the overall efficiency, thus reducing the AEP and capacity factor while increasing LCOE as published in the literature [146]. In this thesis, performance degradation is defined as “any impact that has a negative effect on the annual energy production, relative to the optimum operational output at a given inflow condition. Thus, there is no necessity that performance degradation is time dependent or homogeneous over a given period”.

In fact, wind turbine performance degradation has different distinct origins when the actual long-term wind resource is not considered or alternatively, normalised for. On the one hand, there is wear and tear as well as operational errors (e.g. pitch and yaw misalignment), where the degradation process is characterised by a low rate of change. In theory, triggers are numerous; such as, leading edge erosion (LEE), fouling, or deformations reducing aerodynamic efficiency [220, 221], reduced system performance in

Table 4.15: Comparison of available PD identification approaches

Approach	Staffell and Green	Wilkinson
Data source	ROC register	SCADA
Data access	Public	Confidential
Data resolution	Monthly	10 minute (1 second) ¹
Methodology	Wind farm simulation of yield output based on NASA data	Remodelling of power curve from operational data
Complexity	High	Low
Analysis type	Holistic	Specific
Embedded PD sources	Wear and tear, operational errors (pitch and yaw misalignment), curtailment, ancillary services; ² downtime (repairs, maintenance, grid faults, etc.)	Wear and tear, operational errors (pitch and yaw misalignment)
Challenges	Correct for curtailment and ancillary services (identify)	Correct for downtime (identify) ¹
Opportunities	Introduce SCADA or Elexon data	Identify impact of curtailment, downtime, and ancillary services

¹ depends on the system and operational SCADA configuration; ² low impact at present, expected to increase in the future [225]

components along the drive train (low and high speed shaft, gearbox, generator due to inadequate lubrication, bearing failures, or gear teeth detachment), power electronics [222] and auxiliary system [223], etc.

On the other hand, there is turbine downtime and hence reduced availability caused by broken parts, characterised by a high rate of change (failure/sensor activation), where the downtime may lead to a significant reduction in annual energy production.

When dealing with wind turbine performance degradation, there is no defined standard; i.e., what sources of PD are included and what are excluded from consideration. As mentioned previously, studies have aimed to quantify long-term performance degradation with different methodologies such as based on the UK's renewables obligation certificates (ROC) register [157] or a supervisory control and data acquisition (SCADA) system respectively [224]. Naturally, both approaches have advantages and disadvantages while considering a different combination of PD sources in the analysis, as contrasted in Table 4.15.

Namely, Staffell and Green's method is essentially a holistic method that is more complicated in its execution and is impacted by the potential inclusion of a bias due to increasing curtailed periods. The latter that is expected with an increasing total wind energy penetration within a network or sub-network [226].

Whereas Wilkinson’s approach isolates a turbine’s wear and tear as well as operational errors; the method neglects to include a turbine’s downtime that impacts the long-term performance. For example, if components fail and require lengthy sourcing or the installation is restricted by weather conditions (especially offshore) a turbine will not produce power for a certain period [227] that is not necessarily extractable of SCADA data (depends on the system and operational configuration).

Consequently, it is impossible to prefer one method over the other, hence depending on the aimed application of a PD metric, one has to differentiate what sources of PD to include and which to exclude. For example, in terms of revenue and economic calculations the holistic approach appears more sensible to apply, because in this application the long-term annual yield matters that is dependent on wind farm availability, wear and tear, operational errors (yaw and pitch misalignment), as well as curtailment. Arguably, the latter factor is an operational restriction characterised by a network’s local capacity limits with no direct impact on degradation.

Therefore, a sensible modification to the holistic approach would be to isolate and identify the impact of curtailment for a given wind farm or area separately. This is in essence challenging, because ROC data does not contain curtailment information; however, can be overcome if SCADA data is accessible, or alternatively through the purchase of Elexon’s metered generation data [228].

Similarly, for Wilkinson’s approach a downtime registry would be required to introduce the impact of repairs, maintenance, grid faults etc. Also, the recorded curtailment periods can be translated into an AEP loss over time caused by de-rating. Consequently, for both methodologies access to more detailed operational data can thus aim to identify and categorise the impact of the different identified sources of performance degradation. Knowledge on the isolated impact of different PD sources can thus help users to apply suitable PD metrics depending on the type of analysis.

With regards to available performance degradation metrics, published data varies with a recorded linear annual degradation of 0.2% as published by Wilkinson [224] with a limited dataset of the first 6 operational years while Staffell and Green’s UK fleet approach observed a linear annual performance degradation of 1.6%. As highlighted

by Rubert et al. [146], LCOE for the design lifetime can thus increase by up to 12.62% based on a simple model, which impact is significant and under such circumstances, essential to take into consideration.

In terms of implementing long-term performance degradation parameters into the presented economic model, two 18 MW wind farms (20 x 0.9 MW and 9 x 2 MW presented in Section 2.1) were subjected to a varying linear, annual PD. The modelled annual energy production, subjected to performance degradation is thus as follows:

$$AEP_{n,\gamma} = AEP(1 - \frac{\gamma}{100})^n \quad (4.18)$$

where γ is the annual degradation factor [%] ranging from 0-2, and n is the year.

Overall, the aim was to analyse the impact of PD on LCOE and LCOE₂ and further evaluate if results are projectable on upscaled turbines; i.e., if the cost percentage impact of PD is comparable to greater scale WTG. Concerning the latter, as identified by Bolinger and Wiser, CAPEX undergoes cyclical variations [229] and turbines within the region of 1-3 MW have comparatively equal CAPEX/MW variations [230]. Further, sub 1 MW as well as above 3 MW substantial cost differences can be observed, although comparatively little project data was analysed. Since 900 kW is at the top of the sub 1 MW classification it is financially considered as a 1 MW turbine, hence CAPEX expenditure is comparable to a 2 MW turbine allowing a comparison of LCOE.

4.5.3 Results

4.5.3.1 Upscaling

Figure 4.15 presents LCOE₂ estimates for an 18 MW wind farm consisting of different turbine size classifications for a 5-year lifetime extension period (no repairs, reconditioning or retrofits required). In addition, data was fitted to an exponential function in the form of $f(x) = ax^b + c$ scoring an R^2 goodness of fit of 0.85 for the cost estimate and roughly 0.69 for the contingency estimate respectively. Both goodness of fit indicators illustrate the great variance within turbine classes (some turbines have comparatively upscaled rotors, presumably for low wind speed regimes), hence the exponential fit and

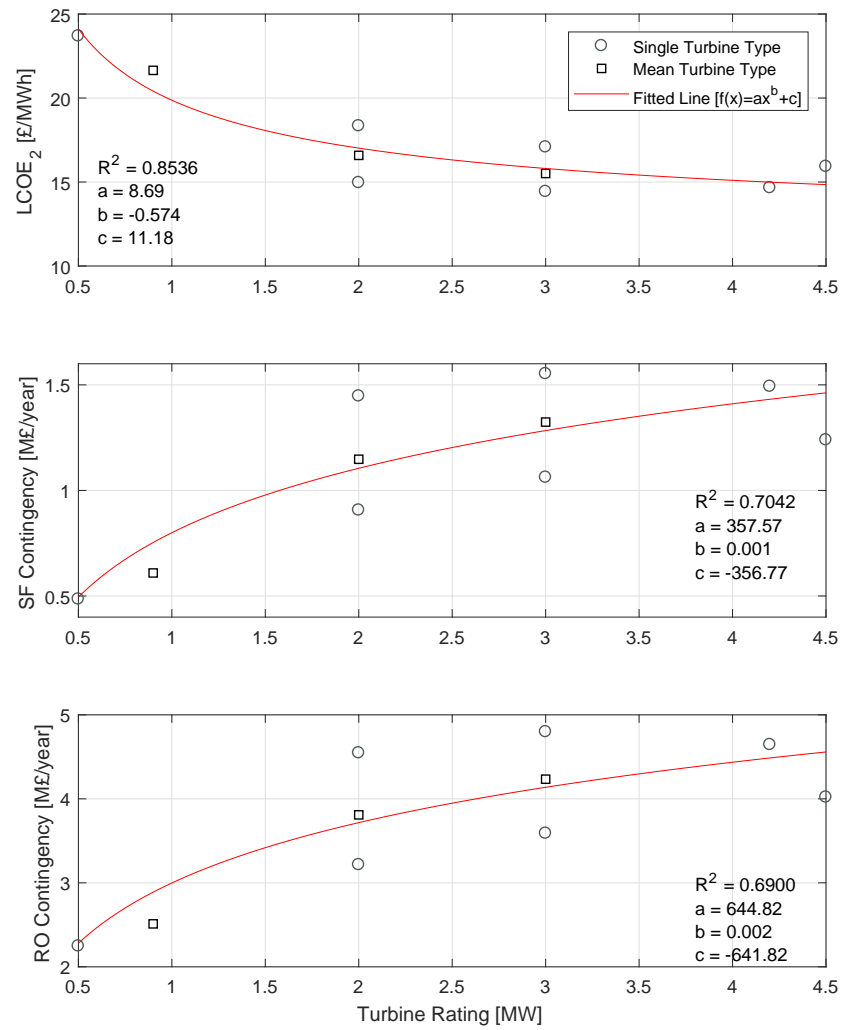


Figure 4.15: LCOE₂ +5 years upscaling results. This analysis is CAPEX independent. Subsidy-free (SF)/Renewable Obligation (RO).

findings require caution in their application.

Findings reveal that cost reductions are most prominent within the sub-2 MW class, with the rate of change (slope of the function) reducing above. In detail, a wind farm consisting of 36 x 0.5 MW rated turbines paired with a lifetime extension strategy of 5 years can achieve $LCOE_2$ of around £23.69/MWh. The generation cost reduces to £16.59/MWh for a 2 MW turbine class, whereas a 3 MW turbine class results in $LCOE_2$ of £15.51/MWh. Within the 4 MW range there are fewer turbines commercially available; however, the Enercon E-141 with a rating of 4.2 MW (a significantly upscaled rotor diameter in this class) scores the lowest price per unit energy; i.e., £14.64/MWh. The contingency parameter defines the maximum available budget to spend on unexpected repairs and retrofits along the lifetime extension period in order to deliver a specified operating profit [145]. In the applied model this is implemented by a defined maximum cost of energy threshold. The threshold is set in order to achieve a profit of £7.25/MWh⁵, thus for the subsidy-free scenario the threshold is set £7.25 below the average day-ahead spot-market electricity price of the past 5 years [206]. For the renewable obligation (RO), the threshold is set £7.25 below the RO revenue stream defined by the 2017-2018 buy-out price and day ahead spot-market electricity price [206, 207]. The applied threshold is therefore £36.24/MWh for the subsidy-free environment and £81.82 for the RO respectively. Equally to the $LCOE_2$ results, the available annual contingency within the RO and subsidy-free framework increases with a significant rate of change below 2 MW, with an observable subsequent slowdown (Figure 4.15 centre and bottom graph). Besides an increase in contingency, fewer turbines are deployed, resulting in a substantial increase of available contingency per turbine.

4.5.3.2 Performance degradation

Figure 4.16 presents the impact of PD on the economics of lifetime extension for a wind farm consisting of 20 x 0.9 MW WTGs. The figure's x-axis represents an increasing PD corresponding to a percentage drop in AEP with the top graph presenting the impact in percent on the $LCOE_2$ metric on the left y-axis (solid line) for different life extension

⁵This is derived from an assumed ROI of 20% based on a CAPEX of £1.6 million for a 20 year design lifetime, thus a profit of £16,000/MW/Year.

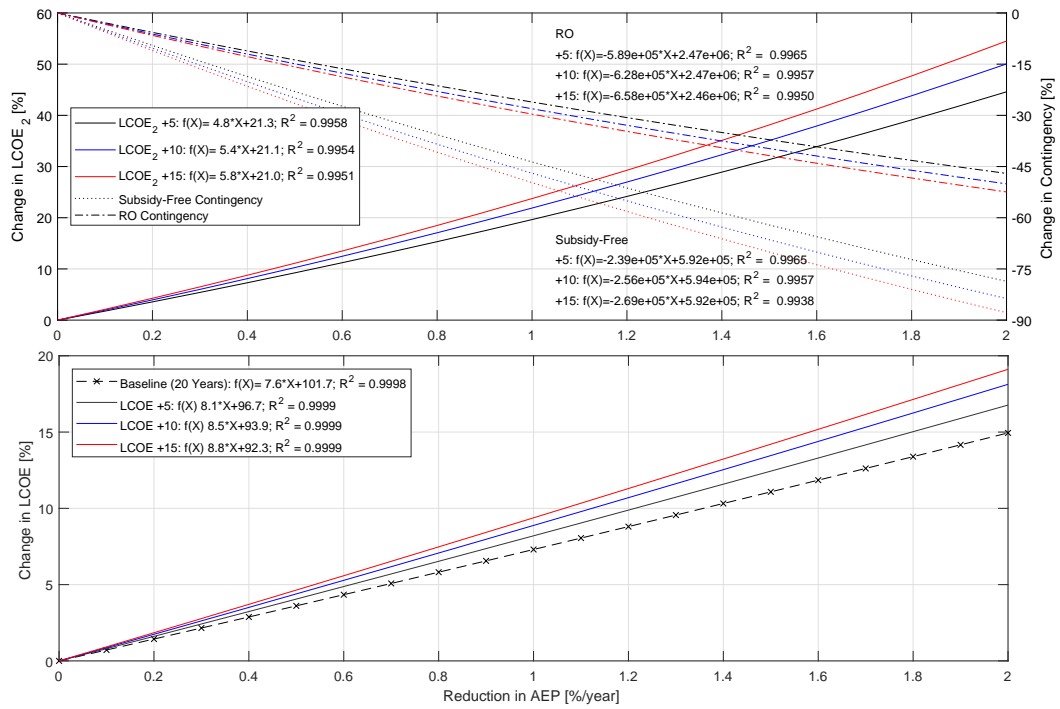


Figure 4.16: Impact of PD on an 18 MW wind farm consisting of 20 x 900 kW WTGs (LCOE applies CAPEX assumption).

scenarios. A lifetime extension of 5 years is marked in black, of 10 years in blue, and of 15 years in red. In addition, the top graph presents the impact in percent on the available annual contingency under the RO (dashed line) and subsidy-free environment (dotted line) on the right y-axis. The bottom graph presents the impact of PD on LCOE for the design life of an asset (dashed black line with marker) and design life plus lifetime extension (solid line).

Concerning the latter economic metric, as argued by Rubert et al. [145], the inclusion of design life on a lifetime extension cost metric is advised against (severe discounting, asset is written off, and CAPEX dependency). Nevertheless, for the purpose of integrity results are presented. Overall, findings are further fitted to a linear function to interpolate results.

First of all, based on the applied methodology a reduction in AEP reduces yield and variable OPEX. Therefore, both effects counter-balance each other to a certain degree. However, there is a greater impact on yield, increasing the cost of energy and therefore

Table 4.16: Comparison of the impact of PD on LCOE and LCOE₂ of a 0.9 MW versus a 2 MW WTG in %.

Turbine Rating [MW]	Annual PD [%]	LCOE Baseline	LCOE +5	LCOE +10	LCOE +15	LCOE ₂ +5	LCOE ₂ +10	LCOE ₂ +15
0.9	0.2	1	2	2	2	4	4	4
2	0.2	1	2	2	2	3	4	4
0.9	1.6	12	13	14	15	34	38	41
2	1.6	12	13	14	15	31	35	38

reducing the annual contingency. Second, the impact of PD on the 20-year design lifetime is in agreement with findings from the simple analysis executed by Rubert et al. [146] with an increase of LCOE of 11.8% (1.4%) if an annual PD of 1.6% (0.2%) is encountered. Third, a comparison of the impact of PD reveals a much greater sensitivity of the LCOE₂ methodology (top graph) than the non-advised LCOE approach (bottom graph). In detail, results indicate that an annual PD of 1.6% (0.2%) elevates LCOE₂ by 34-41% (3.6-4.3%) contrary to the LCOE metric with an increase of around 13-15% (1.6-1.8%).

With regards to the impact on the available contingency of the aimed lifetime extension period, findings also reveal a significant impact. Overall, an annual PD of 1% reduces the available RO contingency by 28%, whereas in the subsidy-free environment a reduction of 47% is observed.

In addition to Figure 4.16, Figure 4.17 of the Appendix presents the impact of PD on an 18 MW wind farm consisting of 9 x 2 MW rated turbines. Findings are further contrasted in terms of the percentage impact on i) cost of energy in Table 4.16 and ii) contingency in Table 4.17. Results reveal a comparable impact with regards to LCOE and LCOE₂ modelling, whereas minor impact differences are observable for the RO contingency estimates. Substantial differences are observable for the subsidy-free contingency. This is due to the fact that the baseline contingency for the 900 kW turbine is substantially lower than the 2 MW's, relatively to both RO cases.

4.5.4 Discussion and Future Work

This work's results are aimed at an asset's design life of 20 years, albeit a great share of WTG installations are nowadays designed for 25 or even 30 years of operation [231]. In

Table 4.17: Comparison of the impact of PD on annual contingency of a 0.9 MW versus a 2 MW WTG in %.

Turbine Rating [MW]	Annual PD [%]	SF +5	SF +10	SF +15	RO +5	RO +10	RO +15
0.9	0.2	-10	-10	-11	-6	-6	-7
2	0.2	-7	-8	-8	-5	-6	-6
0.9	1.6	-66	-70	-74	-39	-42	-44
2	1.6	-49	-52	-55	-36	-39	-41

such instances, upscaling $LCOE_2$ results are still valid since the LTE period is considered as a separate investment case at the end of design lifetime. Further application is however limited as modelling PD, or any conventional LCOE calculation is dependent on the design life, hence the suggested model requires modification. Therefore, LCOE and PD results are only valid for a 20 year design lifetime while $LCOE_2$ estimates are generically applicable.

Overall, the proposed upscaling and PD methodology works well if no component replacement is required. However, in deviating scenarios with component reconditioning or retrofitting, it is challenging to model turbine spare part expenditure (part of the LTEA). This is because an ex works CAPEX distribution as well as CAPEX per installed MW may not develop homogeneously with upscaling (there is evidence that the CAPEX/MW has equal price fluctuations in between 1-3 MW turbines as discussed in Section 2.2). Therefore, due diligence is required in CAPEX modelling. In addition, component replacement installation expenditure requires scrutiny as well, since greater rated cranes are necessary with substantially higher mobilisation and daily rates. This can be further explored in order to model asset specific requirements. Nevertheless, it is expected that operators and owners will approach LTE from a more strategic point of view (+10-15 years vs. +5 years), especially for greater rated WTGs (2–3 MW) with greater budgets to spend for the LTEA (including component replacements). Given the difficulty in modelling component replacements, the available contingency may be applied to compare the necessary expenditure to the set budget.

Further, modelling PD in combination with component replacement, draws challenges to predict yield improvements (e.g., replacement of eroded blades), besides the ability to identify root causes of performance degradation down to a component level in the

first place. To take this further, a turbine drive train has many components, hence sources of PD can vary greatly as highlighted in Section 4.5.2. Second the impact of PD may or may not be significant nor quantifiable from turbine data (reduction of 0.2% annually [224]); i.e., an annual degradation of less than 1% appears impossible to account to a specific component's output. Nevertheless research activities are executed such as for leading edge erosion by Offshore Renewable Energy Catapult (OREC) whose results suggest that the AEP can be increased by 1.5-2% following a moderate blade erosion repair [232].

With respect to the presented upscaling results, overall the methodology is applied irrespectively of differences in turbine design, hence the power coefficient with respect to the wind speed, $C_p(v)$ might deviate. In addition, a site's environmental conditions can vary significantly impacting the LCOE assessment besides modelling inaccuracies; e.g., due to the application of the log-law above 100 m height. While is it impractical to present the depth of possible modelling combinations, attached to this work is a database allowing users to identify i) baseline LCOE, ii) baseline + lifetime extension LCOE, as well as iii) the advised LCOE₂ estimate for different lifetime extension scenarios (+5-15 years) under varying input parameters. The latter includes to vary i) the turbine rating, ii) the turbine and site parameters (mean wind speed, $C_{p,max}$, turbulence intensity, and Weibull shape factor), and iii) the cost scenario (central, optimistic, and pessimistic – Table 6.3). The tool is accessible in [219].

The UL 4143 lifetime extension standard “Outline of Investigation for Wind Turbine Generator - Life Time Extension (LTE)” [197,233] states that individual turbines within a wind farm can be clustered into cells for the LTEA. Naturally, clustering activities decrease the CAPEX_{LTE} of the load and operational analysis as well as administration per turbine. Clustering may or may not be applicable, depending on the site's external and operational conditions, as well as the applied aero elastic simulation model. In addition, the LTEA is dependent on local standards and regulations driving the cost; e.g., in Germany aero-elastic simulations are required whereas in Denmark inspections are sufficient [144]. Therefore, modelled CAPEX_{LTE} that are presented in Table 4.13 may deviate significantly and may not be comparable to countries outside the UK.

Nevertheless, sensitivities are also modelled and adjustable in the cost scenario tool attached to this work (Table 6.3 of the Appendix).

With regards to the lifetime extension period, the set contingency threshold depends on an owner's or operator's operational framework as well as aimed profit margin. Further, the threshold definition is likely dependent on economies of scale; i.e., for greater rated turbines, a lower profit margin per MWh may be acceptable, based on a relatively greater AEP [MWh/MW] (Figure 4.14e). As a consequence, due diligence is required to evaluate a suitable threshold for a lifetime extended site.

While this work's model applies an annual linear PD, in reality fluctuations in the rate of change are likely to be observed. Future work, could aim to identify the impact of the different sources of PD over time (Table 4.15) and model a case study accordingly. Based on general industrial feedback summarised by Ziegler et al. [144] as well as discussions with operators in the field, we are of the opinion that performance degradation is likely to impact a turbine at a later stage of life than at the beginning (warranty and performance based maintenance contracts are often in place to maintain a specified availability [146]). We further think that an average fleet degradation parameter will be somewhere in between 0.2-1.6 [%/year]. Although, we believe on average, PD lies within the lower band of the given spectrum if the impact of curtailment is identified and compensated for. This is also in agreement with recent findings from Olauson et al. [234], concluding a lifetime energy loss of 6%, which according to this work's model corresponds to an annual PD of 0.6% over a 20-year design life. Lastly, the degree of performance degradation is highly dependent on an asset's O&M procedures, thus well maintained turbines are likely less impacted by degradation processes.

4.5.5 Section Conclusions

This work aims to give an overview of the impact of upscaling and PD on the economics of lifetime extension. Results presented are derived from a model with limitations, hence its application requires careful evaluation if actual conditions are comparable to the applied model input. If input data differs significantly, it is possible to replicate the tool and adapt changes according to an asset's unique requirements as this model

is limited to central case assumptions. Nevertheless, to overcome this limitation, a tool is provided allowing users to adjust selected input parameters.

In summary, this work serves as a continuation of an economic lifetime extension decision support tool [145], in order to serve the need to understand the impact of upscaling and PD as well as a combination of both on an asset. Turbine owners and operators can take these findings into consideration when subjecting a wind farm to an economic LTEA, or replicate the tool if input data differs significantly.

4.5.6 Section Appendix

As a supplement to this work, a database is published allowing users to adjust any combination of i) the turbine rating, ii) turbine and site parameters (mean wind speed, $C_{p,max}$, turbulence intensity, and Weibull shape factor), and iii) the cost scenario (central, optimistic, and pessimistic) [219].

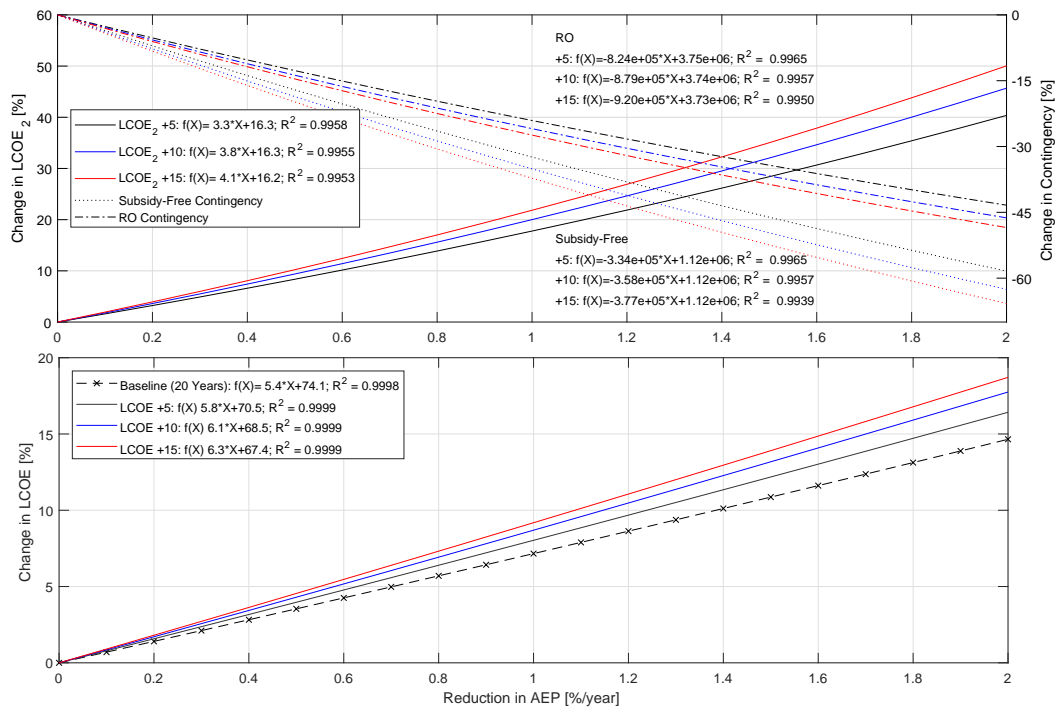


Figure 4.17: Impact of PD on an 18 MW wind farm consisting of 9 x 2 MW WTGs (LCOE applies CAPEX assumption).

4.6 Lifetime Extension - The Case of BVG Associates

In this work, the developed academic lifetime extension methodology illustrated in Section 4.4 is applied in a real life application in which BVG Associates disclosed all operational data of two onshore wind assets that reach their end of design life in 2020 in the UK. The case studies explore the potential to extend both assets' lifetime by a minimum of 7 years under varying economic parameters. While the wind farm *Site A* appears to be commercially feasible when looking at increasing the operational lifetime, the site *Site B* appears critical and decommissioning is advised after the end of design lifetime. Assuming that both wind farms are operated by the same owner, it can further be explored to use *Site B*'s healthy turbine spare parts to either store or straight away replace critical or worn-out components at *Site A* in order to reduce the cost of replacements and thus levelised cost of energy. Due to confidentiality, input data cannot be shared, thus the provided data in Table 4.18 is not disclosed.

4.6.1 Introduction

Lifetime extension of wind farms is becoming more and more attractive; however, when operating a wind farm at the end of lifetime careful consideration of input parameters is necessary to derive a suitable lifetime extension strategy. In addition, the required lifetime extension capital expenditure ($CAPEX_{LTE}$) depends on asset specific regulations as explored in this work. Overall, the work presupposes sufficient technical remaining useful lifetime for continued operation and focuses on deriving the economic business case.

4.6.2 Methodology

The lifetime extension decision-making methodology is schematically illustrated in Figure 6.8, where the lifetime extension period is treated as a separate investment and calculated based upon levelised cost of energy ($LCOE_2$). To calculate $LCOE_2$, the net present value (NPV) of costs is divided by the NPV of the annual energy production

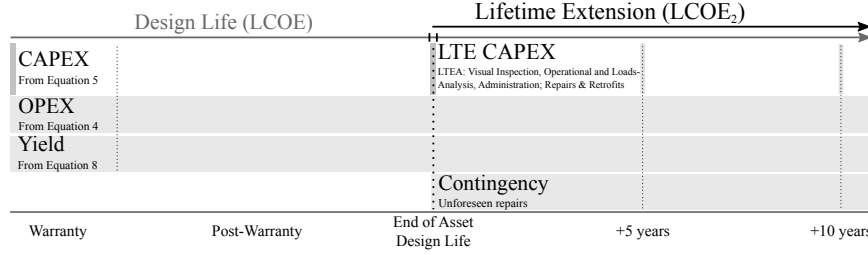


Figure 4.18: Lifetime extension decision methodology [145].

(AEP):

$$LCOE_2 = \frac{NPV_{costs}}{NPE} = \frac{C_0 + L_0 + \sum_{n=1}^T \frac{F_n + O_n + V_n}{(1+d)^n}}{\sum_{n=1}^T \frac{E_n}{(1+d)^n}} \quad (4.19)$$

where NPE is the net present energy, C_0 the equity capital expenditure of component replacements ($CAPEX_{Replace,E}$), L_0 the lifetime extension capital expenditure ($CAPEX_{LTE}$), n is the time period after the design lifetime, T the final year of operation (end of extended lifetime), F_n the constant annuity payment of the component replacement's expenditure debt in period n ($CAPEX_{Replace,D}$), O_n the fixed operating cost including decommissioning⁶ in period n , V_n the variable operating cost in period n , E_n the energy generated in period n , and d the discount rate. This extended lifetime methodology is equipped with operational data in terms of cost and yield parameters. The prior includes the CAPEX LTE and operational and maintenance (O&M) expenditure and the latter identified through operational knowledge or alternatively, the application of a Weibull wind distribution in combination with a turbine's power curve [106]. Of course all variables are ideally based upon the operational design lifetime and may be adjusted depending on; e.g., failure and reliability data.

With respect to the available contingency C_n , the $LCOE_2$ of Equation 4.19 is replaced by a defined maximum threshold cost (TH) and the equation is iteratively solved by varying C_n until $LCOE_2$ matches the TH:

⁶onshore it is expected that the scrap value equalises decommissioning costs; offshore this is certainly not the case

$$TH = \frac{C_0 + L_0 + \sum_{n=1}^T \frac{F_n + O_n + V_n + C_n}{(1+d)^n}}{\sum_{n=1}^T \frac{E_n}{(1+d)^n}}. \quad (4.20)$$

4.6.3 Case Studies

In this work, two wind farms (*Site B* and *Site A*) are considered that are characterised by the same turbine type and total rated power. A detailed overview of both asset's operational data is illustrated in Table 4.18. Although the sites are fairly similar, the main difference is that *Site B* wind farm has severe operational constraints, i.e., curtailment due to noise restrictions (40% of gross yield), whereas *Site A* experiences average losses due to grid constraints, outages, wake impacts of approximately 5%. For both wind farms, a renewed environmental impact assessment (EIA) is expected to be necessary, thus planning extension costs are budgeted. For the *Site B* wind farm there is further a planning risk contingency budgeted as the local neighborhood is likely to oppose any lifetime extension permit.

Assuming that the foundation and tower are able to facilitate the target lifetime extension period, components along the drive train may require replacement. This is budgeted as $CAPEX_{SPARE,D}$ and $CAPEX_{SPARE,E}$ with a 70/30% debt-equity split, the latter budgeted as a constant annuity with the interest rate set as 3.5% [235]. Time assumptions for the necessary crane service team for component replacements were evaluated and agree with modeled data [145]. The operational cost data, $CAPEX_{LTE}$, and component replacement costs are further modeled with a standard deviation of $\pm 10\%$ for the pessimistic and optimistic scenario respectively. This serves, if expected costs are above or below the estimate. Due to *Site A*'s and *Site B*'s unique position of being eligible for 7 additional years of continuous ROC support until 2027, any modeling will be subjected to an initial subsidised and subsequently subsidy free period [236].

4.6.4 Results

4.6.4.1 Site A

As the wind resource may vary over the years as well as within one wind farm, the $LCOE_2$ results are presented based on a varying annual energy production (AEP).

Table 4.18: Wind farm operational parameters. Operational, CAPEX_{LTE}, and component replacement expenditure is further subjected to a $\pm 10\%$ variation.

Wind Farm	Site B	Site A
Turbine information		
Rated power [MW]		
Turbine model		
Number of turbines in wind farm		
Baseline operational period	20	20
Operational expenditure		
Extended period [y]	5–15	5–15
Variable costs [£/MWh]		
Fixed costs [£/MW/y]		
Insurance [£/MW/y]		
Connection & system charges [£/MW/y]		
Total O&M expenditure [£/MW/y]		
Expected yield		
Yield - Gross [MWh/WTG/y]		
Losses curtailment [MWh/WTG/y]		
Losses excl. curtailment [MWh/WTG/y]		
Yield - Nett [MWh/WTG/y]		
Mean wind speed at hub height [m/s]		
CAPEX_{LTE}		
Visual inspection [£/WTG]		
Operational analysis [£/WTG]		
Loads analysis [£/WTG]		
Planning extension [£/WTG]		
Planning extension risk [£/WTG]		
Legals extension [£/WTG]		
Consultancy [£/WTG]		
Administration [£/WTG]		
Other items		
Discount rate [%]		
Commercial threshold		
Subsidy-free Revenue [£/MWh]		
RO Revenue [£/MWh]		
Component replacement (total)		
Gearbox [£/WTG]		
Generator [£/WTG]		
Blades [£/WTG]		

Each scenario's results are presented based on three graphs; one graph illustrating the $LCOE_2$ based on no reconditioning and the exchange of the entire drive train, one graph with a single component exchange (gearbox, generator, blades), and one final graphs for any combination of drive train component exchange. Any component replacement is scheduled at the end of design lifetime in year 20. In addition a table of the remaining annual contingency of all scenarios is presented.

Figure 4.19 presents the $LCOE_2$ of no reconditioning as well as the replacement of the entire drive train, Figure 4.22 when exchanging a single drive train component, and in Figure 4.25 when reconditioning any two drive train components. The results are further compared to the expected revenue stream threshold (TH) of (i) the renewable obligation (RO), and (ii) the subsidy-free sport market.

If no component replacement is necessary, the $LCOE_2$ for continued operation is £43 with a significant contingency of £66,644 based on the RO revenue stream as illustrated in Table 4.19.

A single component replacement appears feasible only under the continued RO subsidy, scoring a remaining contingency of £57,538, £56,683, £36,740 for the generator, gearbox, and blades exchange respectively as illustrated in Table 4.19.

A double component replacement also appears feasible; however, in all considered cases, the remaining contingency is £28,063 for an exchange of blades and gearbox, £28,918 for the exchange of blades and generator, and finally £48,860 for the exchange of the gearbox and generator.

If the entire drive train were to exchanged, this would be feasible with a contingency of £20,240, though this contingency is quite low and if encountered with a mean AEP below 1.5 GWh economic feasibility is not met.

After 2027, if the remaining useful lifetime (RUL) of the wind turbine is sufficient, the turbine appears suitable to continue to operate as exemplified in the $LCOE_2$ of £42,94 of no retrofit. Actually, the $LCOE_2$ would be lower as the cost for the EIA, loads and operational analysis are already budgeted in the first 7 additional years of operation. In the period above 7 additional years, if any kind of replacement is necessary, turbine decommissioning is advised.

4.6.4.2 Site B

Findings of *Site B* are presented in Figure 4.20 to 4.26 and Table 4.20, in identical form to the previous case study. First of all, the continued operation in a subsidy free environment does not meet the defined TH, hence decommissioning would be advised. Since the wind farm is also eligible for 7 additional years of RO subsidies, the operation would only be profitable if no additional expenses occur; however, the remaining annual contingency of £4,572 suggests a high risk exposure with limited funds to cover any eventualities.

Having experienced significant opposition at *Site B* from neighbours, it is likely that any lifetime extension process may be opposed which is further budgeted as a risk contingency of £28,571 shifting the results negatively. In other words, the project would not meet commercial success under the RO as indicated in Figure 4.21 to 4.27 and Table 4.21. An extension period is thus not advised from a commercial point of view.

4.6.5 Section Conclusions

This work scrutinised the commercial evaluation of *Site A* and *Site B* wind farm under varying economic parameters. The operator of both wind farms is advised to continue operation of *Site A* and decommission *Site B* at the end of design lifetime. Further, it is suggested to sacrifice *Site B*'s spare parts to store or exchange replacement components at *Site A*. This would further reduce elaborated $LCOE_2$ of the replacement scenarios as the component costs are significantly less, because only the component dismantling costs are necessary (crane and service personnel).

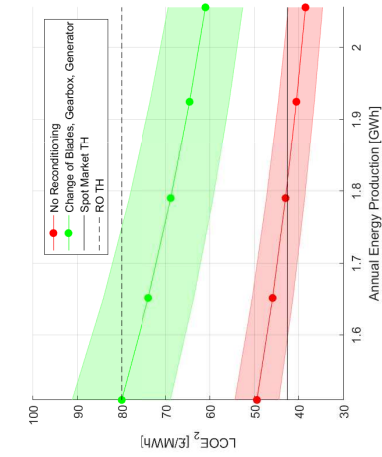


Figure 4.19: *Site A* LCOE₂ of no recon- ditioning and drive train exchange based on 7 years of additional life.

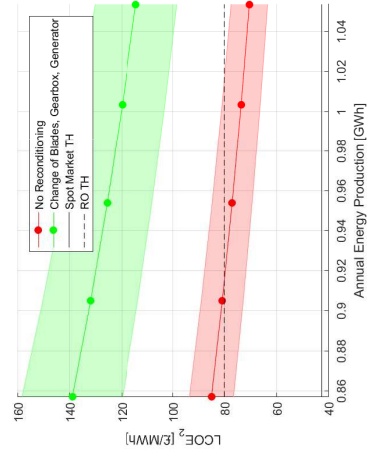


Figure 4.20: *Site B* LCOE₂ of no recon- ditioning and drive train exchange based on 7 years of additional life.

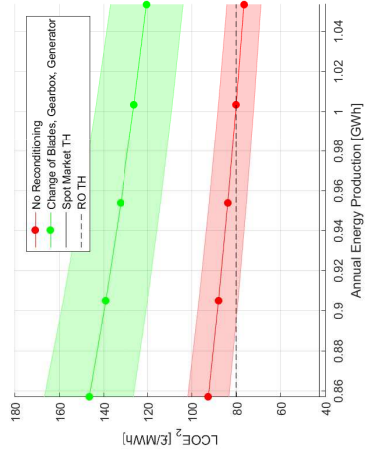


Figure 4.21: *Site B* with risk LCOE₂ of no reconditioning and drive train ex- change based on 7 years of additional life with risk contingency.

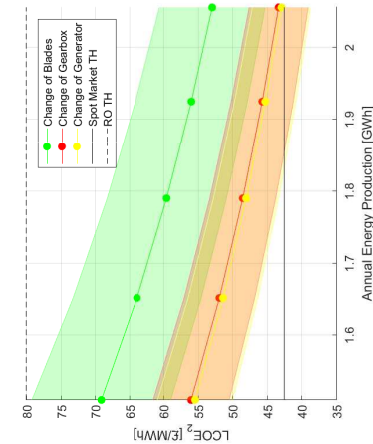


Figure 4.22: *Site A* LCOE₂ of single component replacement (+7 years).

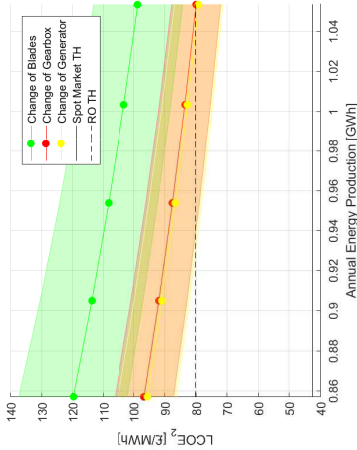


Figure 4.23: *Site B* LCOE₂ of single component replacement (+7 years).

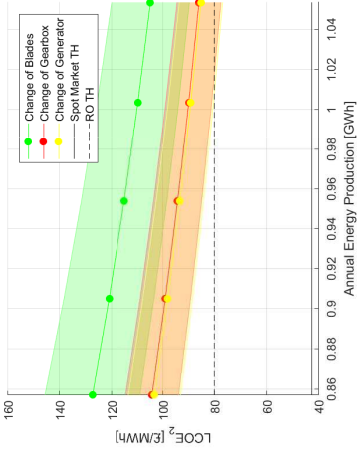


Figure 4.24: *Site B* with risk LCOE₂ of single component replacement (+7 years) with risk contingency.

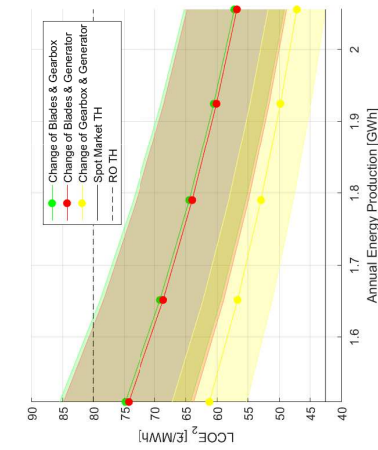


Figure 4.25: *Site A* LCOE₂ of double component replacement (+7 years).

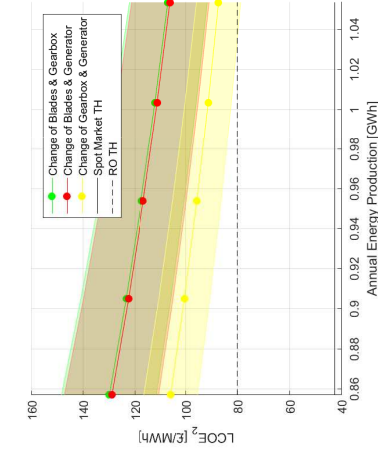


Figure 4.26: *Site B* LCOE₂ of double component replacement (+7 years).

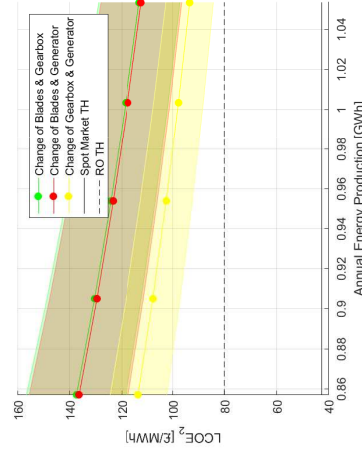


Figure 4.27: *Site B* with risk LCOE₂ of double component replacement (+7 years) with risk contingency.

Table 4.19: Site A annual contingency of 7 additional years under RO based on mean AEP of 1.78 GWh.

Type of Replacement	Contingency [£]
None	66,644
Blades	36,740
Gearbox	56,683
Generator	57,538
Blades, Gearbox, & Generator	20,240
Blades & Gearbox	28,063
Blades & Generator	28,918
Gearbox & Generator	48,860

Table 4.20: Site B annual contingency of 7 additional years under RO based on mean AEP of 0.95 GWh. N/A: costs are higher than the set threshold.

Type of Replacement	Contingency [£]
None	4,572
Blades	N/A
Gearbox	N/A
Generator	N/A
Blades, Gearbox, & Generator	N/A
Blades & Gearbox	N/A
Blades & Generator	N/A
Gearbox & Generator	N/A

Table 4.21: Site B with risk annual contingency of 7 additional years under RO based on mean AEP of 0.95 GWh with risk contingency. N/A: costs are higher than the set threshold.

Type of Replacement	Contingency [£]
None	N/A
Blades	N/A
Gearbox	N/A
Generator	N/A
Blades, Gearbox, & Generator	N/A
Blades & Gearbox	N/A
Blades & Generator	N/A
Gearbox & Generator	N/A

Chapter 5

Structural Health Monitoring of Wind Turbine Structures

Having established a framework for the economic lifetime extension decision-making, a great importance is to determine the structural integrity in order to define the technical lifetime extension feasibility. For this reason, this Chapter is aimed at structural health monitoring purposes of tower and foundation components. The latter that may also be applied to reconsider foundation design assumptions in order to support the reuse of foundations for greater rated turbines, the application of less raw materials or in general design optimisation. As such, this Chapter is subdivided into 4 sections. Section 5.1 presents the aimed sensor for the field trial and the fatigue testing of the transducer's characteristics. This is followed by the processes aimed at improving the sensor in Section 5.2. The foundation field trial and sensor monitoring results are presented in Section 5.3. Lastly, the testing of a new sensor design variant is presented in Section 5.4.

5.1 Characterisation of metal-packaged fibre Bragg gratings under fatigue loading

5.1.1 Sensor Design

Advantages of the application of optical fibres equipped with FBGs are summarised in Table 3.2. No commercially available solution seems to exist that can be used directly or can be adapted for condition monitoring of reinforced concrete structures. Some commercial solutions employing FBGs are available, offered for example by Micron Optics [237]; however, the key disadvantages of these sensors are their inadequate form factor, which make them incompatible with steel rebars (as the sensors are designed for mounting on flat surfaces) and their high cost. Also, other sensor types, including wireless surface acoustic wave (SAW) transducers have previously been tested by the research team at Strathclyde, demonstrating limited performance. Therefore, the proposed metal-packed sensors are the preferred choice for this application as they offer considerable robustness, relative ease of deployment, small size, multiplexibility and relatively low cost [86].

Initially there were two available temperature sensor designs as schematically illustrated in Figure 5.1a-b; a metal-packaged temperature sensor incorporating a brazed kovar capillary and steel shim (Figure 5.1a), and an epoxy bonded design (Figure 5.1b). In the case of the brazed kovar capillary and steel shim temperature sensor, silver alloy seals both ends of a kovar capillary (ID 2.3 mm, OD 1.6 mm, L 25 mm) with an FBG sitting inside. The epoxy based temperature sensor consists of two copper tubes that are sealed with epoxy and filled with thermal grease. In order to improve robustness and performance of the temperature sensor by eliminating the requirement to apply epoxy as a bonding agent, a new temperature sensor design was proposed. This also involves the kovar capillary which is further protected by a soldered copper tube and an optional soldered shim. This allows the sensor to be spot welded to a metal surface resulting in a more robust design that is immune to external impacts. This design is further illustrated in the bottom of Figure 5.1. Such a robust construction is essential to withstand

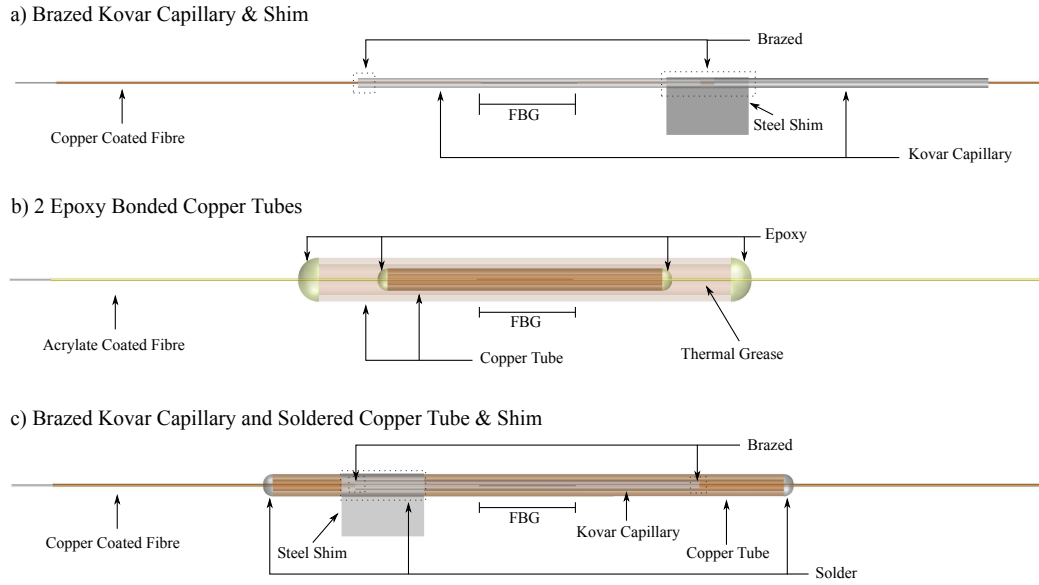


Figure 5.1: Schematic Overview of FBG Temperature Sensors

concrete pouring and compaction using pneumatic shakers that may induce stresses in the vicinity of the sensor, potentially resulting in changing the sensor sensitivity or even permanently damaging the sensor. Therefore, having a protective layer is a key requirement. Two concurrent sensor variants for measuring strain were considered sharing the same geometry as illustrated in Figure 5.2. The sensor comprises an FBG inscribed in copper coated fibre that is enclosed in a kovar capillary and equipped with two metal shims to allow attachment to a weldable structure. The second sensor variant involves an FBG that is prestressed before capillaries are joined during the brazing process. The reason for this is that, although for concrete structures compression forces are assumed to be mostly absorbed by concrete, in reality compression forces are still experienced by the steel. Therefore, in order to prevent internal buckling of the sensor fibre, prestress is applied as an alternative design option.

The temperature sensors vary in length from 20 to 32 mm. The strain sensor is longer, with a total length of approximately 47 mm, because a third kovar capillary is required. Including the dimension of the steel shim, the spot weldable sensors are approximately 8.5 mm in width, whereas the epoxy bonded temperature sensor's width is 1.6 mm. These dimensions are flexible though hence, depending on requirements, the parameters

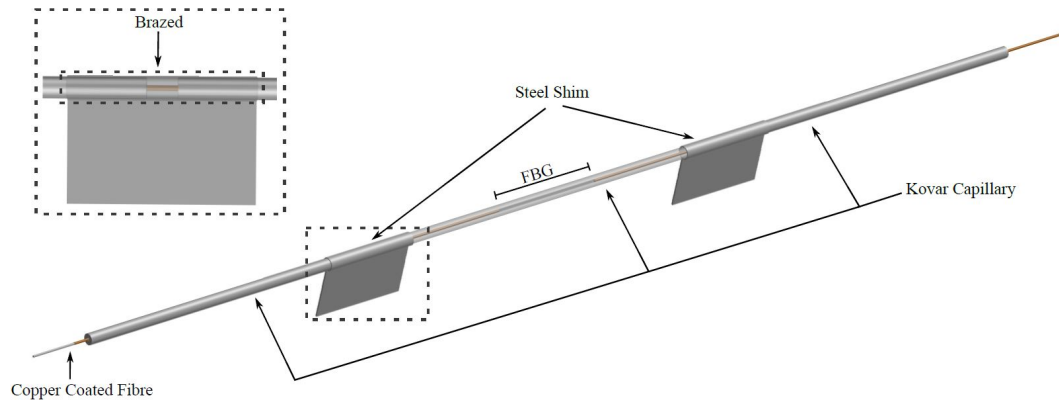


Figure 5.2: Schematic Overview of Strain Sensor

can deviate to for example reduce the total length of the sensor.

5.1.2 Sensor Fabrication

The layout for the sensor manufacture is illustrated in Figure 5.3. The commercially sourced metal coated optical fibre comprises standard single mode glass fibre ($\varnothing 125 \mu\text{m}$) coated in copper ($\varnothing 170 \mu\text{m}$) and equipped with an FBG of the length of 7 mm, written in a 10-15 mm stripped fibre section. The FBG is placed inside a kovar capillary (ID $200 \mu\text{m}$; OD $700 \mu\text{m}$) and sealed at both ends with a silver brazing alloy (melting point: $610\text{-}850^\circ\text{C}$). During brazing, high frequency current (200-300 A, 400 kHz) is passed through the induction heating coil for a total duration of 30 s. Thus, temperatures of $610\text{-}620^\circ\text{C}$ are reached within the bonded parts, sufficient to melt the brazing alloy. With this set-up the curie point of kovar (430°C) is exploited, thus protecting the FBG placed inside the kovar capillary from excessive thermal stress that could potentially cause the grating to erase¹. Overall, approximately 50% of reflected FBG intensity is lost throughout this heating process, which is acceptable from the point of view of peak detection by the optoelectronic sensor interrogation system.

The actual process of prestressing the fibre is labour intensive and technically challenging as the fibre requires prestressing without damaging the gripped fibre section. It is therefore of interest whether actual prestress adds further benefits; i.e., if prestress-

¹The physical mechanisms of thermal stability of FBGs can be found in open literature; i.e., [238]

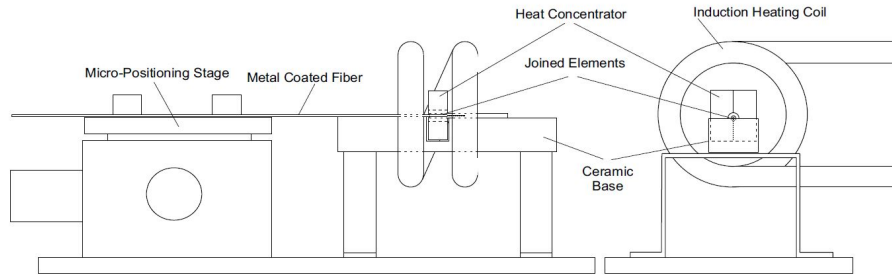


Figure 5.3: Layout of Sensor Manufacture [60]

ing the sensor will actually improve compression resistance and also if compressive forces will reach critical buckling levels, which is the subject of this investigation. One disadvantage of applying prestress is that relaxation and creep due to constant mechanical stress could cause the sensor to change its behaviour over time. However, since temperatures in the turbine application are expected to remain far below 40% of the solder melting point (the generally accepted threshold for the onset of creep [239]), it is expected that the effects of creep will be minimal. Nevertheless, this needs to be investigated as part of a further stage of a fatigue analysis.

5.1.2.1 Methodology

Before evaluation of thermal coefficients of temperature and strain sensors, each design was assembled and the centre wavelength of the FBG reflection peak was recorded to gain knowledge about the behaviour of prestressed and non-prestressed sensors during fabrication. FBGs with centre wavelengths, λ_B , at around 1550 nm were inscribed into copper coated fibre. During the brazing process the FBGs were interrogated with a Micron Optics sm125-500 interrogator at a sampling rate of 2 samples per second (S/s).

5.1.2.2 Results of Brazing Monitoring

For both sensor designs (prestressed and non-prestressed) the wavelength response during the first brazing process exhibits an equal reaction; i.e., due to induced thermal stress the wavelength increased by around 4.5 nm due to thermo-optic effect within the grating and gradually reduced back to the initial wavelength at the process start. Fig-

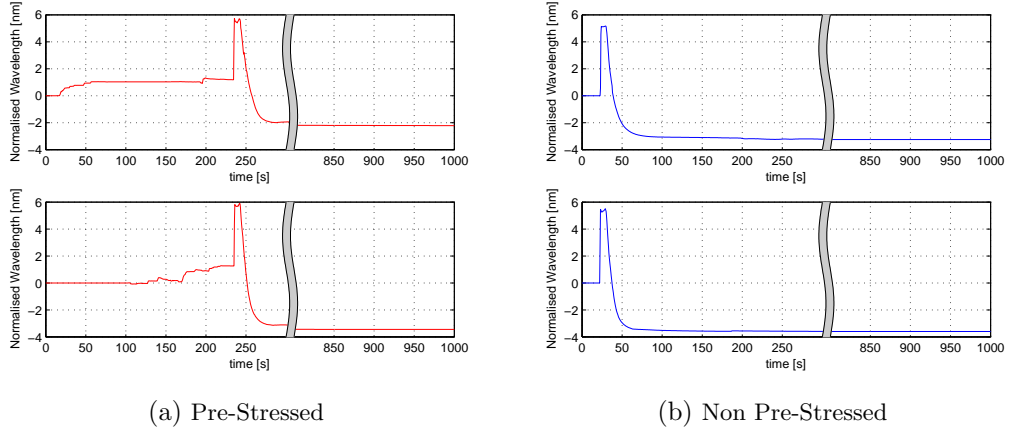


Figure 5.4: Shift in FBG centre wavelength during brazing of second capillary end

Figure 5.4 presents the FBG centre wavelength of the second brazing process (to realise the sealing of the second end of the capillaries) for the two strain sensor designs. As illustrated, the second brazing process results in equal shifts of the centre wavelength for both sensor designs. This is not intuitive since one sensor was prestressed by 1 nm and hence it was expected that the final wavelength shift should have been reduced by the equivalent amount. Table 5.1 further displays the change in λ_B of the FBG from the start of the brazing process to the end. As mentioned earlier both sensor designs show an equal reaction; i.e., eventually reaching a compressed state.

The wavelength spectrum has been monitored in order to evaluate if the sensor's readings are impacted by the formation of side lobes. However, as exemplified in Figure A.4 of the Appendix, the spectrum does not suggest this, hence it appears that the process eventually results in fibre compression in both cases. One possible explanation of this counterintuitive result is that the fibre softens during brazing to the point that the initially applied stress in the fibre is reduced significantly or removed altogether due to a rapid annealing of glass. According to Kalli et al. [240] annealing of silica glass can occur even at relatively low temperatures of around 100 °C.

Table 5.1: Second Brazing Process - Wavelength Shift

Sensor	Type	Delta Start/End [nm]
STRAIN 1	Pre-Stressed	-2.25
STRAIN 2	Pre-Stressed	-3.44
STRAIN 3	Non Pre-Stressed	-3.25
STRAIN 4	Non Pre-Stressed	-2.65
STRAIN 5	Non Pre-Stressed	-3.60

5.1.3 Thermal Characterisation and Calibration

5.1.3.1 Sensor Characterisation and Calibration

As presented in Table 3.2, the FBGs reaction to thermal as well as mechanical stress is characterised by a linear response making it mathematically simple to use. However, for the considered sensor designs, it is further of interest to characterise their behaviour under the influence of thermal stress to evaluate what design delivers the most reliable performance based on such indicators as sensitivity (wavelength change per °C) and repeatability. This is important in order to be able to isolate mechanical strain from $\Delta\lambda_B$ (recapture Section 3.3.1: Equation 3.4 and 3.11).

As indicated in Table 3.2 the spectral shift in temperature is significantly smaller than the strain induced shift in civil engineering applications which places a demand on the interrogator resolution and accuracy. It is important to ensure reliable temperature readings to be able to provide accurate temperature compensation even though foundations are usually buried and thus internal temperatures change at a low rate as the soil and concrete act as a thermal insulator.

5.1.3.1.1 Methodology

In this test the sensors were placed in a Carbolite PN 60 oven and gradually heated from 25 °C to 65 °C, with measuring points every 10 °C, and then cooled in a similar fashion. In order to improve accuracy of the reference temperature reading, the oven was equipped with a Pico SE012 temperature probe with an accuracy of 0.03 °C.

Temperature reference data was read by a Pico high accuracy data logger and manually saved every 4 hours at the given settling point together with each sensors reflected wavelength that was monitored by a Micron Optics sm125-500 interrogator. Eight sensors in total were thermally cycled:

- two brazed kovar capillary and shim temperature sensors (Figure 5.1a)
- two epoxy bonded temperature sensors (Figure 5.1b)
- one brazed kovar capillary with soldered copper tube and shim temperature sensor (Figure 5.1c)
- two pre-stressed and one non pre-stressed strain sensor (Figure 5.2)

Based on findings from McKeeman [65], all sensors were simultaneously calibrated in three temperature cycles.

5.1.3.1.2 Results

The FBG centre wavelength shifts with temperature are presented in Figure 5.5 for the epoxy bonded temperature sensors, in Figure 5.6 for the metal-packaged temperature sensors, and in Figure 5.7 for the metal-packaged pre-stressed and non-pre-stressed strain sensors. Data points for each thermal cycle are fitted to a linear function and normalised by subtraction of the y-intercept in order to allow a graphical comparison of the slope of each sensor that represents temperature sensitivity. Measurement results are further detailed at 65 °C showing in red each heating cycle and in blue each cooling cycle. Also, to gauge the closeness of the data points to the fitted regression line, in general terms indicating the quality of the measurement process, the r-squared value for each linear fit is given as well as the exact slope that represents the change in wavelength in nm per °C.

Overall one can see that the epoxy bonded temperature sensors significantly change their behaviour after the first heating cycle and for the first entire cycle (heating and cooling) it appears that the heating response differs from the cooling response (Figure 5.5a). This is observed for both epoxy bonded temperature sensors, although eventually

heating and cooling show a similar response after two cycles. The observed differences in response of the two epoxy bonded temperature sensors are caused by the small difference in sensor lengths and the positioning of bonding locations and also, to a lesser extent, due to a different amount of thermal grease used. For the metal-packaged temperature sensors, in the case of the brazed kovar capillary and shim construction, the first heating cycle deviates before stabilising with a relatively constant slope (Figure 5.6a-b). In comparison to the epoxy bonded copper temperature sensors, sensitivity to temperature fluctuation is greater which is counterintuitive since copper has a greater thermal expansion coefficient than kovar. It appears that much of the actual expansion of the copper must be compensated by the presence of epoxy in the design.

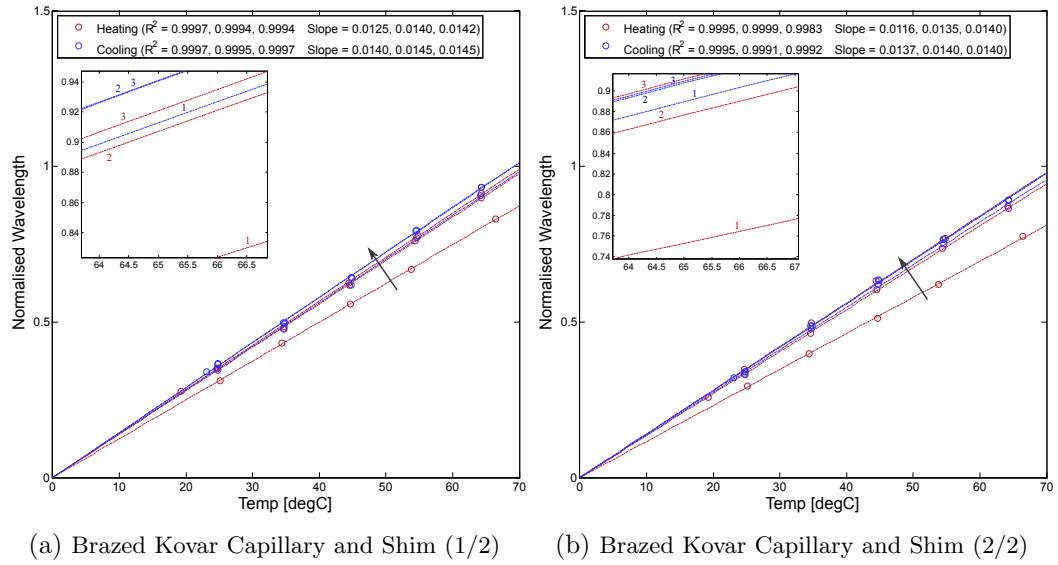


Figure 5.5: Characteristics of the epoxy bonded temperature sensors thermally cycled three times. The characteristics are normalised by subtraction of the y-intercept.

On the contrary the temperature sensor based around the metal-packaged brazed kovar capillary with soldered copper tube and shim (Figure 5.6c) responds in a repeatable fashion from the first cycle, although this design has the lowest sensitivity. It appears that within this sensor the fibre at the end of the FBG where the kovar capillary ends must have broken during fabrication and therefore its temperature sensitivity of 10.3 pm per °C is equal to the response of an unstrained FBG, hence purely due to the thermo-optic effect. This was confirmed by the fact that this sensor could only be interrogated

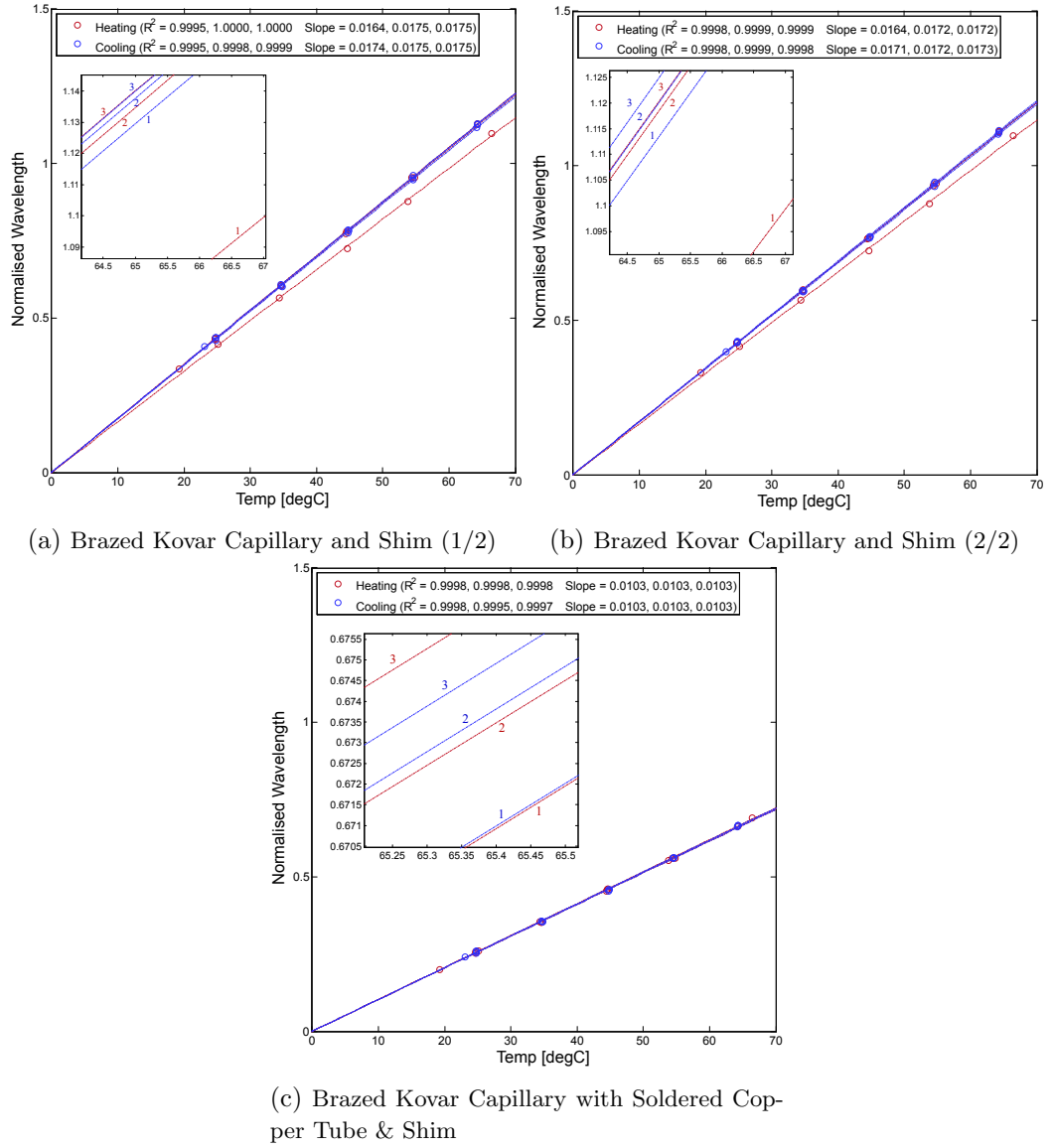


Figure 5.6: Characteristics of the metal packaged temperature sensors thermally cycled three times. The characteristics are normalised by subtraction of the y-intercept.

from one side, indicating that the fibre leading to the FBG on the other side broke during fabrication. Even though, under these circumstances, the sensor demonstrates an outstanding performance as a temperature sensor, because the FBG is completely shielded from the mechanical interaction with the capillary, this transducer would be impractical as it can only be addressed from one side, preventing multiplexing. Another test was scheduled to evaluate exactly the same set-up to determine the response

while ensuring integrity of the fibre. With regards to the temperature sensors based on two epoxy bonded copper tubes, performance has been inferior in comparison with the fully metallic construction, with the response to heating and cooling being different. In addition, the observed shift is much greater for the epoxy bonded design than in the metal-packaged temperature sensors. It should be noted that one sensor performed marginally better than the other.

The metal-packaged strain sensors exhibited comparable results to the brazed kovar capillary and shim temperature sensors as both sensor types have a very similar construction. In more detail, initial heating response differs from subsequent behaviour (probably caused by relief of internal friction triggered by the brazing process), where the non-prestressed sensor demonstrates a significant change in response, contrary to its counterpart, as exemplified in Figure 5.7c. However, following the first cycle, both strain sensor designs demonstrate similar responses, although the non-prestressed sensor is slightly less sensitive (shows a lower slope) as illustrated by a comparison of the graphs in Figure 5.7a-b with that in Figure 5.7c. Based on findings from the temperature cycles (Figures 5.5-5.7), evidence suggests that the metal-packaged temperature sensors are superior in terms of repeatability than the competing epoxy bonded temperature sensor design.

Since temperature sensors can potentially be embedded within the interrogation cable, it is not necessary to spot weld them to the reinforcement bar. This enables an easier as well as quicker installation and the ability to fully characterise the sensor within the laboratory. On the downside, axial mechanical stresses along the cable within the foundation can possibly induce strain and thus corrupt temperature measurement readings. Therefore, double capillary temperature sensors were subjected to axial stress. Findings reveal that the epoxy bonded temperature sensors transmit mechanical stress to the FBG, whereas the brazed kovar capillary with soldered copper tube fully isolates the FBG from axial stress. As mentioned before, the latter is broken at one end, hence in this case the test was repeated to verify this result as illustrated in Section 5.2.2. With regard to the strain sensors, at this stage it was yet unknown whether prestress-

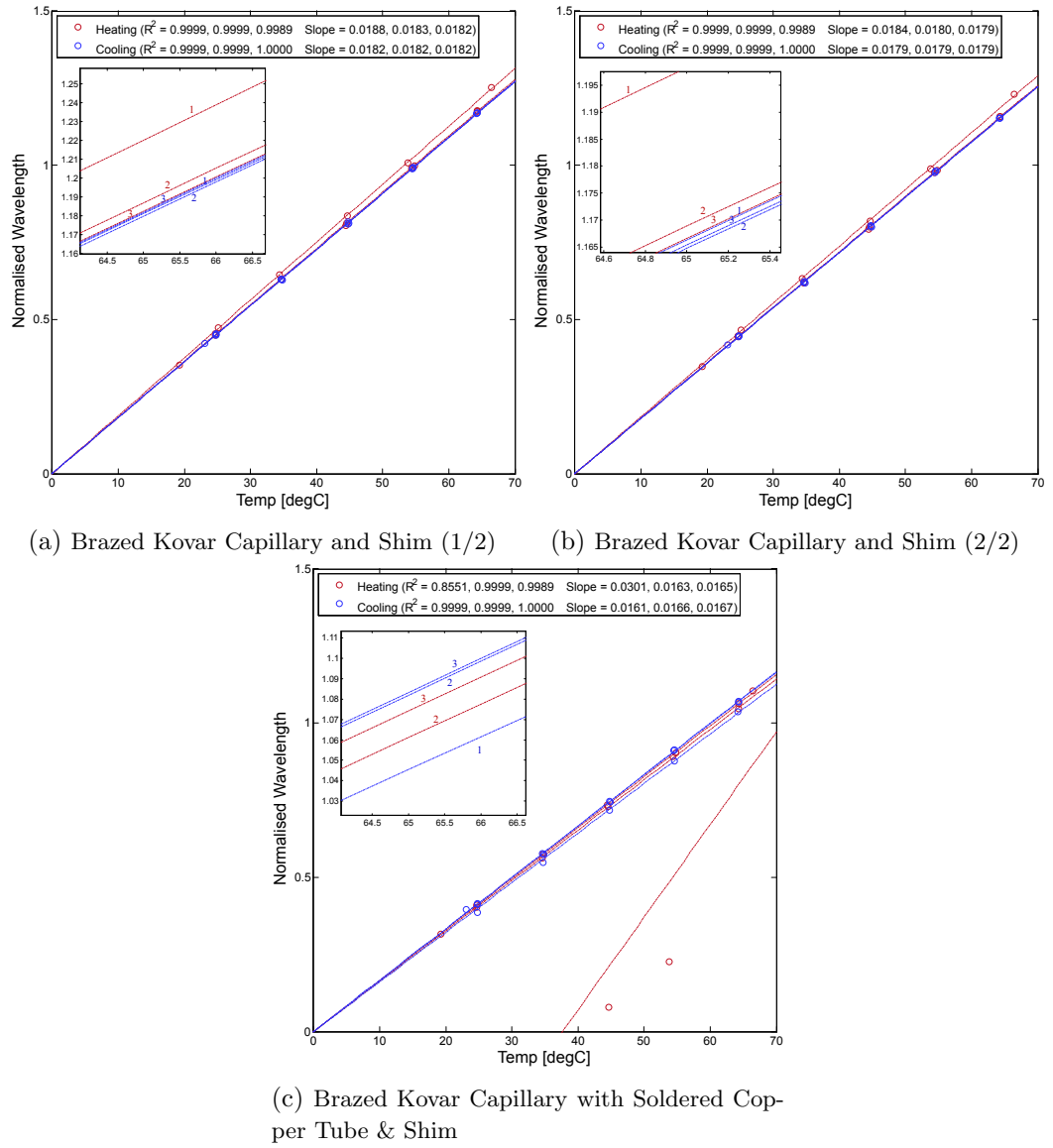


Figure 5.7: Characteristics of the metal packaged strain sensors thermally cycled three times. The characteristics are normalised by subtraction of the y-intercept.

ing the sensor does result in superior sensor characteristics for the intended application (foundation condition monitoring). As the sensors are subsequently characterised under thermal stress when attached to a B500B reinforcement bar with a diameter of 20 mm (as encountered in civil engineering applications), the superior temperature sensors (metal-packaged) and both strain sensor designs were selected in order to further evaluate their thermal behaviour.

5.1.3.2 Calibration of Sensors Attached to Reinforcement Bar

One steel reinforcement bar (B500B; 20 mm) as shown in Figure 5.27 was instrumented with sensors spot welded onto its surface. The spot welding was performed using a 30-J energy setting of the spot welding unit. One side was instrumented with the prestressed strain sensor combined with the brazed capillary and shim temperature sensor (Figure 5.27a) and 180 degrees apart, the non prestressed strain sensor and the brazed capillary with soldered copper tube and shim temperature sensor (Figure 5.27b). The steel rod is characterised by a significantly higher thermal expansion coefficient (10^{-5} per $^{\circ}\text{C}$) than kovar (5.86×10^{-6} in between 25 to 100 $^{\circ}\text{C}$) and due to its high stiffness (large diameter in comparison with the sensor), it is expected to overcome the thermal expansion of the kovar capillary of the strain sensors, defining their new thermal response. However, it should be noted that the temperature sensors are spot welded at one end only, and thus are expected to be unaffected by the thermal expansion of the rebar. Therefore, it is important to repeat thermal cycling of the strain sensors now attached to the rebar in order to determine their new temperature response. This is necessary in order to be able to later isolate strain measurements by processing out the change in wavelength due to temperature as demonstrated by Equation 3.11. The results are presented in Figure 5.9 for both temperature sensors (brazed capillary and shim temperature sensor and the brazed capillary with soldered copper tube and shim) and in Figure 5.10 for both strain sensors (prestressed and non-prestressed). As expected, both temperature sensors demonstrate the same responses as before hence, as intended, they can be used to determine the local temperature in order to provide temperature compensation for the strain sensors. Both strain sensors have now become more sensitive to temperature changes due to the added expansion of steel. In practice, it will not be practicable to perform temperature characterisation of the sensors spot-welded in the field. Therefore, an approximate value of the coefficient of thermal expansion (CTE) will have to be used in future, with the allowance for some systematic error. Detailed error analysis will be carried out in the form of (i) lab temperature sensitivity tests and (ii) temperature compensation coefficients, although it is expected that due to the relatively small changes in temperature due to the large



(a) Pre-Stressed Strain Sensor & Brazed Capillary and Shim



(b) Non Pre-Stressed Strain Sensor & Brazed Capillary with Soldered Copper Tube and Shim

Figure 5.8: Sensors attached to Reinforcement Bar

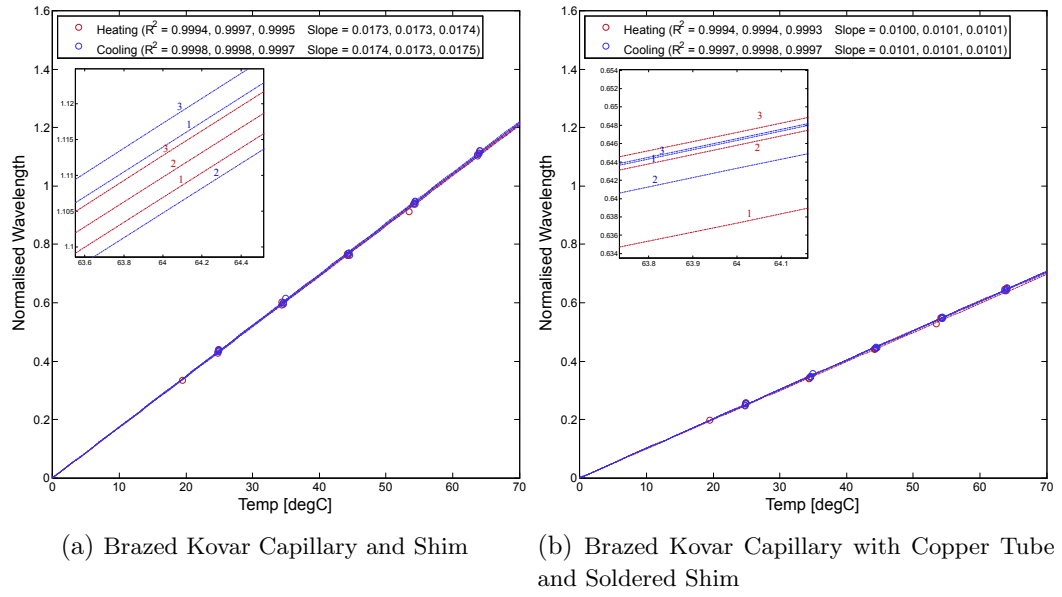


Figure 5.9: Characteristics of the temperature sensors attached to reinforcement bar cycled three times. The characteristics are normalised by subtraction of the y-intercept.

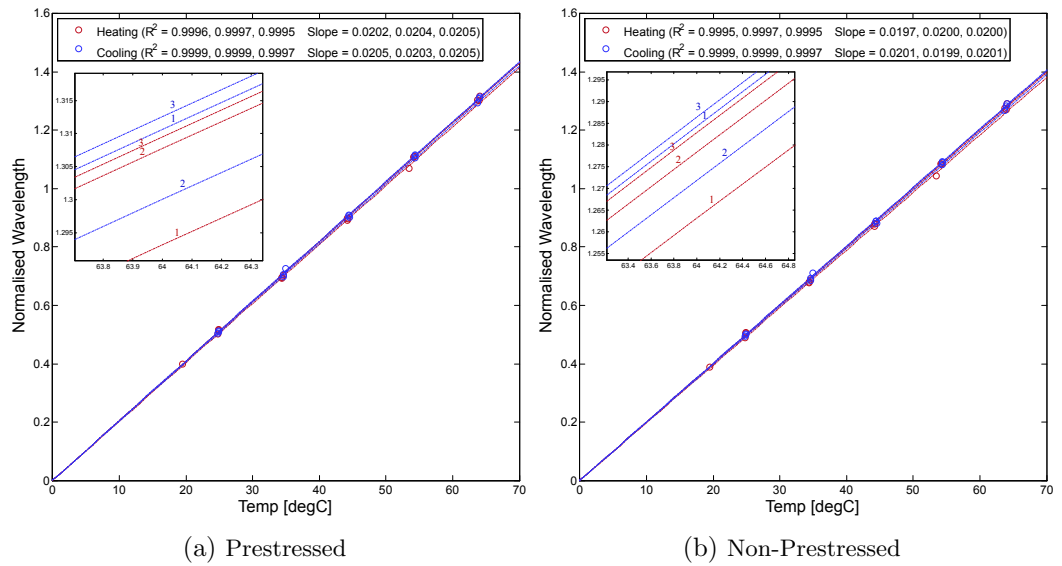


Figure 5.10: Characteristics of the strain sensors and reinforcement bar cycled three times. The characteristics are normalised by subtraction of the y-intercept.

thermal inertia of the foundation, the effect of the temperature measurement inaccuracy on strain measurement will be minimal. At this time, however, the sensors were able to be characterised in order to compensate for temperature induced strain. In the

next section the reinforcement bars, with two sets of sensors attached are cycled under fatigue loading in order to evaluate whether they undergo any structural changes that could influence the accuracy of strain measurement. The epoxy bonded temperature sensors were dismissed along the course of the testing as their repeatability was worse than the metal-packaged temperature sensor and additionally mechanical axial strain was transferred.

5.1.4 Fatigue Experiment

This section presents the results of fatigue tests carried out on the sensors characterised thermally in Section 5.3.3.3. For this set of experiments the reinforcement bar with attached sensors was cycled under axial fatigue loading in an Instron 8802 servo-hydraulic machine as illustrated in Figure 5.11.

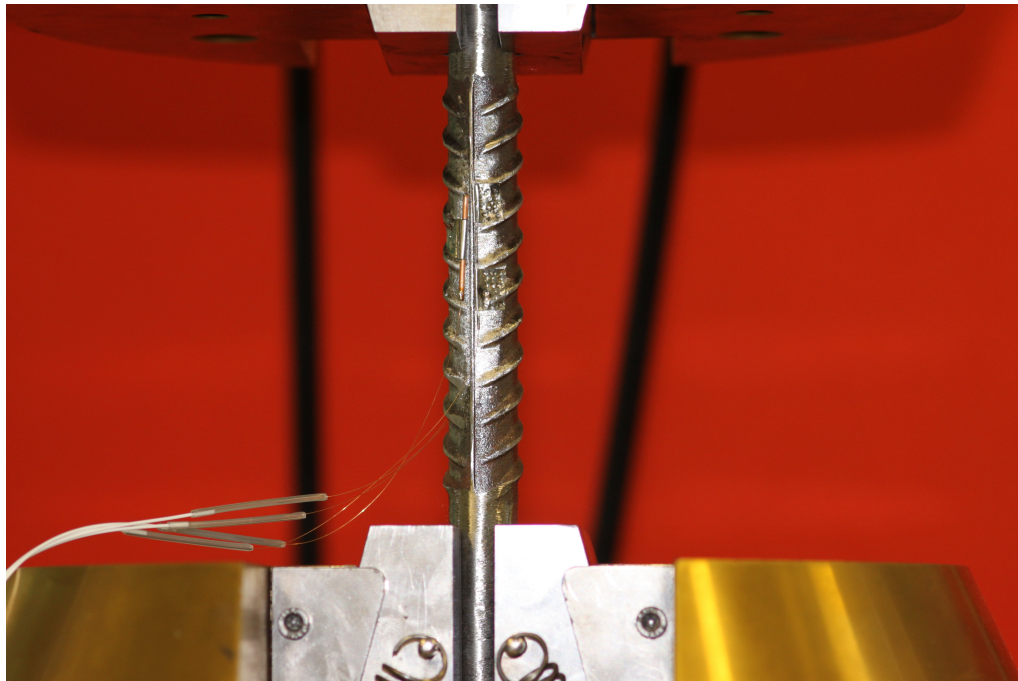


Figure 5.11: Instron 8802 Rebar & Sensor Fatigue Test

5.1.4.1 Methodology

Foundations are subjected to static gravity loading as well as dynamic (fatigue) loading. Dynamic loading within wind turbines is the ultimate structural fatigue example, with the number of cycles in the region of 10^8 to 10^9 over a turbine's lifetime, where large-scale turbines are placed at the lower end as the angular velocity reduces with increasing rotor diameter [68]. The amount of total cycles during a wind turbine's lifetime is much greater than for example in aerospace or automotive applications [121]. Therefore, it is of paramount importance to ensure that the sensors, which will measure the parameters of the foundation from which its structural health can be ascertained, are able to themselves withstand such great number of loading cycles, reliably and accurately sensing over the foundation lifetime. Furthermore, it is important to discover any potential design limitations through repeated loading in the laboratory setting. Finally, as strain transfer from the structure to the sensor is imperfect due to several bonded interlayers as illustrated in Figure 5.2, testing is required to establish the strain transfer coefficient (STC) and also understand its variance from sensor to sensor. Some theoretical investigations concerning strain transfer are included in the following references [57–59, 63]. In the first test the machine force was selected to vary sinusoidally from positive 31.4 kN to negative 31.4 kN (stress ratio $R^2 = -1$; fully reversed), corresponding to ± 100 MPa of stress or ± 0.5 me of strain at a frequency of 10 Hz, with the set loading amplitude as expected to be encountered in wind turbine foundations through FEM modelling [86]. During severe compression the sample could potentially buckle; however, based on the Euler Buckling formula the critical buckling force P_c can be approximated:

$$P_c = \frac{\pi^2 EI}{L_e^2} \quad (5.1)$$

where E is the Young's modulus, I the second moment of area, and L_e the effective sample length that depends on how the sample is gripped (in this case both ends are fixed thus L_e is half of the sample length L) [241]. With this it was determined that the applied compression load is significantly less than P_c . The machine data (force

²Ratio of minimum stress to maximum stress in one cycle of loading in a fatigue test. Tensile stresses are considered positive and compressive stresses negative

and displacement) was recorded with a frequency of 1 kHz, whereas the sensors were interrogated with a Smart Fibres - SmartScan unit at a frequency of 250 Hz, resulting in 25 points per period. This was sufficient to be able to faithfully reproduce the estimated sinusoidal output waveform. After completion of 10^6 cycles the test was stopped.

5.1.4.2 Results

5.1.4.2.1 Fatigue Results

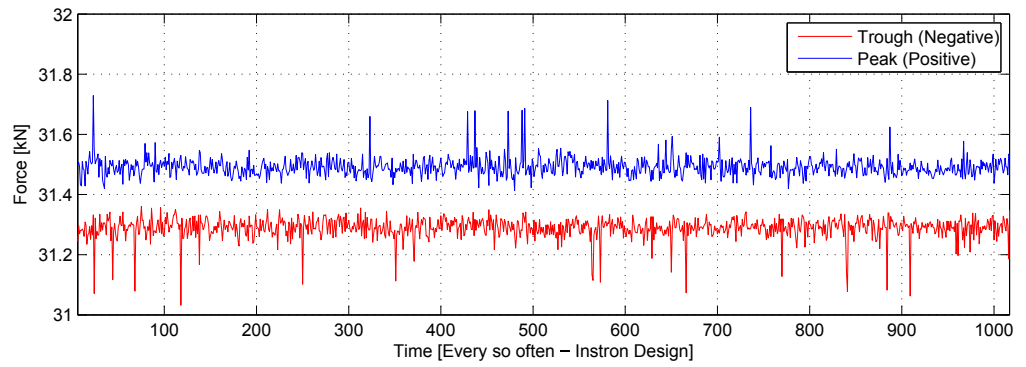
The results of this test are presented in Figure 5.12. The top graph shows amplitude readings from the applied machine force, the middle graph compares the normalised force and normalised strain readings from the prestressed strain sensor and, lastly, the bottom graph displays readings from both prestressed and non-prestressed sensors that were cut into 59 s segments and analysed using a fast Fourier transform (FFT), where the peak magnitude at 10 Hz was re-transformed into the amplitude (time domain) and plotted for each minute-window up to one million cycles.

The x-axis in Figure 5.12c represents the number of cycles to illustrate the sensor behaviour as it undergoes fatigue aging. From the top graph it is possible to evaluate how consistent the force application by the machine is. Data is initially recorded every period, then every tenth, hundredth, thousandth and, finally, every 5000th period, with each absolute periods peak and trough values plotted. The force is applied by the machine with the resolution of ± 0.1 kN, which is in agreement with the force data records illustrated in Figure 5.12a, with the exception of some occasional outliers that breach this threshold, nevertheless remaining within $\pm 1\%$ of the total applied force. Peak values compared to the trough values are higher, since the rebar is gripped with an initial offset under tension of around 0.2 kN. Based on the monitored machine output, the force input to the reinforcement bar appears constant over time.

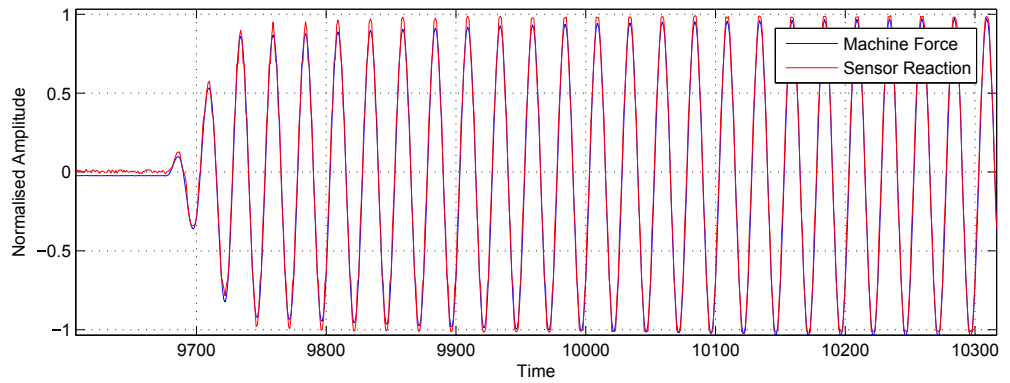
In Figure 5.12b the machine force and sensor data is normalised with respect to its maximum value for the considered length of 23 periods, cross-correlated in Matlab, and then plotted on the same graph. This illustrates how the actual sensor output

agrees with the machine input. The sensor appears to represent the force amplitude and phase faithfully.

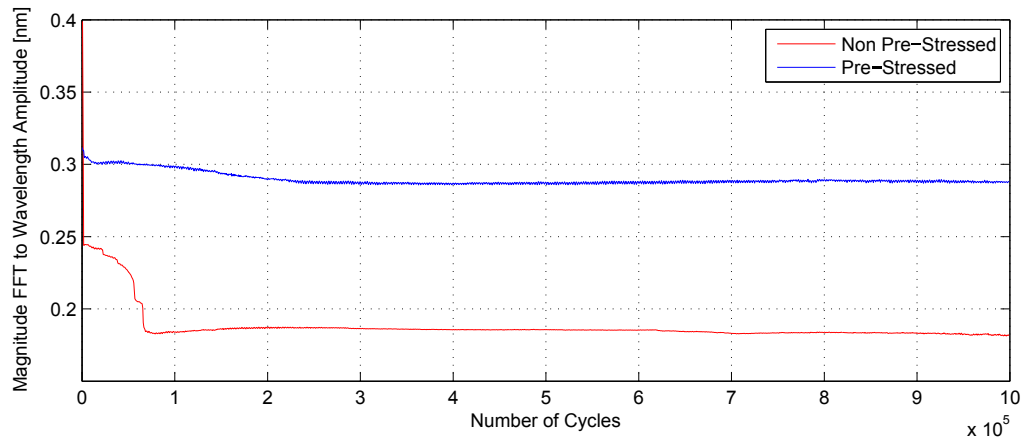
The bottom graph in Figure 5.12 shows the change in amplitude of the prestressed and non-prestressed sensors outputs over time, indicating the degree of performance deterioration over time. The maximum mechanical stress applied to the rebar is expected to reach $0.5 \text{ m}\epsilon$, hence a 100% strain transfer would result in the sensor readings reaching an amplitude of 0.61 nm based on the centre wavelength as demonstrated in Equation 3.5 and 3.6 of Section 3.3.1, where under the assumption that fibre strain is homogeneous and isotropic, pe is the effective photoelastic coefficient (numerically ≈ 0.22), and ϵ is the applied strain. Figure 5.12c shows that the non-prestressed sensors output deteriorates significantly within the first 70,000 cycles, decreasing from an initial amplitude of 0.39 nm down to 0.185 nm . Applying Equation 3.6 to calculate the amount of strain transferred to the sensor, these wavelength amplitudes correspond to an initial strain of $0.32 \text{ m}\epsilon$ (STC of 0.65) reducing down to $0.15 \text{ m}\epsilon$ (STC of 0.31). On the other hand, the prestressed sensor appears to behave fairly consistently with an initial amplitude response of 0.31 nm , representing a strain of $0.25 \text{ m}\epsilon$ (STC of 0.51) reducing to 0.28 nm ($0.23 \text{ m}\epsilon$; STC of 0.46) until reaching $2 * 10^5$ cycles and then remaining constant over the lifetime of 10^6 cycles until the test was stopped. Hence, the prestressed sensor experiences a reduction in the response of around 10% until settling at a constant level. Also, data was analysed in order to evaluate whether sensors undergo hysteresis, thus machine data (force and displacement) was separately plotted against both sensors data and fit to a first degree polynomial. Results are illustrated in Figure A.5 for the non-prestressed strain sensor and in Figure A.6 for the prestressed strain sensor of the Appendix. From Figure Figure A.5 and Figure A.6 it is possible to observe that both strain sensors do not experience significant hysteresis. In addition parameters for the polynomial fit are listed in Table 5.2 based on different cycles throughout the first fatigue experiment. Overall, the fitted data is in agreement with Figure 5.12c as the prestressed strain sensor responds constantly above $2 * 10^5$ cycles, whereas the non-prestressed strain sensor responds constantly above $1.44 * 10^5$ cycles.



(a) Machine Force - Peak & Trough Values



(b) Force Input vs. Sensor Output



(c) FFT of Sensor Data during 10^6 Cycles

Figure 5.12: First Fatigue Test - Rebar & Sensor

After the test both sensors were visually examined to determine if any visible damage occurred. It was discovered that the non-prestressed sensor's spot weld gave away on one side, explaining why the strain transfer coefficient dropped after 70,000 cycles. The

Table 5.2: Correlation Machine and Sensor Data

	Pre-Stressed				Non Pre-Stressed			
Cycle Number	Sensor & Force Slope	Y-Intercept	Sensor & Displacement Slope	Y-Intercept	Sensor & Force Slope	Y-Intercept	Sensor & Displacement Slope	Y-Intercept
1	0.0098	1564.43	1.42	1530.21	0.0126	1547.37	1.82	1503.57
144.000	0.0093	1564.45	1.38	1531.63	0.0059	1547.47	0.86	1526.84
300.000	0.0090	1564.47	1.33	1532.66	0.0059	1547.49	0.87	1526.82
800.000	0.0091	1564.47	1.36	1531.9	0.0059	1547.49	0.87	1526.71
1.000.000	0.0091	1564.48	1.34	1532.57	0.0058	1547.49	0.85	1527.15

pre-stressed sensor's spot weld remained properly attached.

As previously stated, the second test was carried out in a similar fashion to the first test; however, machine force was doubled, now varying from positive 62.8 kN to negative 62.8 kN, corresponding to ± 200 MPa of stress or ± 1 m ϵ of strain with a sinusoidal input waveform at a frequency of 10 Hz. According to Tilly [97] at this stress range (400 MPa) the rebar is expected to break at around 10^5 cycles, hence in this test sensors are evaluated under extreme conditions, where the structure itself would be expected to fail.

Figure 5.13 presents the results of the second fatigue test, where the reinforcement bar cracked at around 0.96×10^5 cycles (which was expected as previously stated); however, both strain sensors survived the testing still performing their basic measurement function. The prestressed sensor commences at an amplitude of 0.53 nm (0.44 m ϵ ; STC of 0.44), hence with a slightly lower STC than at the end of the first fatigue test. During the course of such significant cyclic loading the prestressed sensor is shown to

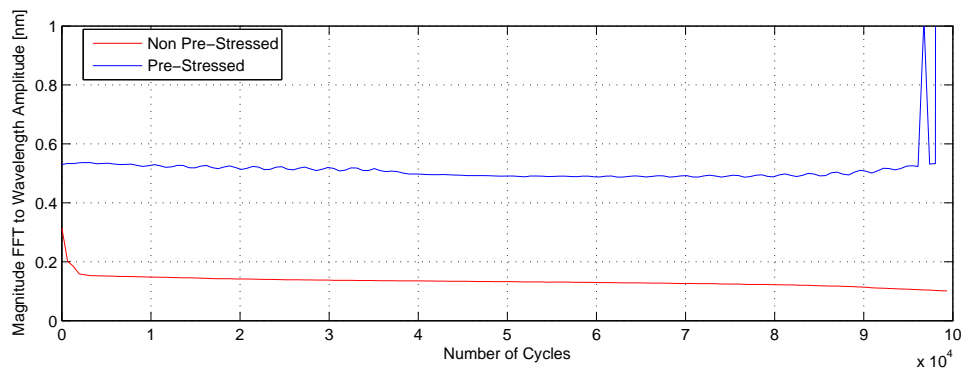


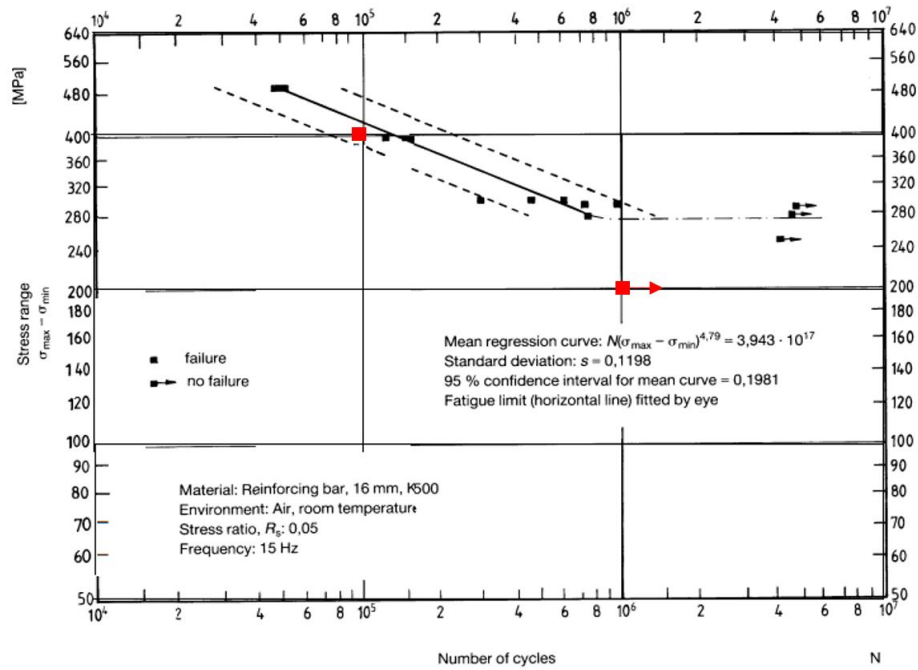
Figure 5.13: Second Rebar and Sensor Fatigue Test

still maintain a relatively constant response, once again within the range of 10%. The cause for the large variation in the response of the prestressed sensor around the rebar breakage point are due to the fact that the steel shim tore apart, thus, at that stage, the transferred forces were much higher than before since less material was available to take up the total force. This demonstrates that a strong bond can be achieved with spot welding.

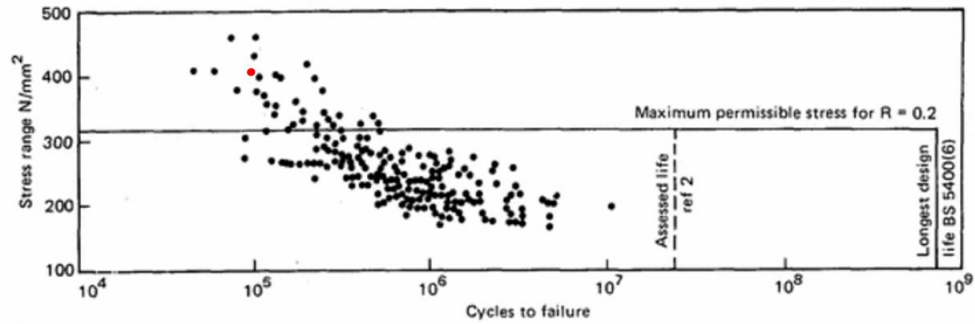
The non-prestressed strain sensor's response further declined caused by further deterioration of the spot-welded shim. In the post-test visual inspection to evaluate how many spot welds remained attached, by applying small force to the steel shim using tweezers, it was revealed that 80% of spot welds disattached from the reinforcement bar.

With regards to the experienced cycles to failure, the results of both fatigue tests are in good agreement with available research [242, 243] as illustrated in Figure 5.14a and Figure 5.14b, albeit both fatigue tests were executed consecutively. Therefore, in the case of the second test, in fact cumulative fatigue damage of $1.1 * 10^6$ cycles led to the breakage. This offers reassurance that the spot welding process does not impact the reinforcement bar's fatigue properties³ which is in agreement with Perry et al. [63]. Further, the fractured reinforcement bar surface was analysed in order to determine the crack origin. Figure 5.15 shows a photograph of the fractured surface, illustrating four distinct regions; 1) crack initiation, 2) crack growth within the “fish eye”, 3) crack growth outside the “fish eye”, and 4) rapid fracture in agreement with [97, 245]. At the same time, the location of crack initiation lies within the spot welded area of one of the temperature sensors. Therefore, there is the possibility that a spot weld caused an internal material defect that might have caused the fracture location; however, taking available fatigue research into consideration, spot welding did not impact fatigue properties. Therefore, from this single test, it is possible to observe that the spot weld might have caused the location where the structure fractures, but its fatigue resistance is not reduced. In order to gain a more representative picture further rebar and sensor

³The reader is referred to Ref. [244] for the impact of spot welding on the heat affected zone and the changes of physical properties of steel.



(a) Rebar Fatigue Cycles in Comparison to Available Research (1/2) [242]. In red are the tested sample's results.



(b) Rebar Fatigue Cycles in Comparison to Available Research (2/2) [243]. In red is the tested sample's result.

Figure 5.14: Rebar Fatigue Cycles in Comparison to Available Research

fatigue tests are conducted as illustrated in Section 5.2.3.

5.1.4.2.2 Sensor's Characteristics

Before the commencement of the fatigue tests several initial tests were conducted in order to ensure that the long-term tests run according to requirements. Therefore, as illustrated in Table 5.3, a total of six tests were conducted in which the applied force, frequency, and number of cycles were varied. The results for each test's initial

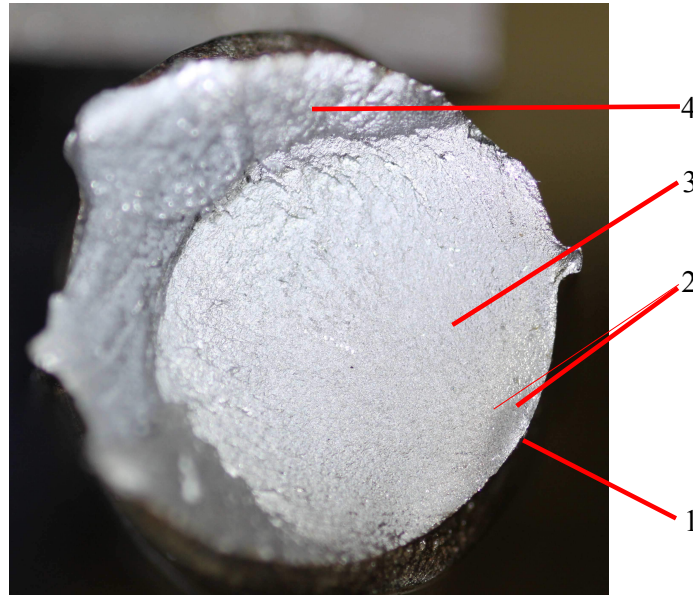


Figure 5.15: Rebar Fracture Surface

cycles (sensor centre wavelength vs. machine force) are shown in Figure A.7 of the Appendix for the non-prestressed sensor and in Figure A.8 for the prestressed sensor. The non-prestressed sensor tends to exhibit a more symmetrical response than the prestressed sensor as the peak and trough characteristics deviate (initially in tension the signal is constant for a short time in contrast to the non prestressed sensor). Further

Table 5.3: Testing Series

Test	Frequency [Hz]	Force [kN]	Stress [MPa]	Strain [$\mu\epsilon$]	Cycles
1	0.25	15.7	50	0.25	10^1
2	0.25	15.7	50	0.25	10^1
3	0.25	31.4	100	0.5	10^2
4	10	31.4	100	0.5	10^2
First Fatigue	10	31.4	100	0.5	10^6
Second Fatigue	10	62.8	200	1	10^5

when comparing each test's initial FBG centre wavelength as listed in Table 5.4, the prestressed sensor's wavelength reduces along the set of tests in contrast to the non-prestressed sensor's wavelength that maintains a constant value. This indicates that the applied prestress may have reduced incrementally, resulting in significant changes

in response. As prestressing the sensor adds further complexity to the fabrication process, these findings may indicate that prestressing may not be required. Further detailed tests are required to verify these conclusions. Also, Table 5.4 lists the change in STC over time for the first initial tests. In both cases the strain sensor's STCs start at a relatively high value and then subsequently decrease. Eventually the prestressed sensor has a STC of 0.44 after $1.1 * 10^6$ cycles and the non-prestressed sensor of 0.072 respectively, where the latter experiences this significant loss of STC due to the failure of the spot welded shim.

Table 5.4: Initial Reflective Wavelength & STC

Test	1	2	3	4	First Fatigue
Prestressed [nm]	1564.71	1564.64	1564.64	1564.51	1564.40
Non-Prestressed [nm]	1547.36	1547.36	1547.36	1547.40	1547.37
Prestressed STC [%]	67.6	64	51	49	49
Non-Prestress STC [%]	71.7	71.6	70	68.3	41.7

5.1.4.3 Section Conclusions

The results of this series of initial laboratory experiments conducted on the sample of FBG based temperature and strain sensors exhibiting differing design and manufacturing features have led to the following preliminary conclusions:

- Two different temperature sensors (brazed capillary and shim and the brazed capillary with soldered copper tube and shim) were subjected to mechanical loading in order to test their ability to isolate temperature measurement from mechanical stress. Results show that no mechanical strain is transferred from the reinforcement bar over the shim into the FBG in both cases; however, since the sealed temperature sensors (brazed capillary with soldered copper tube and shim) broke at one end, this test is repeated in Section 5.2.2. Another test is designed to evaluate axial strain transfer to the sensor in order to allow placement of the temperature sensor within the interrogation cable.

- Overall, based on the findings of this series of experiments, it is possible to conclude that the prestressed strain sensor behaves non-symmetrically. The reasons for this behaviour are currently unknown, and further investigations are needed to gain better understanding of this phenomenon. Also, the tests show that the prestressed strain sensor seems to partially lose its prestress as evidence suggests in Table 5.4. Nevertheless, after the prestressed strain sensor undergoes initial changes, the centre wavelength response appears symmetrical, and stable behaviour had been observed for up to 10^6 cycles.
- The fatigue results indicate to what degree the sensors undergo performance degradation within the first 10^3 cycles, with the reduction of STC from around 0.7 down to 0.45, despite evidence of a strong spot weld bond as observed with the prestressed strain sensor. Following this initial reduction in STC, during the fatigue test, the STC remained generally constant with a reduction of 10% to 0.44. On the contrary, the non-prestressed strain sensors STC reduced to 0.072, although this was caused by poor spot welding. Therefore, further tests are required to gain better understanding of the behaviour.
- As highlighted earlier this test has also confirmed that attention must be given to the problem of spot welding. The tests have revealed that the interconnection of copper coating, capillary and shims appear to be of good quality, but the quality of spot welding needs to be improved. When such sensors are deployed, great care is required to ensure a strong bond between the sensors shim and reinforcement bar. This involves production and/or preparation of adequate sensor shims as well as ensuring that reinforcement bars are free of oxidation, corrosion, and grease. One possible option to improve the brazing process would be to use a vacuum chamber where brazing is performed in order to prevent oxidation. Nevertheless, at present, acceptable results are achieved with the application of brazing flux.
- It was shown that the spot welding process does not impact reinforcement bar fatigue properties as the cumulative damage is in agreement with available liter-

ature on cycles to failure.

- Both strain sensor types are required to be further subjected to tests in order to verify these initial findings. In the case of the metal-packaged prestressed strain sensor, the existing results need to be verified and in the case of the metal-packaged non-prestressed sensor, fatigue experiments are required to be repeated under the same test conditions in order to evaluate the sensor for a total of 10^6 cycles while ensuring adequate quality of spot-welding. This is carried out in Section 5.2.3
- The spot welding process requires to be further evaluated (see Section 5.2.1) as well as the process to mechanically expose the sensor to stresses prior to installation and thermal characterisation to ensure stable operation. The process of prior mechanically cycling before installation has been successfully applied in other applications such as sensors to monitor prestressed tendons in previous work [63,64].

5.2 Sensor Improvement

Based upon findings presented in Section 5.1, this section deals with the verification and sensor improvement of flaws identified in Section 5.1.4.

5.2.1 Evaluation of Spot Weld Process

For the first experiment, steel shims are spot welded to a B500B reinforcement bar (diameter: 20 mm) while iterating the transferred spot weld energy ranging from 20 to 35 J. Subsequently the shim is gripped with a pair of pliers and physically removed. Based upon the required force and rupture behaviour, the attachment strength is evaluated. Taking the gathered information into consideration, it is aimed to identify the most suitable energy level to attach sensors to the reinforcement bar as during previous fatigue test, one sensor's spot welded shim detached from the reinforcement bar and thus corrupted measurement data.









Energy Intensity [J]	Attachment	Rupture Pattern	Bonding Strength
20			Poor
25			Fair
30			Excellent
35			Excellent

Figure 5.16: Spot Weld Evaluation

Table 5.16 depicts photographs of the spot welded shim attachment to the reinforcement bar as well as the rupture characteristics after physical removal under varying energy settings ranging from 20 to 35 J. Each tests' bonding strength is evaluated qualitatively with a scale ranging from poor to excellent.

Test results reveal an initial increasing bonding strength with increasing energy intensity, although this appears to plateau at 30 J where no real benefit can be observed with greater energy levels. Therefore, a set-up of 30 J appears most suitable for the field installation. Also, in the first test (20 J) a corroded shim area marked in red outside the tested width was subjected to a spot weld to demonstrate its effect. One

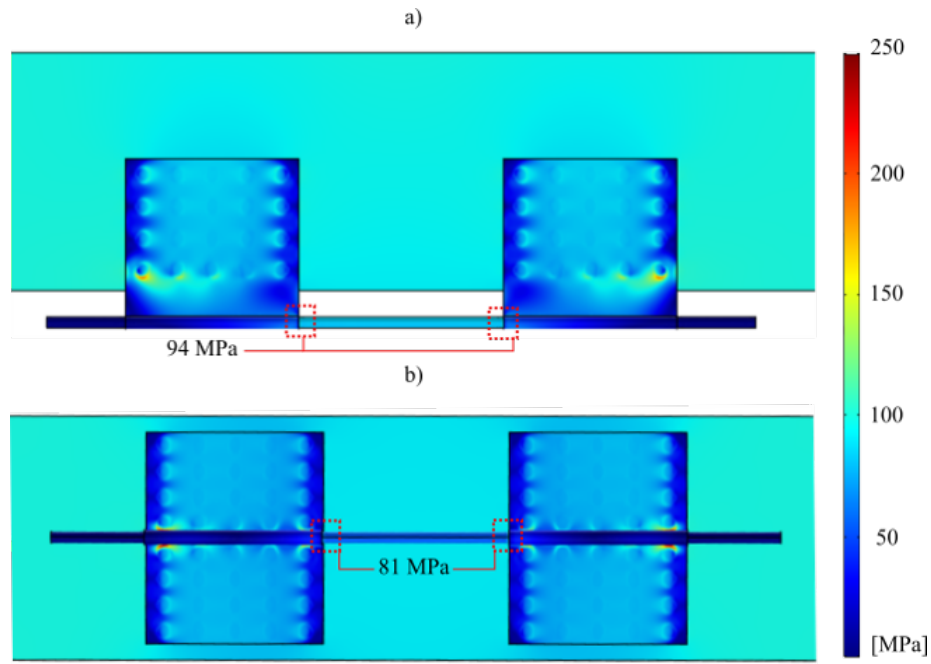


Figure 5.17: Weld Area FEM

can see, that the entire shim burned off as illustrated in the rupture photograph on the bottom left of the steel shim. This, once again re-confirms the importance of surface preparation of the steel shim and reinforcement bar.

Besides the spot welding evaluation it was also desirable to evaluate the stress distribution of the spot welded area. For this, a model was created in COMSOL with the results illustrated in Figure 5.17. This enables to determine the most critical spot weld connections as well as the appropriate care in spot weld execution. As illustrated in Figure 5.17, the most critical locations are the outward spot welds of the first row. If a spot weld in one of these critical areas is of insufficient quality, this would result in a poor overall result.

5.2.2 Embedded Temperature Test

The intention was to design a multiplexible temperature sensor that can be placed within the interrogation cable in order to (i) reduce the requirement to use spot welding as well

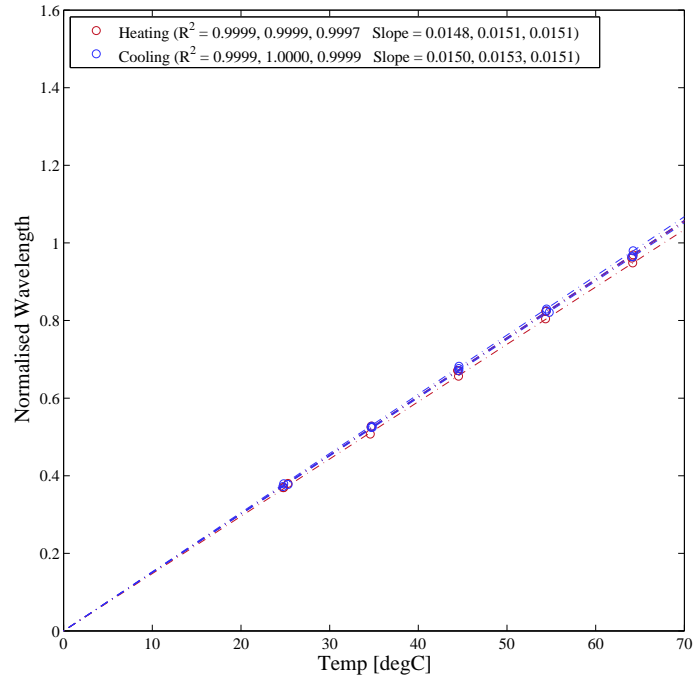


Figure 5.18: Characteristics of the metal-packaged strain and temperature sensors thermally cycled three times. The characteristics are normalised by subtraction of the y-intercept.

as to (ii) minimise the area of sensor exposure, outside the interrogation cable, within the foundation. Since the brazed kovar capillary and soldered copper tube and shim temperature sensor (Figure 5.1 c) broke at one end of the FBG location in a previous experiment, the test was repeated. This lab test revealed that the design illustrated in Figure 5.1 c, is highly repeatable in its response to temperature variations as illustrated in Figure 5.18 with a slope of 15.1 pm/deg C. Further the embedded temperature sensor isolates axial strain well based on manually applied mechanical stress exposure to the fibre ends.

5.2.3 Sensor Improvement Iterations

Main aim of further sensor testing was to understanding the sensor's weaknesses and improve its manufacture and design to increase reliability and repeatability under fatigue loading. Overall, several sensor design iterations and tests were performed as summarised in Table 5.5. Although, improvements were achieved (in-house manufactured sensor suffered a degradation of 8.8% over 10^6 cycles), in comparison to commercially available sensors such as the Micron Optics reference sensor, the tested sensors cannot compete. Based on the testing results summarised in Table 5.5, it is likely that the following factors are responsible for the degradation:

- **Materials:** based on the "Dumbbell 3" fatigue test, the degradation is determined to be introduced by the layers after the copper coating (brazing alloy, kovar, or steel). According to [246], Kovar has sufficient fatigue resistance, hence the brazing joint is likely the weakest link.
- **Heat control:** during the manufacturing process it is difficult to control the heat, thus in multiple occasions it has been observed that the copper coating burned entirely resulting in a poor bond in between the remaining carbon layer and brazing material.
- **Gripping width:** based on the UV epoxied copper coated fibre results, it is thought that the sensor brazing design layout is not sufficient for the capillary effect to pull enough brazing material inside the kovar tube to increase its gripping friction. Removal of the top kovar half-tube for 4 mm was not successful as illustrated in the "Dumbbell 3" fatigue test.
- **With regards to the applied UV Epoxy (EPO Tek OG198-55),** the fatigue results (Figure A.9c of the Appendix) reveal a high repeatability over time; however, when looking into the exact response it is possible to observe that the actual UV epoxy behaves in a non-linear fashion with regards to strain exposure (the force increased by a factor of 2.4 whereas the actual amplitude increased by a factor of 3.75). This behaviour was confirmed in another test, where 5 different epoxy types

where analysed, with the MBond AE10 Epoxy demonstrating superior results [247]. This UV epoxy is therefore not recommended for strain measurements.

In order to conclude the metal-packaged strain sensor testing, it is important to summarise the observed drawbacks along the extensive metal-packaged sensor testing:

- Observed performance deterioration along all fatigue tests and sensor variants.
- Substantial fibre compression inside the Kovar tube after manufacture within the order of 1.6-3.4 nm (Section 5.3.3.2 & 5.1.2.1).
- Challenges with repeatable manufacture.
- Complexity of manufacture (several different materials act together).
- Robustness - due to the sensor length, the kovar capillary can bend/break easily, because of the lever arm.
- Challenges with sensor packaging (from the kovar diameter the width requires to be stepped up until the diameter matches the steel armour's diameter (Figure 5.24) thus the actual lever arm is further increased in reinforced concrete applications.

Based on the findings it is therefore recommended to explore new sensor variants, to be initially tested in the lab and subsequently deployed as a field trial if lab results appear promising.

5.3 Installation of Embedded Optical Sensors within a Wind Turbine Foundation at the Windfarm

This project's selected site is owned by SSE and is located in Scotland. The development is for 32 WTGs, a combination of 2 Vestas V112-3.3MW with a hub height of 69 m and 30 Vestas V117-3.45MW with a hub height of 76.5 m respectively [248]. Once completed the site will have a total maximum capacity of 110 MW. The site layout is given in Figure A.11 of the Appendix, as well as in a schematic drawing (Figure

Table 5.5: Summarised sensor fatigue tests

Test ID	Description	Test Environment	Result	File
Dumbbell 1	Ensure good spot welding bond by extensive sensor surface preparation; Micron Optics Reference Sensor	Amplitude: $\pm 0.5\text{ m}\epsilon$ (σ : $\pm 100\text{MPa}$); R = -1; f = 12 Hz; SmartScan at 500 Hz; Machine: Instron 8802; Cycles: 10^6 ; Specimen Geometry: Dumbbell	No observable improvement in sensors' response; Machine very stable over time from Micron Optics reference sensor	Appendix Figure A.9a
Dumbbell 2	Application of stop-flow paint (no brazing material at the spot weld location; Butterfly attachment style)	Amplitude: $\pm 0.5\text{ m}\epsilon$ (σ : $\pm 100\text{MPa}$); R = -1; f = 10 Hz; SmartScan at 500 Hz; Machine: Instron 8802; Cycles: 10^6 ; Specimen Geometry: Dumbbell	Improved strain transfer; Butterfly attachment reduced performance degradation - 8.8% (conventional attachment -18.9%)	Appendix Figure A.9b
Dumbbell 3	Attachment of a copper coated FBG with UV Epoxy to evaluate the bond of silica, carbon, and copper coating. Concerning the UV sensor manufacture, the transducer was prestressed to 1.2mm and attached to the right and left of the FBG along the copper coated section with UV epoxy along a width of 10mm each side. After curing of the UV epoxy the prestress dropped by around 20%; Friction: it is thought that during the brazing the gripped brazing width is not wide enough as the higher the gripping width the greater the overall friction. Therefore, the kovar capillary is cut in half at one side to ensure there is a wider brazing area.	Run 1: Amplitude: $\pm 0.5\text{ m}\epsilon$ (σ : $\pm 100\text{MPa}$); R = 1; f = 15 Hz; SmartScan at 500 Hz; Machine: Instron 8802; Cycles: 1.7^6 ; Specimen Geometry: Dumbbell; Run 2: Amplitude: $\pm 1\text{ m}\epsilon$ (σ : $\pm 200\text{MPa}$); R = 1; Cycles: 1.6^6	Both metal-packaged sensor variants' response is not repeatable; one sensor is characterised by a significant performance degradation and the other one has insufficient strain transfer thus a comparatively small amplitude. In the first run, the UV epoxied copper coated fibre is stable over time and further in the second test the sensor is picking up the crack propagation and elongation well. The epoxy does however respond non-linear to force making it less suitable for strain sensor installations	Appendix Figure A.9c

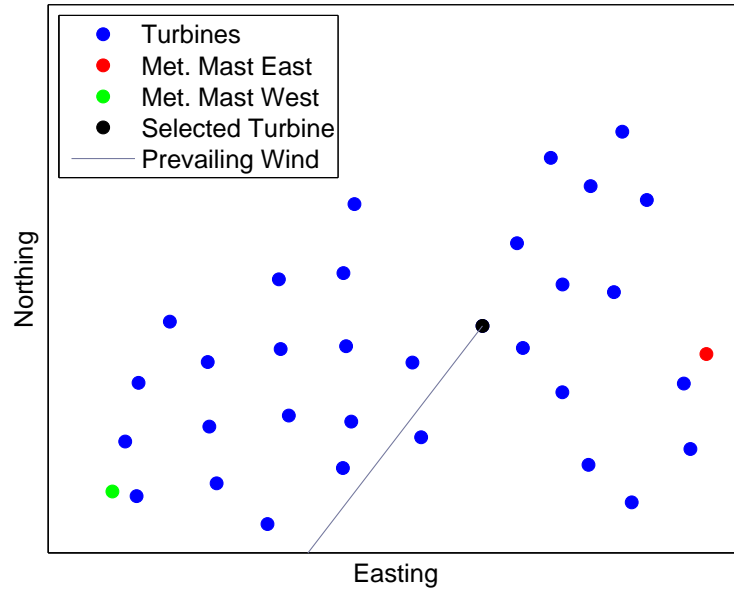


Figure 5.19: Turbine Site Layout. For the elevation profile, the reader is referred to Figure A.11 of Appendix A.

5.19) presenting all relative turbine locations (blue), the selected turbine to equip its foundation (black) as well as both permanent met. masts (green and red). Readings from three site masts (one temporary, two permanent) are illustrated in Figure 5.20. All three met. mast observations are in close agreement revealing a predominant wind direction coming from 230 degrees, hence a south-western wind inflow. The presented turbine layout in Figure 5.19 is further estimated to be exposed to the identified predominant wind direction of 230 degree. This also reveals that there is no wake impact expected at this inflow condition.

The turbine equipped with foundation sensors is T22 (Figure 5.19 - black dot), a Vestas V117-3.45MW with a hub height of 76.5 m.

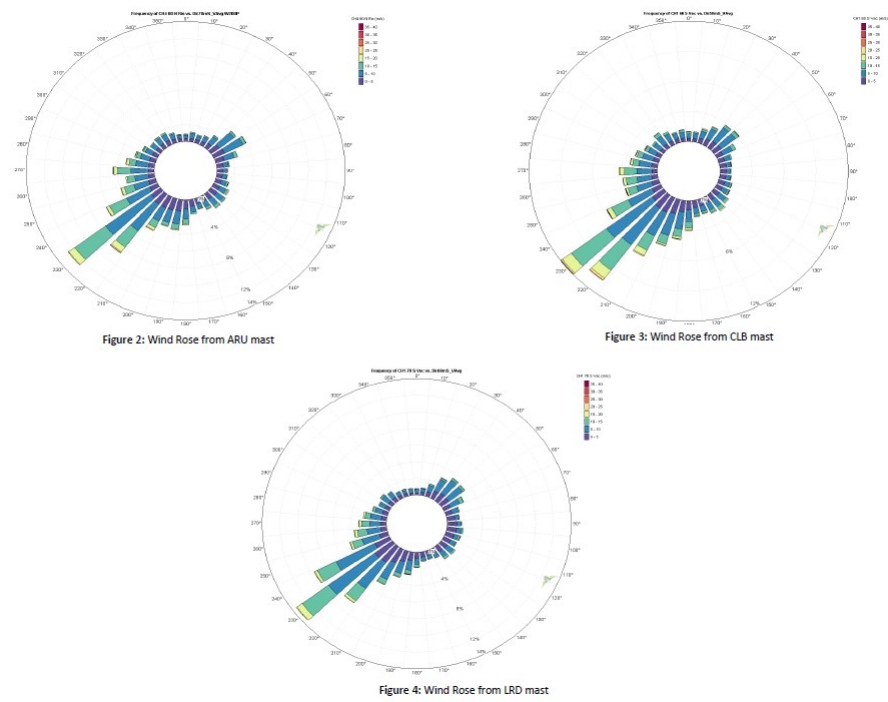


Figure 5.20: Wind Rose of Wind Farm.

5.3.1 V117 - Foundation and Finite Element Analysis

5.3.1.1 General Information

The turbine's foundation design is a submerged gravity foundation made of a circular reinforced concrete slab incorporating a circular pedestal upstand. The foundation is symmetric about any axis in plan and the main slab has a haunched profile in section with the depth increasing at a constant rate towards the foundation centre. The mechanism for transferring tower moments into the foundation is direct via a circular assembly of full length anchor bolts. A cross-sectional technical drawing is illustrated in Figure A.12 of the Appendix. The material for the reinforcement is grade B500B (hardened rebar steel with a yield of 500 MPa), whereas the main slab's material is C35/45 concrete and C45/55 for the pedestal.

There are multiple rebar shapes applied in this wind turbine foundation; predominately radial, circumferential, orthogonal bars as well as shear links.

5.3.1.2 Finite Element Model

The foundation FE model's mesh and boundary conditions are illustrated in Figure 5.21a and 5.21b respectively. Only one half of the model is shown for simplicity, as geometry and loading conditions are symmetrical. The model includes several dead loads: the weight of the concrete foundation, W_c , and tower, F_z , along with the weight of the ballast, W_b . Soil-structure interactions were modelled using a linear spring constant on the bottom surface of the base, with lift-off occurring for positive vertical displacements. The concrete was assumed to have a constant elastic modulus of $E_c = 35$ GPa. Horizontal slippage of the foundation, bolt loads and hydrostatic uplift were not included in the model, nor were torsional moments about the tower axis.

Strains within the foundation were studied for overturning moments, M_{res} , ranging from 0 MNm to 30 MNm. An overview of the selected parameters, their ranges and source of information is illustrated in Table 5.6.

As the foundation's reinforcement was not included in the model, absolute stress and strain values are not accurate. However, comparisons of fractional strain changes be-

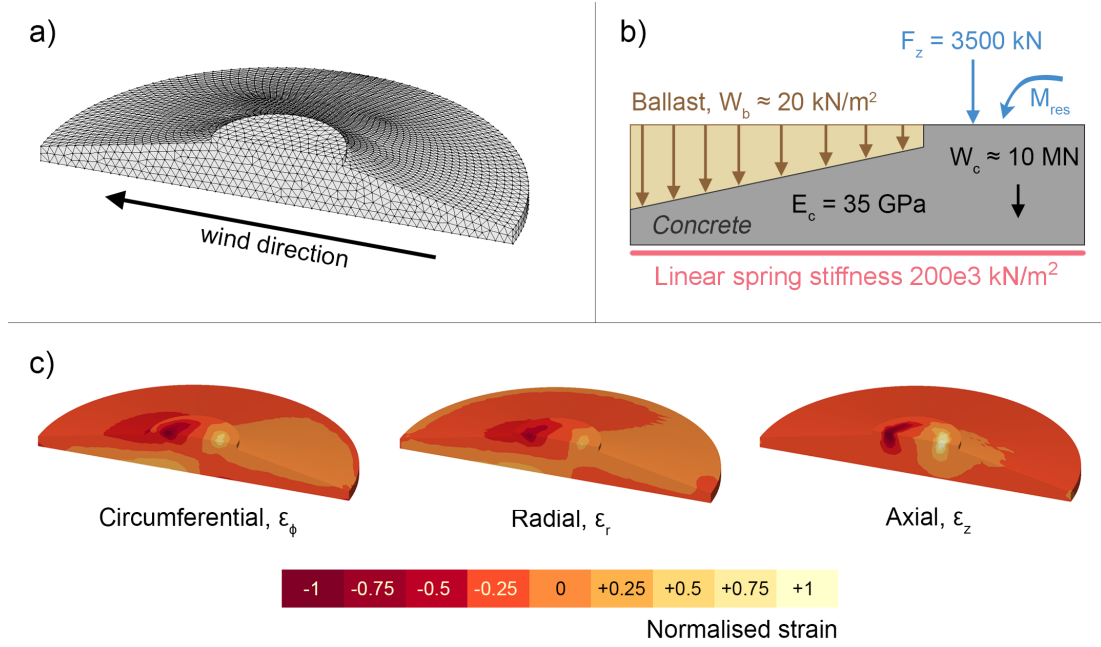


Figure 5.21: FE model a) mesh and wind vector; b) boundary conditions; and c) typical normalised strain profiles in circumferential, radial and axial directions.

Table 5.6: FEM Parameters and Possible Ranges

Item	Value	Range	Unit	Source	Comment
Soil Spring stiffness	200	11-230	MN/m ³	SWECO	Spring stiffness (N/m) per unit area (m ²), hence (N/m ³)
Ballast	20	18-20	kN/m ³	SWECO	Wet vs. dry backfill & depth (linear equation)
F_z (turbine weight)	3500	N/A	kN	Vestas	Turbine weight (357 t)
Weight foundation (density)	2500	N/A	kg/m ³	SWECO	Foundation weight (1020 t)
Concrete Elasticity	35	35-42	Gpa	SWECO	Conservative assumption applied
Overturning Moment, M_{res}	N/A	0-30	MNm	Vestas & Thrust data	The ULS is defined at 50 MNm
Soil Bearing Capacity	>500	N/A	kPa	SSE	The soil bearing capacity is greater 50 t/m2

tween locations or between load cases are valid, and these were used to inform sensor placement. Typical circumferential, radial and axial strain profiles are shown in Figure 5.21c, where negative numbers represent compression. As expected, on the side of the foundation opposite to the prevailing wind direction, there are compressive stresses on the top surface, while the bottom surface is under tension.

5.3.2 Network Requirements and Sensor Packaging

The following practical aspects and constraints with regard to the advanced optical sensor network that was installed at the site had to be considered:

First of all, each sensor required a certain spectral bandwidth, so that when multiplexed, centre wavelengths of the spectrally adjacent sensors do not overlap. Temperature sensors are expected to remain within -20 to $+70$ °C, whereas strain sensors are expected to reach maximum strain levels of $0.5\text{ }m\epsilon$ as determined by work by Perry et al. [89]. This equates to a total of 2.6 nm of the spectrum per strain sensor and 1.6 nm per temperature sensor.

Secondly, the supplier's manufacturing constraints with regard to the FBGs inscribed in copper coated fibres placed some restriction on which centre wavelengths were available to this project, namely: 1535, 1543, 1551, 1558, and 1567 nm.

Thirdly, the interrogation spectrum of the sensor interrogator had to be taken into account. For this project the selected interrogator, a Smart Fibres SmartScan device offered a wavelength range of 40 nm (1528-1568 nm) on four parallel channels.

Apart from these physical constraints, network redundancy can help to counteract the potential loss of multiplexed sensors by running multiple separate networks. Therefore, for the total of 10 strain and 6 temperature sensors that were proposed for the site, it was intended to divide them into four separate channels: two including three strain sensors and two temperature sensors (channel 1 and 2) and two including two strain sensors and one temperature sensor (channel 3 and 4) as illustrated in Figure 5.22.

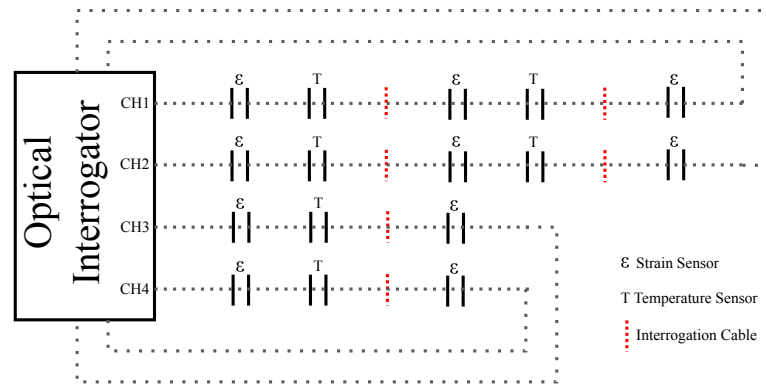


Figure 5.22: Schematic optical network diagram

Also, two mirrored sensor networks are required to place sensors upwind as well as downwind, along the prevailing wind direction.

Due to the guided through rebar structure, it was not practical to prepare complete interconnected sections in advance. Therefore, sensors were manufactured as modules, either as a single strain sensor or a strain sensor coupled with temperature sensor. This allowed for the installation of sensors as the construction of the rebar cage progressed as, otherwise, some locations would not be possible to reach as the steel placement progressed. As a downside, this required connection and sealing of each module's end. Note that to increase redundancy in this experimental installation, each module was connected to the cable at both ends. This enabled interrogation from either end and thus increased the likelihood of survival of the sensors should some addressing cables be damaged. In addition, the modular strain and temperature combination allowed to reduce installation time significantly. Modules were terminated with Diamond DiaLink connectors (with exceptionally small diameter), thus placement within a steel armour (ID 6 mm) was possible as an effective means of protection in this harsh environment. Between modules, tactical tight buffered optical cable was applied, again, suitable for deployment where extreme environmental conditions are present.

The length of the strain sensor was required to be as small as possible to fit in most locations, particularly between orthogonally positioned steel bars, meaning the geom-

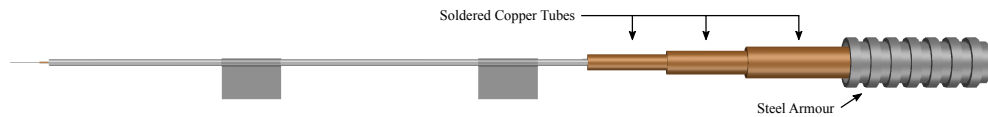


Figure 5.23: Strain sensor's designed end

entry of the sensor placement onto the rebar required a step wise increase in diameter to prevent the kovar capillary from bending. Such an approach also allowed a robust connection of each module's end with steel armour that was crimped at each side and sealed with shrink sleeve to prevent water ingress. The actual design is illustrated in Figure 5.23 where three copper tubes with a continually increasing diameter, each with a length of 20 mm were soldered in place and the steel armour was crimped to the highest-diameter tube. To prevent any potential damage to the sensor, a stainless steel half tube was positioned on top of the strain sensor and copper tubes, with both ends secured with epoxy. Along the strain sensor, flexible silicone was applied to not distort the instrument's characteristics. The half steel tube protected the sensor from any excessive impacts or forces, for example, due to workers accidentally stepping on the cables or when the concrete shakers make direct contact with the sensor modules during the concrete pour.

The temperature sensors were spliced on one end of the strain sensors and positioned within the steel armour, hence no steel shim was required as illustrated in Figure 5.1c (the sensors were not directly attached to reinforcement bar). Within the vicinity of the temperature sensor, it was important to maintain the cable straight to prevent the outer copper tube of the temperature sensor from bending as this could bend the internal kovar capillary and thus change the characteristic of the sensor. Therefore, these areas were marked on the outside of the shrink sleeve for the purpose of identification.

5.3.3 Sensor Preparation

5.3.3.1 Sensor Fabrication

As a recap, the layout for the sensor manufacture is illustrated in Figure 5.3. The commercially sourced metal coated optical fibre comprises standard single mode glass fibre (ID $125\ \mu\text{m}$) coated in copper (total diameter of $170\ \mu\text{m}$) and equipped with an FBG of the length of 7 mm, written in a 10-15 mm stripped fibre section. The FBG is placed inside a kovar capillary (ID $200\ \mu\text{m}$; OD $700\ \mu\text{m}$) and sealed at both ends with a silver brazing alloy (melting point: $610\text{-}850\ ^\circ\text{C}$). During brazing, high frequency current (200-300 A, 400 kHz) is passed through the induction heating coil for a total duration of 30 s. Thus, temperatures of $610\text{-}620\ ^\circ\text{C}$ are reached in order to melt the alloy. With this set-up the curie point of kovar ($430\ ^\circ\text{C}$) is exploited, thus protecting the FBG from excessive thermal stress that could potentially cause the grating to erase. Overall, approximately 50% of reflected FBG intensity is lost throughout this heating process, which is acceptable from the point of view of peak detection by the optoelectronic sensor interrogation system.

Although the sensor design is inferior to commercial sensors at high loading, (i) there are no suitable commercial alternatives and (ii) the expected encountered load is observed to be low in range with a maximum of $0.5\ m\epsilon$, thus the decision was made to install the “dumbbell 2 with the shim on one side” type sensor variant that fatigue result is illustrated in Figure A.9b and summarised in Table 5.5 (8.8% degradation at high loading over 10^6 cycles). At the expected loading profile, the team is confident no or an insignificant deterioration is observable (1-2% over 5 years).

Figure 5.24 depicts one of the ten manufactured strain sensors. Despite applying flux to prevent oxidation of the steel shim during the brazing process, usually some debris remained. As this could reduce the quality of the spot-welding the sensor to steel rebar, the steel shim was cleaned with fine sandpaper (P400). Figure 5.25a shows the internal arrangement of the strain and temperature module. Tactical tight buffered cable was connected at both ends, with the strain sensor and its gradual increase in cable diameter on the left and the shielded temperature sensor on the right. Since the inter-

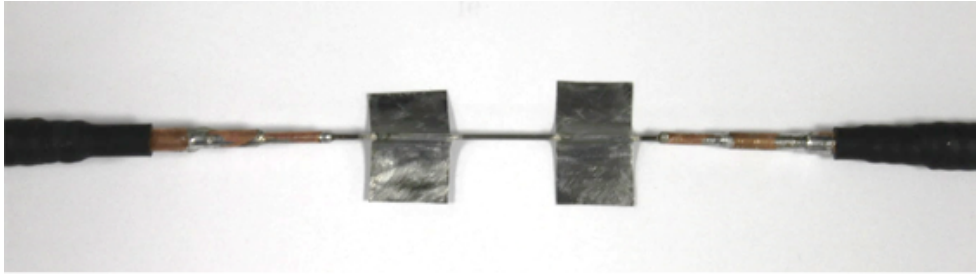


Figure 5.24: Manufactured FBG strain sensor

nal cable had sharp edges that could potentially get stuck within the steel armour, the fibre with its splice protectors was placed within a polyurethane half tube and sealed with silicone as illustrated in Figure 5.25b. To prevent an additional layer that can increase the thermal inertia of the temperature sensor this section had no additional coating. As a final manufacturing step, steel armour was placed over this arrangement and crimped at both ends. Further, shrink sleeve was placed over the armour to prevent water ingress. The modules packaged for transportation to site are illustrated in Figure 5.25c. The two golden stripes on each sensor module indicate the location of the temperature sensor to ensure this location does not experience bending during installation as this could affect the transducer's sensitivity as mentioned beforehand.

Table 5.7 presents a detailed overview of the four separate channels consisting of the sensor modules. Overall, there are more strain sensors than temperature sensors because it was expected that, due to the thermal inertia of the foundation, the rate of change of temperature would be small. Additionally, due to the symmetrical geometry of the foundation, the temperature profile would not experience significant differences. Therefore, it is assumed that, through interpolation, an accurate temperature profile can be reconstructed based on the discrete and sparse temperature measurements. The knowledge of temperature local to the strain sensors is important for accurate determination of strain as discussed in [249].



Figure 5.25: SSE Sensor Overview

Table 5.7: Sensor identification overview

Channel	Type	Module ID	Sensor ID	Wavelength [nm]
1	Temp	I	TR1	1533
1	Strain	I	TR1	1543
1	Temp	II	TR1	1566
1	Strain	II	T15 2b	1553
1	Strain	III	TR2	1559
2	Temp	IV	TR2	1567
2	Strain	IV	TR2	1543
2	Temp	V	TR4	1558
2	Strain	V	TR3	1535
2	Strain	VI	T16 2b	1553
3	Temp	VII	TR3	1543
3	Strain	VII	TR3	1535
3	Strain	VIII	TR5	1559
4	Temp	IX	TR5	1535
4	Strain	IX	TR6	1543
4	Strain	X	T19 2b	1559

5.3.3.2 Evaluation of Sensor Brazing

Based upon findings from Section 5.1.2 it is evident that the sensor brazing process eventually shifts the FBG centre wavelength into compression. In fact, the sensor production has multiple parameters that can further influence its characteristics; there are four different materials with different thermal expansion coefficients (silver solder, steel, kovar, and copper), the alignment within the production rig can introduce changes in experienced temperatures as well as the usage of varying amounts of applied materials such as the width of the steel shim, the brazing paste or the amount of brazing foil. Actually, the steel shim (highest thermal expansion coefficient) can be taken out of this equation as the same process can be observed during the manufacture of the brazed kovar capillary temperature sensor where no shim is applied. Figure 5.26 presents a scatter diagram displaying the recorded maximum positive difference (caused by induction heating) from the initial centre wavelength versus the total compression from the initial wavelength for a total of seven produced sensors. A pattern emerges where

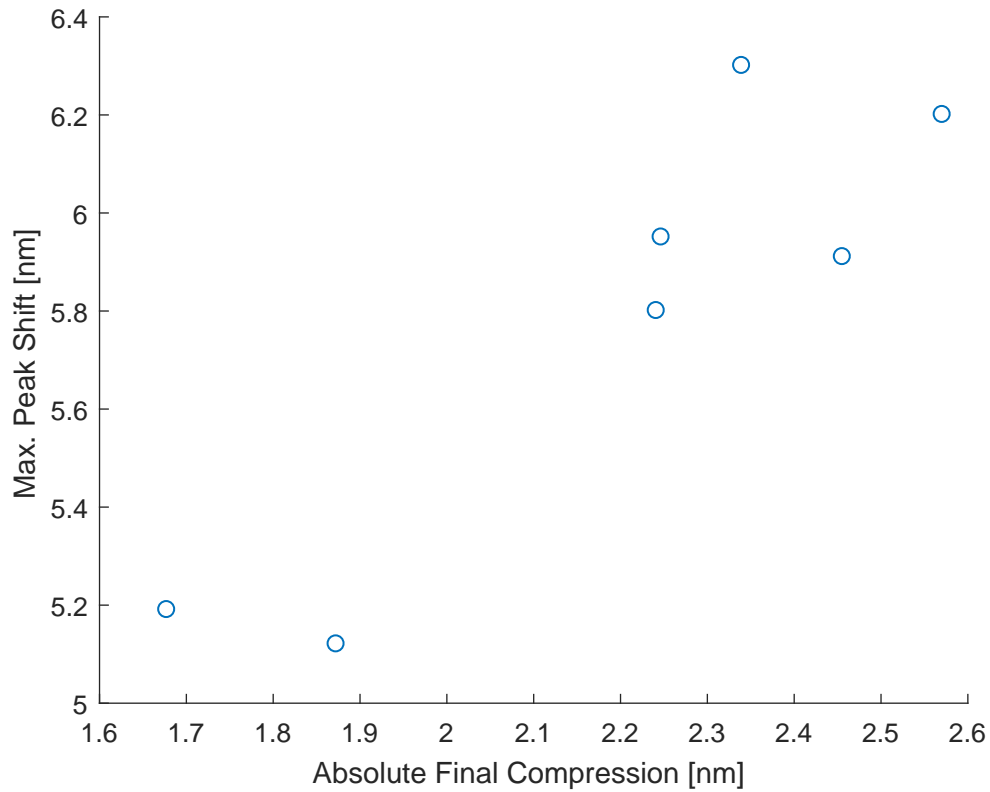


Figure 5.26: Scatter diagram of manufactured sensor's maximum peak shift vs. the absolute final compression

a greater maximum peak shift results in a greater final compression with some scatter that could be introduced due to slightly changing parameters as mentioned before. Since the kovar's thermal expansion coefficient is roughly 11 times greater than of the optical fibre made of silica, the kovar capillary elongates at a much greater rate during the induction heating. Therefore, it is expected that once the solder solidifies (at a relatively high temperature) it will lock the coated fibre and the kovar capillary at a time where the fibre is much less elongated, thus during subsequent cooling the actual FBG will be subjected to compression as the kovar capillary contracts. As a consequence, the actual temperature difference during the induction process has a significant impact as observed in Figure 5.26.

To mathematically evaluate the eventual compression, it is first important to evaluate the strain transfer of the copper coated FBG when brazed in to a kovar capillary. The thermal coefficient of kovar, α_k , in between 25 and 500 °C is around $6.15 * 10^{-6}$ per °C, thus the theoretical change in the centre wavelength, $\Delta\lambda_{BS}$, is:

$$[(1 - p_e) * \alpha_K + \alpha_n] * \lambda_B * 1000 = 15.98pm \quad (5.2)$$

Where p_e is the effective photo-elastic coefficient (numerically around 0.22), α_F is the thermal expansion coefficient of silica ($0.55 * 10^{-6}/^\circ\text{C}$), α_n the coefficient for the change of refractive index ($5.86 * 10^{-6}/^\circ\text{C}$), λ_B the base wavelength (1540 nm), and 1000 the coefficient to transform the result in pm [250].

From the thermal calibration it is known that the temperature sensor's sensitivity, k_T , on average is 15.18 pm/°C [251], thus the strain sensibility, S_S , is:

$$\frac{k_T}{\Delta\lambda_B} = 0.913 \quad (5.3)$$

hence 91.3% of thermal strain is transferred.

When the solder solidifies it will actually lock the optical fibre and the kovar capillary with an assumed strain transfer coefficient of 91.3% and will further contract due to the cooling down to room temperature with a nominal temperature difference, ΔT , of approximately 550°C. Therefore, the contraction in terms of length, dL , of the kovar capillary is:

$$dL = \alpha_K * \Delta T * L \quad (5.4)$$

Where L is the length of the kovar capillary (25 mm). Consequently, the induced negative strain from the contraction of the kovar capillary, ϵ_K , is:

$$\frac{dL}{L} = 3.2m\epsilon. \quad (5.5)$$

Substituting α_K with ϵ_K in Equation 5.2 as well as introducing the change of temper-

ature (550 °C) results in the approximated expected change in wavelength, $\Delta\lambda_{BApprox}$:

$$[0.78 * (\epsilon_K - \alpha_F * \Delta T) + \alpha_n * \Delta T] * \lambda_B = 8.37nm \quad (5.6)$$

which is the sum of the strain impact:

$$\Delta\lambda_{BS} = 0.78 * \epsilon_K * \lambda_B = 3.84nm \quad (5.7)$$

and temperature impact:

$$\Delta\lambda_{BT} = (-\alpha_F + \alpha_n) * \Delta T * \lambda_B = 4.53nm. \quad (5.8)$$

In fact, this change of wavelength is well in agreement with recorded data (Figure 5.4) showing an overall reduction in the centre wavelength of approximately 8-9 nm (positive induction shift plus eventual compression). Also, when subjecting the model's parameters to a sensitivity analysis, $\Delta\lambda_{BApprox}$ appears most sensitive to changes in ΔT that is in agreement with observations from Figure 5.26, thus giving confidence in the approach. Contrary changes of thermal coefficients within identified bands has an insignificant impact on $\Delta\lambda_{BApprox}$.

Conclusion and Limitations

There are many limitations to this approximation. First the entire model is based upon the temperature sensor without the steel shim attached that could potentially introduce changes; however, recorded data from the temperature sensor brazing and the strain sensor brazing have shown equal wavelength shifts, thus allowing it to be used as an approximation. Second, in fact the optical fibre within the kovar capillary has bare silica fibre at the location of the FBG as well as burned/oxidised copper at both sides facilitating the connection of brazing paste and kovar capillary. This copper width has not been taken into account. Third, in terms of the temperature profile the kovar capillary is heated on one end causing a natural temperature profile over

its length that is approximated to an average 550°C . The exact temperature profile could be modelled based on FEM. Also, during solidification there will be a period with slippage shortly above the solidification temperature well as a period where there are two phases (solidified and liquid areas) impacting the identified STC of 91.3%. Fourth, during the induction process, the initial sudden increase in the centre wavelength is a response to the induction heating process resulting in temperatures at the FBG in between $500\text{-}650^{\circ}\text{C}$. At this temperature available research [240,252] suggests that type 1 FBG exposure to high temperatures over long periods causes annealing resulting in a reduction in the centre wavelength. Annealing is the process that relieves internal stresses by heating and then slowly cooling a glass structure. However, the induction heating is characterised by a rapid heating and subsequent cooling at room temperature, hence there is a limited exposure to such high temperatures (seconds/minutes vs. hours in observed annealing processes). In addition, during the first brazing the FBG experiences an equal temperature profile and stabilises at the exact initial centre wavelength, thus annealing processes appear highly unlikely to take place. Fifth, it is likely that after the sensor reaches its ultimate compression the bare fibre section within the kovar capillary will experience buckling that is however, limited by the internal walls of the capillary.

Although, there are several limitations to this approach, results suggest that the kovar capillary is the significant factor being capable to cause such a severe wavelength change, compressing the fibre within the capillary. Potentially more detailed modelling could be introduced however, this approximation as well as gathered data from observation appear reasonable to conclude that no more detailed modelling is required.

5.3.3.3 Thermal Characterisation and Calibration

It is important to ensure reliable temperature readings to be able to provide accurate temperature compensation even though foundations are usually buried and thus internal temperatures change at a low rate as the soil and concrete act as a thermal insulator.

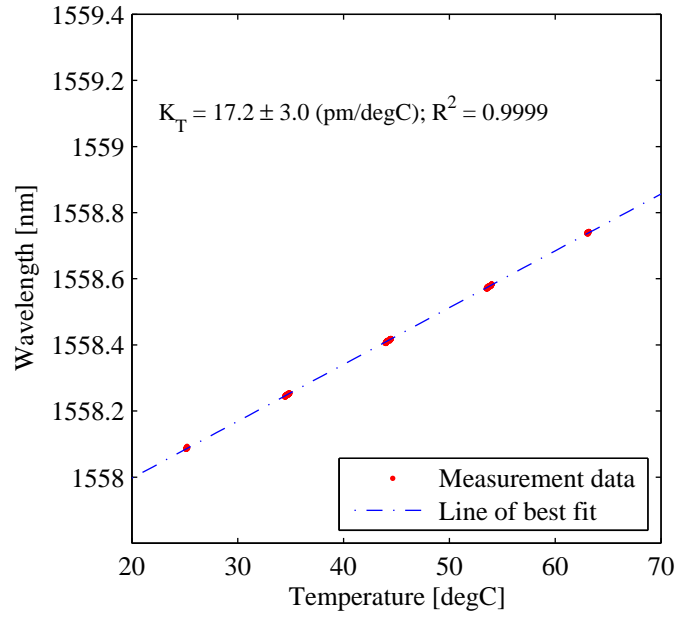
5.3.3.3.1 Methodology

To carry out thermal characterisation, the ten modules were placed in a Thermotron S-16 environmental chamber and gradually heated in 10 °C steps from 25 °C to 65 °C, and subsequently cooled in the same gradual manner. The chamber was programmed to settle for one hour at each temperature step. In order to improve accuracy of the reference temperature reading, the oven was equipped with a Pico SE012 temperature probe with an accuracy of ± 0.03 °C. Temperature reference data was read by a Pico high accuracy data logger and automatically saved every 60 seconds together with each sensor's reflected centre wavelength that was monitored by a Micron Optics sm125-500 interrogator. The sensor modules underwent 5 thermal cycles, although the first cycle was removed from the analysis as within this first cycle, the sensors moved slightly within the environmental chamber. Twenty consecutive measurement points were used for the analysis after the environmental chamber settled at each stage; thus, in total, each calibration is based upon 640 individually recorded measurement points.

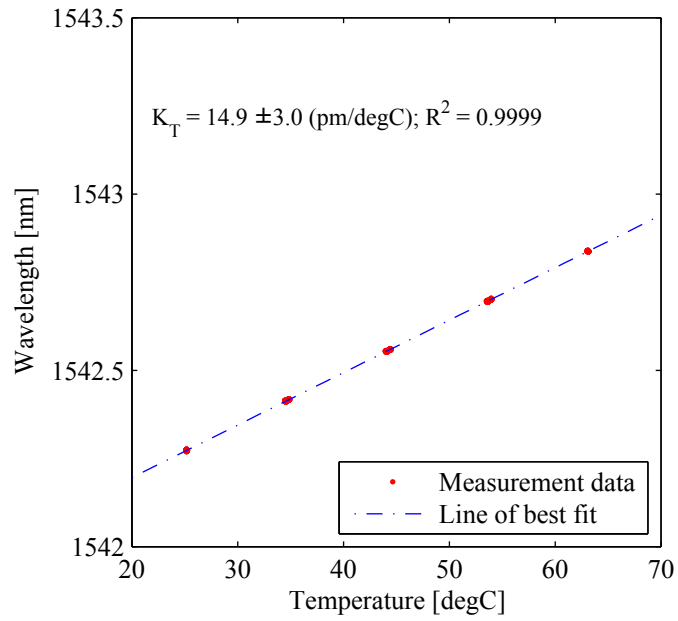
5.3.3.3.2 Results

Some representative results from the thermal characterisation and calibration are presented in Figure 5.27a (strain sensor VIII, as listed in Table 5.7), and Figure 5.27b (temperature sensor VII as listed in Table 5.7). All the strain and temperature sensors' characteristics are summarised in Tables 5.8 and 5.9, respectively. Detailed graphs for each sensor are included in Figures 16 to 34 of the Appendix. Each detailed graph represents each sensor's thermal sensitivity, also known as thermal coefficient K_T , as well as its accuracy based on a 95% confidence interval. In addition, the degree of linear fit R^2 is given. Overall thermal sensitivity of the temperature sensors, with a spread of 14.4 to 16 pm/°C (Table 5.9), is lower than strain sensors exhibiting a spread of 17.3 to 18.6 pm/°C (Table 5.8). These results are in agreement with the previous experiments since the additional steel shim of the strain sensors has a higher thermal expansion than kovar itself, which, consequently, leads to a greater overall expansion and thus sensitivity [249].

Except for temperature sensor IX, all the sensors respond in a highly repeatable man-



(a) Example of thermal characterisation of strain sensor (VIII)



(b) Example of thermal characterisation of temperature sensor (VII)

Figure 5.27: Example of SSE sensor thermal characterisation

ner with an error of ± 0.2 to 0.4 °C. Temperature sensor IX exhibited an error of ± 1.9 °C. On close inspection, it transpired that the error was caused by an incorrect FBG peak detection set-up within the interrogator, resulting in wavelength jumps of approximately 28 pm. For data analysis, the peak detection jumps were filtered from the data set, now resulting in a sensitivity of 14.7 pm/°C and an error of ± 0.21 °C. Also, for any future measurements the peak detection was correctly set.

Similarly, except for strain sensor X, all the strain sensors behaved in a highly repeatable manner, with an error of ± 0.17 to 0.46 °C. Strain sensor X deviated significantly from this range to an error of ± 2.27 °C or ± 40.6 pm/°C (Figure A.17c). However, upon close inspection, it became evident that the sensor must have either moved within the environmental chamber or some internal stresses were relieved caused by the heat treatment during the second cycle, thus its characteristic was based upon the last 3 cycles, not four (Figure A.17d).

Table 5.8: Overview of all strain sensors' thermal characteristics

Channel	Sensor ID	Sensitivity [pm/°C]	Error [\pm pm]	Error [\pm °C]
1	I	18.6	8.5	0.46
1	II	18	5.4	0.3
1	III	17.6	4.7	0.27
2	IV	17.3	8.1	0.47
2	V	18.6	4.3	0.23
2	VI	17.9	6.7	0.37
3	VII	18.1	4.6	0.26
3	VIII	17.2	3	0.17
4	IX	17.4	3	0.17
4	X	17.8	4.3	0.24

Table 5.9: Overview of all temperature sensors' thermal characteristics

Channel	Sensor ID	Sensitivity [pm/°C]	Error [\pm pm]	Error [\pm °C]
1	I	14.4	5.8	0.4
1	II	15.6	4	0.26
2	IV	16	4.5	0.28
2	V	15.4	4.6	0.3
3	VII	14.9	3	0.2
4	IX	14.8	28	1.9

5.3.4 Sensor Installation

5.3.4.1 Assessment of Sensor Placement and Orientation

A circular foundation with tapered slab designed for the Vestas V117 wind turbine to be erected at the wind farm was considered as a test vehicle for the bespoke optical strain and temperature modules. The locations for sensor placement within the foundation were based on the following set of information:

- 3D FEM foundation model (LUSAS) [89]
- Consultation with foundation designers (SWECO)
- Foundation geometry and access (2D CAD Drawings)
- Reinforcement cage installation process
- Wind rose & site assessment

Based on the provided environmental data from three meteorological masts (met. masts) as well as data from a site assessment, turbine T22 was selected for the proposed field trial. This location is characterised by the highest annual mean wind speed as it resides on top of a mountain. The turbine hub height will be 76.5 m and there will be no corridor for wake interaction. It was proposed that the sensors be placed along the prevailing wind direction in order to maximise strain readings. Consequently, the foundation floor was marked along 230 deg based on the provided wind roses shown in Figure 5.20. On site, the wind direction was identified with the help of a compass.

The sensor location experiencing the greatest loading was based on the information from a 3D FEM foundation model [89]. The FEM model revealed that the greatest strain levels can be anticipated 6 m from the outside of the foundation base, hence it was decided to position the sensors within this area. The key steel components of the foundation are the orthogonal, circumferential, and top and bottom radial reinforcement bars the latter two held together by shear links. Concerning the reinforcement bar selection for sensor instrumentation, all available types are aimed to be equipped

on either end of the foundation (mirrored).

One important constraint to consider is the geometry of the reinforcement cage. Even though a specific high stress region is identified for the sensor placement, it is possible that the geometry of the steel cage does not allow sensible sensor placement at such identified location. In addition, the reinforcement cage is built in stages where sensor placement could block subsequent fixing of steel reinforcement bars. Therefore, 2D CAD foundation drawings were taken into consideration to identify suitable locations within the vicinity of the maximum stress/strain regions determined by the FEM model for each strain sensor placement. The final selection was eventually coordinated and agreed with the industrial partners.

Figure 5.28 illustrates a schematic overview of the proposed sensor placement. The five red dots indicate the sensor location at each side along the prevailing wind direction. The grey lines indicate the foundation edges, whereas the black lines indicate reinforcement bars. The top drawing of Figure A12 displays a scaled plan view enabling view of the orthogonal and circumferential reinforcement bars.

The orthogonal reinforcement bars' orientation is directed by the placement of the wind turbine ducts, the alignment that did not agree with the prevailing wind direction. Therefore, the sensor's location is calculated by trigonometry, hence intersecting the prevailing wind direction at an angle of 70° . The foundation design has multiple orthogonal bars placed on top of each other; however, possible sensor placement was constrained to just one location. This location is the bottom orthogonal reinforcement bar ($\varnothing 32$ mm, ID: 10e) that is placed on top of the bottom radial ring of the foundation ring cage (the ring cage is displayed in Figure A.18 of the Appendix). It was proposed that the orthogonal strain sensor was to be placed on to the bottom of the reinforcement bar. This is to ensure that the maximum stress/strain level is recorded by the sensor when bend as the highest stresses occur either on the top or bottom when the turbine tower is rocking fore and aft.

The circumferential reinforcement bar consists of three segments that require to be

rotated in order to be able to place sensors on either side of the foundation along the axis of the prevailing wind direction. The circumferential reinforcement bar ($\varnothing 25$ mm, ID: 31G) selected for sensor placement is positioned at 5.9 m outside of the foundation edge and forms the bottom mat of the reinforcement cage. The circumferential strain sensor was intended to be fixed to the bottom of the reinforcement bar in order to allow placement of bottom radial reinforcement bar on top and avoid collision with the sensor. The bottom drawing of Figure 5.28 displays the elevated foundation view enabling to sight the top and bottom radial reinforcement bars as well as the shear link that is placed in between reinforcement bar 510 and 100.

The selected top radial reinforcement bar ($\varnothing 25$ mm, ID: 510) is the vertically highest positioned radial reinforcement bar in the foundation as illustrated in Figure 12. The most sensible location for the strain sensor is at 6.2 m outside of the foundation base. This is because of the presence of other reinforcement bars within the vicinity of 6 m from the outside of the base, where the sensor placement would overlap with circumferential reinforcement bars that positions shall not be adjusted. The sensor was intended to be attached to the bottom of the reinforcement bar 510. This ensures that the sensor is protected from stepping on and from pneumatic concrete shakers that cannot come in direct contact with the sensor after placement.

The selected bottom radial bar ($\varnothing 25$ mm, ID: 100) belongs to the bottom mat of the foundation reinforcement cage. Sensor placement appears most sensible at 5.6 m outside the foundation base due to the presence of other reinforcement bars within the vicinity of 6 m from the outside of the base. In terms of the sensor installation onto reinforcement bar 510, it was proposed that the strain sensor was to be attached to the top of the bar. The top has been selected because there is a wider available space and there are further bottom radial reinforcement bars above securing this location from workers to step and as well as from the direct impact of pneumatic concrete shakers.

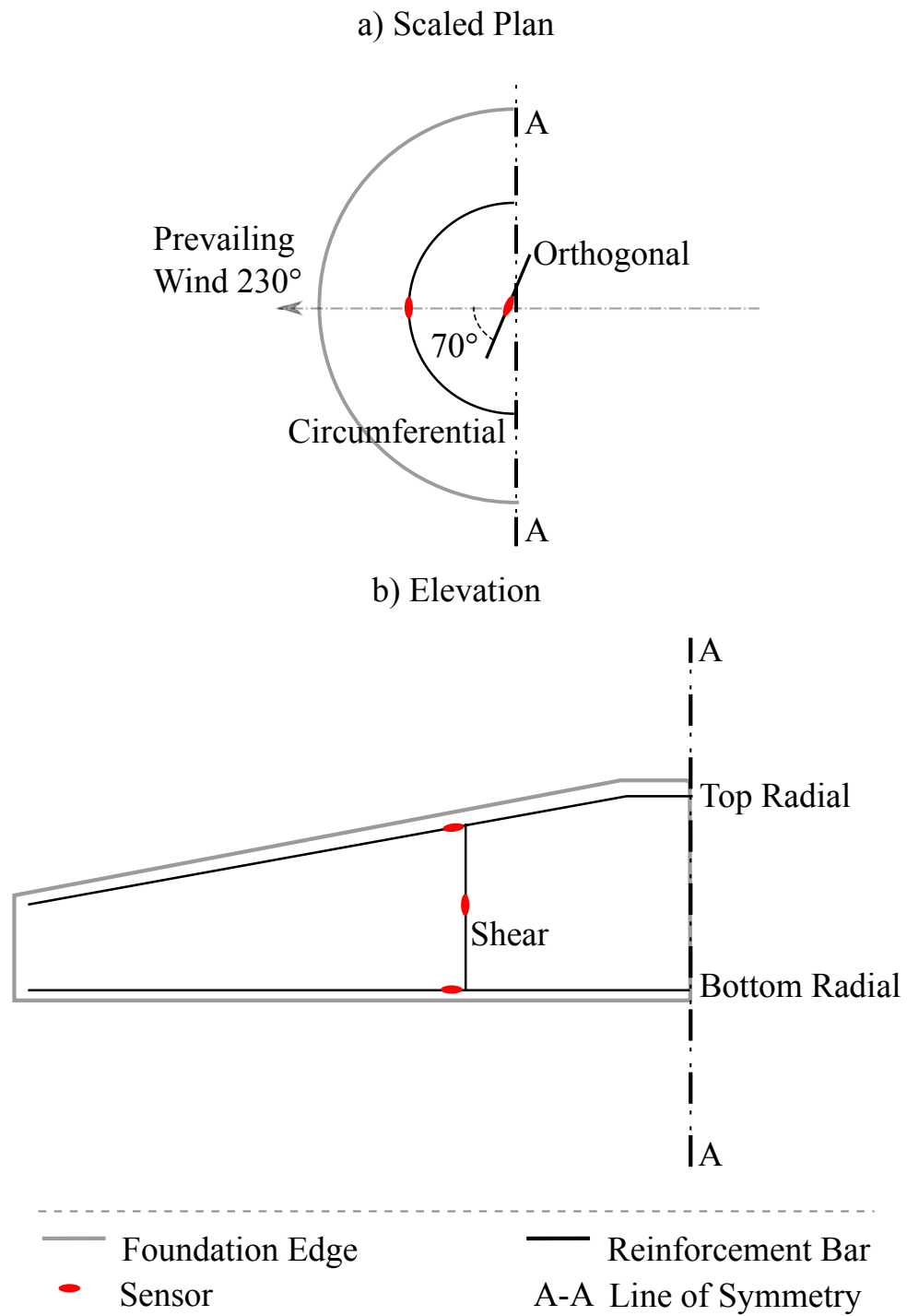


Figure 5.28: Schematic overview of sensor locations. The A-A line is the foundation centre. Red dots indicate the strain sensor placement within the foundation

The selected shear link ($\varnothing 8$ mm, ID: 612) is the one closest to the determined highest stress/strain regions than the remaining shear links in the vicinity. More specifically it is placed 6 m from the outside of the foundation base. Therefore, it was proposed that the sensor was to be placed in the centre of the foundation height and installed onto the reinforcement bar facing the foundation ring cage.

Figure 5.29 further illustrates a 2D foundation CAD drawing where the selected reinforcement bars are highlighted in red.

5.3.4.2 Sensor Installation

Each sensor installation followed the following procedure:

1. Identification of rebar location
2. Surface preparation of reinforcement bar to remove rust and debris
3. Spot welding of sensors to the cleaned reinforcement bar
4. Attachment of protective steel half tube
5. Attachment of temporary protection
6. Placement of reinforcement bar in foundation
7. Cable connectorisation
8. Removal of temporary protection after 12 hours to allow curing of the epoxy and silicone
9. Final cable connectorisation

As an outcome of the sensor placement assessment of section 5.3.4.1, the intended sensor location was known, thus at the site the sensor area was marked with spray paint after measurement to ease installation. Surface preparation is critical to ensure reliable sensor attachment using spot welding [249]. Therefore, care was taken to prepare the surface with drill sanding bits, initially with P80 grit and subsequently

with P400. Figure 5.30 a) illustrates the surface preparation process. A fully prepared reinforcement bar is shown in photograph b). Once the surface was prepared, the sensor was attached with a portable spot welding unit (intensity setting adjusted to 40 J per spot weld) as shown in Figure 5.30 c)⁴. Photograph d) illustrates the finished result the sensor attached onto the reinforcement bar.

As explained in Section 5.3.2, in order to protect the sensor, a half steel tube was placed on top of the sensor. This was kept in place with flexible silicone along the strain transducer and fixed with epoxy at both ends. The half steel tube placement is further illustrated in photograph e) of Figure 14. In order to keep the half steel tube in place during the epoxy/silicone curing process, the arrangement was wrapped in cling film. This also offered shielding from water ingress. Depending on the circumstances, sensors were either installed outwith the foundation (Figure A.19a of the Appendix) or within (Figure A.19b of the Appendix), although most installations were carried out outwith for health and safety reasons and to not to disturb steel workers. Overall, sensor modules were installed as follows, where strain and temperature modules are abbreviated S&T and strain sensors alone, S, respectively:

- Channel 1: orthogonal (S - III), circumferential (S&T - II), and bottom radial (S&T - I)
- Channel 2 (direction facing the side entrance): orthogonal (S - VI), bottom radial (S&T - IV), and circumferential (S&T - V)
- Channel 3 top radial (S&T - VII) and shear link (S - VIII)
- Channel 4 (direction facing the side entrance): top radial (S - X) and shear link (S&T - IX)

For Channel 1 and 2, the sequence of module multiplexing is also kept as initially aimed since this can potentially help to locate weak areas/connections that were damaged during installation or concrete pour. In more detail, information from the interrogation spectrum paired with knowledge about how it should be can help to identify at what

⁴Before installation, the sensor was fully cleaned from oxidation and deposits caused by the induction heating process in the laboratory

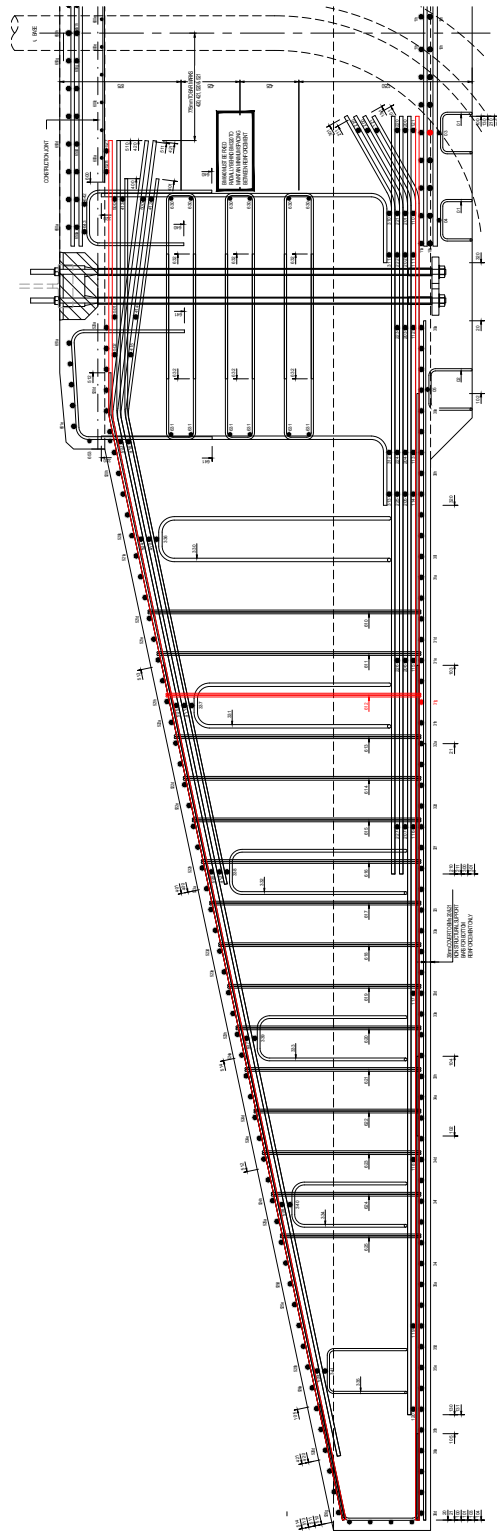


Figure 5.29: Rebar selection

stage the multiplexed interrogation cable is damaged. This is not required for channel 3 and 4 as there are only two modules anyway making it clear to assess as no module sits in between.

Against the initial planned sensor placement (Section 5.3.4.1) some sensor locations deviate due to the actual sequence of construction of the reinforcement cage and installation errors. In particular, all radial sensors (top & bottom) and both shear links could not be positioned directly at 230° . After installation, the circumferential distance was measured and the angular difference calculated. As a result, the previously mentioned sensors are positioned at a direction of 236.25° ; however, as exact measurement was not possible with the available compass (due to the vicinity of steel), wind entry corridors of $5\text{-}10^\circ$ are intended to be evaluated rather allowing for minor placement errors, based on SCADA input data that could also experience slight inaccuracies in its calibration. Furthermore, both bottom radial sensors were not installed as initially planned as the bars were rotated by the steel workers and the sensors faced upwards. The bottom radial strain sensor (IV) of channel 2 is situated at 5 o'clock looking from the direction of the side entrance and the bottom radial strain sensor (I) of channel 1 is placed at 9 o'clock looking from the opposite of the side entrance (reinforcement bar BM100 is straight and can be freely rotated). Unfortunately, this was noticed too late in the process and could not be rectified as several more steel layers were already placed above. At the same time with the use of FEM, this error can be taken into account in order to extract maximum stress levels for fatigue calculations.

In addition, due to a communication error the top radial strain sensor (X) of channel 4 is placed at 5 o'clock looking from the side entrance although aimed at installation at 6 o'clock, thus facing downwards. This could not be rectified either, because the top radial reinforcement bar is bend as illustrated in Figure 12 thus it is impossible to rotate the sensor to the correct placement. Once again, FEM modelling can be applied to extract maximum stress levels.

Cables between sensors were pre-prepared (distances were extracted from foundation CAD drawings) and tested in the lab, thus sensor modules could be quickly inter-

connected. Steel armour was placed over this interconnection and crimped onto the tactical tight buffered optical cable. Shrink sleeve was placed over this section and heated with a 110V heat gun to achieve sealing against water ingress. Cables running within the foundation towards the foundation centre were attached to reinforcement bars with cable ties. From the centre a duct provided by SSE guided the cables out of the foundation. It was not possible to check the optical network integrity after all modules were installed and interconnected due to severe weather conditions, preventing the use of the sensor interrogator. This was unfortunate, as it is now very difficult to narrow down the potential causes of sensor losses; i.e., due to the installation process or due to the concrete pouring and compaction process or movement of cable ducts. At the same time, during sensor installation, no visible faults were observed that could have negatively impacted the sensor network, nor the sensors.

At the end of the installation process, the cables exiting the ducts were placed inside waterproof polyethylene bags that placed inside tough bags connected to the ducts to seal the cable and connectors from rain.

5.3.4.3 Results

It became apparent early on during the concrete pour that two interrogation cables had been damaged (location and damage mechanism were not provided) and were removed from the foundation entirely by the foundation contractor. As a consequence, channel 4 was lost completely. It is difficult to judge what could have happened although, on closer inspection of the removed cable, it is possible to observe that the crimped steel armour at the module connection must have failed to sit tight on the buffered cable. As the cable must have been subjected to severe stresses, possibly when adjusting the position of the cable ducts, this point of weakness must have given in and the cable broke.

Two weeks after the concrete pour, each channel was interrogated to evaluate the health of installed sensor network. Upon arrival it was evident that two bags have disconnected from the ducts (red circles in Figure 5.31), the duct of channel 3 was

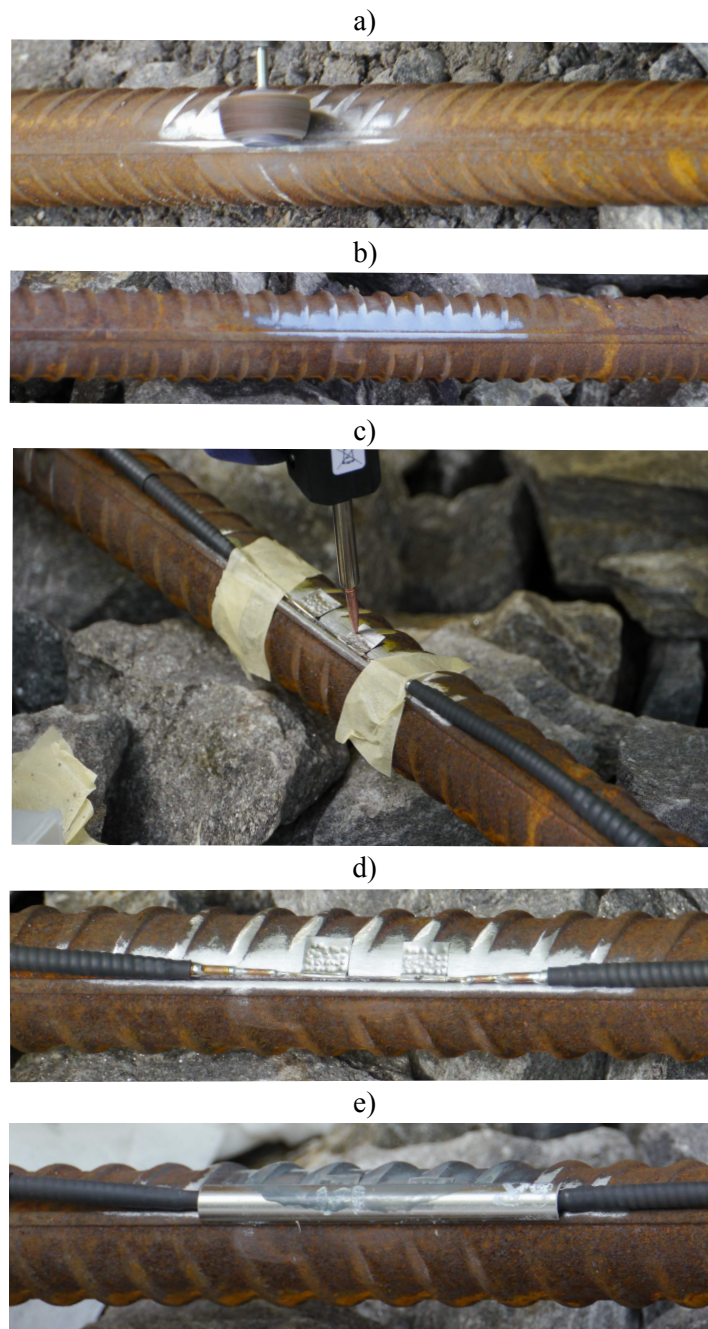


Figure 5.30: Sensor installation overview - a) surface preparation, b) prepared surface, c) sensor attachment (spot welding), d) attached sensor, e) sensor protection

empty as the cables were pulled out (blue circle in Figure 5.31), and the remaining duct remained sealed as left after installation. In total 4 out of 16 sensors (ten strain sensors and six temperature sensors) survived. As the sensors are spectrally encoded and are characterised by unique peak wavelengths, it was possible to identify which sensors can still be interrogated:

- V circumferential (temperature & strain) of the site entrance area side and
- IX shear link (temperature & strain) of the same site

Based on the evidence that both responding modules (V & IX) survived entirely (strain and temperature sensor) the concrete pour it appears unlikely that a module got damaged internally. Therefore, the crimped connections in between modules and interrogation cables are likely to have failed here as well rather than something within a module. Nevertheless, it appears that in these two cases where modules survived, the crimped connection from one side was rugged enough to withstand impacts during the concrete pour.

It is to note that there is a chance that where the cable protection failed at the end



Figure 5.31: Inspection of foundation after concrete pour

of the duct (red circles in Figure 5.31), the internal fibre might have broken allowing

it to be re-spliced once the turbine is erected. This could potentially reactivate some sensors, although the chances of that are thought to be small.

5.3.5 Results of Monitoring Campaign

Due to access restrictions, the team could not frequently access the turbine to monitor the foundation sensors during curing and foundation installation. As such, only two dates were available to evaluate the impact of the turbine weight and rheological strain (creep and shrinkage) [253]. The first date was shortly after concrete curing, while the second date was shortly before turbine commissioning. Results show that both foundation strain sensors experience a tension of around $360 \mu\epsilon$ that is in the same order of magnitude as identified by Bai et al. [55]. It is worth noting that, as expected, the foundation temperature sensors did not experience such a transition.

The following Section presents data readings from 67 days of measurement recorded between June and August 2017. Before, the FBG strain gauge data was analysed, their signal was temperature compensated with the pre-characterised temperature sensors as presented in Section 5.3.3.3 and outliers were filtered out, the latter likely to be introduced by FBG peak detection errors in the interrogation system. The process is exemplified in Figure 5.32 of a tower location and in Figure 5.33 of a foundation location. In order to translate the change in recorded wavelength to a strain and hence stress value, the field trial's set-up was replicated in a laboratory to identify the sensor's operational sensitivity for the tower and foundation sensors as highlighted in Section 5.1.

5.3.5.1 Sensor Data

Figure 5.34 presents the time series of the normalised strain of the circumferential strain sensor in comparison to the parallel tower strain sensor (T1). In addition, Figure 5.35 presents the circumferential's time series, although in comparison to the 90 degree rotated tower strain data (T2).

The operational data was further tested under the hypothesis of an underlying normal

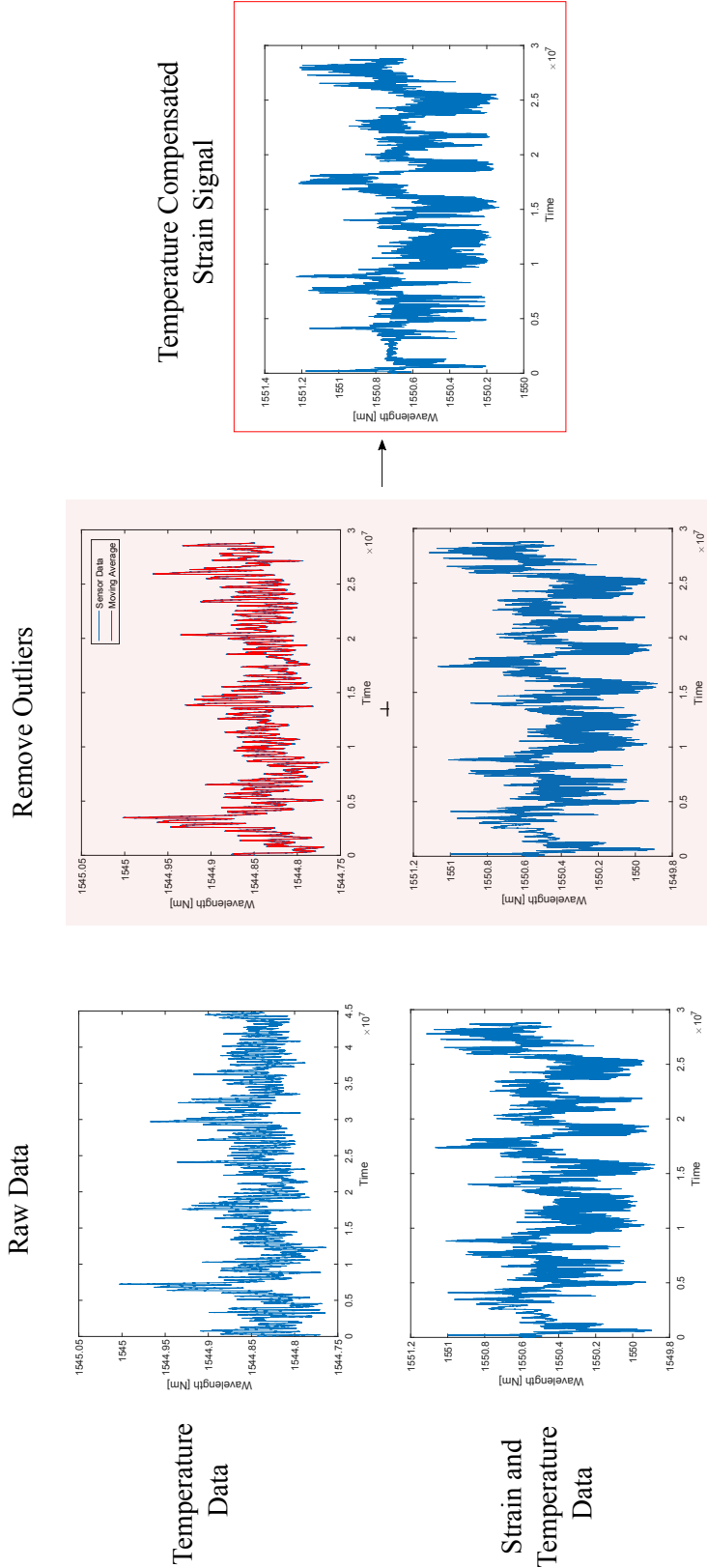


Figure 5.32: Signal processing and temperature compensation of a tower location

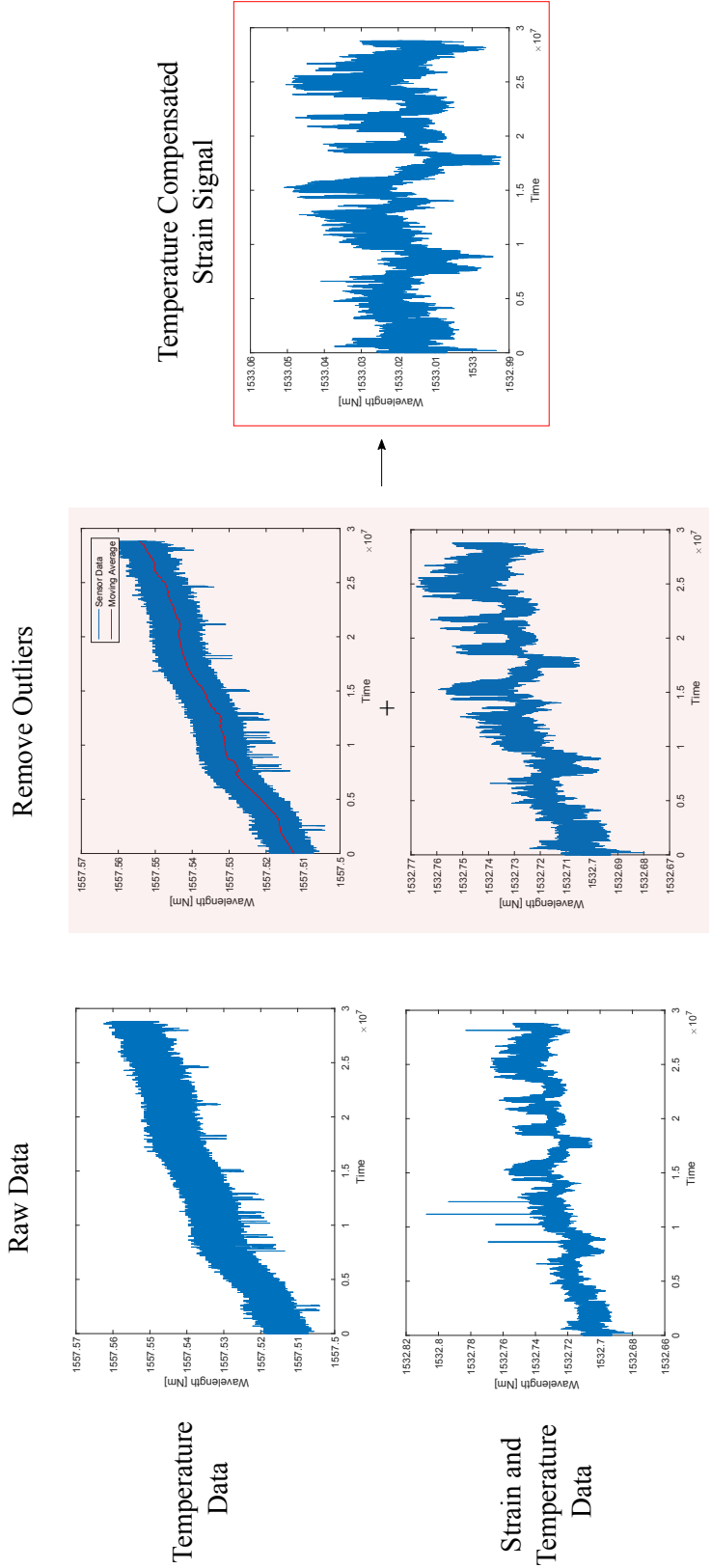


Figure 5.33: Signal processing and temperature compensation of foundation location

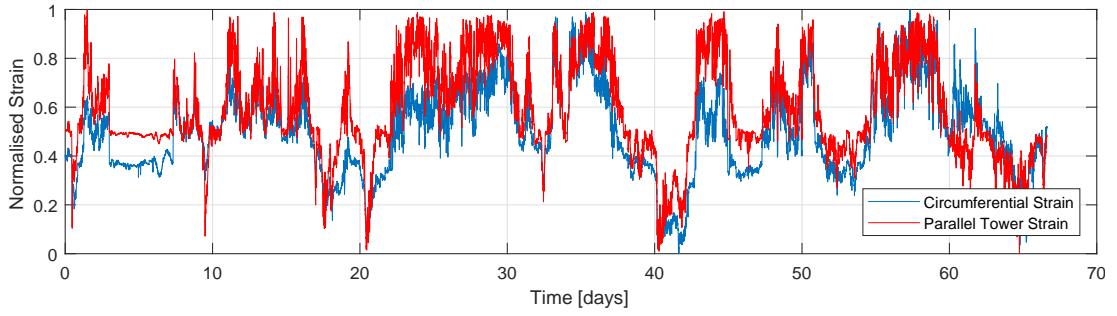


Figure 5.34: Time series of normalised strain of circumferential foundation and parallel tower sensor. Each sensor is normalised separately.

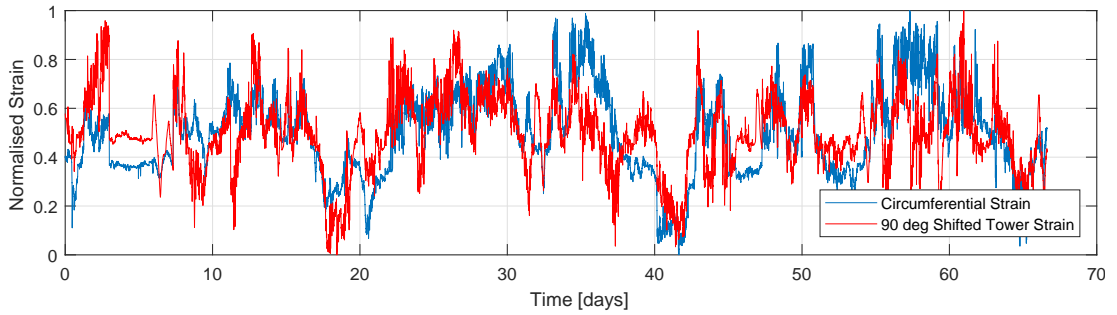


Figure 5.35: Time series of normalised strain of circumferential foundation and 90 deg rotated tower sensor. Each sensor is normalised separately.

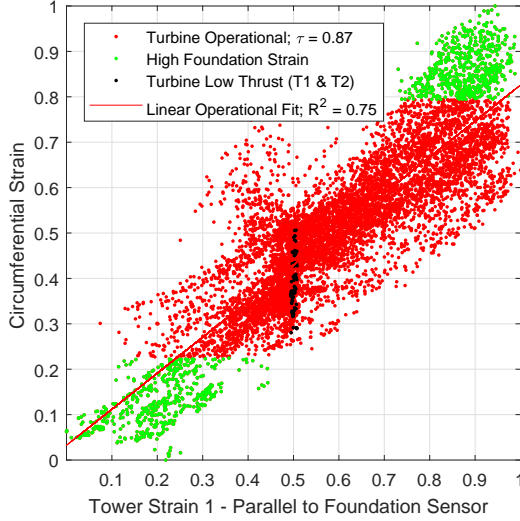


Figure 5.36: Normalised correlation of shear link strain with parallel tower sensor.

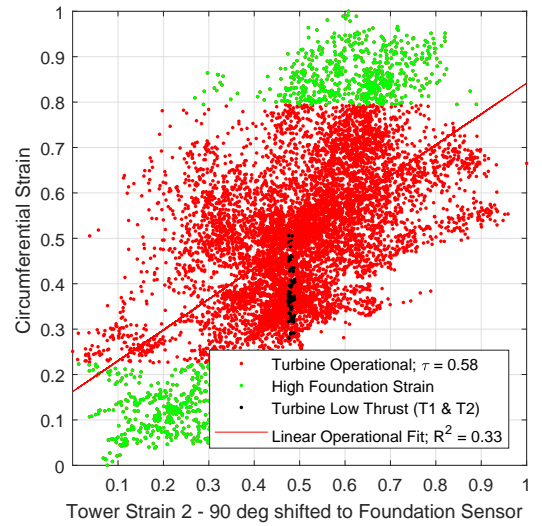


Figure 5.37: Normalised correlation of shear link strain with 90 deg rotated tower sensor.

distribution by means of the Kolmogorov-Smirnov and Lilliefors test. Both tests confirmed that the strain data is normally distributed. Therefore, the Pearson correlation coefficient, τ was selected to determine the degree of correlation of the operational data [254]. The circumferential sensor correlation is illustrated in Figure 5.36 and 5.37. In addition, the operational data was fitted to a linear function and the fit was tested by means of R^2 . Findings are further classified in three operational modes of the turbine: i) operational (red data points), ii) under vertical dead load tower strains (T1 and T2) and iii) under high foundation strain (green data points). Each point represents the 10-minute mean of 1599 hours of measurements.

Results show a strong positive correlation between the measured parallel tower strain with a correlation coefficient, τ of 0.87, whereas a moderate positive correlation with the 90 degrees rotated tower strain ($\tau = 0.58$). With respect to the shear link strain measurements, unfortunately three days after turbine commissioning a peak detection error occurred. Therefore, 1.6 days of operational data is available. Overall, findings are slightly different for the shear link strain measurements as illustrated in Figure 5.38 – 5.40. Findings also show a strong positive correlation ($\tau = 0.90$) with the parallel tower FBG strain gauge and a weak positive correlation ($\tau = 0.5$) with the 90 degrees rotated tower sensor, respectively.

Figure 5.42 further displays a noise component that is picked up in the foundation strain signals. This noise first appeared when the turbine got energised and is further picked up in the foundation temperature sensors. The signal component periodically varies in frequency and magnitude and does not coincide with any of the turbine's natural modes. Based on this evidence, this is likely caused by vibrations of either the wind turbine generator's (WTG) hydraulic system and or the transformer. The latter that is located inside the turbine on top of the foundation.

Furthermore, all correlation graphs display a certain level of noise that is likely caused by i) slight errors in the temperature compensation, ii) a causality of the combination of T1 and T2's vertical tower strain on the foundation strain, iii) the underlying fluctuating foundation vibration as illustrated in Figure 5.42, and iv) the impact of yawing and the turbine's control such as for example the individual pitch control algorithm.

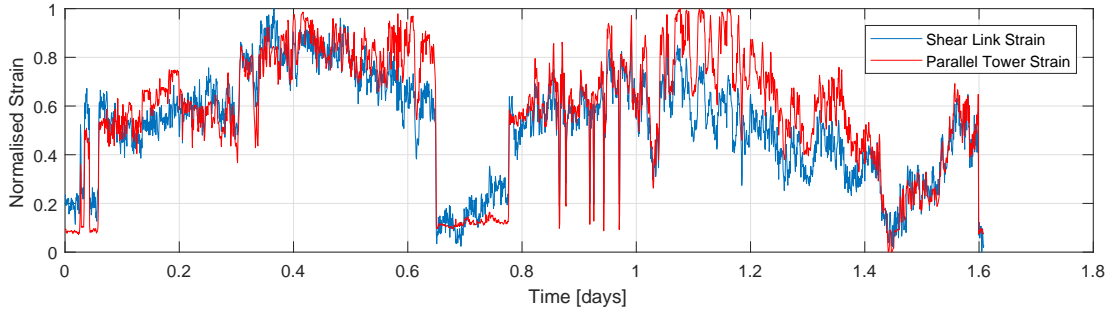


Figure 5.38: Time series of normalised strain of shear foundation and parallel tower sensor. Each sensor is normalised separately.

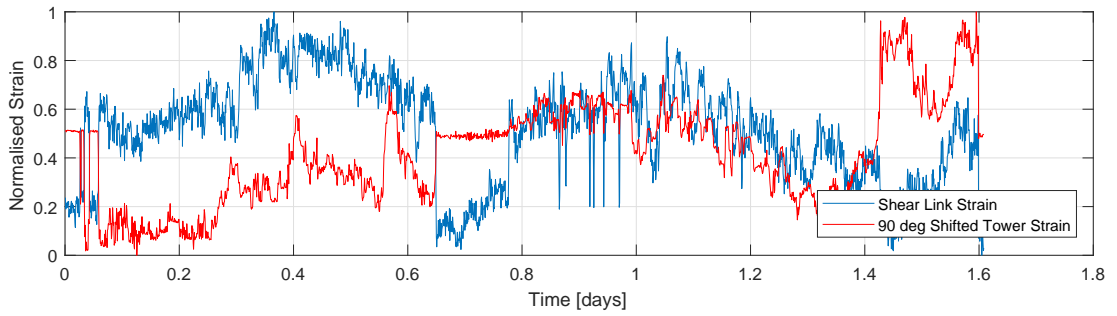


Figure 5.39: Time series of normalised strain of shear foundation and 90 deg rotated tower sensor. Each sensor is normalised separately.

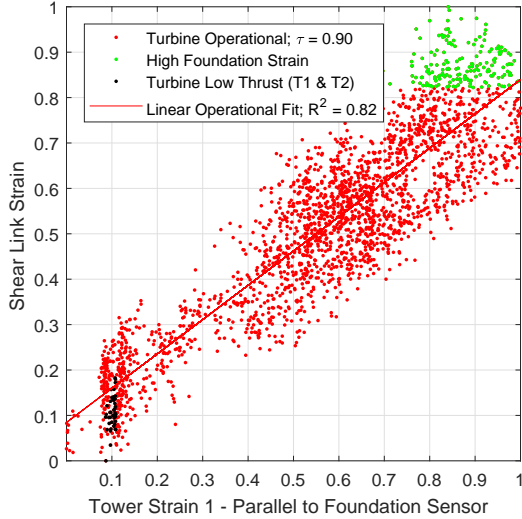


Figure 5.40: Normalised correlation of shear link strain with parallel tower sensor.

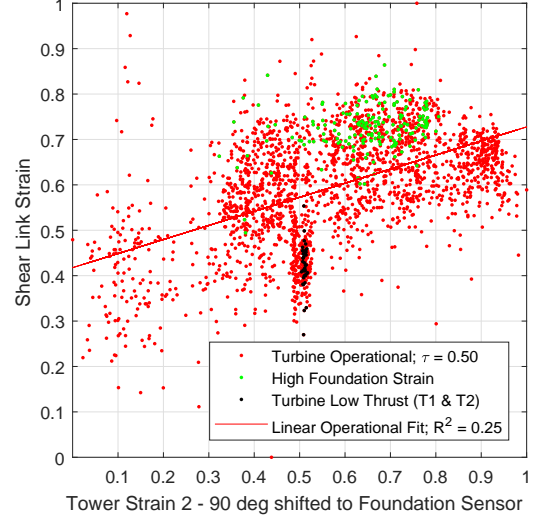


Figure 5.41: Normalised correlation of shear link strain with 90 deg rotated tower sensor.

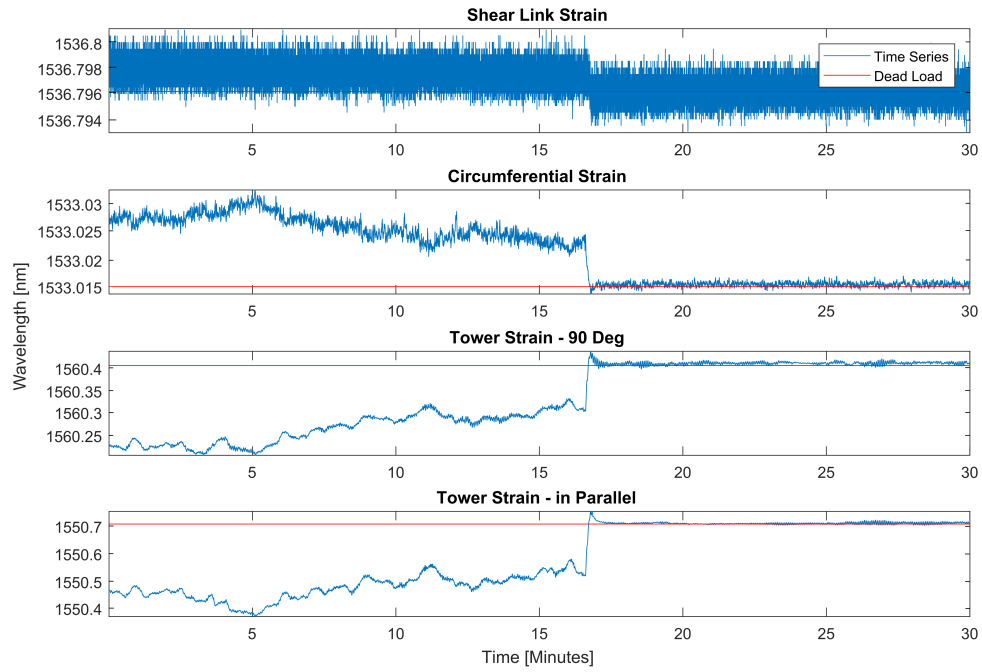


Figure 5.42: Time series of sensor measurements. The red line indicates the dead load condition.

Table 5.10 illustrates the normalised average dead load (compiled from the dead load condition identified in Figures 5.36, 5.37) of the tower and circumferential foundation strain sensor.

Results reveal a normalised average dead load value of 0.5 for T1, thus along the prevailing wind direction and oppositely an equal absolute maximum positive and negative strain was encountered in the observed period. This agrees with expectations as the deployed wind turbine has a predominant bi-directional wind-inflow condition. For T2, the mean is marginally shifted indicating a slight imbalance in the absolute maximum positive and negative strain. This is also expected due to an overall lower probability that the turbine is acting in either of the two directions. Different results are found for the circumferential foundation sensor. In fact, the mean is substantially shifted meaning that the sensor has observed higher tension stresses than compression stresses. This is in agreement with the design assumption; i.e., concrete has essentially no tensile strength, so the steel reinforcement takes up the strain, whereas during compression the concrete is able to withstand the stress, thus alleviating strain from the

reinforcement [255].

Table 5.10: Dead Load Condition

Strain Sensor	Normalised Average Dead Load
Tower T1	0.5
Tower T2	0.48
Circumferential	0.38

For the shear link this analysis was not possible to execute, because in the limited time period the wind inflow was not opposing the predominant wind direction.

5.3.5.2 FE Comparison

It is overall challenging to verify the FE model as it is a stationary model, while the turbine is subjected to a stochastic wind inflow, hence characterised by a dynamic response. Further complexity arises from multiple other reasons, namely: i) the turbine operates under different control regimes such as for example below and above rated, paired with an individual pitch control algorithm, ii) there is currently no available access to high frequency supervisory control and data acquisition (SCADA) measurements, and iii) the turbine's nacelle orientation with respect to the sensor direction is unknown, although the power spectral density of the tower base FBG strain gauges can give a reasonable estimate. Given such challenges, the aim is to evaluate if the measured strain ranges agree with those expected from the FE model or alternatively by what magnitude the strain is under or overestimated.

Generally, the sensor data agrees with the simplified FE model, the results of which are shown in Figure 5.43 and Figure 5.44. Indeed, the circumferential strain sensor experiences a substantially higher strain magnitude than the shear link. The lack of deformation in the axial direction is highlighted by the deformed mesh in Figure 5.44 and this confirms operator's existing knowledge. This is also the reason why the shear link strain in Figure 5.42 appears noisy in relation to the circumferential sensor's measurements. The circumferential strain reaches $95 \mu\epsilon$ whereas the shear link reaches maximum strains of $6 \mu\epsilon$. This is in agreement with the FEA's data that suggest a reduction of the shear link strain by an order of magnitude in comparison to the

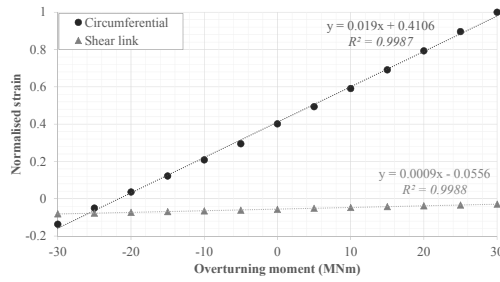


Figure 5.43: Normalised change in strain in shear link and circumferential rebars, extracted from the FE model. Positive overturning moments follow the wind vector given in Figure 5.21

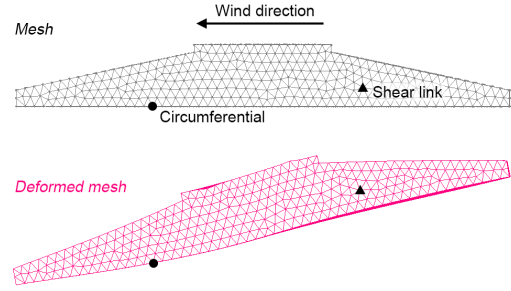


Figure 5.44: Mesh and sensor locations before and after loading (deformed mesh scaled by 10^3).

circumferential rebar's strain.

Figure 5.43 also illustrates that the foundation system favours positive (tensile) circumferential strains, regardless of the direction of the wind. The reason for this is the impact of the foundation, tower and ballast dead loads, and the fact that the soil below the foundation only supports compression (due to the lift-off boundary condition). The overturning moment zero crossing-point in Figure 5.43 cannot yet be directly compared with the measured data, as SCADA data (and hence knowledge of overturning moments) is not available at the time of writing.

5.3.6 Validation

Figure 5.45 and Figure 5.46 illustrate the power spectral density (PSD) of the different strain and temperature signals allowing to identify structural modes, the rotor frequency (1P) as well as the rotor frequency's harmonics (nP) [256,257]. For the identification of the signals system frequencies, Table 5.11 is taken into consideration and used as a reference of the frequency domain analysis.

With regards to the installed tower FBG strain gauges, both tower pairs (strain gauges are 180 degrees apart) show an equal PSD. This is in agreement with Newton's third law of motion [262], verifying a correct installation with the sensors exhibiting identical strain transfers. The tower temperature sensor has a significantly different PSD, suggesting that the actual tower strain is not picked up in the signal; however, a dom-

Table 5.11: Natural Frequencies of Wind Turbines [Hz]

Turbine	Blade Radius [m]	1 st Blade Flap	1 st Blade Edge	1 st Tower Fore-Aft	2 nd Tower Fore-Aft	Source
Siemens 2.3 MW	49	0.99	1.8	0.34	2.2	[258]
SuperGen 5 MW	63	0.68	1.08	0.28	2	[259]
NREL 5 MW	63	0.66	1.07	0.32	2.9	[260]
DTU 10 MW	89	0.61	0.93	0.25	1.38	[261]

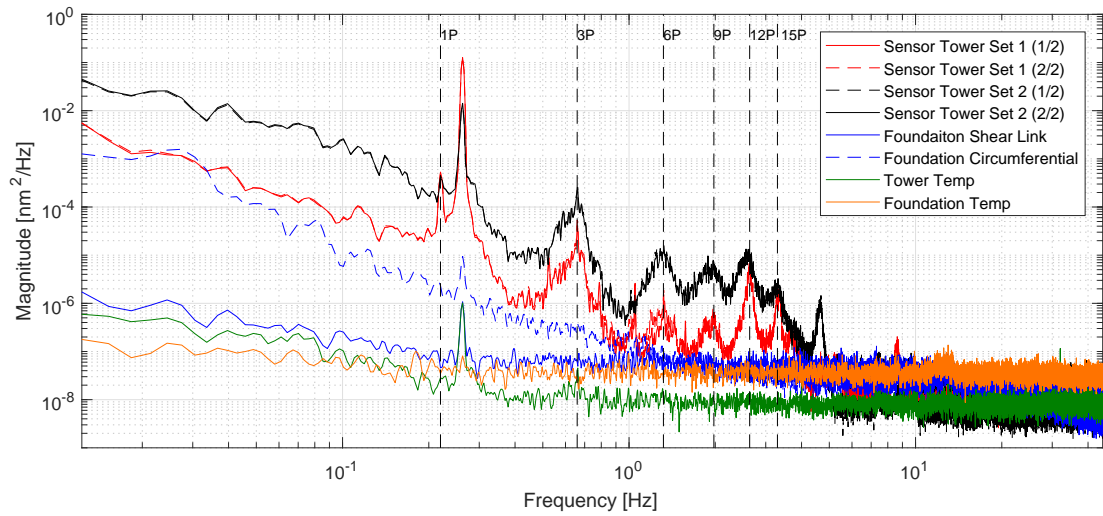


Figure 5.45: Power spectral density of strain and temperature sensors with rotational sampling and harmonics. Temperature sensor: raw data; FBG strain gauge: temperature compensated.

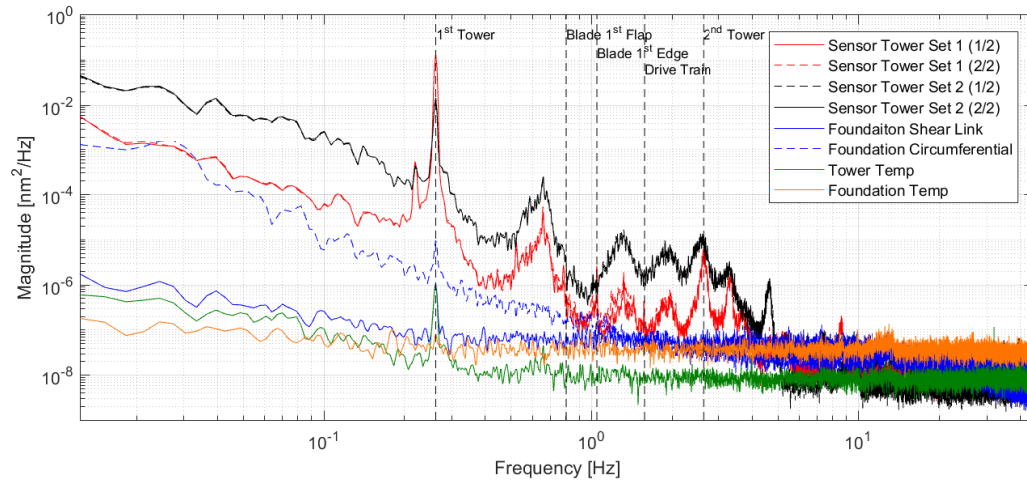


Figure 5.46: Power spectral density of strain and temperature sensors with natural frequencies. Temperature sensor: raw data; FBG strain gauge: temperature compensated.

inant structural mode is picked up. In essence, it is challenging to completely isolate a temperature sensor from the structure's vibration, but given that the power in the mode is significantly lower in magnitude compared to the power level observed in the strain sensors, this is acceptable. Further, the temperature sensors are filtered with a moving average within the window of 80 s, hence effectively eliminating these signals altogether. Temperature readings are therefore observed as fit for purpose for temperature compensation of the corresponding tower FBG strain gauges.

With regards to the foundation FBG strain gauges, both PSDs have an equal distribution, although the shear link has a lower overall magnitude. This difference agrees with the FE model as well as feedback from the foundation designer. Both foundation sensors further pick up the first tower mode, giving confidence in their readings. The foundation temperature sensor's PSD picks up the first tower mode; however, similarly to the tower sensors on a much lower magnitude allowing confidence in its application for temperature compensation. In addition, at lower frequencies, the power in the foundation temperature signal (e.g. daily variations) is lower than the tower temperature sensor, which is expected as the temperature changes at a higher rate at

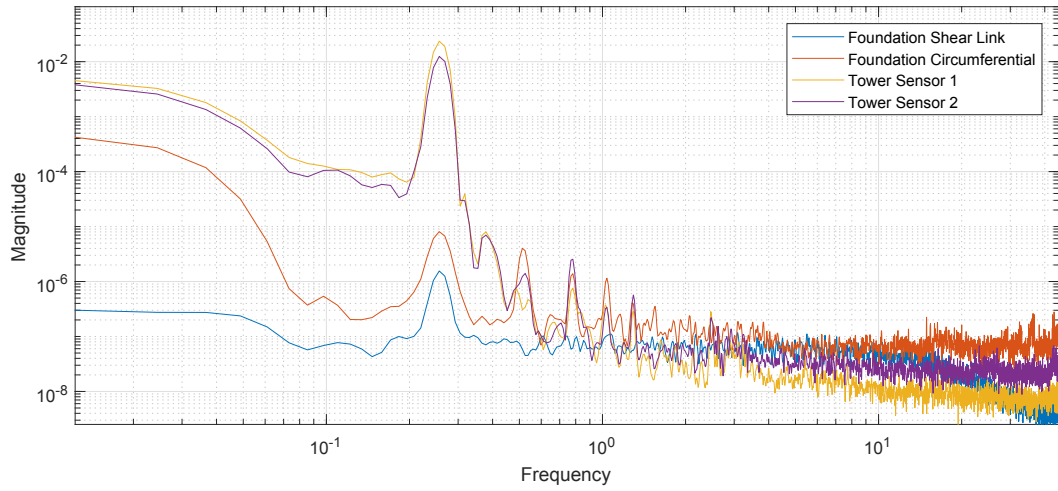


Figure 5.47: Power spectral density of foundation and bottom tower FBG strain gauges. Temperature sensor: raw data; strain gauge: temperature compensated.

the bottom tower section than in the buried foundation. Further, results are in agreement with findings of the PSD of the turbine's emergency stop, executed as part of the commissioning as illustrated in Figure 5.47. This data illustrates well how the optical strain gauges detect the turbine's propagating natural modes and their harmonics.

For the tower sensors, the signal was further long-term evaluated based on a calibration technique suggested in the IEC 61400-13 standard, where the yaw retwist events can be used to evaluate the sensor sensitivity and potential long-term drift [263]. Over the monitoring period, 4 yaw retwist events were observed in total. Figure 5.48 and Figure 5.49 present the absolute change in sensitivity in between both tower sensors and over time (slight changes may be induced by a variation in wind load) as well as the long-term drift pattern.

Overall, tower sensor 1 has an average sensitivity of $46.4 \mu\text{m}$ whereas tower sensor 2 has $47 \mu\text{m}$, respectively. The results thus indicate that the sensors were installed with an equal sensitivity with an absolute error of 1.1% which is insignificant and acceptable as the impact is negligible on the overall fatigue analysis. With regards to the long

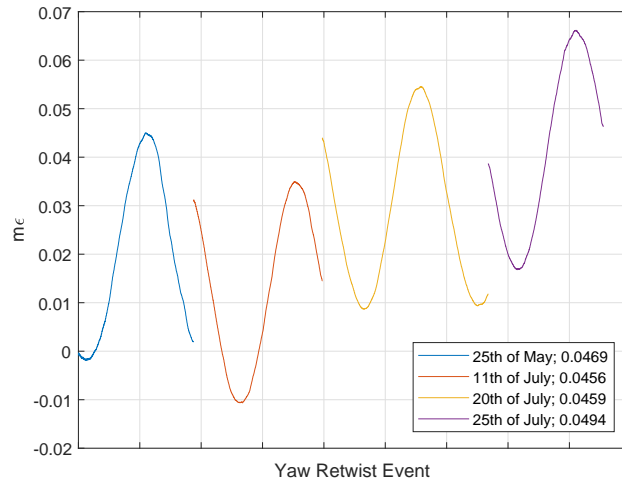


Figure 5.48: Long term validation based on yaw retwist events for tower sensor 1. The x-axis represents separate time events with the exact date of retwist illustrated in the legend. Each retwist event is roughly a 10-minute period. The legend also states the magnitude of the observed signal at the given time.

term drift, it is possible to observe that both sensors marginally drift by roughly $20\mu\text{m}$ which is in comparison to the absolute observed measurement range of $1200\mu\text{m}$, 1.6% and thus considered acceptable.

The analysis is also executed for the circumferential foundation strain as illustrated in Figure 5.50. Overall, it is observable that the absolute magnitude increased from $1.16\mu\epsilon$ to a plateau of $2.3\mu\epsilon$ with an observable drift of $1.5\mu\epsilon$. The latter that is in comparison to the absolute observed range of the total observed strain 1.7% and thus acceptable. The difference in the observed magnitude can be considered significant and might be attributed to micro-cracking of the concrete. Further long-term data may help to evaluate if the micro cracks stabilised over time.

5.3.7 Commercial Evaluation

While this field trial is part of Strathclyde's Technology and Innovation Centre research and development project, its commercial implications are important to consider for potential future installations. In order to evaluate how the economy of scale could influence the cost of the system, it is important to first determine the feasible number

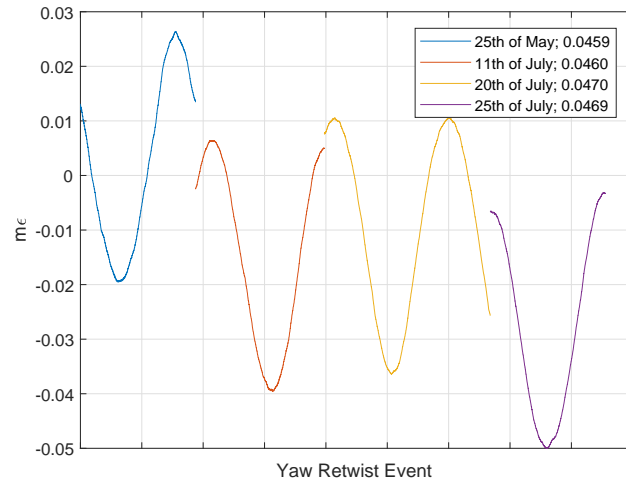


Figure 5.49: Long term validation based on yaw retwist events for tower sensor 2. The x-axis represents separate time events with the exact date of retwist illustrated in the legend. Each retwist event is roughly a 10-minute period. The legend also states the magnitude of the observed signal at the given time.

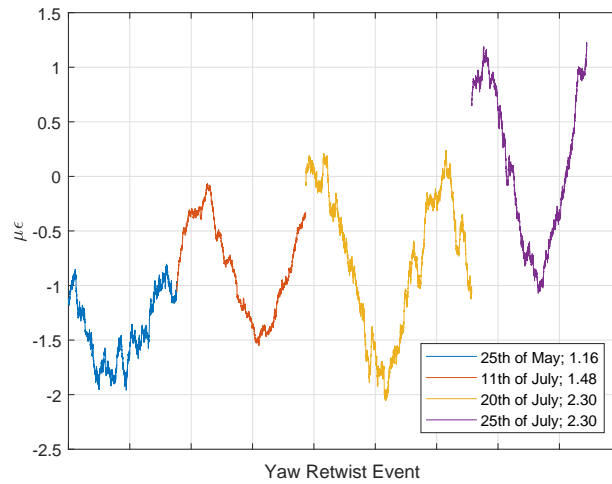


Figure 5.50: Long term validation based on yaw retwist events for circumferential foundation strain. The x-axis represents separate time events with the exact date of retwist illustrated in the legend. Each retwist event is roughly a 10-minute period. The legend also states the magnitude of the observed signal at the given time.

of wind turbine foundations that could be instrumented. Based on a conservative estimate that in 2017 there will be 7GW of newly installed onshore capacity in Europe (0.45 GW UK), paired with an average turbine size of 2.5 MW, this results in 2800 individual turbines (UK: 1.88MW - 225 turbines - UK average turbine size is 2 MW [236]). Furthermore, a conservative assumption that every 10th turbine foundation could be instrumented with an optical sensor SHM (structural health monitoring) system results in a total of 280 installations p.a. (23 for the UK) - based purely on the forecasts for 2017. With regards to potential price reductions due to economies of scale, the greatest identified cost drivers will be accrued in the following system components:

- Sensor interrogator
- Military cable & connectors
- FBG inscribed in copper coated fibre
- SmartAggregates (distributed temperature sensors)

These system components were subjected to pricing quotations based on the number of predicted installations in Europe. For all other items, quotes for bulk orders have not been obtained as their capital expenditure is on average one order of magnitude lower than the items listed above, but a cost reduction of 5% for 10 installations and 10% for 100 installations has been assumed. Manual labour would potentially be subjected to a more significant cost reduction as processes can be standardised allowing sensors to be manufactured in batch with potential for process automation during manufacture. Any reduction in cost would depend on the level of investment in the manufacturing process development/improvement and an organisation contracted to undertake sensor production. Since this is unknown at present, these costs have not been included in the actual breakdown of cost, limiting it purely to physical system components.

Each installation is assumed to be the same as the one described in this work, thus including the preparation and deployment of a total of 20 sensors (12 strain and 8 temperature including spares). Furthermore, based on learning experiences, the cost reduction of the required cost-critical components is assumed with greater economies of scale due to an overall reduction in component damage during manufacture.

Chapter 5. Structural Health Monitoring of Wind Turbine Structures

Installation costs such as accommodation, transportation, labour, overheads, NRE (non-recurring engineering) etc. are not included as such items vary greatly and thus depend on the entity undertaking the installation, location, time of the year, and degree of potential to plan ahead as well as availability and experience of staff.

Table 5.51 provides a breakdown of cost for a potentially follow-on installation, 10 installations and 100 installations. Additionally, the cost of installation of SmartAggregate temperature sensors is provided as an option or project add-on.

The summary of cost savings based on the economies of scale are presented in Table

Item	Qty	Follow-on installation		Qty	10 installations		Qty	100 installations		
		£/unit	£ Total		£/unit	£ Total		£/unit	£ Total	
Sensor manufacture										
FBG in copper coated fibre	30	90.00	2,700.00	25	50.00	1,250.00	20	30.00	600.00	
Tactical cable	32	3.20	102.40	32	3.04	97.28	32	2.88	92.16	
Brazing material	1	30.00	30.00	1	28.50	28.50	1	27.00	27.00	
Sets of Military Pigtailed	12	102.45	1,229.40	10	87.81	878.10	10	79.40	794.00	
Sleeves	1	50.00	50.00	1	47.50	47.50	1	45.00	45.00	
Steel shims	1	100.00	100.00	1	95.00	95.00	1	90.00	90.00	
Kovar capillaries	1	50.00	50.00	1	47.50	47.50	1	45.00	45.00	
Splice Protectors	50	0.15	7.50	50	0.14	7.13	50	0.14	6.75	
CU1300 fibre	4	11.00	44.00	4	10.45	41.80	4	9.90	39.60	
Manufacture expenditure			4,313.30	2,492.81			1,739.51			
Field installation										
Ducts	4	20.00	80.00	4	19.00	76.00	4	18.00	72.00	
Cabling patchcords (military)	18	102.45	1,844.10	18	87.81	1,580.58	18	79.40	1,429.20	
Cabling adapters (military)	20	20.00	400.00	20	19.60	392.00	20	17.50	350.00	
Cable (military)	200	0.88	176.00	200	0.88	176.00	200	0.80	160.00	
Enclosure	1	230.00	230.00	1	218.50	218.50	1	207.00	207.00	
Project consumables	1	1,500.00	1,500.00	1	1,425.00	1,425.00	1	1,350.00	1,350.00	
Interrogator	1	13,518.00	13,518.00	1	8,228.00	8,228.00	1	6,338.00	6,338.00	
UPS	1	300.00	300.00	1	285.00	285.00	1	270.00	270.00	
Container	1	1,500.00	1,500.00	1	1,425.00	1,425.00	1	1,350.00	1,350.00	
Installation expenditure			19,548.10	13,806.08			11,526.20			
Total Costs			23,861.40	16,298.89			13,265.71			
Project add-ons										
Smart aggregates	8	175.00	1,400.00	8	175.00	1,400.00	8	169.50	1,356.00	

Figure 5.51: Detailed commercial Evaluation

Scenario	Manufacture expenditure		Installation expenditure		Total Costs		Interrogator unit of total costs
Follow-on installation	£4313.3	N/A	£19548.1	N/A	£23861.4	N/A	57%
10 installations	£2492.81	-42.2%	£13806.08	-29.4%	£16298.89	-31.7%	50%
100 installations	£1739.51	-59.7%	£11526.2	-41.0%	£13265.71	-44.4%	48%

Figure 5.52: Commercial evaluation results

5.52 with the detailed cost break down presented in Table 5.51. The most significant cost savings can be observed in the sensor manufacture as the total expenditure per installation reduces by 59.7% for 100 installations compared to a follow-on installation (10 installations: -42.2%). For the remaining components, grouped under the title of

installation expenditure, the cost reduction for 100 projects is 41% (10 installations: -29.4%) and is thus lower than the sensor fabrication component; however, the absolute cost of the field installation is significantly higher than the sensor manufacture. Consequently, the cost of a single installation as part of a larger campaign of 100 installations is £13,265.71. This is a reduction of 44.4% (10 installations: -31.7%) compared to a follow-on installation. Although substantial cost reduction can be achieved, the unavoidable application of the relatively expensive interrogator ($> \text{£}5,000$) has a significant impact with a share of 57% for a follow-on installation and 48% of total costs for 100 installations (10 installations: 50%).

5.3.8 Learning Experience

The field implementation and sensor fabrication experiments provided invaluable experience that can help to influence future technical decisions concerning similar activities. The practical knowledge gained during the course of AM06 will help to develop a reliable sensor system capable of being embedded in a concrete wind turbine foundation. Future deployment strategies will be influenced by these early trials with the effect of achieving full success. Table 5.12 lists identified learning experiences combined with a qualitative assessment of their impacts on the installation outcome. A scale of 1 to 5 has been adopted, where 1 means the item has had little negative impact and 5 a significant negative impact. In addition, based on the observed and qualitatively categorised impact, the ability by either Strathclyde or SSE to reduce its negative impact is determined based on a scale of 0 to 5, where 0 means no ability and 5 straight forward ability for improvement. By multiplying the identified impact and Strathclyde's/ SSE's ability for improvement, a score per item was generated that was qualitatively transformed into a high (25:18), medium (17:9), and low (8:1) score. Where an item scores 0 any further recommended action is not applicable (N/A) as there is no identified ability for improvement.

Two items were sub-classified under scheduling and time management learning experiences as potentially having the greatest impact on the improvement of the instal-

lation process: 1) the potential to identify installation dates more accurately, and 2) scheduling of sufficient time for cable installation, e.g., by considering incentivising steel workers to provide larger time windows to allow a more flexible and quality orientated installation.

For example, as far as the identification of installation times is concerned, the team found it difficult to prepare well enough due to some last minute changes. For example, on the arrival date it was anticipated to have two consecutive days to prepare and instrument reinforcement bars; however, upon arrival, the team was informed that foundation works had already commenced and two reinforcement bars had to be fully instrumented within a couple of hours. This unfortunately resulted in a highly rushed installation that, with an improved information exchange, could have been prevented.

Although installation time requirements were advised beforehand, it was difficult to install sensors without time pressure as steel workers had to pause their work during installation. It should be noted that workers were paid by the ton of steel placed rather than per hour, without any additional compensation in case the Strathclyde team interfered with their work. This led to situations where reinforcement bars were already placed in the areas that still required access. For example, the bottom interrogation cables were planned to be properly attached at a later stage; however, this was not possible anymore as access was restricted, and the cables were not attached as it had been ideally planned. In any future installation it is recommended that incentives are considered to compensate steel workers when they have to pause their work to accommodate sensor installation. However, we are yet very thankful for the steel workers' patience and commitment on the occasion of this field trial.

In terms of the installation time requirements, the sensor installation was found to be quicker than anticipated; however, the cabling and connectorisation took longer than initially anticipated. This was mainly due to the difficulty in accessing areas, so future installations will require this aspect to be taken into consideration. Specifically, the

first connections of both orthogonal reinforcement bars required a considerable amount of time as reinforcement bars were positioned within the ring foundation (Figure A.18 of the Appendix) with limited space to manoeuvre.

Overall, scheduling and time management was identified to have a major impact on the installation approach (and success) with significant potential for improvement. As highlighted before, it is possible that the connection between cable and module failed in some locations due to excessive pulling force on the cable as the crimping of the steel armour may have been not strong enough. This issue needs to be investigated and improvements proposed to ensure a more resilient protection of these regions. Other options include the use of military connectors and/or the application of epoxy prior to crimping to increase bonding strength. On the other hand, both surviving modules suggest that the adopted approach is adequate, so, with more time for installation per module, the connections could have possibly been improved as there would have been more time to carry out crimping and evaluate the quality of connection. Further testing and experimental research by Strathclyde will reduce this impact.

In this field trial, sensor modules were terminated with a male and female connector at either end, respectively; however, it was not anticipated that after installation two modules might face each other with the same connector, thus the prepared cable had a much longer distance to travel to the opposite sensor end. This did matter as a module has a length of about 1.2 - 1.4 m and makes a substantial difference in the required cable length. During installation, spare cables could be added to increase the length, as a downside the amount of interconnections would increase. As a learning experience, next time all modules will be equipped with female connectors and the cables between modules with male connectors in order to ensure flexibility in module orientation. As a second benefit, this solution enables a more secure fit of the steel armour as it slips much easier onto the male connector than on the female connector which requires a removal of a dust cap. Removal of the dust cap could however allow dust to enter the connector resulting in attenuation, thus this risk is further contained

Table 5.12: Categorical learning experience

Item	Impact	Ability to Reduce Impact		Score	
		Strath	SSE	Strath	SSE
Scheduling, Time Management, Quality Control					
Identification of installation dates	5	4	4	Hi	Hi
Schedule sufficient time for cable installation	5	0	3	N/A	Med
Quality Control along installation	5	4	4 (incentives?)	Hi	Hi
	5	5	5	Hi	Hi
Other Items					
Module connectorisation	5	5	0	Hi	N/A
Set-Up of container & store equipped rebars during curing	5	3	5	Med	Hi
Selection of ducts	4	5	Requirements?	Hi	N/A
Interaction of zinc spray & silicone & epoxy	1	5	0	Lo	N/A
Improve interrogation cable interconnections	3	5	4 (timing)	Med	Med
Check sensors at each stage (spare parts)	4	4	0	Med	N/A
Presence of Strathclyde team during pouring	3	3	3	Med	Med
Equipment to work more in parallel	2	5	0	Med	N/A

by the suggested approach.

To be weather independent, it was anticipated to set-up a heavy duty tent. Due to strong winds and gusts the identified tent did not survive the first day. Fortunately, this did not have a major impact on this occasion as the weather was pleasant. Nevertheless, in order to reduce the risk for future installation, it is advised to set-up a container on site that can be opened on both sides to offer weather protection and suitable stability. This will offer weather independence considering sensor attachment as well as storage during curing, and is therefore highly advised.

After all sensors were installed and interconnected, the team struggled with the deployment of ducts provided by SSE as they were stiff and coiled up, making it difficult to arrange as planned. These installation difficulties were not foreseen, but it transpires this was one of the reasons why the top interrogation cables were removed entirely during the pour by the contractor. In future installations it is advised to use more suitable, lighter and more flexible ducts.

A potential, although unlikely impact could also arise from the undesired interaction of zinc spray (used to protect sensor shims) with silicone and epoxy. Although this combination of compounds was tested beforehand, the zinc spray was often not allowed to dry before the application of silicon due to the time constraints highlighted before. Further laboratory testing is required by Strathclyde to determine if this indeed could have been an important factor that impacted the success of this installation.

Furthermore, the cabling could have been attached along reinforcement bars with more care at critical transition areas. However, limited time did not allow to ensure quality along the process.

An issue occurred with the sourcing of components, i.e., the robust optical cable was manufactured of poor quality resulting in an highly attenuated signal integrity. Al-

though, the Swiss supplier is well known in the field with appropriate working quality certificates, the poor cable quality might have added to the poor result. Especially, where multiple cables were multiplexed with the dialink connectors that were of very good quality overall.

Retrospectively, it would have also been worthwhile for the Strathclyde team to be on site during the concrete pour to observe the process and evaluate any potential impacts by the poker, as well as to advise if something unexpected happens. In addition, evaluating the networks response before the concrete pour could have helped to determine more accurately the cause of damage while ensuring that all sensors were working prior to the concrete pour. While this would certainly help to gain a more detailed understanding of any potential failures in future, it would have no bearing on the success of a network installed at the time, as once the sensors are installed, it is difficult to make adjustments. With all this said, it is believed that the sensor network was installed correctly, as a 75% failure rate for the sensors is too large to attribute purely to the practical aspects of installation, which were well-practised beforehand.

5.3.9 Discussion and Future Work

Although the sensor network was prepared for rough handling and substantial impacts during the installation and concrete pour, forces in the addressing fibre were much higher than expected. This resulted in the loss of 75% of the installed sensors. The knowledge gained during this installation will inform future work that aims to install optical sensor networks in civil engineering applications with similar complexity. Future work thus entails an investigation to determine forces along the addressing fibre and methods to guide cables in the foundation as well as options for interconnections. It is recommended that military optical connectors are considered for any future installations, although the issue in applying such connectors is their thick module diameter in comparison to the applied reinforcement bars. Alternatively, in order to maintain a slim connector thickness, the presented crimped interconnection may be trialled with additional material layers to enhance strength and resilience. One option may be to add

an epoxy layer at the point of interconnection. The latter is likely to facilitate a slim connection while increasing overall strength; however, on the downside the installation time increases due to epoxy curing. Other options include to pre-cure concrete around the sensor and locations of cable interconnections.

With regards to the results and their validation, the objective was to compare foundation sensor readings with their mirrored counterparts (placed 180 degrees apart in the foundation). This is a similar methodology to the validation of the tower strain gauges. However, because the mirrored strain gauges were lost, this straightforward validation could not be achieved.

Nevertheless, the sensor data agrees reasonably well with the simplified FEAs results as demonstrated in Section 5.3.5.2, besides the ability to detect structural modes and harmonics as presented in Section 5.3.6. In order to gain a more detailed, accurate, and fully validated picture of the overall foundation loading, the project requires a successful repetition. Nevertheless, long-term data acquisition using the existing trial will be valuable to assess the internal health of the foundation, albeit limited to the locations covered by the surviving sensors. At the end of the turbines design life, sensor readings may be applied to aid repowering and lifetime extension decisions, given the difficulty to otherwise internally assess the wind turbine foundation's structural integrity and cumulative fatigue damage. Here, local sensor data may be extrapolated in combination with the results generated by FEA.

5.3.10 Section Conclusions

This work presents the results of a first-time demonstration of reinforcement strain monitoring within an onshore, concrete wind turbine foundation during operation. The sensor design, construction and field installation activities have been invaluable in the learning process to successfully design and deploy a structural health monitoring system for an onshore wind turbine foundation. The results presented may act as a valuable guide for similar projects. The results obtained have locally corroborated finite element models of the foundation and have shown a strong correlation with measured tower dynamics. The gathered sensor data is significantly limited and thus there are

considerate concerns about determining the ability to reuse the foundation for greater scale turbines or to optimise the design; however, an FEM comparison of both sensor measurements was achieved.

5.4 New Sensor Design

Due to the limitations, difficulties, and observed drawbacks of the metal-packaged sensor design, the aim is to design a strain sensor that fits most locations, can be applied at high temperatures, is resistant to humidity and shows repeatable behaviour. For this the brazing process to attach the optical fibre is removed and is it aimed to apply Epoxy within the capillary.

5.4.1 Methodology

The testing procedure is defined through a pre-designed stage-gate process to use resources most economically as illustrated below:

- Stage 1: test process with strain gauge epoxy
 - Pre-braze the shims to a greater diameter steel capillary (19G), thus the optical fibre inscribed with an FBG and epoxy filling capillary (31G) fit in at the same time in the steel capillary
 - Fill the steel capillary with epoxy (Epotek 301)
 - Cure the epoxy
 - Spot weld to metal sample
 - Run long-term static testing ($x > 100$ cycles). Based on previous tests, this is where initial degradation was observed.
- Stage 2: repeat the process (a-e) with copper coated fibre and high temperature resistant epoxy (NCC-3 Ceramic Cement up to 800 deg C)
- Stage 3: if stage 2 successful do fatigue test with stage 2 sensor variant (100.000 cycles). Based on previous tests, this is where the sensors have likely fully settled.



Figure 5.53: New Sensor Iteration Testing

- Stage 4: add humidity to a static test as conventional epoxy is impacted by moisture; however, this sensor variant's epoxy is sealed.

This methodology is selected to ensure to use resources most economically by starting quasi-static testing and upon success advance to the next stage as itemised.

5.4.1.1 Stage 1

The items were purchased and a sensor was built according to the requirement presented in stage 1 methodology. The sensor was spot welded to a dumbbell (S355 steel) and 100 times statically cycled (0.01 Hz) in a Testometric M350-10CT machine as illustrated in Figure 5.53. The maximum machine force was set to 9kN, hence reaching a strain of 1 mstrain (this was the maximum limit of machine force and material sample). The oven was kept constant at a temperature varying between 28-34 deg C. Overall, six total tests were performed, each consisting of 100 cycles.

Results Figure 5.54 illustrates the results of the six sessions, each consisting of 100 static cycles. In detail, the sensor's wavelength range per cycle is illustrated over time

and session. After the first session (uncontrolled ambient temperature of roughly 22 deg C), suspicion was raised that the IMON interrogator was introducing an error due to its internal temperature compensation mechanism (an initial downward trend), which agrees with findings of the sensor working group in different tests. In subsequent testing the interrogator was placed inside the environmental chamber to provide a stable environment. The following three tests (2, 3, 4) with the interrogator in the environmental chamber (32 deg C) are repeatable in their characteristics, characterised by a greater stress range at the beginning that settles after roughly 30 cycles. With respect to the machine readings, the maximum reached force was varying by 0.05% which agrees with the observed sensor strain response fluctuations after reaching 30 cycles as illustrated in Figure 5.54. After completion of the tests, suspicion was raised that the sensor characteristics are dependent on temperature, thus the cycles were carried out at 28 deg C (5) and 34 deg C (6). The sensor results showed a constant response range over the entire test session which is opposing the results from session (2-4). Based on the performed tests, there is no indication of a temperature dependence and a constant response is overall observed. At present, it is unknown why the range is higher in the beginning and converges to a constant range over time for session (1-4). Also, all tests are slightly different in the observed range; however, no degradation is observed over time. Based on the range of carried out tests, it appears that the machine's calibration slightly fluctuates with temperature and sample mount. Nevertheless, the results show repeatability and no degradation from the maximum wavelength range observed in the beginning of each session. It is therefore advised to proceed to stage 2.

5.4.1.2 Stage 2

Due to time limitations and issues with sourcing of the components, this part was not executed and is passed onto a PhD colleague to continue this line of research.

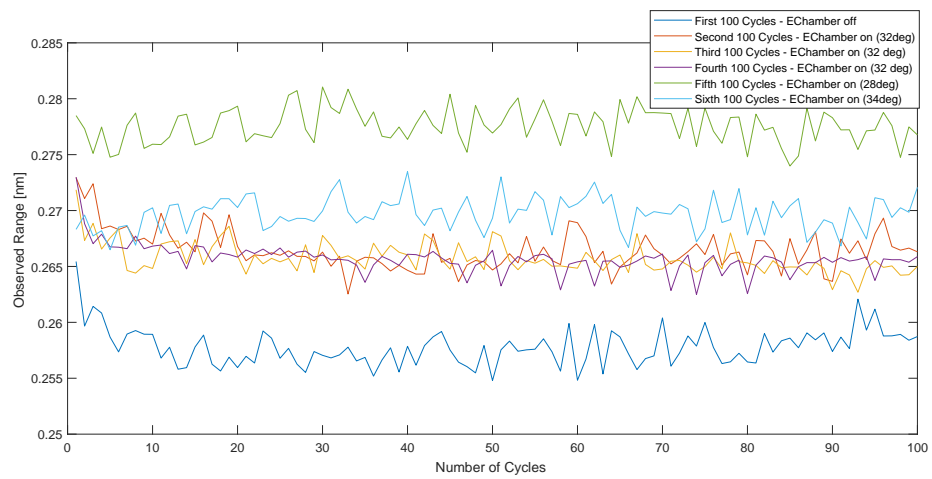


Figure 5.54: New Sensor Iteration Testing Results

Chapter 6

Economic Lifetime Extension Based on SHM

So far, this work has looked on the one hand at the economics of lifetime extension presented in Chapter 3 and on the other hand, on novel optical strain gauge based foundation SHM presented in Chapter 4. In this Chapter, findings are combined to assess the value of a foundation and tower strain measurement campaign to assist lifetime extension decision-making.

6.1 SHM Campaign

6.1.1 Tower SHM

A general review of SHM opportunities, failures, and inspection practices of wind turbines is published by numerous authors [74, 264, 265]. With regards to tower sensor installation and data assessment practices, the reader is referred to Smarsly et al. [266] for a 500 kW wind turbine, Rebelo et al. [267, 268] for a 2.1 MW wind turbine, Loraux and Brühwiler [79] for a 2 MW wind turbine, and Botz et al. [269] for a 3 MW hybrid turbine consisting of a concrete and steel tower section. The 2 MW wind turbine tower fatigue analysis results in a remaining useful lifetime (RUL) of 135 years in a low mean wind speed region (5.9 m/s) [79].

In this work, a turbine with a greater mean wind speed (> 7 m/s) and greater rated

power (> 3 MW) undergoes a load measurement campaign using optical strain gauges at the tower base sampled at a high frequency (> 50 Hz). The overall procedure of the fatigue analysis is taken from available and previously mentioned publications; however, the novelty is to apply SHM information to derive and evaluate the long-term strategic LTE business case for a specific wind farm.

Ideally, strain gauges are installed at the locations on the tower situated in the prevailing wind direction. However, the installation of tower sensors might not be feasible in all areas; access restrictions and risk of damage due to maintenance processes can limit the available positioning of sensors (e.g. in proximity to the foundation-tower bolts that require servicing). Such constraints were encountered in this work; however, as explored below, the problem of imperfect positioning of sensors has not been of serious consequence to the adopted methodology.

The locations of the tower base strain gauges (T1–T4) with respect to north is illustrated in Figure 6.1. The normalised strain data, paired with 30 minute average supervisory control and data acquisition (SCADA) wind speed data (in the respective directional corridor $\pm 10^\circ$) is illustrated in Figure 6.2 for T1 and in Figure 6.3 for the 90° rotated tower strain T2, respectively. Overall, the measurements are well in agreement with the yaw reference SCADA data, allowing confidence in the nacelle sensor calibration.

Based on the measurement campaign, as expected due to access constraints, the sensors are not aligned with the prevailing wind direction. This was confirmed (i) based on the mean SCADA nacelle direction and (ii) since the operational SCADA period of T1's inflow corridor ($\pm 10^\circ$) over the total recorded time covered 7.5% and 3.2% for T2, respectively.

In order to evaluate a component's total lifetime based on measured or simulated data, the recorded signal is decomposed in defined discrete cycle ranges and each range's total number of occurrence is counted through a process referred to as rainflow counting [270]. Since, the rainflow counting algorithm is highly sensitive to changes in the maximum strain as well as in the frequency of occurrence of each range [79], the actual prevailing wind direction requires evaluation.

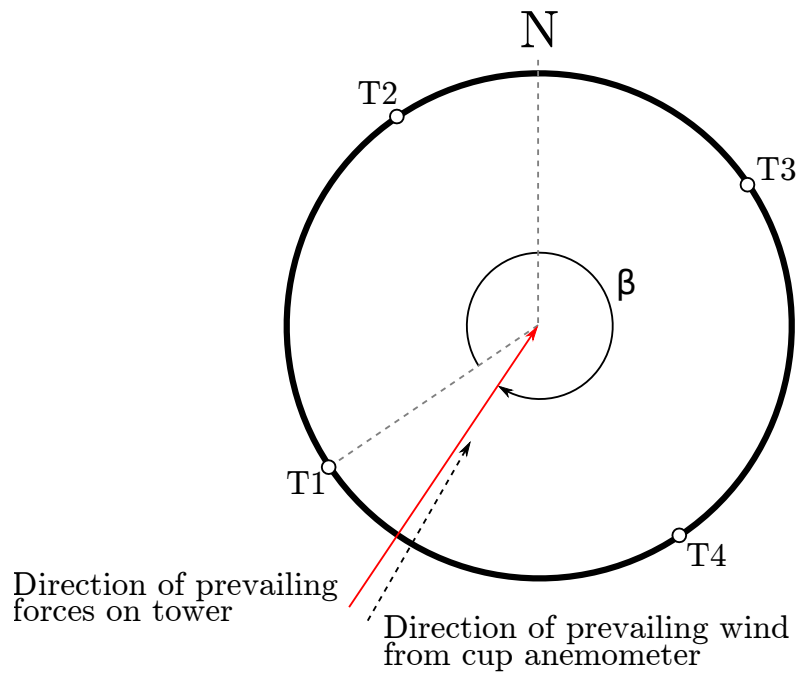


Figure 6.1: Schematic of tower sensor positions with respect to prevailing wind direction

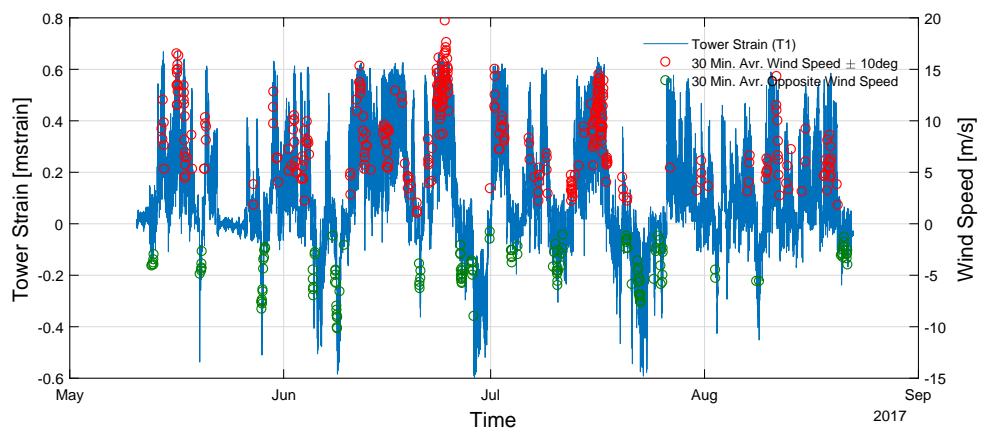


Figure 6.2: Strain data of base tower measurement (T1)

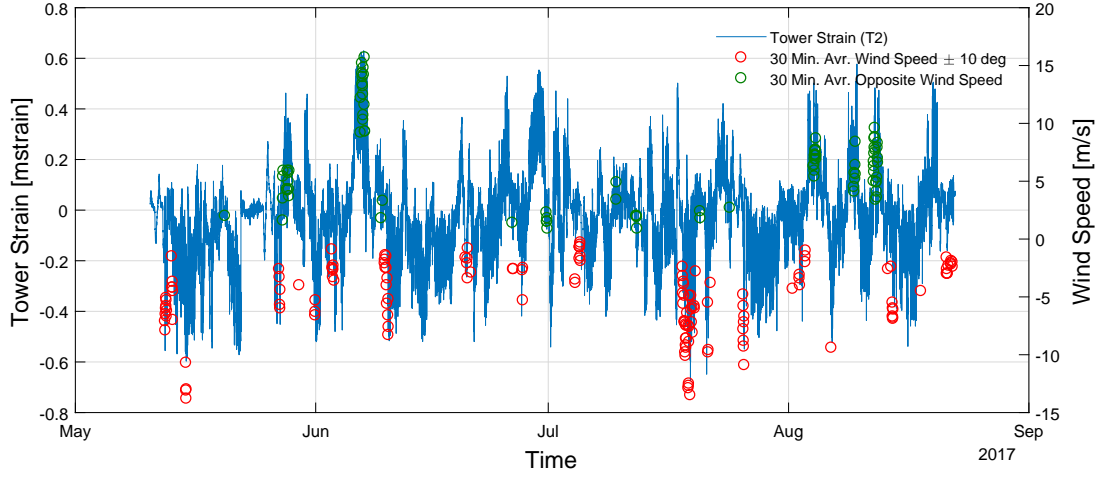


Figure 6.3: Strain data of 90° rotated base tower measurement (T2)

Given that the tower is radially symmetrical and the component's material (S355 steel) is designed to operate in its elastic limit, the stress across the circumference of the tower can be found as a vector sum of the stresses from the sensors. The two sensor strain measurements $v_{T1}(t)$ and $v_{T2}(t)$ respectively from T1 and T2, being positioned on the tower at 90° from each other allows calculation of the magnitude of the resulting vector, $|v(t)|$, and angle, $\gamma(t)$, by:

$$|v(t)| = \sqrt{v_{T1}(t)^2 + v_{T2}(t)^2} \quad (6.1)$$

$$\gamma(t) = \tan^{-1} \left(\frac{v_{T1}(t)}{v_{T2}(t)} \right). \quad (6.2)$$

The direction of the prevailing forces on the tower (which in turn is dictated by the prevailing wind direction), is identified counting the number of occurrences in the angle $\gamma(t)$ using a moving window of 5° as illustrated in Figure 6.4. The prevailing wind direction β with respect to T1 is then identified as the angle with the maximum number of occurrences.

Figure 6.4 indicates that the actual prevailing wind direction does not coincide with any sensor positions as it is not a multiple of 90°. In fact, the actual prevailing wind direction is shifted by 22° counterclockwise with respect to T1, which is also closely in

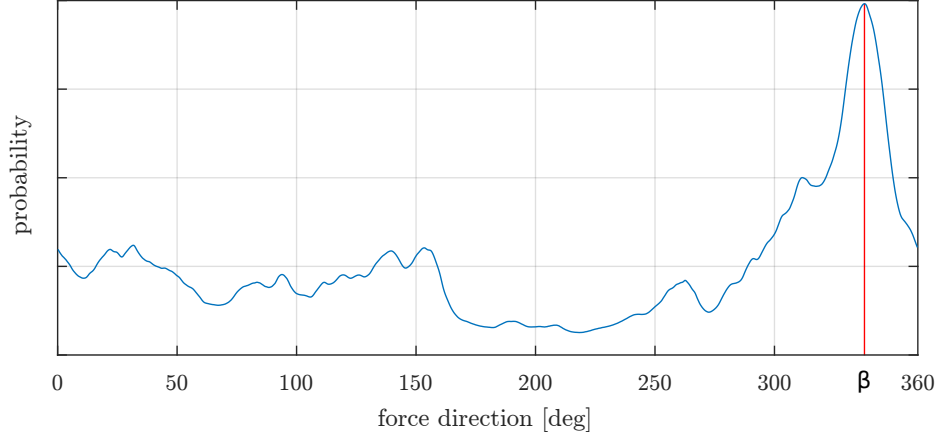


Figure 6.4: Identification of prevailing wind direction, β based on $\gamma(t)$ binning.

agreement with the nacelle's mean SCADA direction with a difference of 3° as illustrated in Figure 6.1.

Further, it is necessary to determine if the strain is positive or negative for the rainflow counting as the range (tension and compression) dictates fatigue cycles. Therefore, the difference between angles is calculated:

$$\alpha(t) = \beta - \gamma(t) \quad (6.3)$$

and the strain variation over time in the prevailing wind direction, denoted as $A(t)$ is calculated by:

$$A(t) = \cos(\alpha(t)) \cdot |v(t)|. \quad (6.4)$$

And for the perpendicular direction as:

$$B(t) = \sin(\alpha(t)) \cdot |v(t)|. \quad (6.5)$$

It was further verified that of this new set of axes, the higher frequented component is selected.

Figure 6.5 displays the calculated strain in the prevailing wind direction. The strain profile is in agreement with the wind speed measurements from the SCADA data. Also, the SCADA data shows that, in the operational corridor considered, the turbine was

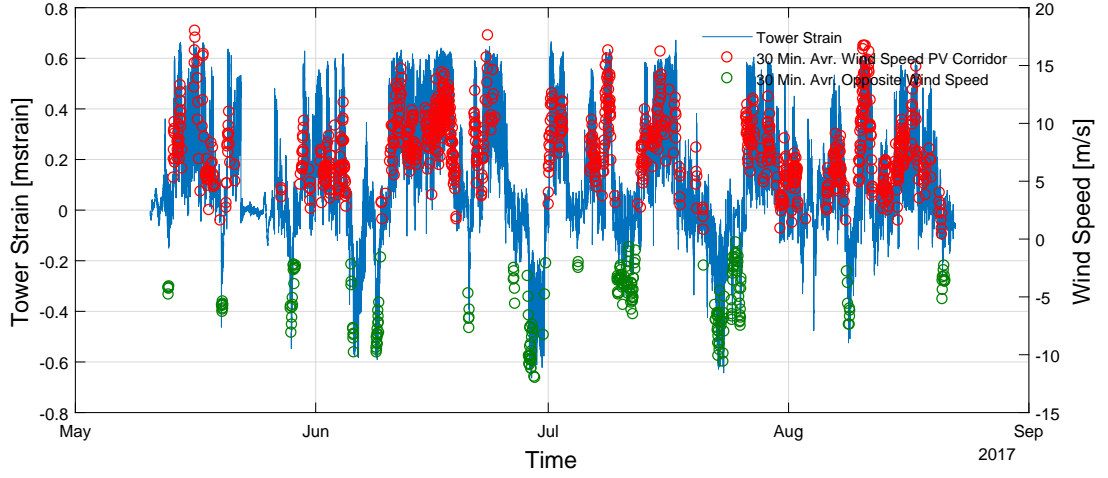


Figure 6.5: Strain data of derived prevailing wind direction

operational for 23% of the total recorded time. This corroborates the above analysis. The tower is usually made from hot-rolled steel, welded together circumferentially and longitudinally [108], with welded flanges at either tower end. As such the S-N curve assumption is dependent on the weld type [107]. The rainflow counting algorithm was applied according to the ASTM standard where half cycles are conservatively treated as full cycles [270,271]. The S-N curve for the tower is used with the following parameters. The endurance limit at 2 million cycles, $\Delta\sigma_C = 72$ MPa [107,111], the constant amplitude fatigue limit at 5 million cycles, $\Delta\sigma_D = 53$ MPa, and the cut-off limit, $\Delta\sigma_L = 29$ MPa according to EN 1993-1-9 [107]. With the established S-N curve, Miner's damage calculation was applied, after the strain was transformed into a stress (Young's Modulus, $E = 200$ GPa), to assess the cumulated fatigue damage D for each S-N curve slope:

$$D_i = S_m^{-m} \sum_i^N n_i \Delta\sigma_i^m \quad (6.6)$$

where S_m and m are material constants. If $\Delta\sigma_i > \Delta\sigma_D$, $m = 3$ and if $\Delta\sigma_L < \Delta\sigma_i < \Delta\sigma_D$, $m = 5$. Otherwise, $D = 0$. The total fatigue damage is thus calculated as exemplified in Equation 6.7.

$$D_{tot} = \sum D_i \quad (6.7)$$

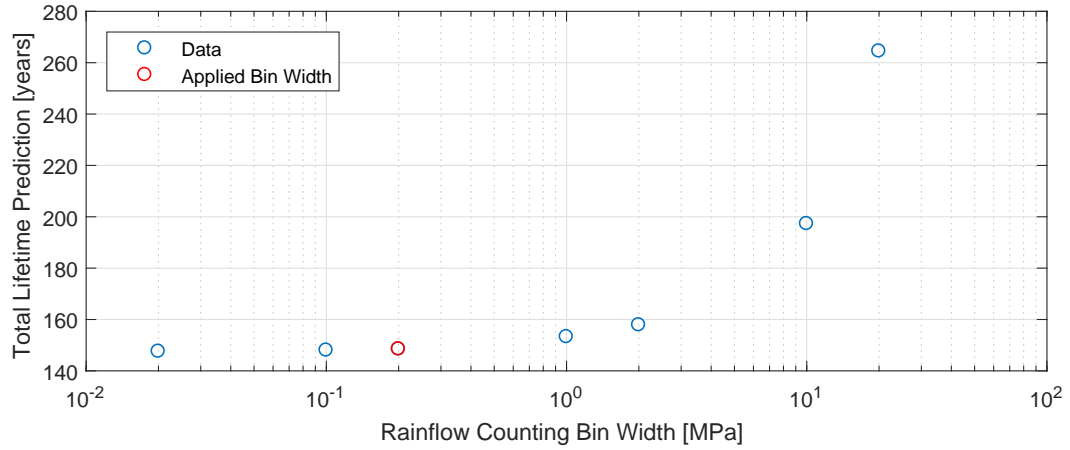


Figure 6.6: Impact of binning width on lifetime prediction

The binning width of the rainflow counting algorithm and sampling frequency determine the accuracy of the lifetime prediction; however, a high sampling frequency in combination with a small binning width, significantly increase processing requirements. As such, the appropriate binning width of 0.2 MPa was identified as illustrated in Figure 6.6 while an appropriate minimum sampling frequency is identified as 100 times the first tower mode as illustrated in Figure 6.7.

The total tower lifetime, based on the recorded measurement data $T1$ was thus estimated to be 163 years and for $T2$ 225 years, respectively. In the prevailing wind direction, the derived and more frequented corridor β , the lifetime analysis resulted in a reduced lifetime of roughly 15 years with a total of 149 years¹. The magnitude of this reduction further allowed confidence in the data processing. In order to verify this result, the lifetime analysis was carried out for varying β (0-180°) as more significant loading, albeit with an overall lower number of occurrence, could have been experienced for wind directions off the prevailing axis. This analysis verified the prevailing wind direction β , identified in Figure 6.4.

Further, based on findings by Rebelo et al. [267,268] and Loraux and Brühwiler [272], the maximum tower stress is likely to be experienced at 30-40% of the hub height.

¹binning width of 0.2 MPa and frequency of 380 times the first tower mode

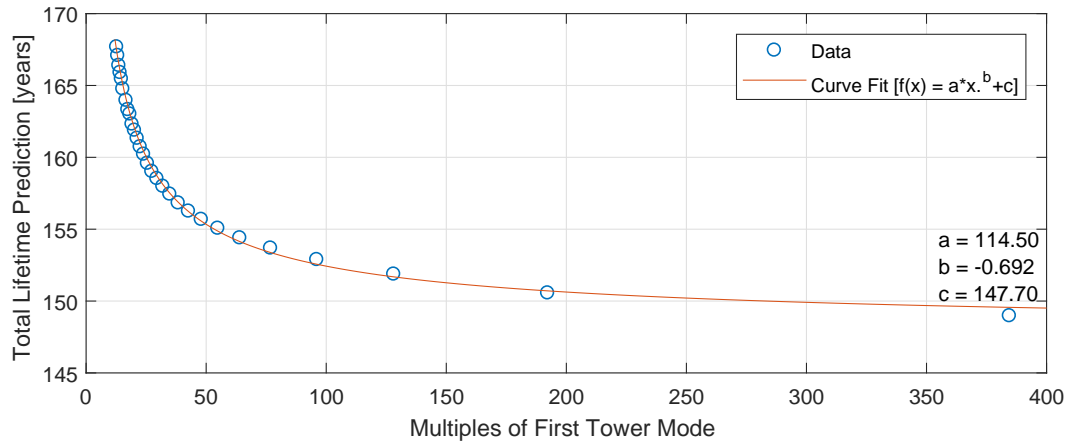


Figure 6.7: Impact of sampling frequency on lifetime prediction based on a 0.2 MPa binning width

At present, the complete tower geometry of the considered wind turbine is unknown. Therefore, a conservatively selected correction factor, derived from the previously mentioned tower monitoring campaigns, is introduced. The corrected total lifetime at the critical tower height is thus identified as 54.7 years. A further correction is required as the outer shell of the tower has a greater stress, thus this correction leads to a total lifetime of 54 years. The overall data processing results are further illustrated in Table 6.1. If residual cycles of the rainflow counting process are treated as half cycles, as suggested by the IEC 61400-13 standard [263], the total lifetime is identified as 55 years.

Overall, from the point of view of the tower a LTE of 15 years thus appears feasible, given considerate safety margin, as the conservatively executed fatigue analysis reveals a total lifetime of 54 years.

6.1.2 Foundation SHM

Overall, SHM of wind turbine foundations is a challenging area of research as highlighted by several studies, since the foundation is mainly inaccessible for inspection [55, 273, 274]. Given that wind turbine foundations (i) are designed for a lifetime of 50 years or more, (ii) their design is based on conservative assumptions, and (iii) they are

Table 6.1: Process of Data Manipulation. PW: prevailing wind, HC: height correction, SC: section correction. Frequency of 380 times the first tower mode.

Analysis	RUL [yr]	Comment
T1 (tower base)	163	Sensor 22° to prevailing wind (clockwise)
T2 (tower base)	224	Sensor 112° to prevailing wind (clockwise)
PW (tower base)	149	Derived prevailing wind with Equation 6.4
PW + HC	55	Corrected for stress at most critical height
PW + HC + SC	54	Corrected for the outer shell

structurally of key importance, there is little concern to accommodate for LTE. Based on an internal strain analysis of the reinforcement cage by Rubert et al. [273], this is further supported. As a consequence, from an economic lifetime extension decision-making perspective, the foundation is not of concern (except when severe cracks are encountered). “Cracking is normal in reinforced concrete structures subject to bending, shear, torsion or tension resulting from either direct loading or restraint or imposed deformations” [94]. Although cracking is expected to some degree, there is a crack width limit, w_{max} that is governed under the service limit state. The acceptable crack width is dependent on the concrete exposure class and type of reinforcement and can be looked up in design codes and guidelines. Also, if cracks appear work by Perry et al. [274] and McAlorum et al. [126] may be applied for SHM. Results thus reveal a possibility of an extended WTG operation of greater than 15 years.

6.2 Lifetime Extension Methodology

The lifetime extension decision-making methodology is schematically illustrated in Figure 6.8, where the lifetime extension period is treated as a separate investment and calculated based upon levelised cost of energy (LCOE₂). To calculate LCOE₂, the net present value (NPV) of costs is divided by the NPV of the annual energy production (AEP):

$$LCOE_2 = \frac{NPV_{costs}}{NPE} = \frac{C_0 + L_0 + \sum_{n=1}^T \frac{F_n + O_n + V_n}{(1+d)^n}}{\sum_{n=1}^T \frac{E_n}{(1+d)^n}} \quad (6.8)$$

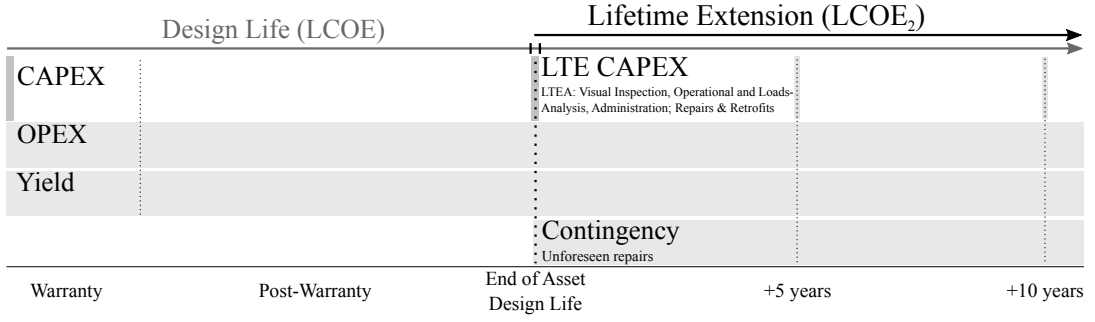


Figure 6.8: Lifetime extension decision methodology [145]

where NPE is the net present energy, C_0 the equity capital expenditure of component replacements ($CAPEX_{\text{Replace,E}}$), L_0 the lifetime extension capital expenditure ($CAPEX_{\text{LTE}}$), n is the period ranging from year 1 after the design lifetime to T the final year of operation (end of extended lifetime), F_n the constant annuity payment of the component replacement's expenditure debt in period n ($CAPEX_{\text{Replace,D}}$), O_n the fixed operating cost including decommissioning² in period n , V_n the variable operating cost in period n , E_n the energy generated in period n , and d the discount rate.

This extended lifetime methodology is equipped with operational data in terms of cost and yield parameters. The prior includes the CAPEX LTE and operational & maintenance (O&M) expenditure and the latter identified through operational knowledge or alternatively the application of a Weibull wind distribution in combination with a turbine's power curve [106]. Of course all variables are ideally based upon the operational design lifetime and may be adjusted depending on; e.g., failure and reliability data.

6.3 Lifetime Extension Case Study

6.3.1 Strategy

The structural integrity of the foundation and tower is one of the main factors in determining economic lifetime extendibility (high replacement costs) and the high im-

²onshore it is expected that the scrap value equalises decommissioning costs; offshore this is certainly not the case

Table 6.2: Wind turbine parameters

Parameter	Value
Cut-in wind speed	3 [m/s]
Cut-out wind speed	25 [m/s]
Rated wind speed	12.5 [m/s]
Turbulence intensity	0.1
Availability	97 [%]
Wake losses	10 [%]
Weibull shape factor	2

portance in serving as a load-carrying component, their RUL is of significant interest for a given wind turbine. As previously discussed, the foundation design lifetime significantly exceeds other components, hence the tower RUL is of greater concern. Therefore, knowledge of the site-specific tower RUL will provide argument for the long-term economic business base.

The results from the SHM campaign presented above indicate that lifetime extension of 15 years appears feasible. Therefore, for the LTE business case the strategic extension period is considered to be 15 years.

6.3.2 Input Data

The turbine's generic parameters are illustrated in Table 6.2. The power curve was reproduced as highlighted by Rubert et al. [145]; however, rather than applying the maximum power coefficient, $C_{p,max}$ to derive the power curve, C_p varies with wind speed, $C_p(v)$ that was derived based on the manufacturer's data sheet ($\rho = 1.225 \text{ Kg/m}^3$). This enables greater accuracy in the yield modeling as outlined by Carillo et al. [186] and Lydia et al. [187]. The turbine's mean wind speed was derived using operational SCADA data, accounting for the impact of curtailment (provided by the operator). Curtailment was included in the model by reducing the average wind speed for the specific wind turbine.

Given that the foundation and tower are able to facilitate the target lifetime extension period, components along the drive train may require replacement. This is budgeted as $CAPEX_{SPARE,D}$ and $CAPEX_{SPARE,E}$ with a 70/30% debt-equity split, the latter

Table 6.3: Lifetime extension cost estimations for a wind farm [145]

Parameter	Central	Range	Unit
O&M			
Fixed	30,192	22,644-37,740	£/MW/y
Variable	5.1	3.83-6.38	£/MWh
Insurance	2,226	1,669-2,782	£/MW/y
Connection charges	3,810	2,857-4,762	£/MW/y
CAPEX LTE			
Visual inspection	2,689	2,017-3,361	£/WTG
Loads Analysis	3,500	2,625-4,375	£/WTG
Operations Analysis	2,000	1,750-2,250	£/WTG
Administration	1,000	750-1,250	£/WTG
Spare parts			
3 blades	238,560	178,920-298,200	£/WTG
Gearbox	147,680	110,760-184,600	£/WTG
Generator	93,152	69,864-116,440	£/WTG
Installation expenditure			
Crane Mob/Dmob	20,000	15,000-25,000	£/Wind Farm
Crane operation	2,000	1,500-2,500	£/day
Service personal	58	43.1-71.9	£/h

budgeted as a constant annuity with the interest rate set as 3.5% [235]. Cost and time assumptions for the necessary crane (1,200 t) and service team for component replacements were evaluated. The time requirement was increased by 50% and the service team number increased by 25% from those from [145]. The overall cost assumptions are summarised in Table 6.3 for the central case as well as optimistic and pessimistic scenario, respectively.

The discount factor is assumed at 7.5%, with inflation set at 1.5% accounted to administration and spare parts of the O&M expenditure.

Also, for the scenario with no component replacement, an annual performance degradation of 0.3% is modeled based on findings by [157, 234, 275]. In the other scenarios, due to component upgrades the performance degradation is likely significantly smaller and thus neglected.

To get greater confidence limits, a Monte Carlo simulation is further applied based on the application of normal distributions. This was executed for the scenario with no component replacement and the exchange of the entire drive train. The annual wind speed was characterised based on SCADA mean data paired with a standard deviation of 7% of the AEP [169]. The cost data was modeled with a standard deviation of 25% as illustrated in Table 6.3. For the component replacement process, if the wind speed is above a certain wind speed threshold, components cannot be lifted. Therefore, the

required crane and service hours were applied based on the minimum expected time and a normally distributed time component added to account for wind related delays. Based on the procedure detailed by Vose [276], the number of required iterations n was identified as 50,000 based on a standard error of 3% and a 90% confidence interval.

6.4 Results

When operating a wind farm, each turbine can be characterised differently; i.e., some turbines have greater average wind speeds than others, depending on the local terrain, wake effects, and operational parameters. With regards to LCOE calculations, the mean wind speed has the greatest impact [70, 145]. When pairing the mean wind speed with operational knowledge (downtime, degradation, curtailment, etc.) the AEP or capacity factor can be derived. Therefore, when operating a wind farm that is reaching its end of design lifetime with fewer revenues or when directly exposed to the spot-market electricity price, some turbines might be less profitable in their continued operation than others. As a consequence, a LTE decision-making requires turbine specific evaluation.

The lifetime extension $LCOE_2$ of the bespoke economic turbine model based on operational wind conditions are illustrated in Figure 6.9 under the assumption of (i) no retrofit and (ii) the exchange of the entire drive train; in Figure 6.10 for a single retrofit of a drive train component; and in Figure 6.11 for any retrofit combination of drive train components. As mentioned before, each scenario has an assumed extended lifetime of 15 years.

The error bands are based on the cost variation illustrated in Table 6.3. A wind farm usually consists of several individual turbines, with varying degree of loading and electricity production, thus when it comes to lifetime extension, not necessary all turbines are economically suitable to keep in operation. Knowing that the annual wind speed and hence AEP has the greatest impact on LCOE, the wind speed is varied in order to determine profitability of the different cases.

With turbines mostly being exposed to the subsidy-free spot market electricity price, a threshold is defined to determine individual turbine suitability. This is defined as 10%

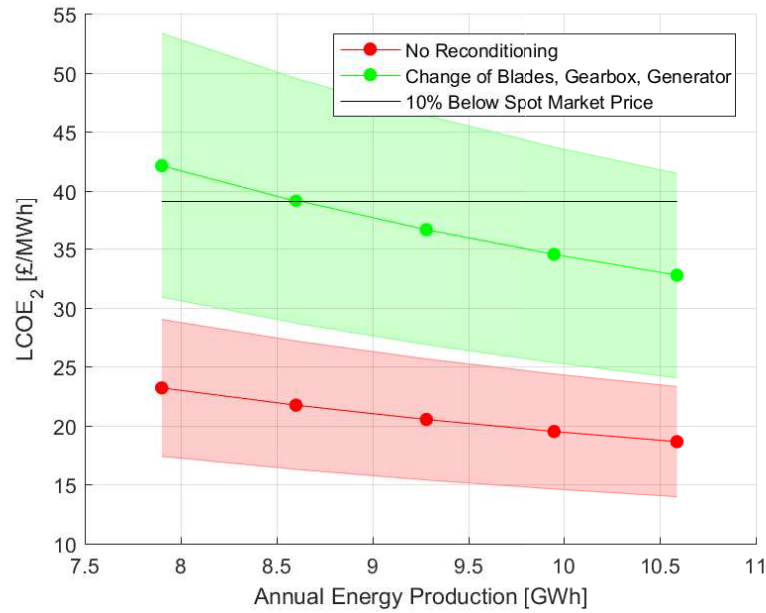


Figure 6.9: LCOE₂ of lifetime extension period with annual energy production (no retrofitting and drive train exchange)

below the average UK's spot market price of the past 5 years [145].

Overall, without any component replacement, the LCOE₂ is significantly below the defined subsidy-free threshold (£39), hence LTE is supported for any of the modeled AEP cases. Alternatively, if the entire drive train requires replacement (blades, gearbox, and generator), this would only be economically viable if the annual energy production is above 8.6 GWh/WTG. The complete range is illustrated in Figure 6.9.

For any single component exchange (blades, gearbox, and generator), all medium cost estimates are below the threshold; however, for the pessimistic cost scenario, the replacement of blades are economically infeasible and decommissioning is advised as illustrated in Figure 6.10 when below 8.3 GWh/WTG.

For any two component replacement scenario, the cases including new blades require at least 7.5 GWh/WTG when paired with a generator exchange, and 7.8 GWh/WTG when paired with a gearbox exchange in order to be economically viable as illustrated in Figure 6.11. The replacement of a gearbox in combination with the generator is feasible in the medium cost scenario; however, in a pessimistic scenario caution is required.

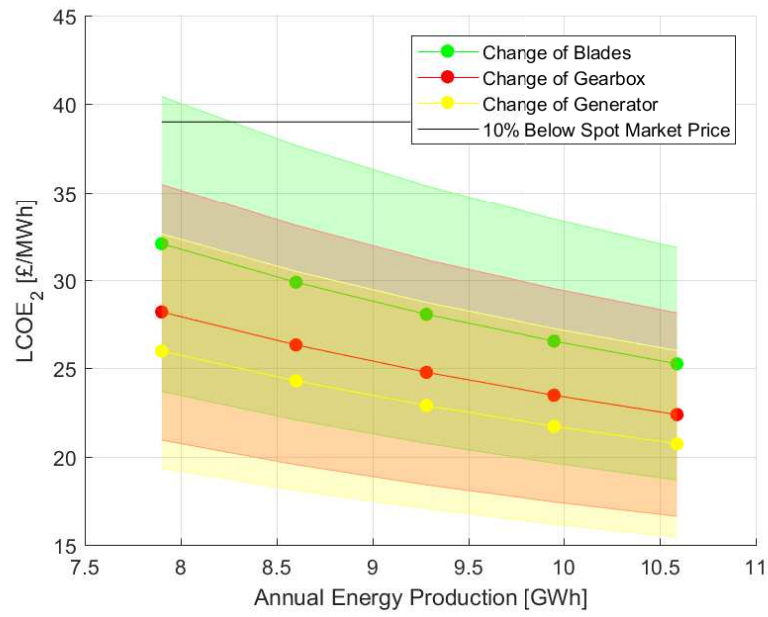


Figure 6.10: LCOE₂ of lifetime extension period with annual energy production (single retrofit)

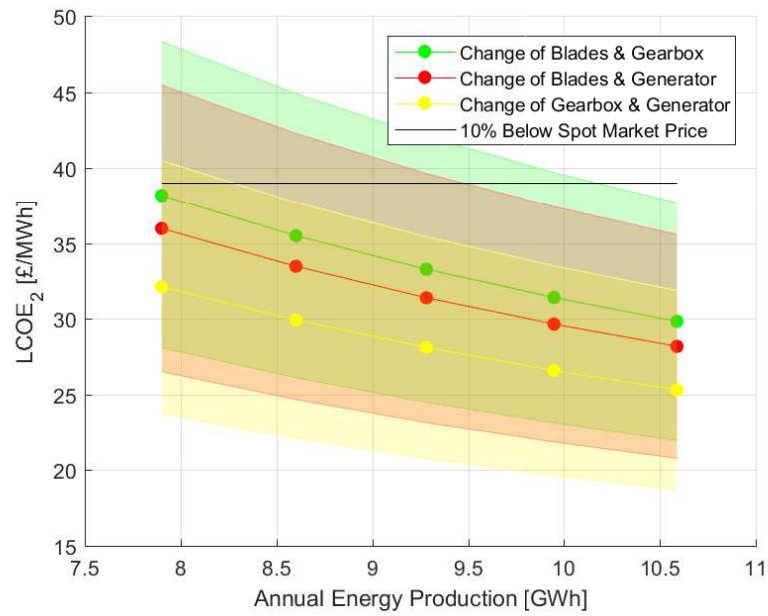
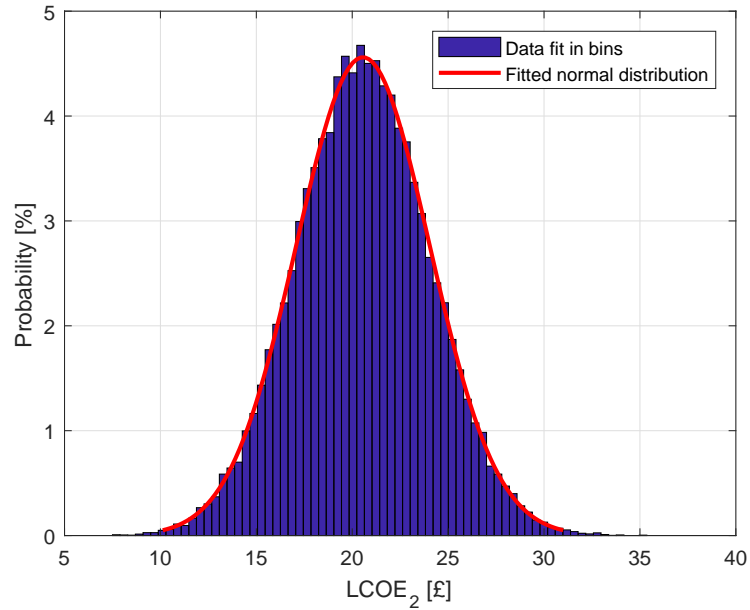


Figure 6.11: LCOE₂ of lifetime extension period with annual energy production (double retrofit)

Table 6.4: Annual Contingency [£] for 15 year LTE under different scenarios. N/A: costs exceed revenue

Scenario	Pessimistic	Central	Optimistic
No Reconditioning	141,363	186,268	231,173
Reconditioning of Blades	37,704	104,901	173,560
Reconditioning of Gearbox	76,837	135,610	195,286
Reconditioning Generator	99,283	153,214	207,719
Reconditioning Blades, Gearbox, & Generator	N/A	24,980	116,871
Reconditioning Blades & Gearbox	N/A	56,138	138,952
Reconditioning Blades & Generator	N/A	73,743	151,385
Reconditioning Gearbox & Generator	37,221	104,452	173,158

Table 6.4 further displays the annual available contingency with respect to (i) the different replacement scenarios and (ii) the expenditure range based on an AEP of 9.3 GWh. As illustrated in Figure 6.8, this parameter indicates the potential money to spend before the project becomes non-profitable along the life extended period; i.e., when decommissioning is advised. The remaining contingency may be applied to support the operational LTE decision-making as the available budget indicates the risk of an aimed strategic decision. An example would be if the replacement of the drive train is strategically considered matched with central cost estimates, as the remaining annual contingency is £24,980/WTG. In such an instant, if severe issues occur (such as a major generator or bearing failure), the project is likely more risky to be profitable than other decisions with a greater annual contingency. This risk can potentially be reduced by in-depth structural analysis and the application of reliability models based on inspection results.

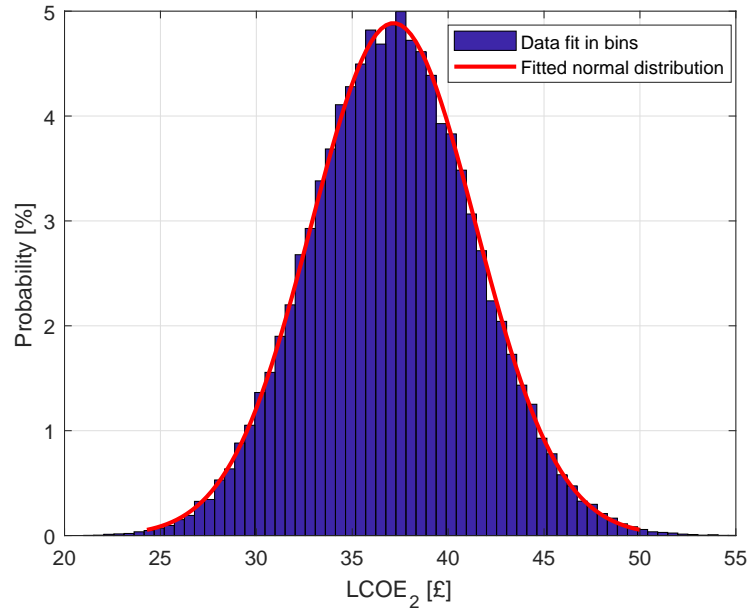
Figure 6.12: Monte Carlo analysis of LCOE₂ of no component replacement

Results of the Monte Carlo simulation are presented in Figure 6.12 with no component replacement and in Figure 6.13 for the replacement of the entire drive train. In addition, Table 6.5 presents the respective P10/50/90 percentiles.

Table 6.5: Project expenditure percentiles [£] based on Monte Carlo simulation

Scenario	P10	P50	P90
No replacement	16.10	20.54	25.02
New drive train	31.68	37.07	42.53

Overall, there is a 90% probability that the LCOE₂ is below £25.02 with no component replacement, whereas when exchanging the entire drive train, there is a 50% chance that LCOE₂ are above £37.07. With respect to the threshold spot market electricity price, there is a 69% chance to be economically profitable. Of course, results of the Monte Carlo simulation will change with differently encountered mean AEP.

Figure 6.13: Monte Carlo analysis of LCOE₂ of drive train exchange

6.5 Discussion and Future Work

Confidence in the SHM measurement campaign increases as a function of the duration of the data monitoring campaign; a longer monitoring period will thus deliver an increase in confidence in the strategic LTE business case.

Applying the AEP of each turbine requires closer examination as often turbines are curtailed due to network restrictions. Therefore, besides looking at the AEP in isolation, curtailment information can deliver a more accurate picture. Also, when having operated a wind farm for 20 years, its grid integration is well understood and thus data readily available.

As identified by Tavner [277], Wilson [278], and Reder [279], wind turbine reliability is correlated with environmental conditions. Thus, a turbine's components have an individual and thus varying load profile. Of course, the design of the respective turbine should accommodate for such differences given the IEC classes (IEC 61400-1). The turbine in question was identified based on the highest annual wind speed of the respective wind farm. Nevertheless, such indicators as turbulence intensity are also important.

The O&M costs may therefore fluctuate per turbine and should ideally be taken into consideration in the economic evaluation. In order to accommodate fluctuations, the optimistic and pessimistic cost bands are presented.

While local wind conditions may change over the years [193, 194], so in turn would the AEP. Therefore, when extracting the AEP, a period of several years should be considered. Ideally, the entire operational life.

It is further possible to extrapolate tower fatigue findings onto each individual wind turbine in the wind farm by application of a tower finite element model and, ideally, analysis of high frequency SCADA data (if available). This may be considered in future work, in order to determine a wind farm lifetime extension strategy, by clustering turbines into cells with different loading. In this regard, low wind speed and turbulence intensity exposed wind turbines might be selected for turbine removal and the spare parts might be stored or straight away used to replace turbine components with higher mean wind speed and turbulence intensity values.

Judging from the cost to carry out a tower measurement campaign (roughly £20,000-30,000), it is suggested that to gain an accurate LTE strategy, the benefit outweighs the costs of the installation of such a system. Of course, the latter depends on the deployed turbine and wind farm size [275] as well as the SHM system design.

It is further suggested to install tower sensor sets (one sensor each side for validation purposes [273]) 90° apart as well as to analyse each wind corridor by varying β in order to cover any eventualities if e.g., the assumed prevailing wind direction does not match the real prevailing wind corridor as highlighted in Section 6.1. In addition, as the cross sectional moment of inertia and bending moment change with tower height, so does the stress distribution. Ideally, the tower wall thicknesses and sectional diameters are measured to derive the maximum stress location. Nevertheless, in the absence of tower geometry data, a correction factor may be applied as highlighted in Section 6.1. Overall, it is strongly recommended to measure the tower's geometry (thickness and diameter with hub height) to identify the most critical stress location. At this location, the fatigue analysis shall be executed. As such, the application of generic or simplified tower geometries may lead to severe uncertainties and inaccuracies of

aero-elastic simulations and thus caution is advised.

The SHM monitoring campaign may be tailored for a global analysis aimed at evaluating stresses of critical tower areas, such as along the entrance door as well as flanges as discussed by Schedat et al. [280].

With respect to the rainflow counting algorithm, it is suggested to use a binning width equal or lower than 0.2 MPa paired with a minimum sampling frequency of 100 times the first tower mode. This allows accurate measurements while maintaining an appropriate accuracy (within 10%). Also, a correction parameter can be applied based on the findings presented in Figure 6.6 and 6.7 if data is available at a lower sampling frequency. It is also strongly recommended to measure the tower's geometry (thickness and diameter with hub height) to identify the most critical stress location. At this location, the fatigue analysis shall be executed. The application of generic or simplified tower geometries may lead to severe uncertainties and inaccuracies of aero-elastic tower simulations.

SHM data combined with economic findings do not suggest that long-term lifetime extensions should be carried out blindly, thus the necessary inspections are key in making sure that the continued operation is safe. For the tower, critical sections are all welded and bolted connections as well as areas with corrosion [23, 77]. An inspection guideline published by DNV GL for the tower and foundation is presented in Table 6.6 of the Section Appendix. In addition, an inspection guideline is published by Megavind [77]. In critical cases, it is further suggested to reduce the inspection interval or to install tailored SHM hardware. For an example of tower flange cracking, the reader is referred to work developed by Do et al. [113]. To access experimental mechanical and fracture properties of welded S355 steel, work by Mehmanparast et al. [281] is suggested.

As illustrated by Helm [282] based on data by the Department for Business, Energy, Industry, and Strategy (BEIS), the electricity price is expected to remain at current prices and then gradually increase from 2020, reaching a high in 2024 before dropping off in the UK. In fact, this requires careful observation and scrutiny in order to define the profitability threshold appropriately.

Finally, great uncertainties origin from the weld assumption; data that is unlikely shared by turbine manufacturers. For example the tower section-flange connection may be a fillet weld, hence considered a FAT class 41. Alternatively, the flange connection might be a 80% penetration butt weld with a FAT class of 80 MPa, thus with a significant higher resistance to fatigue cycles. Potentially, the weld might be analysed with ultrasonic wall thickness measurement devices to get confidence in the selection of FAT classes.

6.6 Section Conclusions

This work explored a case specific lifetime extension decision-making process, based on information gathered through SHM. The process indicates that if the tower and foundation are in a good condition (acceptable level of corrosion, no cracks for the tower; foundation cracks within acceptable limit), these key turbine components are generally well suited to be relied upon for making lifetime extension decision-making. Overall, the results of this study further support the operational knowledge that lifetime extension is highly site specific; however, it is essential to derive a suitable LTE strategy for the continued operation to generate the economic business case. This is especially valid for multi-MW turbines with substantial annual energy production. Besides allowing continued electricity generation and maintaining local O&M jobs, lifetime extension reduces the generation of waste which is of general interest.

6.7 Section Appendix

Table 6.6: Tower & foundation inspection guideline. D is damage, C is cracks, Co is corrosion, Sp is safety sign plates, Ps is prestress, Cf is connection/fitting, and F is function. [23]

Tower Component	Inspection
Tower structure	D,Co,C,Sp
Ladder, fall protection	D,Co,F,Sp
Bolted connections	Co,Ps,C
Foundation, embedded section	D,Co,C
Foundation	D,C
Grounding/Earthing strip	Cf,D,Co

Chapter 7

Conclusion

The overall research approach is schematically illustrated in Figure 7.1, showcasing the thesis objective; i.e., to support the economic and technical lifetime-extension decision-making.

This is carried out in a twofold approach, looking at the commercial decision-making in Chapter 4 with different tools and techniques and in Chapter 5 with specific technical focus on onshore foundations and towers. Based on the research findings, a pathway for strategic lifetime extension is exemplified in Chapter 6.

In the following text, detailed conclusions are drawn for the economic lifetime extension decision-making in Section 7.1, for optical sensor development in Section 7.2 and for supportive lifetime extension SHM in Section 7.3. Finally, the thesis is completed with general recommendations for action in Section 7.4 and a brief outlook is presented in Section 7.5.

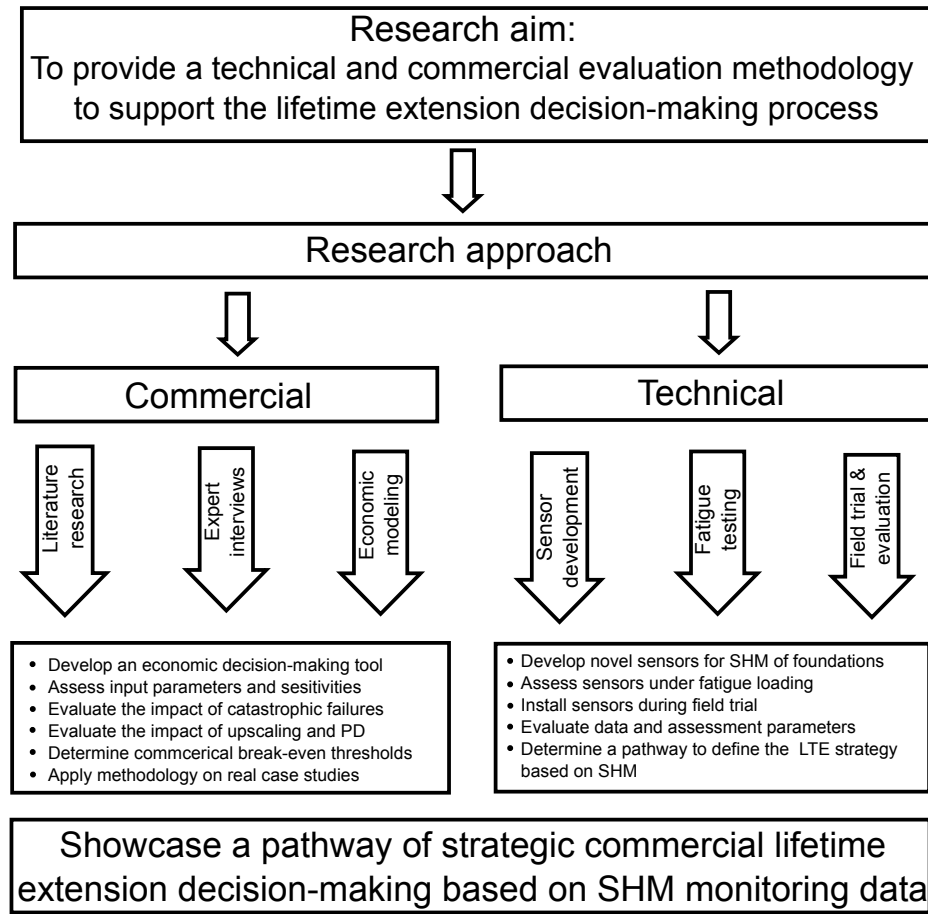


Figure 7.1: Overview of Thesis Research Approach

7.1 Economic Lifetime Extension

Based on the economic lifetime extension research, the following key results are summarized, allowing a concise overview of the findings:

- Greater rated turbines generate relatively more electricity (rated power vs. rotor diameter - πR^2), thus substantially more revenues can be allocated to support LTE. Such as the installation of tower sensors for fatigue analysis.
- Lifetime extension is expected to be the preferred option to repowering based on the current subsidy system in the UK, Germany, Denmark, and Spain.

- It is suggested to model LTE as a separate investment, but to update input parameters based on the total operational experience (see collaboration with BVGAssociates in Section 4.6).
- The LCOE₂ model is mainly dependent on the wind speed. This is hence the most important economic parameter to estimate accurately besides the day-ahead spot market price.
- Lifetime extension processes are highly dependent on national requirements.
- Potential to add further complexity to the model; i.e., failure rates, delaying decommissioning costs (especially offshore), hybrid case studies (subsidised and non-subsidised extension), etc.
- LTE is asset/policy/country dependent, thus standardisation is challenging.

As highlighted in Section 4.4, an economic tool is only useful if appropriate model parameters are applied. This has been achieved by collaborating with BVGAssociates in Section 4.6 and operational data received from the wind farm presented in Section 6. Given that there are unique operational conditions for each wind farm (e.g. noise curtailment, downtime, operational curtailment, degradation, etc.), the analysis requires asset specific evaluation. This can be applied as detailed as down to a single turbine or cluster of turbines. In addition, the derived LTE model may be used to support mergers and acquisitions of wind farms as the economic profitability may be derived based on cost estimates.

7.2 Sensor Development

For the sensor development, the following outcomes are of importance:

- For any further sensor design, a stage gate process is advised to be implemented to ensure resources are utilised most economically as illustrated in Section 5.4. This goes hand in hand with the initial quasi-static testing (up to 1500 cycles) and if successfully, subsequent dynamic fatigue tests.

- Although the manufacture of the metal-packaged strain sensor was improved significantly, this sensor type is suggested to be disregarded due to complexity and process control limitations. Therefore, it is advised to design less complex variants. One promising approach is exemplified in Section 5.4 and it is highly recommended to continue this line of sensor research.

7.3 Supportive Lifetime Extension SHM

Key highlights of the foundation results are itemised below:

- Measured foundation strain is low in magnitude. In detail, significantly below the fatigue cut-off limit.
- It is challenging to install optical sensors in wind turbine foundations (requires packaging and installation refinement).
- Requires in-depth commitment by the operator to support project execution.
- Costly, as there are no commercial services available on greater scale (difficult to make use of economies of scale).
- Fragility of optical addressing is a concern as experiences from the field trial.
- There is significant potential to reduce material (steel/concrete) in the future due to less conservative design assumptions (the considered foundation weighs 1 Mt) or alternatively to reuse foundations for greater scale turbines.

Based on the initial measurement campaign, findings reveal low observed strain ranges reaching a maximum of $95 \mu\epsilon$ that leads to the conclusion that the turbine may operate indefinitely; i.e., it is heavily over-engineered. At the current stage concrete cracking was observable as identified in Figure 5.50. This observation may further change in the future and thus it is impossible to express full confidence in an indefinite operation. Also, environmental effects such as freeze-thaw cycles will affect the structural integrity over time.

Given that a turbine is designed for 20-25 years of operation while the foundation is

designed for 50 years, confidence may be expressed of an extended lifetime of another 20 years, though long-term data would of course reduce uncertainty.

Due to sensor losses in key areas, it is impossible to scientifically provide an argument for design optimisation or the reuse of the foundation with greater scale turbines.

For the tower measurement campaign, the following key highlights are worth noting:

- The tower's weakest links are the welds, especially at the flanges (critical to the weld execution). In addition, the entrance door might be a critical area, especially when aligned with the prevailing wind direction. On the other hand there is evidence that the Magavind project does not see the tower entrance door area as a critical element [77]. This is also confirmed by recent ultrasonic tower wall thickness field measurements of the V117 generator, identifying that the wall thickness is 70 mm at the entrance door, whereas the average tower wall thickness at the sectional height is 40 mm.
- Findings reveal a total lifetime of 54 years for the tower (SCADA average wind speed of 7.35 m/s) based on a limited measurement period at the tower base.
- It is of importance to identify the strain in the actual prevailing wind direction as illustrated in Section 6.1.1.
- Findings reveal that the variation of the tower thickness and sectional diameter influences the stresses along the tower significantly with the highest stresses observed at 30-40% of the hub height as illustrated in Table A.1 and A.2. It is therefore highly suggested to take tower thickness and diameter measurements into consideration to derive the long-term lifetime extension strategy.
- In addition, ideally there is a requirement to correct for the outer fibre of the tower wall; however, this second stress correction is insignificant in comparison to the height correction as identified in Table 6.1.
- In order to select the weld assumption properly, such as for flange-tower welds, ultrasonic wall thickness measurements may help to select the appropriate FAT

class.

- Generic tower geometries will likely introduce severe uncertainties in RUL estimations as it may fluctuate as contrasted in Table A.1 and A.2. Thus geometry measurements are highly suggested to define stresses along the tower height (wall thickness and diameter to derive the cross sectional moment of inertia).

With regards to the tower fatigue findings, results show that the weld assumption is of critical importance; however, the RUL of the considered turbine is estimated to be 54 years (conservative assumptions), which also indicates significant potential to increase the lifetime of the turbine by another 10-15 years without reaching a critical operational region. For the business operation this may be of vital information to consider an extended operation of the wind farm. However, critical areas such as the entrance door and transition pieces require thorough inspection.

While this work analysed a small section of lifetime extension SHM applications, findings are important to limit to this thesis's specific SHM results. The main findings are summarised as follows:

- Steel is forgiving in its response [283]; thus, there are early indicators of fatigue failure. An example crack model is illustrated in Section 3.3.3.4.
- The foundation is at present not of concern as the strain levels are below the fatigue cut-off limit. However, more data might reveal higher stresses due to micro-crack propagation.
- The tower is of importance as it is a load carrying component. Fatigue data of one turbine can be compared to SCADA data and extrapolated onto the entire wind farm.
- So far the tower measurement campaign results in a RUL of 54 years, which is expected to slightly reduce once the winter months are covered.
- Monitoring the tower allows to support the long-term strategic business case for lifetime extension. Tower measurements also enable to define/support a LTE strategy very early on.

- There is potential to determine a global tower SHM analysis to monitor transition pieces, stresses at different tower levels as well as the entrance door.

7.4 Recommendations for Action

Based on the technical and economic findings, the following recommendations for action are summarised when operating beyond the asset's design life:

- Make sure inspections are carried out thoroughly and periodically (including non-destructive inspection of tower welds, blade inspections, etc.). Focus on all items that can cause a catastrophic failure to reach target safety levels, prevent economic loss as well as negative publicity. If uncertain increase frequency of inspection. Develop methods to define risk and probability bands to prevent catastrophic failures.
- Start the economic LTE evaluation in year 12-14 and reconsider operational procedures impacting the RUL. Execute the measurements for at least a year, ideally, for the entire operational time or as long as economically deemed possible.
- Apply lifetime extension either strategically (+10-15 years if the turbine is considered in a good shape) or operationally (+1-5 years if the turbine is considered problematic). This can be based on inspections, load analysis, and or operational data.
- Forecast the electricity price to determine economic feasibility/thresholds for decision-making and swift reactionary responses if failures occur.
- Turbine and foundation SHM may deliver increased certainty in the decision-making, but usually comes at significant expenditure, thus the benefit must be properly assessed. For greater scale wind farms, SHM data collection appears more feasible. The appropriate threshold may be defined in the future.
- It is highly recommended to measure the tower thickness and diameter distribution to gather information about the cross sectional moment of inertia with

height for a representative analysis; i.e, to identify the most critical location with the highest fatigue loading. At the highest stress location, gathered data needs to be evaluated in the prevailing wind direction as exemplified in Section 6.1.1. Also, the application of generic aero-elastic geometries will likely have significant uncertainty involved in assessing the tower's RUL, thus generic models are not recommended.

- Pair tower fatigue data with SCADA and extrapolate onto wind farm (identify critical turbines, or for clustering - UL standard). An aero-elastic code and or tower FEM may support this decision-making.
- The application of aero-elastic codes is not legally necessary in the UK and Denmark; however, when in doubt or of concern of the public image (if a turbine fails), recertification will allow for a stronger sense of security. The latter shall be carried out as part of turbine specific analysis.
- Follow the IEC lifetime extension regulation (currently being developed under the ID of IEC 61400-28 – “Through Life Management and Life Extension of Wind Farms”).
- Follow DNV GL’s initiative to standardise concrete fatigue tests to optimise design assumptions for wind turbine components and facilitate lifetime extension [284].
- There is great potential to extend the LTE LCOE tool to compare investment decision-making to repowering and decommissioning or add failure rates and models. In addition, a socio-economic analysis and policy options might be explored.
- Prepare a failure mode and effect analysis (FMEA) and run a survey for lifetime extension to gain statistically representative failure probabilities and impact [£] parameters to feed into economic models. An initial literature review was carried out with the content accessible in reference [285].
- In combination with an FMEA, reliability considerations are state-of-the-art questions in LTE and need to be addressed.

- There exists merit in embedding sensors in onshore foundations to reduce conservative design assumptions or for reuse purposes for sites that are aimed to be repowered with greater rated turbines; however, any similar effort requires substantial resources and refinement as identified in this field trial. Costs savings of 9% are potentially achievable as a saving in CAPEX as highlighted in Section 4.4.1.1.2.

7.5 Outlook

From a research point of view, lifetime extension offers significant potential for further research. Economic models may be developed with further complexity such as modelling i) end of life failure rates, ii) a hybrid scenario in which the wind farm is partially in a RO subsidy and subsidy-free environment as it will occur for farms reaching their design lifetime before 2027 under the RO, iii) the value of deferring decommissioning costs, iv) a socio-economic analysis versus repowering, v) the business case for a governmental lifetime extension policy, vi) looking at reliability levels and respective confidence parameters, and vii) any considerations offshore. With respect to the governmental lifetime extension policy, lifetime extension may be subsidised to support operators to keep fully working and healthy power plants on the grid, to fulfil the recently renewed and increased European renewable energy targets, while reducing premature decommissioning of assets. Thus, reducing waste, especially left from materials applied in reinforced foundations and blades.

To facilitate this, SHM may provide valuable information to support the long-term business case; however, the actual implementation and scope of data analysis requires further research to determine what is essential (cost-benefit analysis). For the foundation SHM, this work provides invaluable information that may be accessed to support equal activities in the future to prevent the loss of sensors. For the tower analysis, there is potential to execute an in-depth tower monitoring campaign to determine loading patterns, stresses, and strains at all critical areas and interpolate findings based on SCADA data paired with an FE tower model onto the entire wind farm. Economically, this would be feasible at large wind farm sites, such as Whitelee with a rated total

Chapter 7. Conclusion

power of 539 MW.

Appendix A

Graphs, Figures, and Tables

Appendix A. Graphs, Figures, and Tables

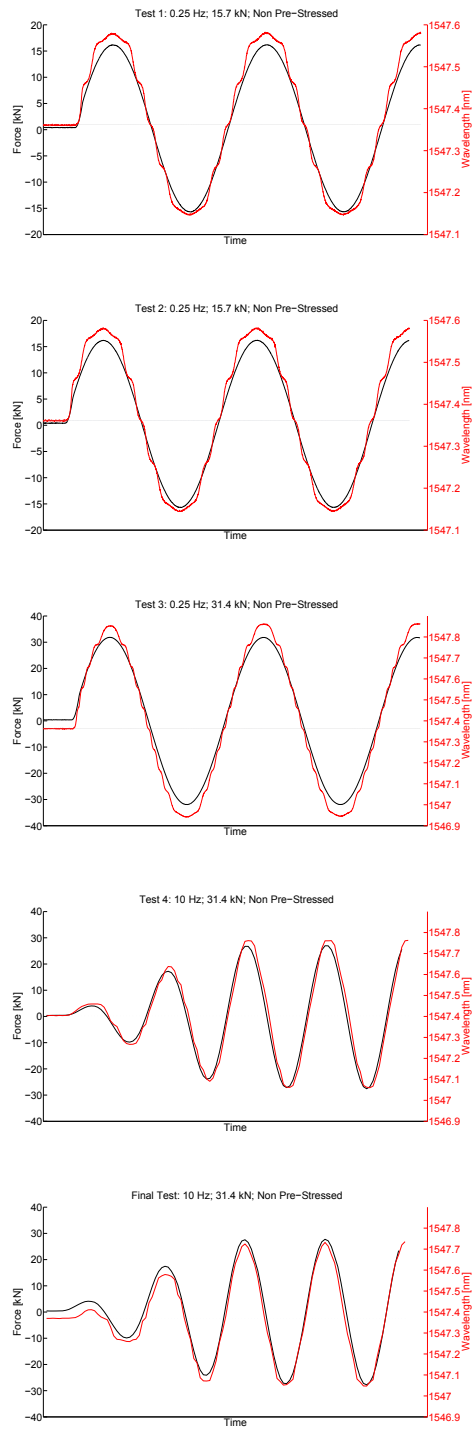


Figure A.7: Non Pre-Stressed Sensor - Characteristics

Appendix A. Graphs, Figures, and Tables

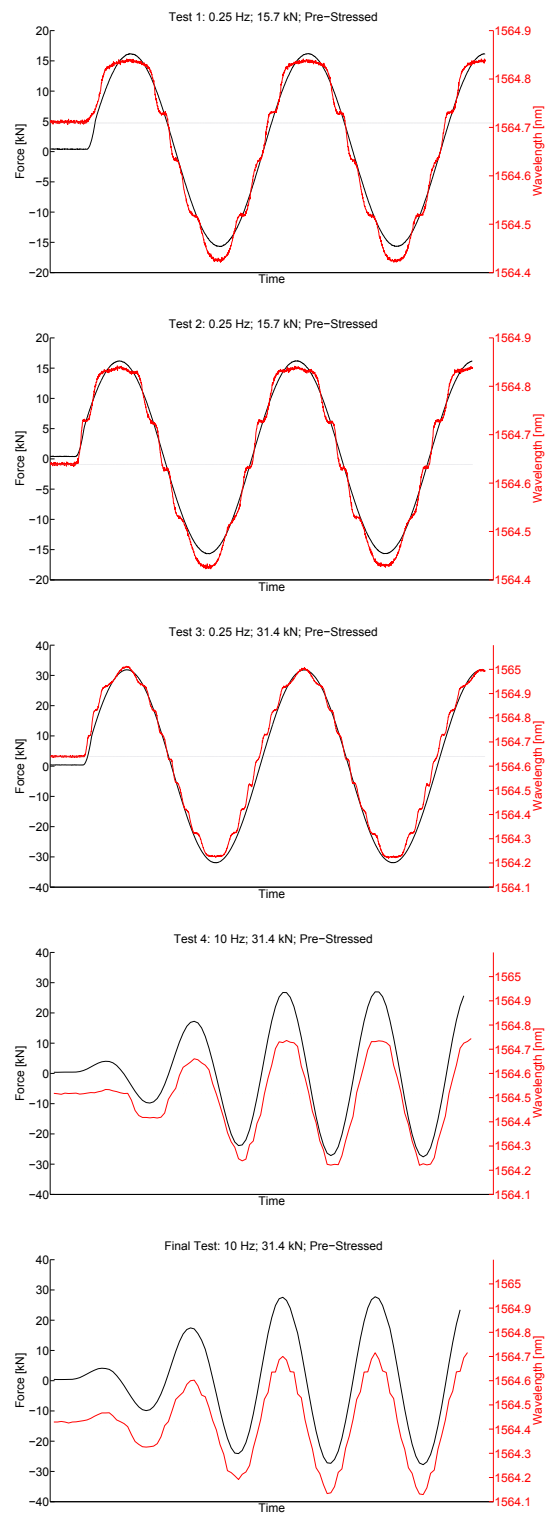
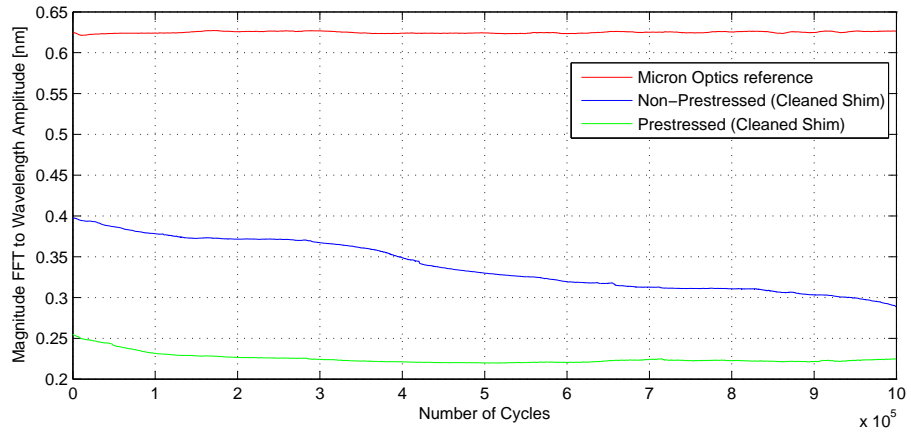
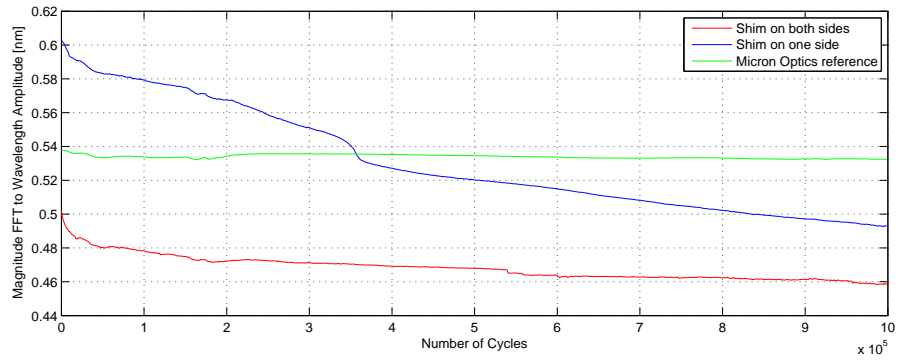


Figure A.8: Pre-Stressed Sensor - Characteristics

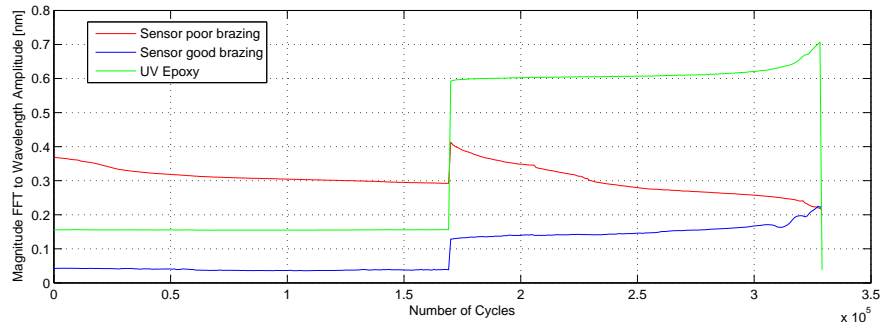
Appendix A. Graphs, Figures, and Tables



(a) Dumbbell 1 fatigue test



(b) Dumbbell 2 fatigue test



(c) Dumbbell 3 fatigue test

Figure A.9: Overview of fatigue test results

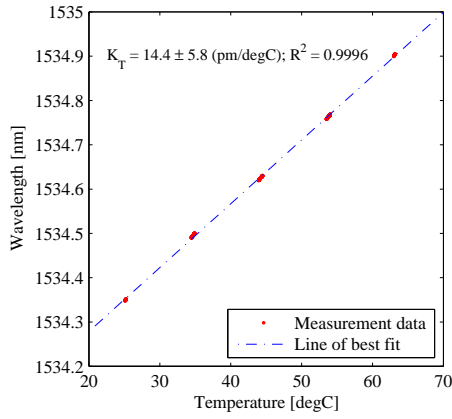
Appendix A. Graphs, Figures, and Tables

1	Tower	Inspection
1.a	Tower structure	D,Co,C,Sp
1.b	Ladder, fallprotection	D,Co,F,Sp
1.c	Bolted connections	Co,Ps,C
1.d	Foundation, embedded section	D,Co,C
1.e	Foundation	D,C,
1.f	Grounding/Earthing strip	Cf,D,Co
2	Nacelle	
2.a	Yaw bearing	T,N,Co,L
2.b	Gear	F,L,W,C
2.c	Nacelle foundation/main frame	D,Co,C
2.d	Nacelle cover	D,Co,C
3	Drive train	
3.a	Hub	D,Co,C
3.b	Main shaft	D,Co,C
3.c	Coupling	D,C
3.d	Main shaft bearings	T,N,L
3.e	Gearbox	T,N,L,W
3.f	Torque support	D,Co,C
3.g	High speed shaft	D,Co,C
3.i	Generator	D,N,L
3.j	Cooling system/circuit	Cf,D,T,C
3.k	Bolted connections	Co,Ps
3.l	Protective covers	D,Co
4	Rotor Blades	
4.a	Blade structure	D,C
4.b	Blade connection	D,T,Co,C
4.c	Bolted connections	Co,Ps
5	Pitch Mechanism	
5.a	Blade tip brakes	D,F,Co
5.b	Blade adjustment	T,F,N,L,W
5.c	Blade bearing	T,N,W
5.d	Coupling elements	D,Co,L,C
5.e	Pitch mechanism	D,F,N,Co,L,C
5.f	Hydraulic components	D,T,F,Co
6	Safety system	
6.a	Rotor locking device	D,Co,Sp
6.b	Yaw locking device	D,Co,Sp,C
6.c	Mechanical brake	F,Co,C,W,C
6.d	Hydraulic components	D,T,F,Co
6.e	Vibration switch	Cf,D,F
6.f	Overspeed gauge	F
6.g	Emergency push buttons	F
6.h	Cable twist sensor	F
6.i	Short circuit protection	F
6.j	Fire extinguisher, first aid box	E
7	Wind sensors	Inspection
7.a	Anemometer	D,F,Co
7.b	Windvane	D,F,Co
8	Yaw Mechanism	
8.a	Yaw drive, gear, pinion	D,F,N,Co,L
8.b	Brake	F,C,W,Ps
8.c	Hydraulic components	D,T,F,Co
9	Hydraulics	
9.a	Pump	T,F,Co
9.b	Accumulator	T,Co,L,Ps
9.c	Hoses including couplings	D,T,Co,C
10	Control and Electrical Installations	
10.a	Cabling	Cf,D,C
10.b	Grounding, machine compon.	Cf,D
10.c	Grounding, lightning protection	Cf,D
10.d	Sliding contacts, main shaft	Cf,D,W
10.f	Hazard beacon	F
10.g	Emergency light, tower	Cf,D,F
10.h	Switch cabinet	D,T,Co,Sp
10.i	Control system	F
10.j	Grid loss	F
10.k	Converter	Sp, D, Cf, T
10.l	Transformer station	Cf,D,T,Sp
10.m	Medium-voltage system	D,Co,Sp
10.n	Power transformer	Cf,D,T,Sp
11	Manuals and documents	
11.a	Operating manual	E
11.b	Maintenance duty book	E
11.c	Maintenance reports	E
11.d	Commissioning report	E
11.e	Building permit	E
11.f	Certification reports	E
11.g	Analysis of oil sample	E
11.h	Inspection papers elevator (pers.)	E
11.i	Inspection papers crane (material)	E
11.j	Certificate of conformance	
		E

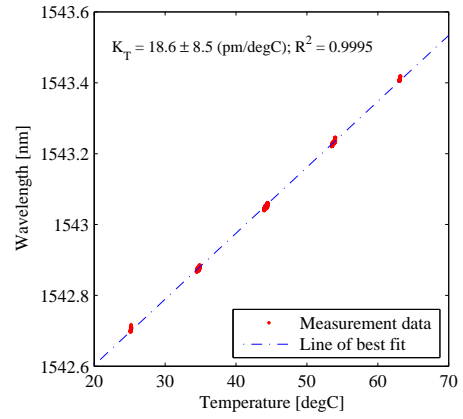
Tested for:			
Damage	D	Connection/fitting	Cf
Examined	E	Tightness	T
Noise	N	Function	F
Cracks	C	Corrosion	Co
Safety sign plates	Sp	Oil level	L
Prestress	Ps	Wear	W

Figure A.13: Lifetime Extension - Inspection List (DNV GL) [23]

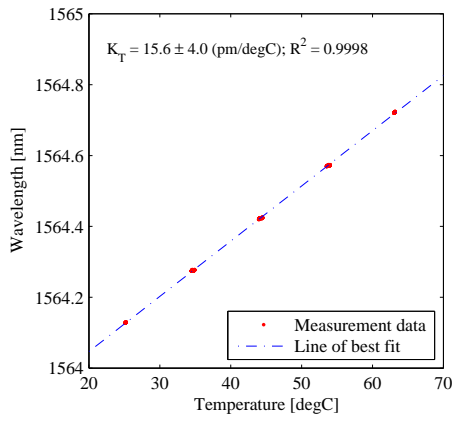
Appendix A. Graphs, Figures, and Tables



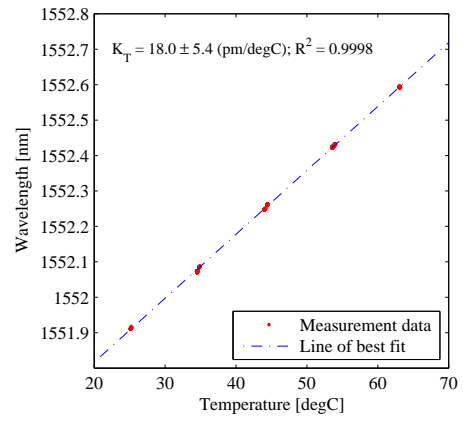
(a) Temperature sensor I



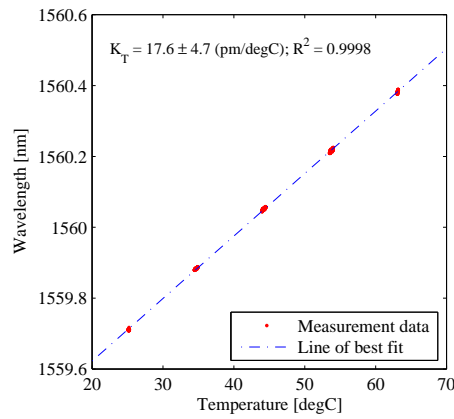
(b) Strain sensor I



(c) Temperature sensor II



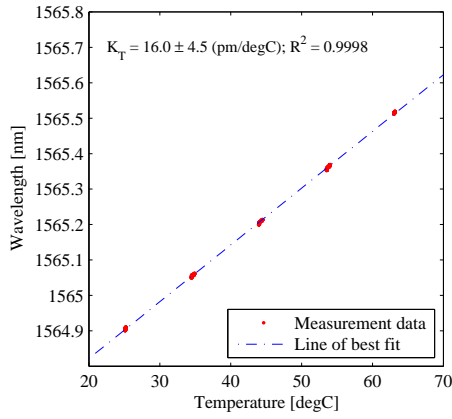
(d) Strain sensor II



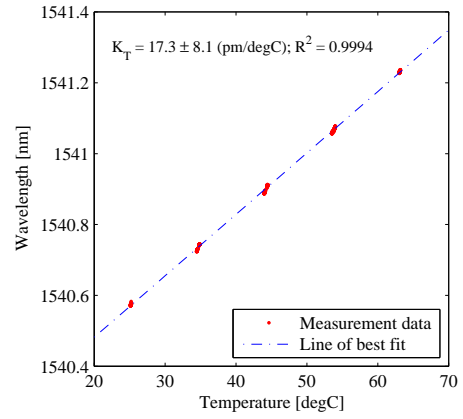
(e) Strain sensor III

Figure A.14: SSE sensor characteristics - Channel 1

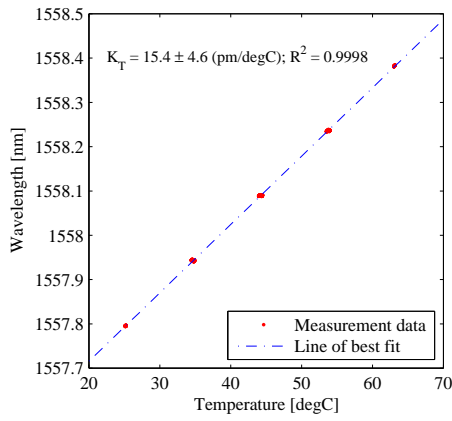
Appendix A. Graphs, Figures, and Tables



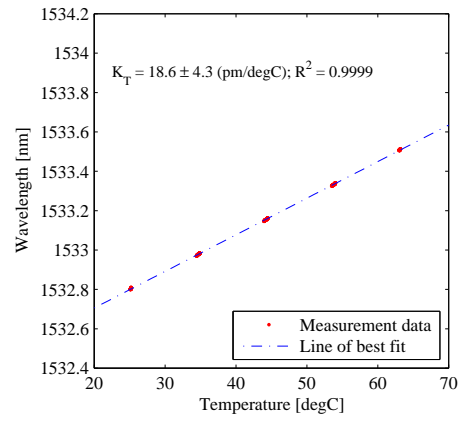
(a) Temperature sensor IV



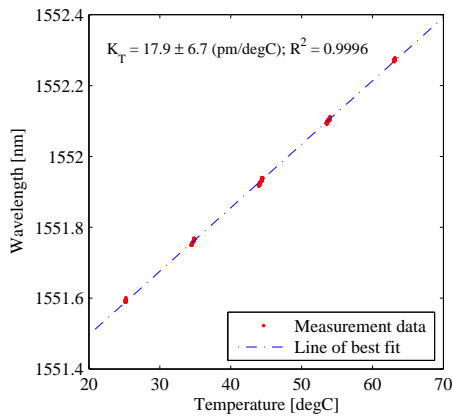
(b) Strain sensor IV



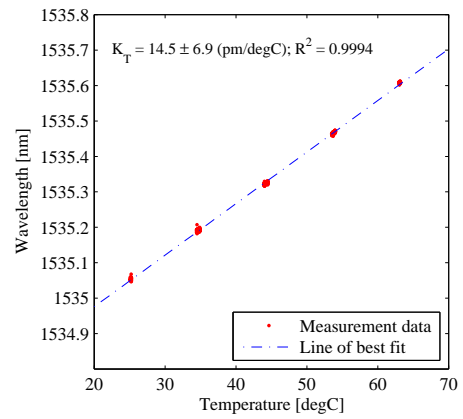
(c) Temperature sensor V



(d) Strain sensor V



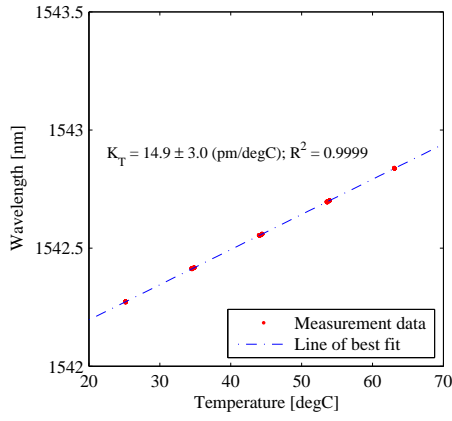
(e) Strain sensor VI



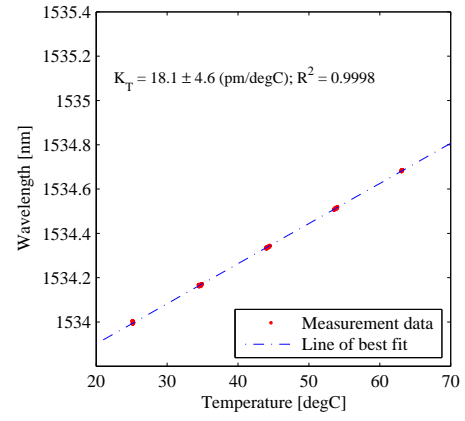
(f) Temperature sensor T1 (Optional)

Figure A.15: SSE sensor characteristics - Channel 2

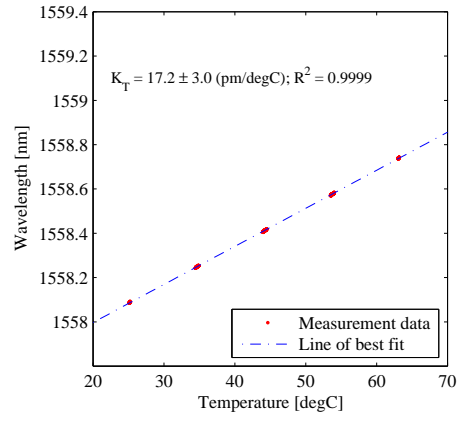
Appendix A. Graphs, Figures, and Tables



(a) Temperature sensor VII



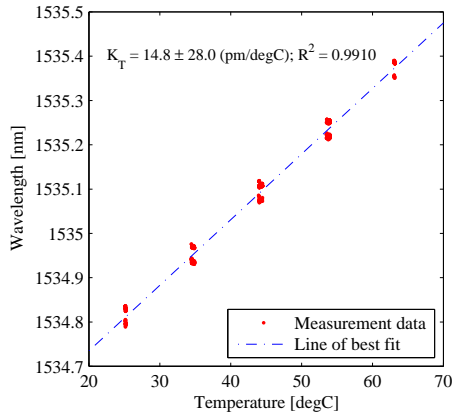
(b) Strain sensor VII



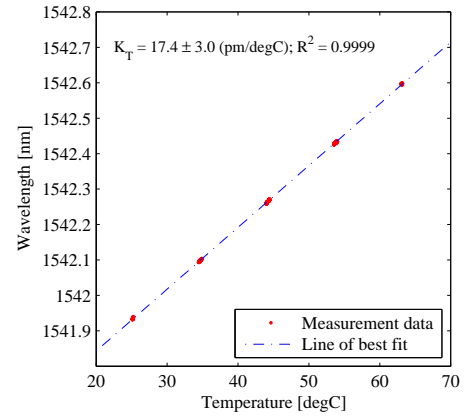
(c) Temperature sensor VIII

Figure A.16: SSE sensor characteristics - Channel 3

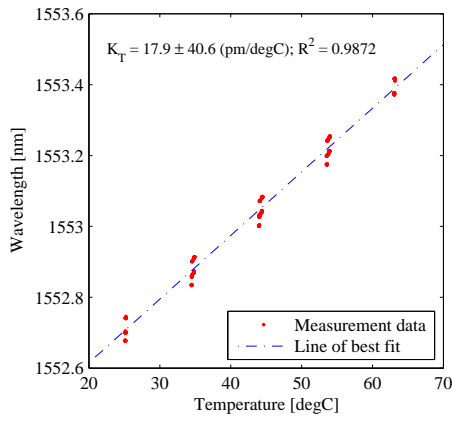
Appendix A. Graphs, Figures, and Tables



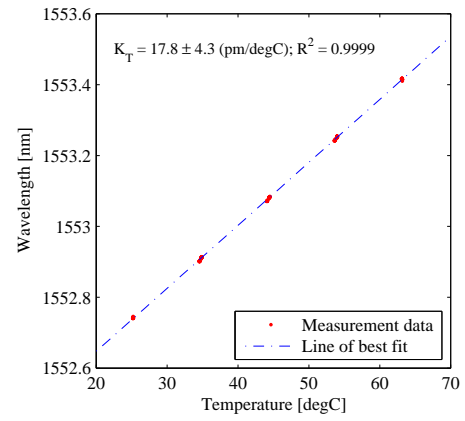
(a) Temperature sensor IX



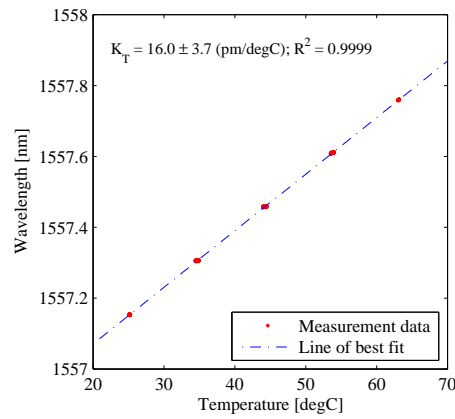
(b) Strain sensor IX



(c) Strain sensor X (4 cycles)



(d) Strain sensor X (3 cycles)



(e) Temperature sensor T2 (Optional)

Figure A.17: SSE sensor characteristics - Channel 4

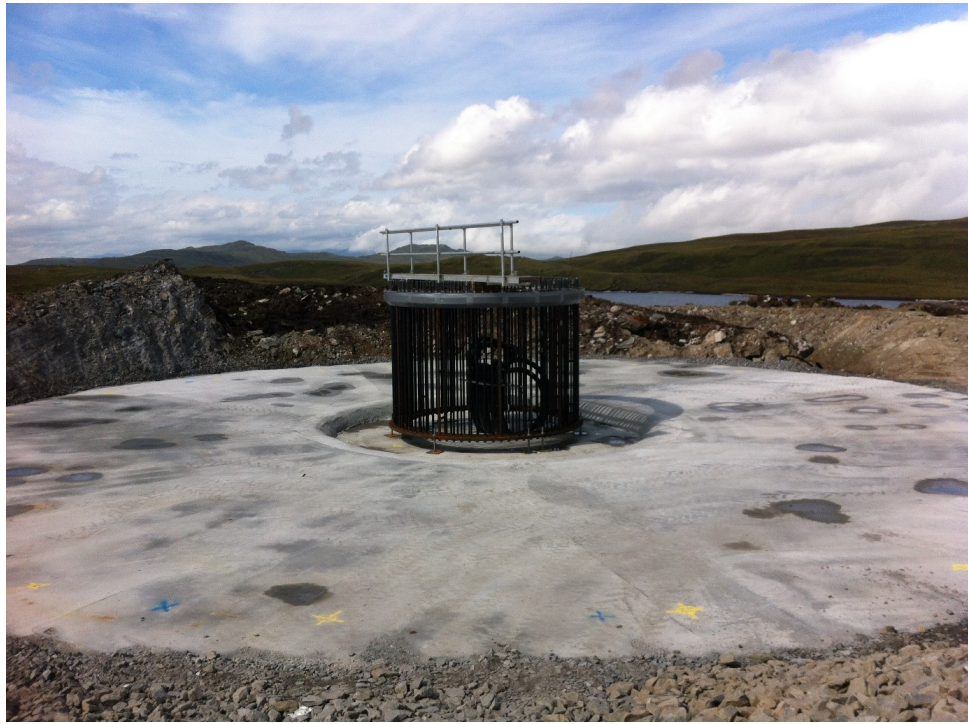


Figure A.18: Foundation ring cage

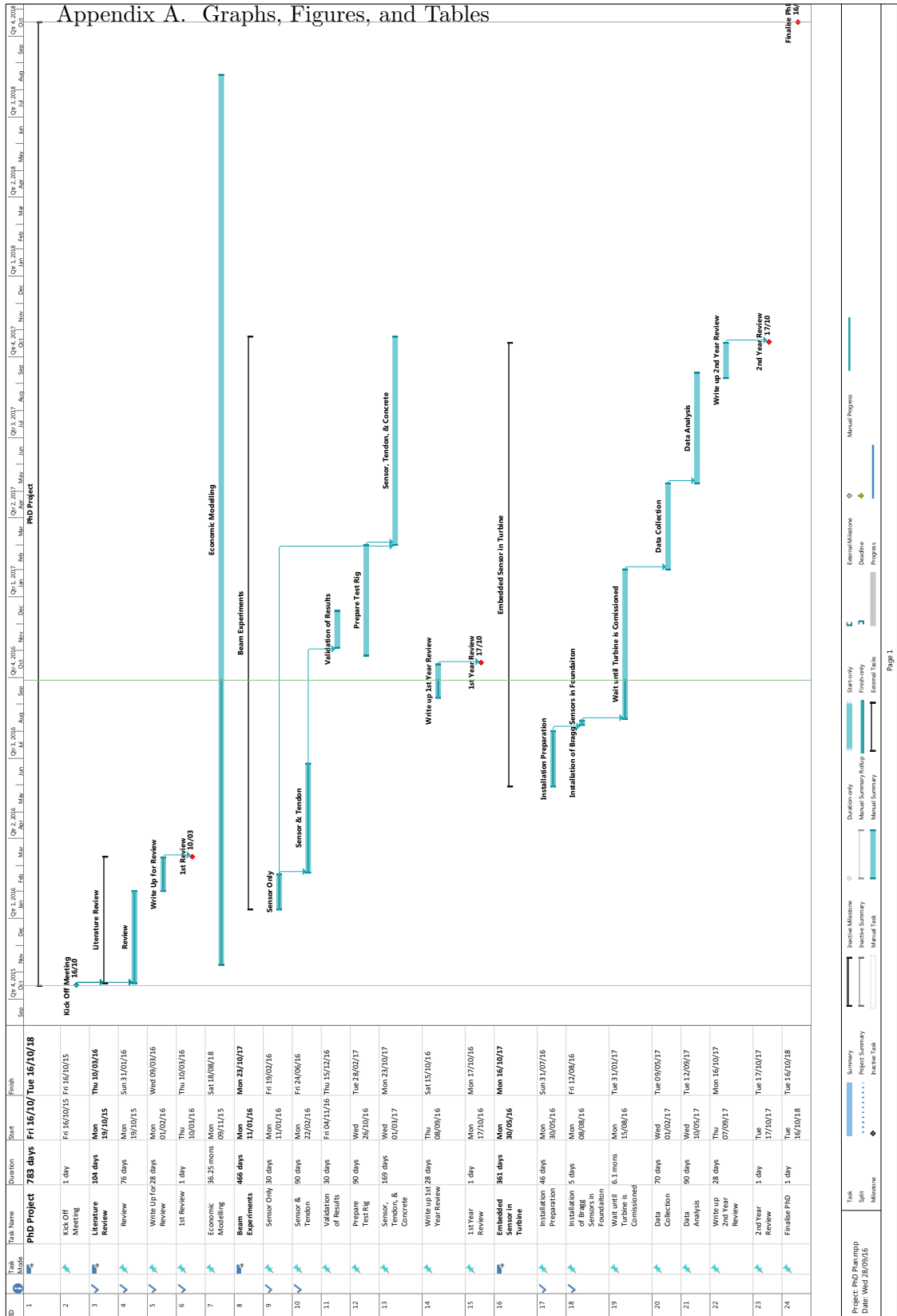


Figure A.1: PhD First Year Project Plan

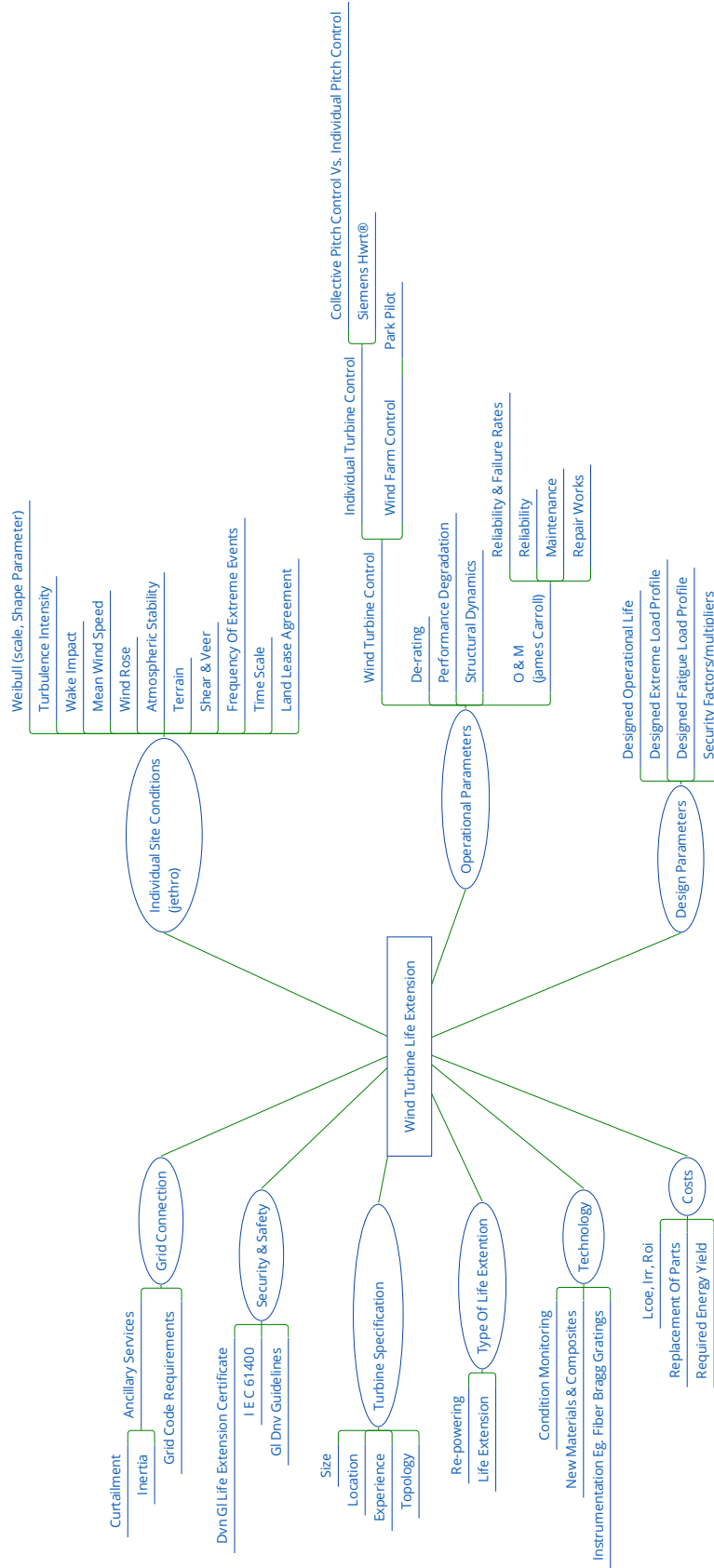


Figure A.2: Mind Map - Life Extension Parameters



Figure A.3: Sensor Temperature Characterisation

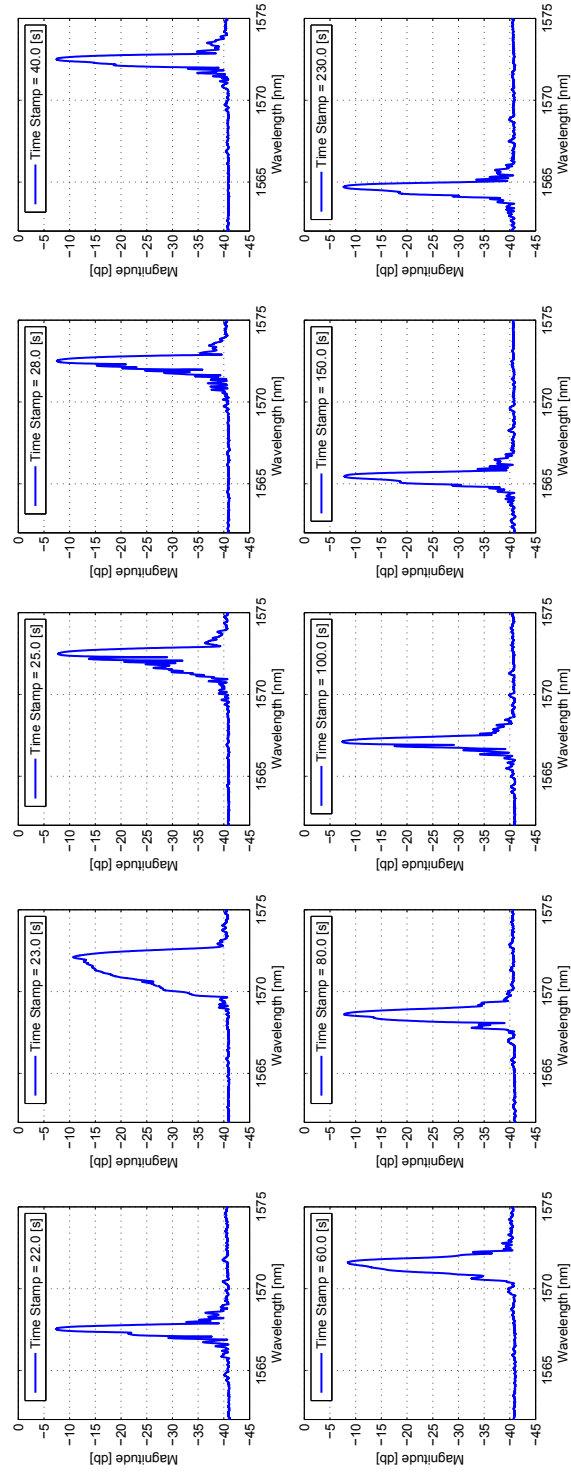


Figure A.4: Second Brazing - Change in Spectrum

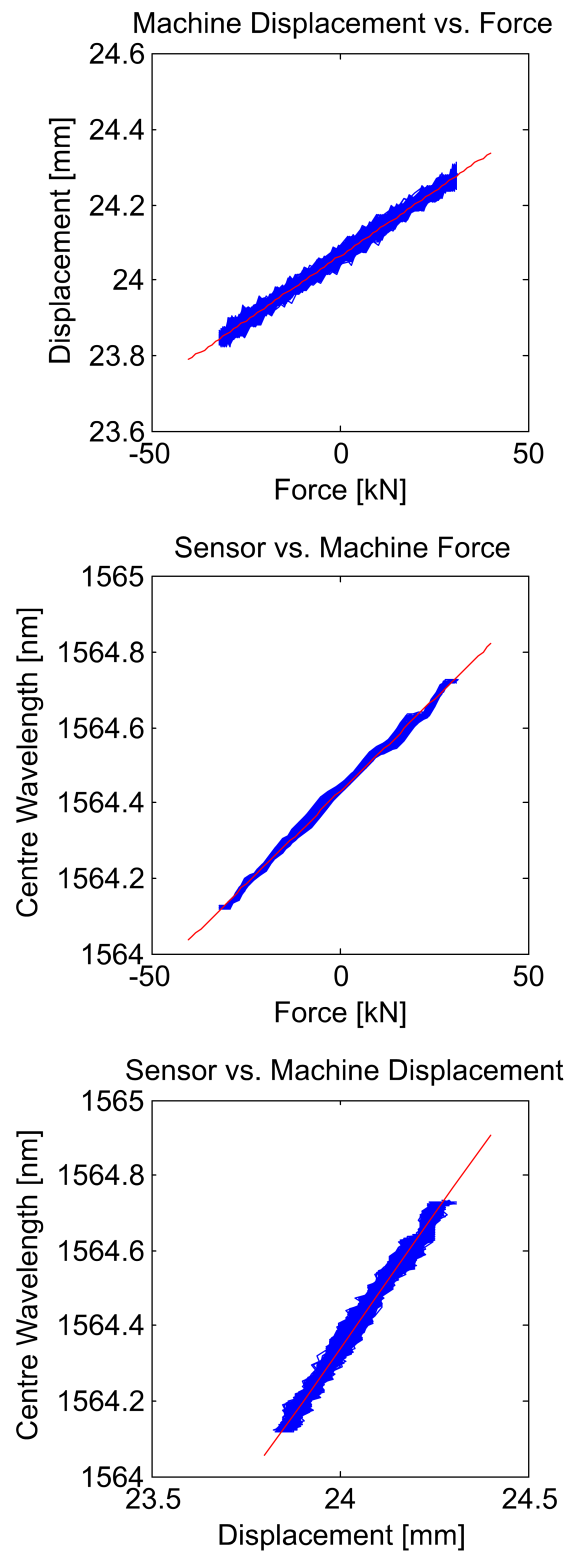


Figure A.5: Hysteresis of Non-Prestressed Sensor and Machine Data

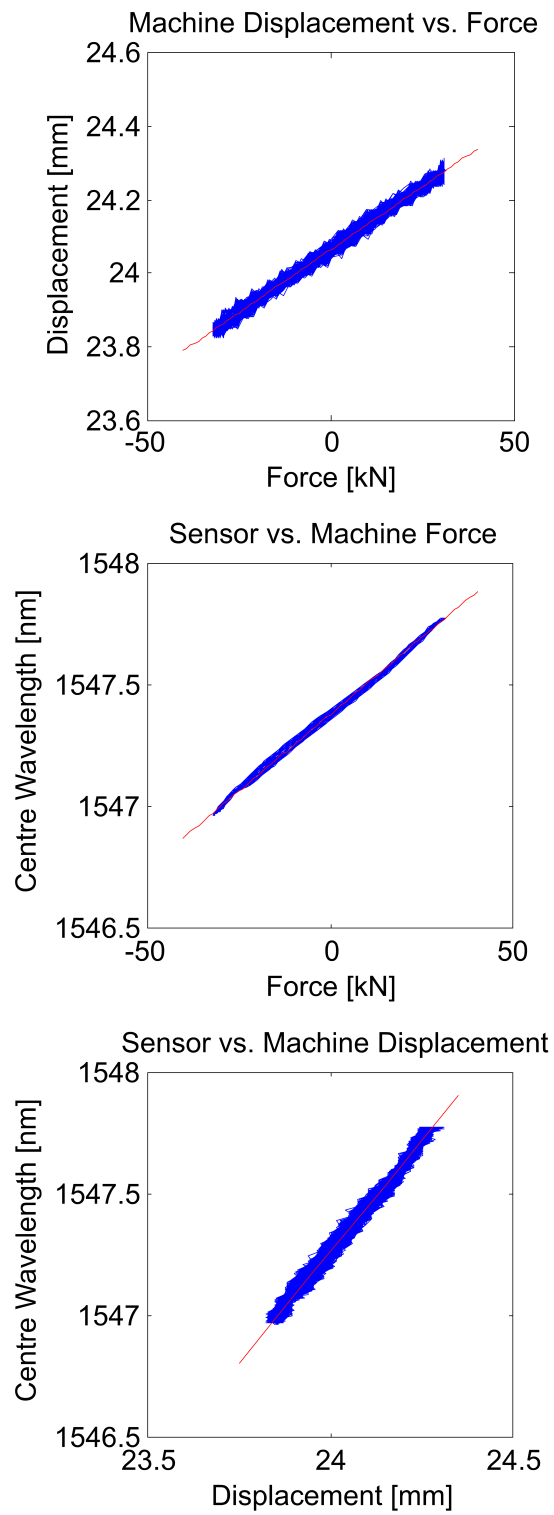


Figure A.6: Hysteresis of Prestressed Sensor and Machine Data

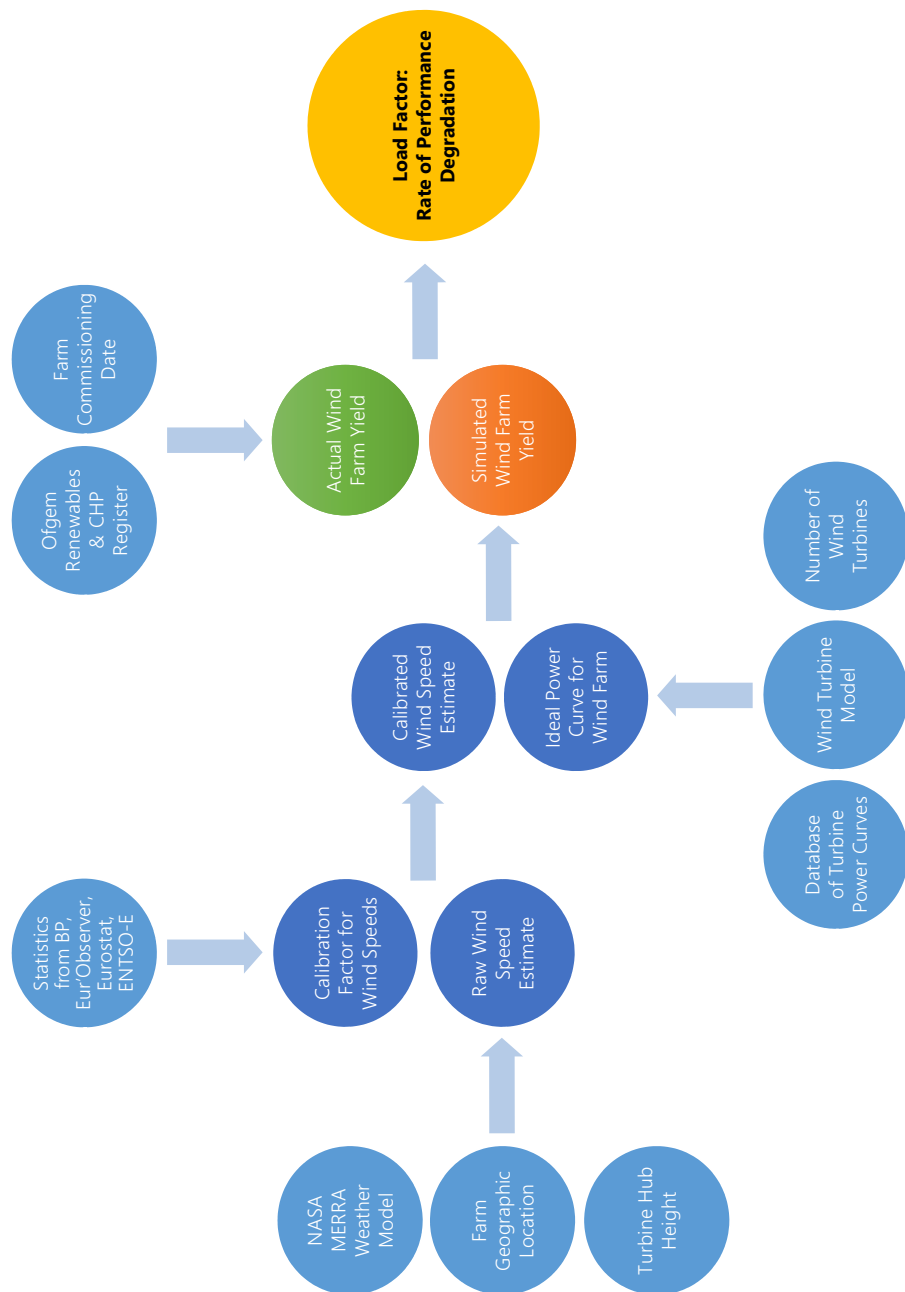


Figure A.10: Methodology - Wind Turbine Performance Degradation

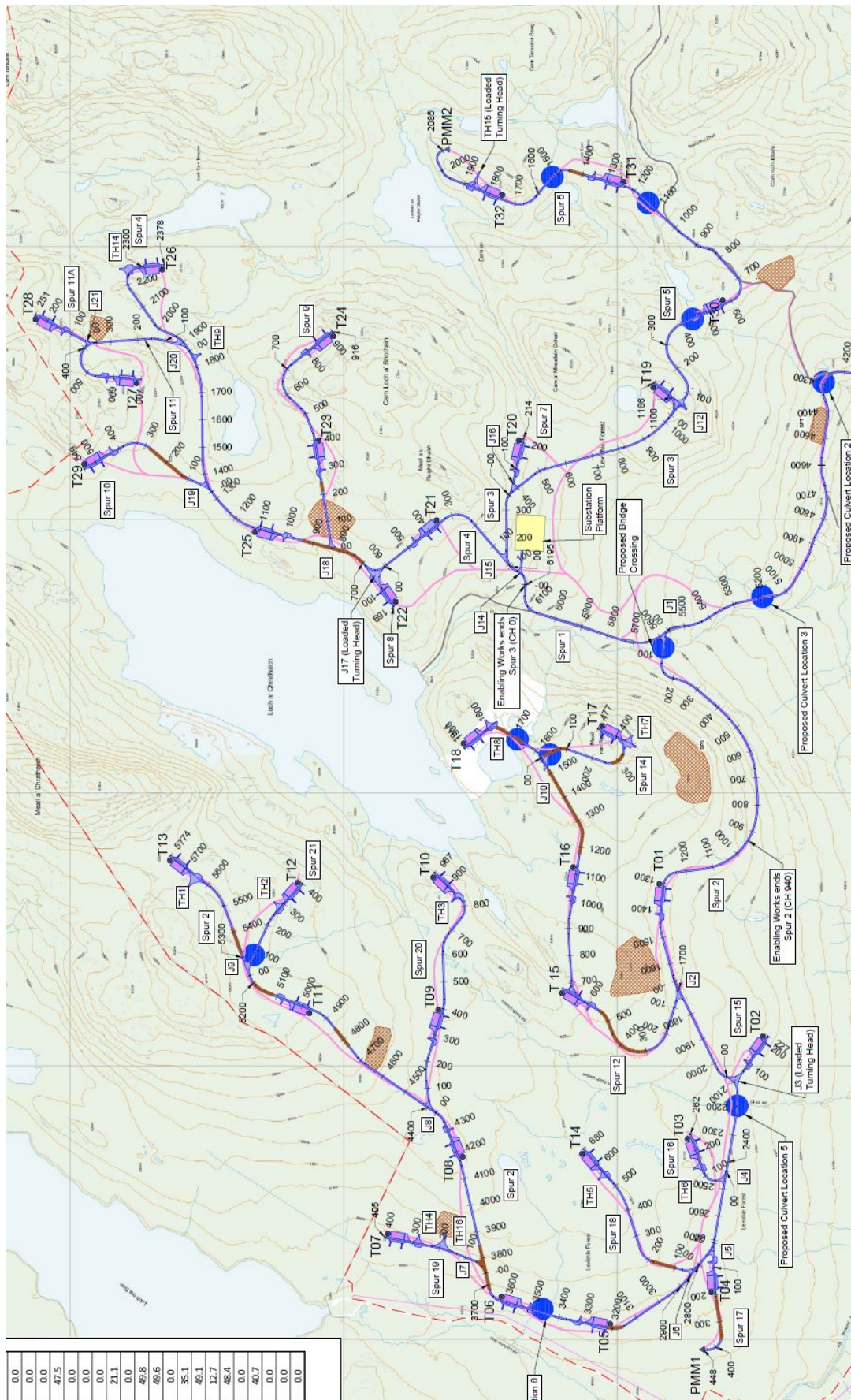


Figure A.11: Site Layout

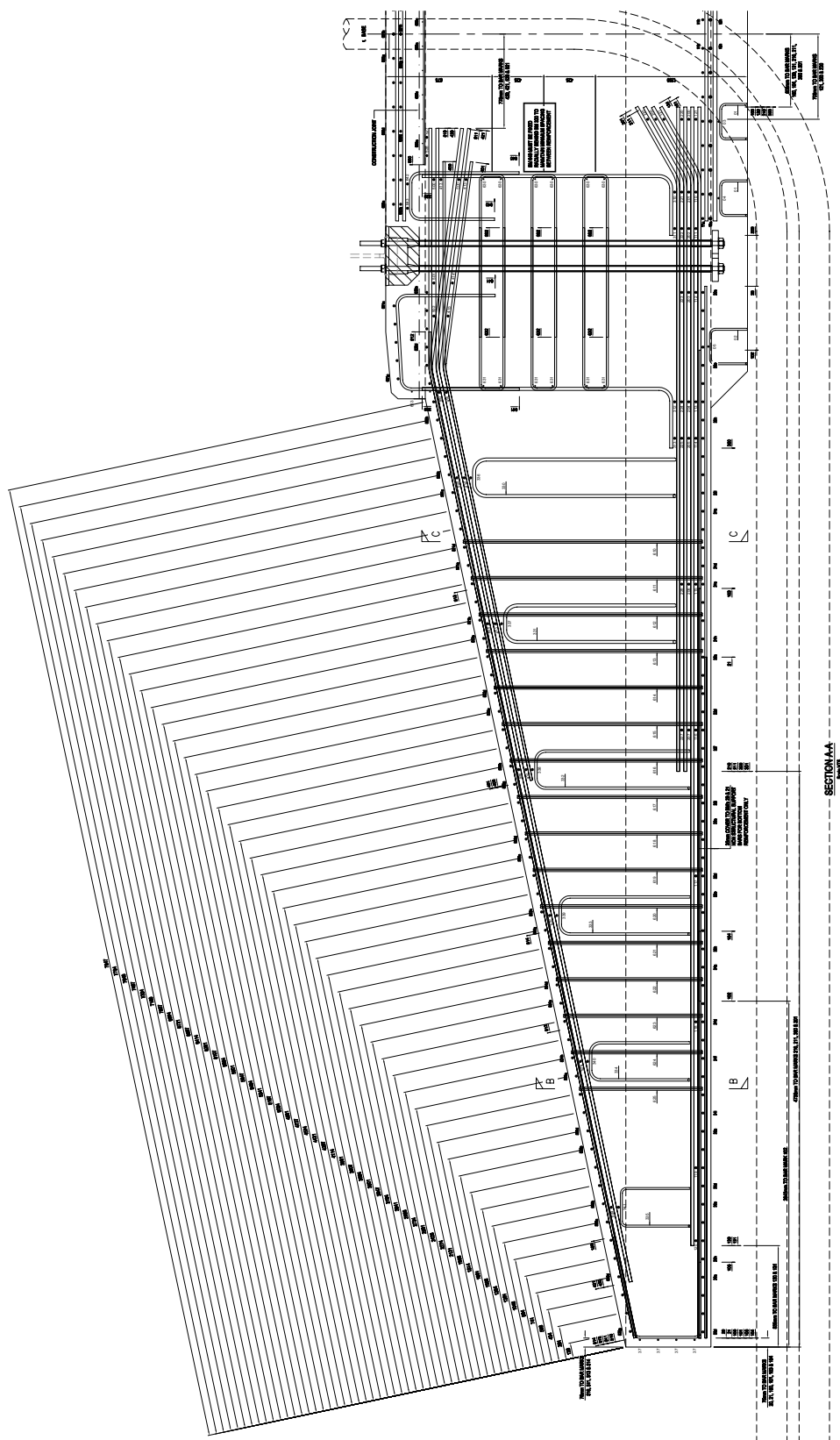


Figure A.12: Foundation Layout



(a) Sensor installation outside of the foundation



(b) Sensor installation inside of the foundation

Figure A.19: SSE sensor site installation

Table A.1: Stress distribution on tower elements (input data from [272]). The cross sectional moment of inertia and derived sectional stress are calculated with Equation 3.25 and 3.24.

Height [m]	Moment Arm [m]	d_{ID} [m]	Thickness [mm]	d_{OD}^I [m ⁴]	d_{ID}^I [m ⁴]	Δ	I [m ⁴]	M(X) [Nm]	Distance outer fibre [m]	σ [N/m ²]	σ [MPa] or [N/mm ²]
90	0	2.4	12	34.52	33.18	1.35	0.07	0.00	1.21	0.00	0.00
72	18	2.72	14	57.03	54.74	2.29	0.11	5882352.94	1.37	71935451.13	71.94
64	26	2.9	17	74.10	70.73	3.38	0.17	8496732.03	1.47	75222747.26	75.22
51	39	3.25	20	117.16	111.57	5.59	0.27	12745098.04	1.65	76341325.75	76.34
36	54	3.55	22	166.84	158.82	8.02	0.39	17647058.82	1.80	80535436.95	80.54
26	64	3.7	25	197.75	187.42	10.34	0.51	20915032.68	1.88	77279006.91	77.28
16	74	4.1	32	300.64	282.58	18.06	0.89	24183006.54	2.08	56790300.84	56.79
0	90	4.1	40	305.28	282.58	22.71	1.11	29411764.71	2.09	55144973.04	55.14

Table A.2: Stress distribution on tower elements (input data from [267, 268]). The cross sectional moment of inertia and derived sectional stress are calculated with Equation 3.25 and 3.24.

Height [m]	Moment Arm [m]	d_{TD} [m]	Thickness [mm]	d_{OP}^4 [m ⁴]	d_P^4 [m ⁴]	Δ	I [m ⁴]	M(X) [Nm]	Distance outer fibre [m]	σ [N/m ²]	σ [MPa]
75.64	0	2.955	18	80.03	76.25	3.78	0.19	0.00	1.48	0.00	0.00
75.492	0.148	2.971	14	80.89	77.91	2.98	0.15	48366.01	1.49	491340.39	0.49
73.082	2.558	3.015	12	85.29	82.63	2.66	0.13	835947.71	1.51	9641646.72	9.64
72.002	3.638	3.034	12	87.45	84.73	2.71	0.13	1188888.89	1.52	13542201.76	13.54
71.152	4.488	3.049	12	89.18	86.42	2.75	0.14	1466666.67	1.52	16543258.48	16.54
69.252	6.388	3.083	12	93.19	90.34	2.85	0.14	2087581.70	1.54	23033364.99	23.03
66.502	9.138	3.133	12	99.33	96.35	2.99	0.15	2986274.51	1.57	31911757.47	31.91
65.842	9.798	3.144	13	100.98	97.71	3.27	0.16	3201960.78	1.57	31335324.94	31.34
63.752	11.888	3.182	13	105.91	102.52	3.39	0.17	3884967.32	1.59	37122270.77	37.12
61.022	14.618	3.231	13	112.53	108.98	3.55	0.17	4777124.18	1.62	44281338.96	44.28
58.622	17.018	3.277	13	119.02	115.32	3.70	0.18	5561437.91	1.64	50122857.95	50.12
58.252	17.388	3.28	14	119.75	115.74	4.00	0.20	5682352.94	1.64	47424799.37	47.42
55.502	20.138	3.33	14	127.15	122.96	4.19	0.21	6581045.75	1.67	53298478.08	53.30
53.812	21.828	3.36	15	132.07	127.46	4.61	0.23	7133333.33	1.68	52920110.89	52.92
51.552	24.088	3.4	15	138.41	133.63	4.78	0.23	7871895.42	1.70	57042242.40	57.04
48.967	26.673	3.448	15	146.32	141.34	4.98	0.24	8716666.67	1.72	61428644.54	61.43
48.817	26.823	3.448	16	146.66	141.34	5.32	0.26	8765086.27	1.72	57862927.28	57.86
46.382	29.258	3.492	17	154.57	148.70	5.88	0.29	9561437.91	1.75	57875978.09	57.88
44.592	31.048	3.524	17	160.26	154.22	6.04	0.30	10146405.23	1.76	60314469.20	60.31
43.982	31.658	3.535	17	162.25	156.16	6.09	0.30	10345751.63	1.77	61120070.21	61.12
41.752	33.888	3.574	18	169.84	163.16	6.67	0.33	11074509.80	1.79	60408323.64	60.41
39.002	36.638	3.622	18	179.05	172.11	6.95	0.34	11973202.61	1.81	63603588.70	63.60
36.252	39.388	3.671	19	189.25	181.61	7.64	0.37	12871895.42	1.84	63022088.65	63.02
34.382	41.258	3.704	19	196.07	188.23	7.84	0.39	13483006.54	1.85	64852066.76	64.85
31.982	43.658	3.746	19	205.02	196.91	8.11	0.40	14267320.26	1.87	67105899.04	67.11
30.752	44.888	3.768	20	210.28	201.58	8.70	0.43	14669281.05	1.88	64737783.94	64.74
28.002	47.638	3.816	20	221.08	212.05	9.03	0.44	15567973.86	1.91	6699719.07	67.00
25.252	50.388	3.864	20	232.29	222.92	9.37	0.46	16466666.67	1.93	69131145.91	69.13
22.362	53.278	3.917	20	245.17	235.40	9.76	0.48	17411111.11	1.96	71146367.23	71.15
22.182	53.458	3.917	21	245.66	235.40	10.26	0.50	17469934.64	1.96	67935408.36	67.94
19.752	55.888	3.962	22	257.54	246.41	11.13	0.55	18264052.29	1.98	66225892.32	66.23
17.972	57.668	3.993	22	265.60	254.21	11.39	0.56	18845751.63	2.00	67286900.47	67.29
17.362	58.278	4.004	22	268.51	257.03	11.49	0.56	19045098.04	2.00	67628606.61	67.63
15.172	60.468	4.043	22	279.01	267.19	11.82	0.58	19760784.31	2.02	68833679.73	68.83
12.582	63.058	4.089	23	292.35	279.56	12.79	0.63	20607189.54	2.04	67088063.14	67.09
11.502	64.138	4.108	24	298.33	284.79	13.55	0.66	20960130.72	2.05	64748201.37	64.75
9.302	66.338	4.147	27	311.47	295.76	15.71	0.77	21679084.97	2.07	58296949.68	58.30
7.789	67.851	4.173	26	318.64	303.24	15.40	0.76	22173529.41	2.09	61202013.04	61.20
5.802	69.838	4.208	26	329.34	313.55	15.79	0.78	22822875.82	2.10	61960359.86	61.96
5.412	70.228	4.215	30	334.00	315.64	18.36	0.90	22950326.80	2.11	53668634.19	53.67
3.082	72.558	4.257	30	347.32	328.41	18.91	0.93	23711764.71	2.13	54371920.50	54.37
2	73.64	4.276	30	353.47	334.31	19.16	0.94	24065359.48	2.14	54698542.90	54.70
0	75.64	4.3	30	361.36	341.88	19.48	0.96	24718954.25	2.15	55565199.41	55.57

Appendix B

LTE Standards

B.1 DNV GL

Simplified Analysis

- load calculation, may be performed using generic turbine model
- calculation of possible extension of lifetime based on environmental conditions as per original design vs. environmental conditions at the site
- possibly accompanied by load measurements

Practical Part

- inspection based on general inspection plan
- visual inspection of all load-transferring and safety-relevant components
- review of maintenance reports and inspection reports for specific turbine
- consideration of SCADA data
- consideration of wind turbine type related field experience
- performance of tests

Detailed Analysis

- load calculation based on specific turbine model

Appendix B. LTE Standards

- calculation of possible extension of lifetime based on environmental conditions as per original design vs. site specific environmental conditions and utilization rate of components
- reserve calculations on load-transferring components
- possibly accompanied by load measurements
- possibly optimization of control system
- consideration of turbine type related field experience
- development of turbine-specific inspection plan

Practical part

- inspection as per turbine-specific inspection plan that has been developed in the analytical part
- visual inspection of all load-transferring and safety-relevant components
- review of maintenance reports and inspection reports for specific turbine
- consideration of SCADA data
- consideration of wind turbine type related field experience
- performance of tests

Probabilistic Analysis

- structural reliability analysis (stochastic approach)
- calculations based on generic or specific turbine model
- selection of reliability levels
- identification of failure modes
- possibly accompanied by load measurements
- possibly optimization of control system

Appendix B. LTE Standards

- consideration of turbine type related field experience
- development of turbine or site-specific inspection plan

Practical part

- inspection as per turbine-specific inspection plan that has been developed in the analytical part
- visual inspection of all load-transferring and safety-relevant components
- review of maintenance reports and inspection reports for specific turbine
- consideration of SCADA data
- consideration of wind turbine type related field experience
- performance of tests

B.2 UL

Step 1: Requirement for external condition

The first step deals with the evaluation of the external environment; i.e., the site's wind conditions:

- (1) Operational historical data shall be used
- (2) SCADA data, met mast data, and/or public databases may be used
- (3) The measurement period shall cover at least 12 months (seasonal variations)

Step 2: Requirement for operation condition

The due diligence for the operational condition deals with the historical characteristics of a power plant and includes the following activities:

- (1) Operational historical data of wind turbine conditions relevant to the structural loading
- (2) SCADA data and operational and maintenance records may be used.
- (3) Wind turbines can be grouped in cells represented by one wind turbine. The selection criteria for the cell definition shall be specified.

Appendix B. LTE Standards

(4) The following information shall be evaluated as a part of the assessment:

(I) General

- (A) Source of the data (e.g. SCADA, OEM records)
- (B) Material and software change logs
- (C) Criteria for the selection of the representative wind turbine
- (D) General description of the wind farm control and communication with the wind turbine controller
- (E) The operational data of the wind turbine including the load relevant events

(II) Load relevant transient events

- (A) Transient events with significant impact on the loads of the wind turbine like:
 - (i) Emergency stops (E-stops) and stops triggered by the safety system
 - (ii) Stops performed by control system
 - (iii) Start ups
 - (iv) Operation with yaw misalignment exceeding the design limits
 - (v) Failure of wind turbine systems
- (B) Wind speed at hub height and electrical power (and/or operating mode), at which the event has occurred
- (C) Total number of events
- (D) Type/reason of event and typology of the braking program used to stop the wind turbine

(III) Power production data

- (A) Power production distribution over time per turbine
- (B) Cumulative power produced per turbine
- (C) Measured power curve based on SCADA data for the representative period/wind turbines

(IV) Parked/idling data

- (A) Number of hours under idling condition
- (B) Wind speeds and wind direction during parked condition
- (C) State of the wind turbine electrical supply during idling state

(V) Maintenance and repair data

- (A) Maintenance report and protocols
- (B) Report of major damages to the wind turbine
- (C) Report of replacements or repairs of components
- (D) Special maintenance, if applicable
- (E) Inspection reports

(VI) Grid related data on site

- (A) Annual number of network outages on the wind farm
- (B) Fault ride through methodology (if present)
- (C) Voltage and frequency range related shut downs or disconnections

Appendix B. LTE Standards

- (D) Ramp rate or power factor related shut downs
- (E) Corrections in the operating strategy for grid suitability
- (F) Other grid related shut downs
- (VII) Other data (if applicable to the site)
 - (A) Number of hours of ice accretion
 - (B) Wind speed during the ice accretion
 - (C) Methodology for ice detection and reaction of the wind turbine
 - (D) Mass of the ice on the blades and the approach used to determine the mass
 - (E) Potential influence of the wind farm controller on the operation of the wind turbine
 - (F) Earth quake
 - (G) Lightning strike
 - (H) Storm events
 - (I) Other geographical characteristics
- (VIII) Control system related data
 - (A) Description of the control system strategy (inputs, outputs, sensors, load reduction and operational strategies)
 - (B) Current software version of the control system
 - (C) Report of the modifications in control system software and the deviation of the parameters or limits from the values considered in the design
 - (D) Modifications in pitch converters (if any)
 - (E) Upgrade in the controller strategy
 - (F) Other changes in control system or safety system related items of the wind turbine

Step 3: Requirement for wind turbine model

The third part deals with the load simulation in order to evaluate a turbine's RUL of its components:

- (1) A list of parameters to generate the simulation model
- (2) For a simulation model that was validated in the course of a wind turbine type certification in accordance with Wind turbines Part 22: conformity testing and certification , IEC 61400-22 or equivalent a prove of the validation shall be provided
- (3) For a simulation model that does not comply with IEC 61400-22 or equivalent. The model generation and validation shall comply with:
 - (I) A detailed procedure of model generation including the data used to build up the wind turbine model
 - (II) Model data validation
 - (III) Validation of aerodynamic model
 - (IV) Validation of structural model

Appendix B. LTE Standards

- (A) To validate the structure model, the 1st Eigen frequency of simulation and measurement shall be compared for tower and blade as a minimum
- (B) Risk analysis
- (V) Load evaluation
 - (A) Load time series generated from simulation shall be compared to MLC for relevant situations to confirm the dynamic behavior
 - (B) DLCs fatigue loading level for the following component shall be compared to MLC:
 - (i) Blade sections (if applicable);
 - (ii) Blade root
 - (iii) Shaft (rotating and non-rotating)
 - (iv) Tower top
 - (v) Tower bottom
 - (vi) Tower sections (if applicable)

Step 4: Requirement for remaining useful life

The forth part deals with the condition if the lifetime extension is suitable from a RUL component point of view:

- (1) The RUL of the wind farm is calculated by representative sample of wind turbines RUL in each cells
- (2) The RUL of the wind turbine is defined by the minimum RUL of the individual components in the wind turbine
- (3) The RUL Criteria is calculated: $FL_{design} \geq FL_{consumed} + FL_{RUL}$ where FL is the fatigue life
- (4) The RUL for any critical components in respect to the structural integrity and the operational safety of the wind turbine shall be derived by comparison of site specific component load to their design load
- (5) The load evaluation shall be based on the standard and the respective edition used as design standard of the wind turbine under assessment

Step 5: Requirement for inspection

The fifth part deals with the required scope of inspections:

- (1) The representative wind turbine used for the LTE shall be inspected for their critical components health condition and functioning
- (2) Further inspections shall be decided based on results from first round of inspections
- (3) The following components as a minimum shall be evaluated as a part of the inspection
 - (I) Over all wind turbine condition
 - (II) Damages on the following components/systems

Appendix B. LTE Standards

- (A) Tower (sections) and foundation
 - (B) Blade
 - (C) Nacelle and hub
 - (D) Bolt connections
 - (E) Bearings
 - (F) Pitch system
 - (G) Yaw system
 - (H) Hydraulic systems
 - (I) Electrical systems
 - (J) Gear box (through videoscopy if applicable)
- (III) Wind turbine operation
 - (IV) Test of safety and control systems
 - (V) Test of all operating states
 - (VI) Personnel safety aspects
 - (VII) Maintenance logs (including the track of the controller, pitch system software)
 - (VIII) SCADA data for the correctness check of operational data
- (4) The inspection as part of the LTE analysis shall take place not earlier than one year before the date the LTE analysis is based on

Step 6: LTE Risk Analysis

The last part deals with the required risk analysis in order to i) evaluate uncertainties in the analysis, ii) address uncertainties in the model, and iii) mitigate their impact:

- (1) General
 - (I) A risk analysis shall be performed to identify uncertainties in the calculation of the remaining useful life time
 - (II) Since the process of calculating the RUL is subjected to the uncertainty; accuracy of simulation data shall be taken into account to derive the safe operation of wind farm based on RUL
 - (III) All steps to calculate the RUL shall be considered in the risk analysis
 - (IV) The failure mode shall be derived
 - (V) Based on wind farm history and operation condition relevant failure modes shall be derived
 - (VI) A justification to decrease the severity level or increase the confidence level on accuracy shall be summarized in a report
 - (VII) A justification of conditions for extended operation of the wind turbine based on risk analysis shall be developed by the applicant. This may include but not only limited to replacements of any wind turbine components, modifications in the operating strategy (e.g. de-rating, curtailment), repair, inspections/maintenance details and software updates

Appendix B. LTE Standards

(2) Risk analysis procedure

- (I) A failure mode shall be derived for the site
- (II) Severity level in the scale of 1 – 10 for each failure mode shall be assigned by the applicant, the severity is defined by the level of impact of failure mode to overall RUL; where 1 is lowest and 10 is highest
- (III) Confidence level on accuracy in the scale of 1 – 10 for each failure mode shall be assigned by the applicant, the confidence level defines how accurate the real site condition is mapped into simulation model; only level 1, 5 and 10 shall be chosen where 1 is highest and 10 is lowest
- (IV) The final risk priority number (RPN) number is calculated as follows: $RPN = (Severity) \times (ConfidenceLevel)$
- (V) A risk analysis shall be carried out to identify uncertainties in the calculation of the remaining useful life time. The risk analysis shall include the determination of consequences of each risk on the RUL (impact on the RUL). In addition, preventive and detection measures shall be specified, if applicable

(3) Risk criteria

- (I) The RPN number defines the confidence level on input used to derive the RUL, RPN shall be less than 50 for any failure mode

Appendix C

LTE Survey Questions

PART I: Company experience with lifetime extension

Introduction

- a) Name:
b) Country:
c) Role:

How does lifetime extension (LTE) affect your business?

Role of the company?

- ☐ Owner: (final decision?)
☐ Operator (asset management):
☐ OEM: (extended designed lifetime, specific services – as G47?)
☐ Independent expert: (technical advice, estimation of remaining lifetime?)
☐ Certification body:
☐ Maintenance services provider:
☐ Research institute:
☐ Politics:
☐ Finance:
☐ Lawyer:
☐ Other:
.....
.....
.....

In your opinion, what is the general motivation of LTE?

(Please specify whether it adds value to Operating Assets (OA) or New Projects (NP); and whether it involves internal decision (ID) or a financial transaction, due diligence (DD))

.....
.....
.....
.....
.....
.....
.....
.....
.....
.....

Figure C.1: Semi-structured survey questions (1/4)

Appendix C. LTE Survey Questions

Concerning the health status of an asset:

- **What activities do you perform to understand the health status of an asset?**

.....
.....
.....

Preventive Maintenance (PM) & Inspections: YES ☐ - NO ☐ - How often?

Monitoring: YES ☐ - NO ☐ - If YES, redirect to next question

- **What do you monitor and what is the role of monitoring? (TI, loads, CMS?)**

Loads: YES ☐ - NO ☐ - If YES, where (tower?), how (sensors?)

.....
.....

- **Do you have a record of operation and maintenance history?**

YES ☐ - NO ☐ - If YES, how? (log books...)

.....
.....

- **How do you plan to use this information in an end-of-life scenario?**

.....
.....
.....
.....
.....

Has your company been involved in any LTE project?

- **How did you assess the remaining useful lifetime?**

.....
.....
.....

Is the interviewee working for a third party involved? YES ☐ - NO ☐

Was the OEM involved? YES ☐ - NO ☐

Was the design model used? YES ☐ - NO ☐

Which data was used for the assessment?

.....

*** Wind conditions: WS ☐ - TI ☐ - shear ☐ - Others ☐

*** Loads: YES ☐ - NO ☐

*** Reliability data: Failure rates ☐ - Others ☐ :

*** How long did it take to be conducted?

Were there any critical components?

.....
.....

- **What investments and retrofits were necessary?**

.....
.....
.....

Figure C.2: Semi-structured survey questions (2/4)

Appendix C. LTE Survey Questions

- **Was re-certification needed?**

.....

- **What were the factors that affected the decision?**

.....

- **Which parameters had major uncertainty?**

.....

From the following chart, what were the most uncertain categories/ parameters?

Operation	Site conditions	RUL assessment	Economics	Legal framework	Other aspects
Performance	Turbulence intensity	Design models	Market price electricity	Insurance	Availability of spare parts
O&M costs	Wind speed	Critical components	Energy yield	Authority requirements	Grid requirements

Figure C.3: Semi-structured survey questions (3/4)

PART II: General aspects of lifetime extension

How do policy and legal aspects play a role for LTE in your country?

c Support:

c Hinder:

- If incentives are existing, are they enough to ensure profitability?

What are the biggest difficulties and concerns?

How do you see the application of the recent DNVGL standard on lifetime extension?

What services does the industry need?

Do you think specific national/European policies need to be formulated?

Figure C.4: Semi-structured survey questions (4/4)

Bibliography

- [1] Tony Blair, “Modernising government,” *White Paper*, no. March, 1999. [Online]. Available: <https://www.wbginvestmentclimate.org/uploads/modgov.pdf>
- [2] European Commission, “Renewable energy progress report,” 2015. [Online]. Available: http://europa.eu/rapid/press-release_IP-15-5180_en.htm
- [3] Climate Policy Observer, “Nine EU countries achieved 2020 renewable energy target,” 2016. [Online]. Available: <http://climateobserver.org/nine-eu-countries-achieved-2020-renewable-energy-target/>
- [4] EWEA, “Wind in Power: 2011 European Statistics.” *Technical Report*, no. February, pp. 1–11, 2012. [Online]. Available: http://www.ewea.org/fileadmin/ewea_documents/documents/publications/statistics/Stats_2011.pdf
- [5] —, “Wind in Power: 2012 European Statistics,” *Technical Report*, no. February, pp. 1–14, 2013. [Online]. Available: http://www.ewea.org/fileadmin/files/library/publications/statistics/Wind_in_power_annual_statistics_2012.pdf
- [6] —, “Wind in Power: 2013 European Statistics,” *Technical Report*, no. February, pp. 1–12, 2014. [Online]. Available: http://www.ewea.org/fileadmin/files/library/publications/statistics/EWEA_Annual_Statistics_2013.pdf
- [7] —, “Wind in Power: 2014 European Statistics,” *Technical Report*, no. February, pp. 1–12, 2015. [Online]. Available: http://www.ewea.org/fileadmin/files/library/publications/statistics/EWEA_Annual_Statistics_2014.pdf

Bibliography

- [8] —, “Wind in Power: 2015 European Statistics,” *Technical Report*, no. February 13, pp. 1–14, 2016. [Online]. Available: http://www.ewea.org/fileadmin/ewea_documents/documents/publications/statistics/Stats_2011.pdf
- [9] J. C. Cornu, “The end of the onshore wind feed-in tariff in France?” 2015. [Online]. Available: <http://www.sgurrenergy.com/author/jean-christophe-cornu/>
- [10] BWE, “Vergleich EEG 2012 und EEG 2014,” *Bundesverband WindEnergie e. V. (BWE)*, 2014. [Online]. Available: <file:///D:/Users/rgb14179/Downloads/bwe-erfolge-vergleich-eeg-2012-und-2014.pdf>
- [11] BMWi, “EEG in Zahlen : Vergütungen, Differenzkosten und EEG-Umlage 2000 bis 2016,” *Bundesministerium für Wirtschaft und Energie*, vol. Oktober, 2015. [Online]. Available: http://www.erneuerbare-energien.de/EE/Redaktion/DE/Downloads/eeg-in-zahlen-pdf.pdf?__blob=publicationFile&v=6
- [12] Nordex, “The all-round Nordex review - Wind Energy Performance,” *Nordex 360*, no. 2, 2014. [Online]. Available: <http://data.worldbank.org/country/south-africa>
- [13] BMWi, “Windenergie auf See,” 2014. [Online]. Available: <https://www.bmwi.de/BMWi/Redaktion/PDF/E/eeg-faktenblatt-windkraft-auf-see,property=pdf,bereich=bmwi2012,sprache=de,rwb=true.pdf>
- [14] —, “Ausschreibungen für die Förderung von Erneuerbare-Energien-Anlagen,” *Bundesministerium für Wirtschaft und Technologie*, Tech. Rep., 2015. [Online]. Available: <https://www.bmwi.de/BMWi/Redaktion/PDF/Publikationen/ausschreibungen-foerderung-erneuerbare-energien-anlage,property=pdf,bereich=bmwi2012,sprache=de,rwb=true.pdf>
- [15] B. Sills, “Spain Halts Renewable Subsidies to Curb 31 Billion of Debts.” [Online]. Available: <http://www.bloomberg.com/news/articles/2012-01-27/spain-suspends-subsidies-for-new-renewable-energy-plants>

Bibliography

- [16] M. Roca, “Spain Caps Earnings From Renewables in Subsidy Overhaul,” 2014. [Online]. Available: <http://www.bloomberg.com/news/articles/2014-06-06/spain-caps-earnings-from-renewables-in-subsidy-overhaul>
- [17] United States Department of Commerce, “Italy,” *International Trade Administration Italy*, 2013. [Online]. Available: http://export.gov/build/groups/public/@eg_main/@reee/documents/webcontent/eg_main_070697.pdf
- [18] Ofgem, “Feed-in Tariff Generation and Export Payment Rate Table for Non-Photovoltaic Installations FIT Year 6 (1 April 2015 to 31 March 2016),” no. April, 2015. [Online]. Available: https://www.ofgem.gov.uk/sites/default/files/docs/2015/07/fit_non-pv_tariff_table_1_october_2015.pdf
- [19] UK Governemnt, “Changes to onshore wind subsidies protect investment and get the best deal for bill payers,” no. June, 2015. [Online]. Available: <https://www.gov.uk/government/news/changes-to-onshore-wind-subsidies-protect-investment-and-get-the-best-deal-for-bill-payers>
- [20] Department of Energy and Climate Change, “Contracts for Difference Allocation Round One Outcome,” Tech. Rep. February, 2015.
- [21] Gamesa, “Life Extension Program,” 2014. [Online]. Available: <http://www.gamesacorp.com/recursos/doc/productos-servicios/operacion-y-mantenimiento/life-extension-eng.pdf>
- [22] —, “Gamesa , first OEM to certify a wind turbine life extension programme,” 2014. [Online]. Available: <http://www.gamesacorp.com/en/communication/news/gamesa-first-oem-to-certify-a-wind-turbine-life-extension-programme.html?idCategoria=0&fechaDesde=&especifica=0&texto=&idSeccion=0&fechaHasta=>
- [23] DNV GL, “Standard: Lifetime extension of wind turbines,” 2016. [Online]. Available: <https://rules.dnvgl.com/docs/pdf/DNVGL/ST/2016-03/DNVGL-ST-0262.pdf>

Bibliography

- [24] Enercon, “Neue EPK-Variante für Anlagen ab dem 20. Betriebsjahr,” Tech. Rep., 2015. [Online]. Available: <http://www.enercon.de/de/aktuelles/neue-epk-variante-fuer-anlagen-ab-dem-20-betriebsjahr/>
- [25] WindPowerMonthly, “Windtech Gamesa and Iberdrola launch new monitoring system,” Tech. Rep. January, 2015.
- [26] M. Hancock, “AW: Technology Implementation,” *Personal Email (10.09.2015)*, 2015.
- [27] D. McMillan, I. Dinwoodie, G. Wilson, A. May, and G. Hawker, “Asset Modelling Challenges in the Wind Energy Sector,” in *Cigre 2014 Paris Session*, 2014.
- [28] W. F. and Williams, “Update on the support mechanism for French onshore wind projects,” 2017. [Online]. Available: <http://www.wfw.com/wp-content/uploads/2017/06/WFW-Briefing-FrenchSupportMechanism-June2017.pdf>
- [29] J. Broehl, “Wind Turbine OEM Consolidation on Full Display in 2017,” 2018. [Online]. Available: <https://www.renewableenergyworld.com/articles/2018/08/wind-turbine-oem-consolidation-on-full-display-in-2017.html>
- [30] J. Murray, “Spain reignites wind energy market as record low bids dominate auction,” 2017. [Online]. Available: <https://www.businessgreen.com/bg/news/3010431/spain-reignites-wind-energy-market-as-record-low-bids-dominate-auction>
- [31] —, “Construction to begin on 'UK's first subsidy free wind farm',” 2018. [Online]. Available: <https://www.businessgreen.com/bg/news/3032689/construction-to-begin-on-uks-first-subsidy-free-wind-farm>
- [32] Y.-J. Rao, “In-fibre Bragg grating sensors,” *Measurement Science Technology*, vol. 8, pp. 355–375, 1997.
- [33] A. Kersey, “A Review of Recent Developments in Fiber Optic Sensor Technology,” *Optical Fiber Technology*, vol. 2, pp. 291–317, 1996.

Bibliography

- [34] K. O. Hill and G. Meltz, “Fiber Bragg grating technology fundamentals and overview,” *Journal of Lightwave Technology*, vol. 15, no. 8, pp. 1263–1276, 1997.
- [35] J. D. Prohaska, E. Snitzer, B. Chen, M. H. Maher, E. G. Nawy, and W. W. Morey, “Fiber optic Bragg grating strain sensor in large-scale concrete structures,” R. O. Claus and R. S. Rogowski, Eds., mar 1993, pp. 286–294. [Online]. Available: <http://proceedings.spiedigitallibrary.org/proceeding.aspx?articleid=1001362>
- [36] R. Maaskant, A. T. Alavie, R. M. Measures, M. M. Ohn, S. E. Karr, D. J. Glennie, C. Wade, G. Tadros, and S. Rizkalla, “Fiber optic Bragg grating sensor network installed in a concrete road bridge,” J. S. Sirkis, Ed., may 1994, pp. 457–465. [Online]. Available: <http://proceedings.spiedigitallibrary.org/proceeding.aspx?articleid=958561>
- [37] W. R. Habel and K. Krebber, “Fiber-optic sensor applications in civil and geotechnical engineering,” *Photonic Sensors*, vol. 1, no. 3, pp. 268–280, 2011.
- [38] J. Salo and I. Korhonen, “Calculated estimate of FBG sensor’s suitability for beam vibration and strain measuring,” *Measurement*, vol. 47, pp. 178–183, jan 2014. [Online]. Available: <http://linkinghub.elsevier.com/retrieve/pii/S0263224113003758>
- [39] J. M. Lopez-Higuera, L. Rodriguez Cobo, A. Quintela Incera, and A. Cobo, “Fiber Optic Sensors in Structural Health Monitoring,” *Journal of Lightwave Technology*, vol. 29, no. 4, pp. 587–608, 2011.
- [40] K. Schroeder, W. Ecke, J. Apitz, E. Lembke, and G. Lenschow, “A fibre Bragg grating sensor system monitors operational load in a wind turbine rotor blade,” *Measurement Science and Technology*, vol. 17, no. 5, pp. 1167–1172, 2006.
- [41] G. Kister, D. Winter, Y. M. Gebremichael, J. Leighton, R. a. Badcock, P. D. Tester, S. Krishnamurthy, W. J. O. Boyle, K. T. V. Grattan, and G. F. Fernando, “Methodology and integrity monitoring of foundation concrete piles using Bragg grating optical fibre sensors,” *Engineering Structures*, vol. 29, pp. 2048–2055, 2007.

Bibliography

- [42] C. Baldwin, J. Kiddy, P. Samuel, J. Coker, and D. Pines, “Fiber optic sensors monitoring transmission ring gears,” *Proceedings of SPIE - The International Society for Optical Engineering*, pp. 720–735, sep 2007. [Online]. Available: <http://proceedings.spiedigitallibrary.org/proceeding.aspx?articleid=824866>
- [43] L. Kruger, P. L. Swart, A. A. Chtcherbakov, and A. J. van Wyk, “Non-contact torsion sensor using fibre Bragg gratings,” *Measurement Science and Technology*, vol. 15, no. 8, pp. 1448–1452, aug 2004. [Online]. Available: <http://stacks.iop.org/0957-0233/15/i=8/a=002?key=crossref.e147be7b81a0e2b196661827fcc1f393>
- [44] J.-M. Lopez-Higenera, M. Morante, and A. Cobo, “Simple low-frequency optical fiber accelerometer with large rotating machine monitoring applications,” *Journal of Lightwave Technology*, vol. 15, no. 7, pp. 1120–1130, jul 1997. [Online]. Available: <http://ieeexplore.ieee.org/lpdocs/epic03/wrapper.htm?arnumber=596957>
- [45] K. Bohnert, P. Gabus, J. Nehring, and H. Brandle, “Temperature and vibration insensitive fiber-optic current sensor,” *Journal of Lightwave Technology*, vol. 20, no. 2, pp. 267–276, 2002. [Online]. Available: <http://ieeexplore.ieee.org/lpdocs/epic03/wrapper.htm?arnumber=983241>
- [46] G. Fusiek, P. Orr, H. Wang, and P. Niewczas, “All-optical differential current detection technique for unit protection applications,” in *2013 IEEE International Instrumentation and Measurement Technology Conference (I2MTC)*. IEEE, may 2013, pp. 1214–1217. [Online]. Available: <http://ieeexplore.ieee.org/lpdocs/epic03/wrapper.htm?arnumber=6555606>
- [47] P. Orr, G. Fusiek, P. Niewczas, A. Dysko, C. Booth, F. Kawano, and G. Baber, “Distributed optical distance protection using FBG-based voltage and current transducers,” in *2011 IEEE Power and Energy Society General Meeting*. IEEE, jul 2011, pp. 1–5. [Online]. Available: <http://ieeexplore.ieee.org/lpdocs/epic03/wrapper.htm?arnumber=6039341>

Bibliography

- [48] T. J. Arsenault, A. Achuthan, P. Marzocca, C. Grappasonni, and G. Coppotelli, “Development of a FBG based distributed strain sensor system for wind turbine structural health monitoring,” *Smart Materials and Structures*, vol. 22, no. 7, p. 075027, jul 2013. [Online]. Available: <http://stacks.iop.org/0964-1726/22/i=7/a=075027?key=crossref.f672e42d8c8b23bf9c563e5e8a7c7566>
- [49] S.-J. Choi, Y.-C. Kim, M. Song, and J.-K. Pan, “A Self-Referencing Intensity-Based Fiber Optic Sensor with Multipoint Sensing Characteristics,” *Sensors*, vol. 14, no. 7, pp. 12 803–12 815, jul 2014. [Online]. Available: <http://www.mdpi.com/1424-8220/14/7/12803/>
- [50] J. Deleuran Grunnet, “Exchange with Jacob Deleuran Grunnet,” *Email Exchange*, 2016.
- [51] J. Wernicke, S. Kuhnt, and R. Byars, “Structural Monitoring System for Offshore Wind Turbine Foundation Structures,” *European Wind Energy Conference and Exhibition*, 2007.
- [52] W. Jiang, Q. Fan, and J. Gong, “Optimization of welding joint between tower and bottom flange based on residual stress considerations in a wind turbine,” *Energy*, vol. 35, no. 1, pp. 461–467, 2009. [Online]. Available: <http://dx.doi.org/10.1016/j.energy.2009.10.012>
- [53] M. Currie, F. Quail, and M. Saafi, “Development of a robust structural health monitoring system for wind turbine foundations,” in *ASME turbo expo 2012 Copenhagen*, 2012.
- [54] M. Currie, M. Saafi, C. Tachtatzis, and F. Quail, “Structural integrity monitoring of onshore wind turbine concrete foundations,” *Renewable Energy*, vol. 83, pp. 1131–1138, nov 2015. [Online]. Available: <http://linkinghub.elsevier.com/retrieve/pii/S0960148115003675>
- [55] X. Bai, M. He, R. Ma, and D. Huang, “Structural condition monitoring of wind turbine foundations,” *Proceedings of the Institution of Civil*

Bibliography

- Engineers - Energy*, pp. 1–19, sep 2016. [Online]. Available: <http://www.icevirtuallibrary.com/doi/10.1680/jener.16.00012>
- [56] M. Hassanzadeh, “Cracks in Onshore Wind Power Foundations,” Elforsk, Tech. Rep. January, 2012.
- [57] H.-n. Li, G.-d. Zhou, L. Ren, and D.-s. Li, “Strain Transfer Coefficient Analyses for Embedded Fiber Bragg Grating Sensors in Different Host Materials,” vol. 135, no. December, pp. 1343–1354, 2009.
- [58] H.-N. Li, G.-D. Zhou, L. Ren, and D.-S. Li, “Strain transfer analysis of embedded fiber Bragg grating sensor under nonaxial stress,” *Optical Engineering*, vol. 46, no. May, p. 054402, 2007.
- [59] Dongsheng, R. Liang, and L. Hongnan, “Mechanical Property and Strain Transferring Mechanism in Optical Fiber Sensors,” *Fiber Optic Sensors*, pp. 439–458, 2012.
- [60] P. Niewczas and G. Fusiek, “Induction heating assisted optical fiber bonding and sealing technique,” in *21st International Conference on Optical Fiber Sensors*, W. J. Bock, J. Albert, and X. Bao, Eds., may 2011, p. 77536H. [Online]. Available: <http://proceedings.spiedigitallibrary.org/proceeding.aspx?articleid=1347129>
<http://proceedings.spiedigitallibrary.org/proceeding.aspx?doi=10.1117/12.885942>
- [61] M. Perry, G. Fusiek, I. McKeeman, P. Niewczas, and M. Saafi, “Metal-packaged fibre Bragg grating strain sensors for surface-mounting onto spalled concrete wind turbine foundations,” vol. 9634, p. 963466, 2015. [Online]. Available: <http://proceedings.spiedigitallibrary.org/proceeding.aspx?doi=10.1117/12.2190188>
- [62] G. Fusiek, M. Perry, and M. Johnston, “Deformation monitoring in prestressing tendons using fibre Bragg gratings encapsulated in metallic packages,” *23rd International Conference on Optical Fibre Sensors*, vol. 9157, pp. 14–17, 2014.

Bibliography

- [63] M. Perry, Z. Yan, Z. Sun, L. Zhang, P. Niewczas, and M. Johnston, “High stress monitoring of prestressing tendons in nuclear concrete vessels using fibre-optic sensors,” *Nuclear Engineering and Design*, vol. 268, pp. 35–40, 2014. [Online]. Available: <http://dx.doi.org/10.1016/j.nucengdes.2013.12.038>
- [64] I. Mckeeman, G. Fusiek, M. Perry, P. Niewczas, and M. Johnston, “In-situ temperature calibration procedure for temperature and strain fibre Bragg grating sensors for monitoring pre-stressing strands,” vol. 9634, no. 1, p. 96345I, 2015. [Online]. Available: <http://proceedings.spiedigitallibrary.org/proceeding.aspx?doi=10.1117/12.2193193>
- [65] I. Mckeeman, P. Niewczas, and M. Johnston, “Identifying fabrication defects of metal packaged fibre Bragg grating sensors for smart pre-stressing strands,” in *2015 IEEE Workshop on Environmental, Energy, and Structural Monitoring Systems (EESMS) Proceedings*. IEEE, jul 2015, pp. 61–65. [Online]. Available: <http://ieeexplore.ieee.org/lpdocs/epic03/wrapper.htm?arnumber=7175853>
- [66] J. Ang, H. Li, I. Herszberg, M. Bannister, and A. Mouritz, “Tensile fatigue properties of fibre Bragg grating optical fibre sensors,” *International Journal of Fatigue*, vol. 32, no. 4, pp. 762–768, 2010. [Online]. Available: <http://www.sciencedirect.com/science/article/pii/S0142112309003223>
- [67] C. Davis, S. Tejedor, I. Grabovac, J. Kopczyk, and T. Nuyens, “High-strain fiber bragg gratings for structural fatigue testing of military aircraft,” *Photonic Sensors*, vol. 2, no. 3, pp. 215–224, 2012.
- [68] J. Weitzenboeck, *Adhesives in Marine Engineering*, 1st ed. Woodhead Publishing, Ltd., 2012.
- [69] D. Milborrow, “Wind Energy Economics,” in *Comprehensive Renewable Energy*. Elsevier, 2012, pp. 469–501. [Online]. Available: <http://linkinghub.elsevier.com/retrieve/pii/B9780080878720002183>

Bibliography

- [70] M. I. Blanco, “The economics of wind energy,” *Renewable and Sustainable Energy Reviews*, vol. 13, no. 6-7, pp. 1372–1382, 2009. [Online]. Available: <http://linkinghub.elsevier.com/retrieve/pii/S1364032108001299>
- [71] C. Mone, M. Hand, B. Maples, and A. Smith, “2013 Cost of Wind Energy Review,” *National Renewable Energy Laboratory*, 2013.
- [72] S. Tegen, M. Hand, B. Maples, E. Lantz, P. Schwabe, and A. Smith, “2011 Cost of Wind Energy Review,” *National Renewable Energy Laboratory*, 2011.
- [73] M. Junginger, a. Faaij, and W. C. Turkenburg, “Global experience curves for wind farms,” *Energy Policy*, vol. 33, no. 2, pp. 133–150, 2005.
- [74] M. Luengo and A. Kolios, “Failure Mode Identification and End of Life Scenarios of Offshore Wind Turbines: A Review,” *Energies*, vol. 8, no. 8, pp. 8339–8354, 2015. [Online]. Available: <http://www.mdpi.com/1996-1073/8/8/8339/>
- [75] J. R. M. Pereg and J. Fernandez de la Hoz, “Life cycle assessment of 1kWh generated by a wind farm Gamesa G90-2.0 MW onshore,” vol. 1, pp. 1–83, 2013. [Online]. Available: <http://www.gamesacorp.com/recursos/doc/rsc/compromisos/clientes/certificaciones-ohsas-y-i/informe-analisis-ciclo-de-vida-g90-english.pdf>
- [76] DNV GL, “Service Specification: Certification of lifetime extension of wind turbines,” 2016. [Online]. Available: <https://rules.dnvgl.com/docs/pdf/DNVGL/SE/2016-03/DNVGL-SE-0263.pdf>
- [77] Megavind, “Strategy for Extending the Useful Lifetime of a Wind Turbine,” 2016.
- [78] L. Ziegler, J. Lange, U. Smolka, and M. Muskulus, “The decision on the time to switch from lifetime extension to repowering,” in *WindEurope, Summit 2016*, Hamburg, 2016.
- [79] C. Loraux and E. Brühwiler, “The use of long term monitoring data for the extension of the service duration of existing wind turbine support structures,” *Journal of Physics: Conference Series*, vol. 753, p. 072023, sep 2016.

Bibliography

- [Online]. Available: <http://stacks.iop.org/1742-6596/753/i=7/a=072023?key=crossref.bb556abb5450ef12dd546de70c99ecb2>
- [80] R. Wiser, K. Jenni, J. Seel, E. Baker, and M. Hand, “Forecasting Wind Energy Costs and Cost Drivers: The Views of the World’s Leading Experts,” 2016. [Online]. Available: https://www.ieawind.org/task_26_public/PDF/062316/lbnl-1005717.pdf
- [81] BBC, “SSE’s Stronelaig wind farm near Fort Augustus approved,” 2014. [Online]. Available: <http://www.bbc.co.uk/news/uk-scotland-highlands-islands-27730168>
- [82] K. Thyagarajan and A. Ghatak, *Fiber Optic Essentials*. Wiley-IEEE Press, 2007.
- [83] A. Othonos, *Fiber Bragg Gratings: Fundamentals and Applications in Telecommunications and Sensing*. Artech House Publishers, 1999.
- [84] R. M. Measures, *Structural Monitoring with Fiber Optic Technology*. Academic Press Inc, 2001.
- [85] R. Kashyap, *Fiber Bragg Gratings*. ACADEMIC PRESS, 2009.
- [86] M. Perry, G. Fusiek, P. Niewczas, and M. Saafi, “AM06 : Wind Turbine Foundation Structural Health Monitoring Report on FEM modelling,” Tech. Rep. June, 2015.
- [87] J. F. Bradley, D. Leviton, and T. Madison, “Temperature-dependent refractive index of silicon and germanium,” NASA Goddard Space Flight Center, Greenbelt, MD 20771, Greenbelt, Tech. Rep. [Online]. Available: <http://cds.cern.ch/record/965045/files/0606168.pdf>
- [88] L. Monette, M. P. Anderson, S. Ling, and G. S. Grest, “Effect of modulus and cohesive energy on critical fibre length in fibre-reinforced composites,” *Journal of Materials Science*, vol. 27, no. 16, pp. 4393–4405, 1992. [Online]. Available: <http://link.springer.com/10.1007/BF00541572>

Bibliography

- [89] M. Perry, G. Fusiek, P. Niewczas, and M. Saafi, “AM06 : Wind Turbine Foundation Structural Health Monitoring,” Tech. Rep. April, 2015.
- [90] B. Glišić and D. Inaudi, *Fibre Optic Methods for Structural Health Monitoring*. Chichester, UK: John Wiley and Sons, Ltd, oct 2007. [Online]. Available: <http://doi.wiley.com/10.1002/9780470517819>
- [91] B. Dupen, “Moment of inertia,” 2011. [Online]. Available: [http://www.etcshipfw.edu/\\$\sim\\$dupenb/ET_200/Momentofinertia.pdf](http://www.etcshipfw.edu/\simdupenb/ET_200/Momentofinertia.pdf)
- [92] A. Ruina, “Beam Deflection Formulae,” *Cornell University*, p. 5, 2012. [Online]. Available: <http://ruina.mae.cornell.edu/Courses/ME4735-2012/Rand4770Vibrations/BeamFormulas.pdf>
- [93] R. Beardmore, “Reinforced concrete beams subject to bending moments,” Tech. Rep., 2011. [Online]. Available: http://www.roymech.co.uk/Related/Construction/Concrete_beams_theory.html
- [94] European Union, “BS EN 1992-1-1:2004 - Eurocode 2: Design of concrete structures - Part 1-1: General rules and rules for buildings,” Tech. Rep., 2004. [Online]. Available: <https://law.resource.org/pub/eu/eurocode/en.1992.1.1.2004.pdf>
- [95] Y. Kondo, “Fatigue Under Variable Amplitude Loading,” in *Comprehensive Structural Integrity*, B. L. Ritchie and Y. Murakami, Eds. Elsevier, 2003.
- [96] H. Bomas, P. Mayr, and T. Linkewitz, “Inclusion Size Distribution and Endurance Limit of a Hard Steel,” *Extremes*, vol. 2, no. 2, pp. 149–164, 1999. [Online]. Available: <http://link.springer.com/10.1023/A:1009918902623>
- [97] G. P. Tilly, “Fatigue of Steel Reinforcement Bars in Concrete: a Review,” *Fatigue and Fracture of Engineering Materials and Structures*, vol. 2, no. 3, pp. 251–268, 1979. [Online]. Available: <http://doi.wiley.com/10.1111/j.1460-2695.1979.tb01084.x>

Bibliography

- [98] A. Fatemi, “Fatigue tests and stress-life approach,” 2015. [Online]. Available: https://www.efatigue.com/training/Chapter_4.pdf
- [99] Y.-L. Lee, P. Jwo, H. Richard, and M. Barkey, *Fatigue Testing and Analysis: Theory and Practice*, revised ed. Butterworth-Heinemann, 2011.
- [100] The College of Engineering at Iowa State University, “Factors that effect fatigue strength,” 2011. [Online]. Available: [http://home.engineering.iastate.edu/\\$\sim\\$sgkstartns/me325/fatigue_2.pdf](http://home.engineering.iastate.edu/\simsgkstartns/me325/fatigue_2.pdf)
- [101] G. E. Dieter and D. Bacon, *Mechanical Metallurgy (Materials Science and Engineering)*, McGraw-Hill, Ed. McGraw-Hill, 1990.
- [102] S.-P. Zhu, Q. Lei, H.-Z. Huang, Y.-J. Yang, and W. Peng, “Mean stress effect correction in strain energy-based fatigue life prediction of metals,” *International Journal of Damage Mechanics*, may 2016. [Online]. Available: <http://ijd.sagepub.com/cgi/doi/10.1177/1056789516651920>
- [103] S. Suresh, *Fatigue of materials*. Cambridge: Cambridge University Press, 1994.
- [104] G. Marsh, C. Wignall, P. R. Thies, N. Barltrop, A. Incecik, V. Venugopal, and L. Johanning, “Review and application of Rainflow residue processing techniques for accurate fatigue damage estimation,” *International Journal of Fatigue*, vol. 82, pp. 757–765, 2016. [Online]. Available: <http://dx.doi.org/10.1016/j.ijfatigue.2015.10.007>
- [105] R. I. Stephens, A. Fatemi, R. R. Stephens, and H. O. Fuchs, *Metal Fatigue in Engineering*, 2nd ed. John Wiley and Sons, 2000.
- [106] T. Burton, N. Jenkins, D. Sharpe, and E. Bossanyi, *Wind Energy Handbook*. Chichester, UK: John Wiley and Sons, Ltd, may 2011. [Online]. Available: <http://doi.wiley.com/10.1002/9781119992714>
- [107] European Union, “EN 1993-1-9 (2005): Eurocode 3: Design of steel structures - Part 1-9: Fatigue,” 2005. [Online]. Available: <http://www.phd.eng.br/wp-content/uploads/2015/12/en.1993.1.9.2005-1.pdf>

Bibliography

- [108] N. Stavridou, E. Efthymiou, and C. C. Baniotopoulos, “Welded connections of wind turbine towers under fatigue loading: Finite element analysis and comparative study,” *American Journal of Engineering and Applied Sciences*, vol. 8, no. 4, pp. 489–503, 2015.
- [109] D. Khatri, “Structural Failures of Wind Towers and Dynamic Analysis Procedures,” in *American Wind Energy Association*, 2009.
- [110] A. Verma, “Adhesive Bonded Towers for Wind Turbines. Design, Optimization and Cost analysis.” 2011. [Online]. Available: http://studenten.tudelft.nl/fileadmin/Faculteit/LR/Organisatie/Afdelingen_en_Leerstoele/Afdeling_AEWE/Wind_Energy/Education/Masters_Projects/Finished_Master_projects/doc/Ankit_Verma.r.pdf
- [111] F. Lueddecke, “Tower Flange Weld Assumption,” 2018.
- [112] H. Sönnerrind, “Singularities in Finite Element Models: Dealing with Red Spots,” 2015. [Online]. Available: <https://www.comsol.com/blogs/singularities-in-finite-element-models-dealing-with-red-spots/>
- [113] T. Q. Do, J. W. van de Lindt, and H. Mahmoud, “Fatigue Life Fragilities and Performance-Based Design of Wind Turbine Tower Base Connections,” *Journal of Structural Engineering*, vol. 141, no. 7, p. 04014183, 2015.
- [114] H. A. Richard and M. Sander, *Fatigue Crack Growth: Detect - Assess - Avoid*. Springer, 2016.
- [115] W. Short, D. Packey, and T. Holt, “A Manual for the Economic Evaluation of Energy Efficiency and Renewable Energy Technologies,” Tech. Rep. March, 1995. [Online]. Available: <http://www.nrel.gov/docs/legosti/old/5173.pdf>
- [116] IRENA, “Wind Power,” 2012. [Online]. Available: http://www.irena.org/DocumentDownloads/Publications/RE_Technologies_Cost_Analysis-WIND_POWER.pdf

Bibliography

- [117] DECC, “Onshore Wind Call for Evidence: Government Response to Part A (Community Engagement and Benefits) and Part B (Costs),” vol. 7, no. June, pp. 66–78, 2013.
- [118] —, “Electricity Generation Costs 2013,” *Department of Energy and Climate Change*, no. July, pp. 1–67, 2013. [Online]. Available: <https://www.gov.uk/government/publications/decc-electricity-generation-costs-2013>
- [119] Mott MacDonald, “UK Electricity Generation Costs Update,” p. 117, 2011. [Online]. Available: <http://www.decc.gov.uk/assets/decc/statistics/projections/71-uk-electricity-generation-costs-update-.pdf>
- [120] J. Aldersey-Williams and T. Rubert, “Levelised Cost of Energy - A Theoretical Justification and Critical Assessment,” *Energy Policy*, vol. submitted, 2018.
- [121] C. W. Kensche, “Fatigue of composites for wind turbines,” *International Journal of Fatigue*, vol. 28, no. 10 SPEC. ISS., pp. 1363–1374, 2006.
- [122] B. Yang and D. Sun, “Testing, inspecting and monitoring technologies for wind turbine blades: a survey,” *Renewable and Sustainable Energy Reviews*, vol. 22, pp. 515–526, 2013. [Online]. Available: <http://dx.doi.org/10.1016/j.rser.2012.12.056>
- [123] P. S. Veers, T. D. Ashwill, H. J. Sutherland, D. L. Laird, D. W. Lobitz, D. a. Griffin, J. F. Mandell, W. D. Músiel, K. Jackson, M. Zuteck, A. Miravete, S. W. Tsai, and J. L. Richmond, “Trends in the design, manufacture and evaluation of wind turbine blades,” *Wind Energy*, vol. 6, no. 3, pp. 245–259, 2003.
- [124] E. Petersen, *1999 European Wind Energy Conference: Wind Energy for the Next Millennium*. Routledge, 2014. [Online]. Available: https://books.google.com/books?hl=en&lr=&id=mGl_AgAAQBAJ&pgis=1
- [125] K. Morgan and E. Ntambakwa, “Wind Turbine Foundation Behavior and Design Considerations,” in *AWEA Windpower Houston*, 2008.
- [126] J. McAlorum, M. Perry, G. Fusiek, P. Niewczas, I. McKeeman, and T. Rubert, “Deterioration of cracks in onshore wind turbine foundations,”

Bibliography

- Engineering Structures*, vol. 167, pp. 121–131, jul 2018. [Online]. Available: <http://linkinghub.elsevier.com/retrieve/pii/S0141029617329644>
- [127] J. van der Tempel and D. P. Molenaar, “Wind turbine structural dynamics-a review of the principles for modern power generation, onshore and offshore,” *Wind Engineering*, vol. 26, no. 4, pp. 211–222, 2003.
- [128] D. Bonnett, “Wind turbine foundations loading, dynamics and design,” *IStructE*, vol. 83, no. 3, pp. 41–45, 2005.
- [129] European Union, “EN 1993-1-1:2005 - Eurocode 3 - Design of steel structures - Part 1-1: General rules and rules for buildings,” 2005. [Online]. Available: <https://law.resource.org/pub/eu/eurocode/en.1993.1.1.2005.pdf>
- [130] Det Norske Veritas/Riso, *Guidelines for design of wind turbines*, 2002. [Online]. Available: <http://homes.civil.aau.dk/rrp/BM/BM8/q.pdf>
- [131] H. Svensson, “Design of foundations for wind turbines,” Ph.D. dissertation, Lund University, 2010.
- [132] Confidential, “Personal Email,” *From 01.02.2016*, 2016.
- [133] V. Schaefer and J. Ashlock, “Foundations for wind turbines,” 2011.
- [134] Det Norske Veritas, “Design of offshore wind turbine structures, Offshore Standard DNV-OS-J101,” 2007.
- [135] N. Vindkraft, “Study of wind turbine foundations in cold climates,” in *Winterwind 2012*, 2012, pp. 1–26. [Online]. Available: http://www.nordiskvindkraft.se/media/29161/Study_of_Wind_Turbine_Foundations.pdf
- [136] The Concrete Centre, “Practical Design to Eurocode 2 Beams,” 2016. [Online]. Available: <https://www.concretecentre.com/TCC/media/TCCMediaLibrary/Presentations/Lecture-10-Foundations-jb-23-Nov-16.pdf>
- [137] L. Doris, “Tim Rubert,” *Email Exchange*, no. November, 2017.

Bibliography

- [138] G. Meyerhof, "Some recent research on the bearing capacity of foundations," *Canadian Geotechnical Journal*, pp. 16–26, 1963.
- [139] Vestas, "Foundation loads V117-3.45 MW, Mk2C, IECS, 76.5 m," 2015.
- [140] International Electrotechnical Commission, "Part 1: Design requirements," Tech. Rep., 2005. [Online]. Available: <http://projecte-hermes.upc.edu/Optatives/A-Windturbinesdesign/PlaAntic/Teoria/Normes/IEC61400-1Designrequirements.pdf>
- [141] J. Martin, "Life Extension," in *RenewableUK - Onshore Asset Management Conference*, Glasgow, UK, 2017.
- [142] Nederlands Elektrotechnisch Comité, "Dutch Lifetime Extension Standard - NPR 8400," 2016.
- [143] K. Denman, S. Lightfoote, and J. Ripa, "Wind Plant Lifetime Extension (LTE) Webinar." [Online]. Available: <https://www.youtube.com/watch?v=45kQ13vgqeY>
- [144] L. Ziegler, E. Gonzalez, T. Rubert, U. Smolka, and J. J. Melero, "Lifetime extension of onshore wind turbines: A review covering Germany, Spain, Denmark, and the UK," *Renewable and Sustainable Energy Reviews*, vol. 82, pp. 1261–1271, feb 2018. [Online]. Available: <http://linkinghub.elsevier.com/retrieve/pii/S1364032117313503>
- [145] T. Rubert, D. McMillan, and P. Niewczas, "A decision support tool to assist with lifetime extension of wind turbines," *Renewable Energy*, dec 2018. [Online]. Available: <http://linkinghub.elsevier.com/retrieve/pii/S0960148117312685>
- [146] T. Rubert, P. Niewczas, and D. McMillan, "Life Extension for Wind Turbine Structures and Foundations," in *International Conference on Offshore Renewable Energy - CORE 2016*, Glasgow, 2016.
- [147] Renewable UK, "UKWED Database 13.12.16," 2016. [Online]. Available: <http://www.renewableuk.com/page/UKWEDhome>

Bibliography

- [148] DONG Energy, “Successful installation of world’s largest offshore wind turbine at Burbo Bank Extension,” 2016. [Online]. Available: <http://www.dongenergy.co.uk/news/press-releases/articles/successful-installation-of-world’s-largest-offshore-wind-turbine-at-burbo-bank-extension>
- [149] Everoze, “Everoze launches online portal to shed new light on ageing renewables assets,” 2016. [Online]. Available: <http://everoze.com/everoze-launches-leaf-portal/>
- [150] RenewableUK, “UK Wind Energy Statistics (UKWED),” 2017. [Online]. Available: <http://www.renewableuk.com/page/UKWEDSearch>
- [151] T. Grimwood, “Onshore wind needs CfD support’, says Cornwall Energy,” 2016. [Online]. Available: <http://utilityweek.co.uk/news/onshore-wind-needs-cfd-support-says-cornwall-energy/1281232#.WHYrYIOLSuk>
- [152] DECC, “Consultation on Renewable Electricity Financial Incentives 2009 Foreword by Minister of State,” 2009. [Online]. Available: http://www.decc.gov.uk/en/content/cms/consultations/elec_financial/elec_financial.aspx
- [153] Department of Energy and Climate Change, “The Renewables Obligation Order 2009,” 2011. [Online]. Available: https://www.gov.uk/government/uploads/system/uploads/attachment_data/file/48010/1251-roo-2009-amended-2011.pdf
- [154] Ofgem, “Guidance for Generators,” 2010. [Online]. Available: https://www.ofgem.gov.uk/sites/default/files/docs/guidance_for_generators.pdf
- [155] WAsP Riso, *European Wind Atlas*. Risø National Laboratory, Roskilde, Denmark, 1989. [Online]. Available: http://www.wasp.dk/dataandtools#wind-atlas__european-wind-atlas
- [156] Danish Energy Agency, “Executive Order on a technical certification scheme for wind turbines no. 73,” 2013.

Bibliography

- [157] I. Staffell and R. Green, “How does wind farm performance decline with age?” *Renewable Energy*, vol. 66, pp. 775–786, 2014. [Online]. Available: <http://dx.doi.org/10.1016/j.renene.2013.10.041>
- [158] B. Tremeac and F. Meunier, “Life cycle analysis of 4.5MW and 250W wind turbines,” *Renewable and Sustainable Energy Reviews*, vol. 13, no. 8, pp. 2104–2110, 2009. [Online]. Available: <http://linkinghub.elsevier.com/retrieve/pii/S1364032109000045>
- [159] R. R. Hill, J. a. Stinebaugh, D. Briand, A. S. Benjamin, and J. Lindsay, “Wind Turbine Reliability : A Database and Analysis Approach,” Sandia National Laboratories, Tech. Rep. February, 2008.
- [160] J. M. Pinar Pérez, F. P. García Márquez, A. Tobias, and M. Papaelias, “Wind turbine reliability analysis,” *Renewable and Sustainable Energy Reviews*, vol. 23, pp. 463–472, jul 2013. [Online]. Available: <http://linkinghub.elsevier.com/retrieve/pii/S1364032113001779>
- [161] G. Wilson, “Operation and Maintenance in the Offshore Wind Sector,” in *Wind CDT Almani Talk*, Glasgow, 2015.
- [162] M. Woebeking, “Turbine size: is big always beautiful?” 2012. [Online]. Available: <http://www.ewea.org/blog/2012/04/turbine-size-is-big-always-beautiful/>
- [163] H. Polinder, F. F. A. Van Der Pijl, G. J. De Vilder, and P. J. Tavner, “Comparison of direct-drive and geared generator concepts for wind turbines,” *IEEE Transactions on Energy Conversion*, vol. 21, no. 3, pp. 725–733, 2006.
- [164] H. Miabhoy, “Final Report Summary - CORETO,” Innovative Technology and Science Limited - INNOTECHUK, Tech. Rep., 2015.
- [165] Der Landrat, “Errichtung einer Windkraftanlage Enercon E-82 E2 in Borgholzhausen,” Kreis Guetersloh, 2012.
- [166] J. McCarthy, “Wind Farm Decommissioning: A Detailed Approach to Estimate further Costs in Sweden,” 2015.

Bibliography

- [167] Hessischer Landtag, “Rückstellungen für Rückbau von Windkraftanlagen in Hessen,” Hessischer Landtag, Tech. Rep., 2014. [Online]. Available: <http://starweb.hessen.de/cache/DRS/19/2/00762.pdf>
- [168] Y. Dalgic, I. Lazakis, and O. Turan, “Vessel charter rate estimation for offshore wind operation and maintenance activities,” in *Developments in Maritime Transportation and Exploitation of Sea Resources*, 2013, pp. 899–907.
- [169] S. J. Watson, P. Kritharas, and G. J. Hodgson, “Wind speed variability across the UK between 1957 and 2011,” *Wind Energy*, vol. 18, no. January 2015, pp. 21–42, 2013. [Online]. Available: <http://onlinelibrary.wiley.com/doi/10.1002/we.1679/full>
- [170] K. Klink, “Trends and interannual variability of wind speed distributions in Minnesota,” *Journal of Climate*, vol. 15, no. 22, pp. 3311–3317, 2002.
- [171] P. P. Revheim and H. G. Beyer, “Inter-annual Variation of Wind Speed in Southern Norway,” in *ECAM, Reading, 12.09.2013*. University of Agder, 2013. [Online]. Available: http://presentations.copernicus.org/EMS2013-507_presentation.pdf
- [172] D. J. Mundform, J. Schaffer, M.-J. Kim, D. Shaw, A. Thongteeraparp, and P. Supawan, “Number of Replications Required in Monte Carlo Simulation Studies: A Synthesis of Four Studies,” *Journal of Modern Applied Statistical Methods*, vol. 10, no. 1, aug 2011. [Online]. Available: <http://digitalcommons.wayne.edu/cgi/viewcontent.cgi?article=1285&context=jmasm>
- [173] Local Government Association, “How much do wind turbines cost and where can I get funding?” 2015. [Online]. Available: http://www.local.gov.uk/home/-/journal_content/56/10180/3510194/ARTICLE
- [174] DECC, “Government Response to the consultations on the Renewables Obligation Transition and on Grace Periods,” 2014. [Online]. Available: https://www.gov.uk/government/uploads/system/uploads/attachment_data/file/289076/Transition_and_Grace_Periods_Government_Response_-_12_Mar_2014.pdf

Bibliography

- [175] —, “UK Energy Statistics, 2015 and Q4 2015,” 2016. [Online]. Available: https://www.gov.uk/government/uploads/system/uploads/attachment_data/file/513244/Press_Notice_March_2016.pdf
- [176] D. Milborrow, “Breaking down the cost of wind turbine maintenance,” p. 1, 2009. [Online]. Available: <http://www.windpowermonthly.com/article/1010136/breaking-down-cost-wind-turbine-maintenance>
- [177] L. Miller, R. Carriveau, S. Harper, and S. Singh, “Evaluating the link between LCOE and PPA elements and structure for wind energy,” *Energy Strategy Reviews*, vol. 16, pp. 33–42, jun 2017. [Online]. Available: <http://linkinghub.elsevier.com/retrieve/pii/S2211467X17300160>
- [178] Statista, “Projected annual inflation rate in the United States from 2010 to 2023,” 2018. [Online]. Available: <https://www.statista.com/statistics/244983/projected-inflation-rate-in-the-united-states/>
- [179] —, “United Kingdom: Inflation rate from 2012 to 2022,” 2018. [Online]. Available: <https://www.statista.com/statistics/270384/inflation-rate-in-the-united-kingdom/>
- [180] —, “Inflation rate in the European Union and the Euro area,” 2018. [Online]. Available: <https://www.statista.com/statistics/267908/inflation-rate-in-eu-and-euro-area/>
- [181] ARUP, “Review of Renewable Electricity Generation Cost and Technical Assumptions Study Report,” 2016. [Online]. Available: https://www.gov.uk/government/uploads/system/uploads/attachment_data/file/566718/Arup_Renewable_Generation_Cost_Report.pdf
- [182] U.S. Department of Energy, “Transparent Cost Database,” 2015. [Online]. Available: <http://en.openei.org/apps/TCDB/>

Bibliography

- [183] IEA, “Technology roadmap - Wind energy,” p. 58, 2013. [Online]. Available: https://www.iea.org/publications/freepublications/publication/Wind_Roadmap.pdf
- [184] Fraunhofer IWES, “Wind Energy Report Germany 2014,” p. 112, 2015.
- [185] R. Wiser and M. Bolinger, “2014 Wind Technologies Market Report,” 2015. [Online]. Available: <https://energy.gov/sites/prod/files/2015/08/f25/2014-Wind-Technologies-Market-Report-8.7.pdf>
- [186] C. Carrillo, A. Obando Montaña, J. Cidrás, and E. Díaz-Dorado, “Review of power curve modelling for wind turbines,” *Renewable and Sustainable Energy Reviews*, vol. 21, pp. 572–581, may 2013. [Online]. Available: <http://linkinghub.elsevier.com/retrieve/pii/S1364032113000439>
- [187] M. Lydia, S. S. Kumar, A. I. Selvakumar, and G. E. Prem Kumar, “A comprehensive review on wind turbine power curve modeling techniques,” *Renewable and Sustainable Energy Reviews*, vol. 30, pp. 452–460, 2014. [Online]. Available: <http://dx.doi.org/10.1016/j.rser.2013.10.030>
- [188] A. Albers, “Power Curve Turbulence Normalisation for Wind Resource Assessments,” in *EWEA*, Barcelona,, 2014. [Online]. Available: http://www.windguard.de/_Resources/Persistent/3fde06642247c75370bf8a1cdad2b7de26a43081/Turbulene-Normalisation-WindGuard-EWEA2014.pdf
- [189] J. Schallenberg-Rodriguez, “A methodological review to estimate technological wind energy production,” *Renewable and Sustainable Energy Reviews*, vol. 21, pp. 272–287, may 2013. [Online]. Available: <http://linkinghub.elsevier.com/retrieve/pii/S1364032112007356>
- [190] C. Johnson, A. Graves, A. Tindal, S. Cox, W. Schlez, and A. Neubert, “New developments in wake models for large wind farms,” in *AWEA Windpower Conference*. Garrad Hassan America Inc: Chicago, IL, 209. [Online]. Available: http://www.gl-garradhassan.com/assets/downloads/New_Developments_in_Wake_Models_for_Large_Wind_Farms.pdf

Bibliography

- [191] M. Ali, J. Matevosyan, and J. Milanović, “Probabilistic assessment of wind farm annual energy production,” *Electric Power Systems Research*, vol. 89, pp. 70–79, aug 2012. [Online]. Available: <http://linkinghub.elsevier.com/retrieve/pii/S0378779612000399>
- [192] S. R. Arwade, M. A. Lackner, and M. D. Grigoriu, “Probabilistic Models for Wind Turbine and Wind Farm Performance,” *Journal of Solar Energy Engineering*, vol. 133, no. 4, p. 041006, 2011. [Online]. Available: <http://solarenergyengineering.asmedigitalcollection.asme.org/article.aspx?articleid=1456211>
- [193] D. Cannon, D. Brayshaw, J. Methven, P. Coker, and D. Lenaghan, “Using reanalysis data to quantify extreme wind power generation statistics: A 33 year case study in Great Britain,” *Renewable Energy*, vol. 75, pp. 767–778, mar 2015. [Online]. Available: <http://linkinghub.elsevier.com/retrieve/pii/S096014811400651X>
- [194] I. Tobin, R. Vautard, I. Balog, F.-M. Bréon, S. Jerez, P. M. Ruti, F. Thais, M. Vrac, and P. Yiou, “Assessing climate change impacts on European wind energy from ENSEMBLES high-resolution climate projections,” *Climatic Change*, vol. 128, no. 1-2, pp. 99–112, jan 2015. [Online]. Available: <http://link.springer.com/10.1007/s10584-014-1291-0>
- [195] R. Wagner, B. Cañadillas, a. Clifton, S. Feeney, N. Nygaard, M. Poodt, C. S. Martin, E. Tüxen, and J. W. Wagenaar, “Rotor equivalent wind speed for power curve measurement comparative exercise for IEA Wind Annex 32,” *Journal of Physics: Conference Series*, vol. 524, p. 012108, 2014. [Online]. Available: <http://stacks.iop.org/1742-6596/524/i=1/a=012108?key=crossref.437de636faf36964cadb3165c32ccd41>
- [196] G. Sinden, “Characteristics of the UK wind resource: Long-term patterns and relationship to electricity demand,” *Energy Policy*, vol. 35, no. 1, pp. 112–127, jan 2007. [Online]. Available: <http://linkinghub.elsevier.com/retrieve/pii/S0301421505002752>

Bibliography

- [197] UL, “Outline of Investigation for Wind Turbine Generator - Life Time Extension (LTE),” 2016. [Online]. Available: [http://www.shopulstandards.com/ProductDetail.aspx?productId=UL4143_1_B_20161031\(ULStandards2\)](http://www.shopulstandards.com/ProductDetail.aspx?productId=UL4143_1_B_20161031(ULStandards2))
- [198] Deutsches Institut für Bautechnik, “Richtlinie für Windenergieanlagen - Einwirkungen und Standsicherheitsnachweise für Turm und Gründung,” 2012. [Online]. Available: https://www.dibt.de/en/Departments/data/Aktuelles_Ref_I.1_Richtlinie_Windenergieanlagen_Okt.2012.pdf
- [199] ReliaWind, “Project final report,” 2011. [Online]. Available: https://setis.ec.europa.eu/energy-research/sites/default/files/project/docs/PublishableSummary-110513_Reliawind_FinalPublishableSummarytoEC.pdf
- [200] J. Carroll, A. McDonald, and D. McMillan, “Reliability Comparison of Wind Turbines With DFIG and PMG Drive Trains,” *IEEE Transactions on Energy Conversion*, vol. 30, no. 2, pp. 663–670, jun 2015. [Online]. Available: <http://ieeexplore.ieee.org/lpdocs/epic03/wrapper.htm?arnumber=6967839>
- [201] J. F. Manwell, J. G. McGowan, and A. L. Rogers, *Wind Energy Explained*. Chichester, UK: John Wiley and Sons, Ltd, dec 2009. [Online]. Available: <http://doi.wiley.com/10.1002/9781119994367>
- [202] E.ON, “Wind Turbine Technology and Operations Factbook,” 2013. [Online]. Available: https://www.eon.com/content/dam/eon-content-pool/eon/company-asset-finder/company-profiles/ecr/2013-09_E.ON_Wind_Turbine_Technology_Factbook.pdf
- [203] N. Conroy, J. Deane, and B. P. Ó Gallachóir, “Wind turbine availability: Should it be time or energy based? A case study in Ireland,” *Renewable Energy*, vol. 36, no. 11, pp. 2967–2971, nov 2011. [Online]. Available: <http://linkinghub.elsevier.com/retrieve/pii/S0960148111001728>
- [204] UK Government, “Renewable sources of energy: Chapter 6, Digest of United Kingdom Energy Statistics (DUKES),” 2016. [On-

Bibliography

- line]. Available: https://www.gov.uk/government/uploads/system/uploads/attachment_data/file/547977/Chapter_6_web.pdf
- [205] R. Yin, *Case Study Research: Design and Methods (Applied Social Research Methods)*, 5th ed. SAGE Publications, 2013.
- [206] NordPool, “N2EX Day Ahead Auction Prices 2012-2016 Daily GBP,” 2016. [Online]. Available: <http://www.nordpoolspot.com/Market-data1/N2EX/Auction-prices/UK/yearly/?view=table>
- [207] Ofgem, “Renewables Obligation (RO) buy-out price and mutualisation ceilings for 2017-18,” 2017. [Online]. Available: <https://www.ofgem.gov.uk/publications-and-updates/renewables-obligation-ro-buy-out-price-and-mutualisation-ceilings-2017-18>
- [208] The European Wind Energy Association, “The economics of wind energy,” p. 158, 2009. [Online]. Available: http://www.johnsoncontrols.pl/content/dam/WWW/jci/be/solutions_for_your/art_of_the_possible/Economics-Wind-Main-Report.pdf
- [209] P. Breeze, “The Cost of Electricity from Wind Turbines,” in *Wind Power Generation*. Elsevier, 2016, pp. 93–97. [Online]. Available: <http://linkinghub.elsevier.com/retrieve/pii/B9780128040386000116>
- [210] N. Douglas, “The Levelised Cost of Wind Energy,” in *Renewable Wales*, 2016. [Online]. Available: <http://renewable-wales.com/wp-content/uploads/2016/06/Spkr-4-Neil-Douglas-Maximising-the-value-of-your-wind-asset.pdf>
- [211] IRENA, “Wind Power Technology brief,” 2016. [Online]. Available: http://www.irena.org/DocumentDownloads/Publications/IRENA-ETSAP_Tech_Brief_Wind_Power_E07.pdf
- [212] G. Mitchell, *The Practice of Operational Research*. Chichester: John Wiley and Sons., 1993.
- [213] M. Pidd, *Tools for Thinking: Modelling in Management Science*. Chichester: John Wiley and Sons.

Bibliography

- [214] W.-G. Früh, “Long-term wind resource and uncertainty estimation using wind records from Scotland as example,” *Renewable Energy*, vol. 50, pp. 1014–1026, feb 2013. [Online]. Available: <http://linkinghub.elsevier.com/retrieve/pii/S0960148112005174>
- [215] D. Hdidouan and I. Staffell, “The impact of climate change on the levelised cost of wind energy,” *Renewable Energy*, vol. 101, pp. 575–592, feb 2017. [Online]. Available: <http://linkinghub.elsevier.com/retrieve/pii/S0960148116307856>
- [216] T. Rubert, “Lifetime Extension Cost Database (6 x 900 kW Wind Farm),” 2017. [Online]. Available: <http://dx.doi.org/10.15129/cc9f8eac-d501-41b3-a1b9-3c3a94418e06>
- [217] S. Emeis, “Current issues in wind energy meteorology,” *Meteorological Applications*, vol. 21, no. 4, pp. 803–819, oct 2014. [Online]. Available: <http://doi.wiley.com/10.1002/met.1472>
- [218] S.-E. Gryning, E. Batchvarova, B. Brümmer, H. Jørgensen, and S. Larsen, “On the extension of the wind profile over homogeneous terrain beyond the surface boundary layer,” *Boundary-Layer Meteorology*, vol. 124, no. 2, pp. 251–268, jul 2007. [Online]. Available: <http://link.springer.com/10.1007/s10546-007-9166-9>
- [219] T. Rubert, “Multiple Turbines Lifetime Extension LCOE Database,” 2017. [Online]. Available: <http://dx.doi.org/10.15129/df362a6b-a6a9-4d60-b515-233f7286b67b>
- [220] N. Gaudern, “A practical study of the aerodynamic impact of wind turbine blade leading edge erosion,” *Journal of Physics: Conference Series*, vol. 524, p. 012031, 2014. [Online]. Available: <http://stacks.iop.org/1742-6596/524/i=1/a=012031?key=crossref.ce2c95aa1636e810836dfb0186948033>
- [221] A. Sareen, C. A. Sapre, and M. S. Selig, “Effects of Leading-Edge Protection Tape on Wind Turbine Blade Performance,” *Wind Engineering*, vol. 36, no. 5, pp. 525–534, 2012.

Bibliography

- [222] B. Le and J. Andrews, “Modelling wind turbine degradation and maintenance,” *Wind Energy*, vol. 19, no. 4, pp. 571–591, apr 2016. [Online]. Available: <http://doi.wiley.com/10.1002/we.1851>
- [223] S. Wan, L. Cheng, and X. Sheng, “Effects of Yaw Error on Wind Turbine Running Characteristics Based on the Equivalent Wind Speed Model,” *Energies*, vol. 8, no. 7, pp. 6286–6301, jun 2015. [Online]. Available: <http://www.mdpi.com/1996-1073/8/7/6286/>
- [224] M. Wilkinson, “Long-term Performance of Wind Farms,” in *EWEA Workshop 2014*, no. December, 2014, pp. 1–27.
- [225] NationalGrid, “Frequency Response Volumes,” 2017. [Online]. Available: <http://www2.nationalgrid.com/UK/Industry-information/Electricity-transmission-operational-data/Data-explorer/Outcome-Energy-Services/>
- [226] P. Grünewald, E. McKenna, and M. Thomson, “Going with the wind: temporal characteristics of potential wind curtailment in Ireland in 2020 and opportunities for demand response,” *IET Renewable Power Generation*, vol. 9, no. 1, pp. 66–77, jan 2015. [Online]. Available: <http://digital-library.theiet.org/content/journals/10.1049/iet-rpg.2013.0320>
- [227] X. Jia, C. Jin, M. Buzza, W. Wang, and J. Lee, “Wind turbine performance degradation assessment based on a novel similarity metric for machine performance curves,” *Renewable Energy*, vol. 99, pp. 1191–1201, dec 2016. [Online]. Available: <http://linkinghub.elsevier.com/retrieve/pii/S0960148116307194>
- [228] ELEXON, “Data Flows,” 2017. [Online]. Available: <https://www.elexon.co.uk/about/other-services/data-flows/>
- [229] M. Bolinger and R. Wiser, “Understanding trends in wind turbine prices over the past decade,” Lawrence Berkeley National Laboratory, Berkeley, Tech. Rep., 2011.

Bibliography

- [230] R. Wiser and M. Bolinger, “2015 Wind Technologies Market Report,” 2016. [Online]. Available: <https://energy.gov/sites/prod/files/2016/08/f33/2015-Wind-Technologies-Market-Report-08162016.pdf>
- [231] E. De Vries, “Enercon raises the bar,” 2017. [Online]. Available: <http://www.windpowermonthly.com/article/1428420/exclusive-enercon-raises-bar>
- [232] OREC, “Catapult delivers first blade leading edge erosion measurement campaign,” 2016. [Online]. Available: <https://ore.catapult.org.uk/press-release/catapult-delivers-first-blade-leading-edge-erosion-measurement-campaign/>
- [233] V. Rajput, “From financial death to the life Life Time Extension (LTE),” in *WindEurope Summit 2016*, Hamburg, 2016.
- [234] J. Olauson, P. Edström, and J. Rydén, “Wind turbine performance decline in Sweden,” *Wind Energy*, aug 2017. [Online]. Available: <http://doi.wiley.com/10.1002/we.2132>
- [235] WindEurope, “Financing and investment trends,” 2016. [Online]. Available: <https://windeurope.org/about-wind/reports/financing-investment-trends-2016/>
- [236] T. Rubert, L. Ziegler, E. Gonzalez, D. McMillan, U. Smolka, and J. J. Melero, “The UK’s Lifetime Extension Environment of Onshore Wind Turbines,” in *RenewableUK Onshore Asset Management 2017*, Glasgow, UK, 2017.
- [237] Micron Optics, “Micron Optics - Sensor Overview,” 2015. [Online]. Available: <http://www.micronoptics.com/products/sensing-solutions/sensors/>
- [238] G. Brambilla, “High-temperature fibre Bragg grating thermometer,” *Electronics Letters*, vol. 20020690, 2001.
- [239] F. Abe, “Creep-Resistant Steels,” in *Creep-Resistant Steels*. Elsevier, 2008, ch. Part I: Ge, pp. i–iii. [Online]. Available: <http://linkinghub.elsevier.com/retrieve/pii/B9781845691783500243>
- [240] K. Kalli, G. Simpson, H. Dobb, M. Komodromos, D. Webb, and I. Bennion, “Annealing and temperature coefficient study of type IA fibre Bragg gratings

Bibliography

- inscribed under strain and no strain - implications to optical fibre component reliability,” *Photonics Europe*, vol. 6193, pp. 1–12, 2006. [Online]. Available: <http://eprints.aston.ac.uk/24187/>
- [241] I. A. Assakkaf, “Columns: buckling,” 2003. [Online]. Available: <http://www.assakkaf.com/courses/enes220/lectures/lecture27.pdf>
- [242] G. P. Tilly, “Fatigue testing and performance of steel reinforcement bars,” *Matériaux et Constructions*, vol. 17, no. 1, pp. 43–49, jan 1984. [Online]. Available: <http://link.springer.com/10.1007/BF02474055>
- [243] Nordtest, “Steels for concrete reinforcement: axial load fatigue testing of bars,” Tech. Rep., 1989. [Online]. Available: http://www.nordtest.info/images/documents/nt-methods/mechanics/NTmech014_Steelsforconcretereinforcement_Axialloadfatiguetestingofbars_NordtestMethod.pdf
- [244] Z. Hongyan and J. Senkara, *Resistance Welding: Fundamentals and Applications*, second edi ed. CRC Press, 2011.
- [245] V. Kazymyrovych, “Very high cycle fatigue of engineering materials Very high cycle fatigue of engineering materials,” Karlstad University, Karlstad, Tech. Rep., 2009.
- [246] T. V. Baughn and S. Chen, “Low Cycle Fatigue in RF Microwave Module Housings,” in *International Electronic Packaging Technical Conference and Exhibition*, 2003.
- [247] J. McAlorum, T. Rubert, G. Fusiek, I. McKeeman, L. Clayburn, M. Perry, and P. Niewczas, “Comparison of epoxy and braze-welded attachment methods for FBG strain gauges,” in *2017 IEEE SENSORS*. Glasgow, UK: IEEE, oct 2017, pp. 1–3. [Online]. Available: <http://ieeexplore.ieee.org/document/8234109/>
- [248] Vestas, “Vestas receives 110 MW order for upgraded 3 MW platform in the UK,” Tech. Rep. December 2015, 2017. [Online]. Available: [https://www.vestas.com/en/media/\\$\sim\\$/media/ef523e0066af49d79c48e3de425e40aa.ashx](https://www.vestas.com/en/media/\sim/media/ef523e0066af49d79c48e3de425e40aa.ashx)

Bibliography

- [249] T. Rubert, G. Fusiek, P. Niewczas, J. McAlorum, and M. Perry, “Characterisation of metal-packaged fibre Bragg gratings under fatigue loading for structural health monitoring in civil engineering applications,” AM06 Project Report, Tech. Rep., 2016.
- [250] M. Kreuzer, “Strain measurement with fiber bragg grating sensors,” Tech. Rep., 2015. [Online]. Available: http://micronoptics.ru/uploads/library/documents/FBGS_StrainMeasurement_mo.pdf
- [251] T. Rubert, G. Fusiek, J. McAlorum, M. Perry, P. Niewczas, and A. Brotherston, “Installation of embedded optical sensors within a wind turbine foundation,” AM06 Project Report, Tech. Rep., 2016.
- [252] K. E. Chisholm, K. Sugden, and K. Bennion, “Effects of thermal annealing on Bragg fibre gratings in boron/germania co-doped fibre,” *J. Phys. D: Appl. Phys.*, 1998.
- [253] B. Glišić, D. Posenato, D. Inaudi, and A. Figini, “Structural health monitoring method for curved concrete bridge box girders,” M. Tomizuka, Ed., mar 2008, p. 693204. [Online]. Available: <http://proceedings.spiedigitallibrary.org/proceeding.aspx?doi=10.1117/12.778643>
- [254] J. Osborne, *Best Practices in Quantitative Methods*, 1st ed. SAGE Publications, Inc, 2008.
- [255] C. Honeywill and M. Ellse, *Electricity and Thermal Physics*, 2nd ed. Nelson Thornes, 2004.
- [256] P. Welch, “The use of fast Fourier transform for the estimation of power spectra: a method based on time averaging over short, modified periodogram,” *IEEE Trans Audio Electroacoustics*, vol. 15 (2), pp. 70–73, 1967.
- [257] S. Kay, *Modern spectral estimation: theory and application*. Prentice Hall, 1987.
- [258] R. Kazacoks, “Internal Siemens 2.3 MW Bladed Model,” 2018.

Bibliography

- [259] D. W. Thompson, “Doctoral Thesis: Mitigating Size Related Limitations in Wind Turbine Control,” no. October, 2017.
- [260] J. Jonkman, S. Butterfield, W. Musial, and G. Scott, “Definition of a 5-MW Reference Wind Turbine for Offshore System Development,” no. February, 2009. [Online]. Available: <http://www.osti.gov/servlets/purl/947422-nhrlni/>
- [261] C. Bak, F. Zahle, R. Bitsche, T. Kim, A. Yde, L. C. Henriksen, A. Natarajan, and H. Morten, “DTU Wind Energy Report-I-0092,” 2013.
- [262] W. Thomson and P. G. Tait, *Natural Philosophy*. Oxford: MacMillan and Co., 1870.
- [263] IEC, “61400-13 2001,” pp. 0–4, 2003.
- [264] N. Beganovic and D. Söffker, “Structural health management utilization for lifetime prognosis and advanced control strategy deployment of wind turbines: An overview and outlook concerning actual methods, tools, and obtained results,” *Renewable and Sustainable Energy Reviews*, vol. 64, pp. 68–83, oct 2016. [Online]. Available: <http://linkinghub.elsevier.com/retrieve/pii/S1364032116301952>
- [265] M. L. Wymore, J. E. Van Dam, H. Ceylan, and D. Qiao, “A survey of health monitoring systems for wind turbines,” *Renewable and Sustainable Energy Reviews*, vol. 52, pp. 976–990, dec 2015. [Online]. Available: <http://linkinghub.elsevier.com/retrieve/pii/S1364032115007571>
- [266] K. Smarsly, D. Hartmann, and K. H. Law, “An Integrated Monitoring System for Life-Cycle Management of Wind Turbines,” *International Journal of Smart Structures and Systems*, vol. 12, no. 2, pp. 209–233, 2012.
- [267] C. Rebelo, M. Veljkovic, L. S. Da Silva, R. Simões, and J. Henriques, “Structural monitoring of a wind turbine steel tower - Part I: System description and calibration,” *Wind and Structures, An International Journal*, vol. 15, no. 4, pp. 285–299, 2012.

Bibliography

- [268] C. Rebelo, M. Veljkovic, R. Matos, and L. Simões Da Silva, “Structural monitoring of a wind turbine steel tower - Part II: Monitoring results,” *Wind and Structures, An International Journal*, vol. 15, no. 4, pp. 301–311, 2012.
- [269] M. Botz, S. Oberlaender, M. Raith, and C. U. Grosse, “Monitoring of Wind Turbine Structures with Concrete - steel Hybrid - tower Design,” *8th European Workshop On Structural Health Monitoring (EWSHM 2016)*, no. August, pp. 5–8, 2015.
- [270] H. J. Sutherland, *On the Fatigue Analysis of Wind Turbines*, Albuquerque, New Mexico, 1999.
- [271] ASTM, “Standard Practices for Cycle Counting in Fatigue Analysis. Standard E1049-85,” 2011.
- [272] C. Loraux, “Long-term monitoring of existing wind turbine towers and fatigue performance of UHPFCR under compressive stresses,” 2018. [Online]. Available: <https://infoscience.epfl.ch/record/234540>
- [273] T. Rubert, M. Perry, G. Fusiek, J. McAlorum, P. Niewczas, A. Brotherston, and D. McCallum, “Field Demonstration of Real-Time Wind Turbine Foundation Strain Monitoring,” *Sensors*, vol. 18, no. 1, p. 97, dec 2017. [Online]. Available: <http://www.mdpi.com/1424-8220/18/1/97>
- [274] M. Perry, J. McAlorum, G. Fusiek, P. Niewczas, I. McKeeman, and T. Rubert, “Crack Monitoring of Operational Wind Turbine Foundations,” *Sensors*, vol. 17, no. 8, p. 1925, aug 2017. [Online]. Available: <http://www.mdpi.com/1424-8220/17/8/1925>
- [275] T. Rubert, D. McMillan, and P. Niewczas, “The Effect of Upscaling and Performance Degradation on Onshore Wind Turbine Lifetime Extension Decision Making,” *Journal of Physics: Conference Series*, vol. 926, p. 012013, nov 2017. [Online]. Available: <http://stacks.iop.org/1742-6596/926/i=1/a=012013?key=crossref.63b19258ed5ed2069d531236b4256c69>

Bibliography

- [276] D. Vose, *Risk Analysis: A Quantitative Guide*. Wiley, 2008.
- [277] P. Tavner, D. M. Greenwood, M. W. G. Whittle, R. Gindele, S. Faulstich, and B. Hahn, “Study of weather and location effects on wind turbine failure rates,” *Wind Energy*, vol. 16, no. 2, pp. 175–187, mar 2013. [Online]. Available: <http://doi.wiley.com/10.1002/we.538>
- [278] G. Wilson and D. McMillan, “Assessing Wind Farm Reliability Using Weather Dependent Failure Rates,” *Journal of Physics: Conference Series*, vol. 524, p. 012181, jun 2014. [Online]. Available: <http://stacks.iop.org/1742-6596/524/i=1/a=012181?key=crossref.b8dc65677e053e3646aa421e267e73ed>
- [279] M. Reder and J. J. Melero, “Modelling the effects of environmental conditions on wind turbine failures,” *Wind Energy*, may 2018. [Online]. Available: <http://doi.wiley.com/10.1002/we.2201>
- [280] M. Schedat, T. Faber, and A. Sivanesan, “Structural health monitoring concept to predict the remaining lifetime of the wind turbine structure,” *Domestic Use of Energy, DUE 2016*, 2016.
- [281] A. Mehmanparast, J. Taylor, F. Brennan, and I. Tavares, “Experimental investigation of mechanical and fracture properties of offshore wind monopile weldments: SLIC interlaboratory test results,” *Fatigue and Fracture of Engineering Materials and Structures*, no. May, pp. 1–17, may 2018. [Online]. Available: <http://doi.wiley.com/10.1111/ffe.12850>
- [282] D. Helm, “Cost of Energy Review,” 2017.
- [283] C. R. Brett, S. A. Lockyer, K. A. Soady, and S. Thomson, “Development of a Repair Technique for Cracking in Wind Turbine Nacelle Bed Plates.pdf,” in *WindEurope*, Amsterdam, 2017. [Online]. Available: <http://proceedings.windeurope.org/confex2017/posters/PO167.pdf>
- [284] DNV GL, “IMPROVED UNDERSTANDING OF CONCRETE FATIGUE ALLOWING MORE OPTIMIZED DE-

Bibliography

- SIGN,” 2018. [Online]. Available: <https://www.dnvgl.com/news/improved-understanding-of-concrete-fatigue-allowing-more-optimized-design-121750>
- [285] T. Rubert, “LTE FMEA Study.” [Online]. Available: <https://drive.google.com/drive/folders/1ukVRyj5jrK4Z8gOrGDb7Av07Ky3CDS2K?usp=sharing>